Development of opto-acousto-optical methods for three dimensional material imaging with nano-acoustic longitudinal and transversal waves

Théo Thréard

DOCTORAT BRETAGNE LOIRE SCIENCES POUR L'INGENIEUR

Le Mans Université

THÈSE DE DOCTORAT DE

LE MANS UNIVERSITÉ

ÉCOLE DOCTORALE N° 602
Sciences pour l'Ingénieur
Spécialité : *Acoustique*

Par

Théo THRÉARD

Development of opto-acousto-optical methods for three dimensional material imaging with nano-acoustic longitudinal and transversal waves.

Thèse présentée et soutenue à « Le Mans Université », le « 06 Décembre 2021 »
Unité de recherche : « Laboratoire d'acoustique de l'Université du Mans (LAUM), UMR-CNRS 6613»
Thèse N° : 2021LEMA1031

Reviewers :

Natalia DEL FATTI Professeure des universités - Université Lyon 1
Osamu MATSUDA Associate professor - Hokkaido University

Jury composition :

Président :	Philippe DJEMIA	Professeur des universités - Université Paris 13
Dir. de thèse :	Vitalyi E. GUSEV	Professeur des universités - Le Mans Université
Co-dir. de thèse :	Samuel RAETZ	Maître de conférences - Le Mans Université
	Nikolay CHIGAREV	Ingénieur de recherche - Le Mans Université

Invité(s) :

David HURLEY Director - Center for thermal energy transport under irradiation - Idaho University

To my parents, Christine and Didier.
To my brothers, Julien and Loann.
To Meryem.

Please consider not printing this document, for the sake of our planet.

ACKNOWLEDGEMENTS

A Ph.D. thesis is a personal and professional three years experience, resulting in (i) the following manuscript from the scientific point of view and (ii) life-long memories from colleagues, collaborators and friends. I will try to transpose via the following acknowledgements how lucky I have been, and how grateful I am, to the people that crossed my road during my stay at the acoustic laboratory of Le Mans University (LAUM - UMR CNRS 6613).

The work that is presented in this manuscript is the result of three wonderful years of collaboration with a great number of people that I wish to acknowledge in the following pages.
First over all, I would like to warmly thank my Ph.D. supervisors: Pr. Vitalyi Gusev, Dr. Samuel Raetz and Dr. Nikolay Chigarev, for giving me their trust, and the opportunity to accomplish this work with them. It has been a real pleasure to work with each of you three. I have learned a lot thanks to your complementary skills and approaches, and I can not thank you enough for it. I wish every Ph.D. student to have the chance of being so nicely supervised as I have been during these three years, on both personal and scientific aspects. Indeed, in addition to being dedicated and pedagogical mentors, you have always been caring about my well-being, especially in the tough situations that we have faced in the second half of the thesis. For all these reasons: merci infiniment.
I would like to acknowledge Pr. Natalia Del Fatti and Pr. Osamu Matsuda for accepting to review my thesis work, as well as Pr. Philippe Djemia and Dr. David Hurley for having agreed to be part of the jury.
Moreover, I am really thankful to Dr. David Hurley's team in Idaho National Laboratory, and in particular to Dr. Zilong Hua, for the fruitful discussions and collaborations around the ceria sample they provided us, and for the associated EBSD datas. Working with you has definitely been a source of inspiration and motivation.
I am also really grateful to Pr. Matsuda and Pr. Oliver Wright for accepting me in an internship program at Hokkaido University, even though a (nanometer-sized) virus decided otherwise. I am thankful to the CEED office at Hokkaido University and in particular to Ms. Eriko Yoshida for keeping us updated during more than one year on the possibility to finally come to Hokkaido. I did not set a foot on Hokkaido's island, but I have felt warmly welcomed, thanks a lot. I am also grateful to the Institut d'Acoustique - Graduate School (IA-GS) for granting me the scholarship that would have helped me finance the internship.

I wish to thank Pr. Laurent Simon for providing me extended documentation on the wonderful time-frequency world and for his help understanding it. I also want to thank Dr. Charfeddine Mechri for pointing me to the wavelets direction and for the interesting discussions we had.

This Ph.D. thesis has been prepared at the acoustic laboratory of Le Mans University (LAUM - UMR CNRS 6613), and I have been part of the "Laser Ultrasonics" team. I would like to thank the (past and actual) members of this team (Samuel, Nikolay, Vitali, Vincent, James, Guqi, Artem, Romain, Elton, Sandeep, Juliette, Louise, Nicolas, Yves and Lou-Anne) for their constant efforts in organising group meetings where we were able to present ongoing work in a relaxed and conducive atmosphere. I am especially grateful to two post-docs with whom I had the privilege to work with: Dr. Elton de Lima Savi and Dr. Sandeep Sathyan. I have learned a lot from you, in particular on the experimental aspect of this work. Elton helped me handling the imaging system with confidence at the beginning of the PhD, and Sandeep taught me (among a lot of his skills) the efficient way to conduct experiments, also pointing out interesting aspects of our work during our many discussions, while I disappointingly failed to make him speak a single word of french..!
Having the possibility to do this Ph.D. work with confidence, in a great environment, is owing to the different members of the LAUM. I am thankful to the laboratory heads, Pierrick Lotton, Laurent Simon and Paola Bertelli, as well as the laboratory council, for accepting me as a Ph.D. representative, and for their constant efforts in making the laboratory a good working place, for everyone. The year 2020 has been handle in a "familial" way, making sure no one was left alone, highlighting the peculiar but attaching (likeable) way the LAUM is managed. I feel privileged to have been a small part of the story of the LAUM.
I am also thankful to the administrative members of the LAUM that were always available and making their best for helping us in accomplishing the different administrative tasks required during these years. I am thus thanking in particular Anne-Marie, Paola, Jana, Sandrine and Veroniqua with whom I had usually worked with.
A good part of this work was experimental, and the help provided with efficiency and rapidity contributed to the success of the experiments. I am thus grateful to the technical members of the LAUM and in particular to James Blondeau. I wish to warmly thank the NETA team, with whom we have been working on the experimental ASOPS scanning system, the JAX-M1. Their reactivity, availability and confidence helped us develop the imaging system in the best direction possible for our research. I would thus like to thank Xavier Trindon, Julien Michelon and Allaoua Abbas in particular.
On a final note to the laboratory, I am thinking about my "first team", the MGZZ, or "Granular team", with Georgios, Florian, Li-Yang, Shilin, Vincent and Vitali. Thanks for introducing me to the research world during my Master internship, in a good but productive mood. GG guys !
Finally, I am in debt to Paola Bertelli for the different good-looking pictures of the setup, the samples and...myself. Thank you for becoming such a good friend !

Looking back at this first day in January 2014, and the first proper acoustic course of my life, never would have I thought about switching roles and teaching, in practicals and in the frame of student projects, to Bachelor and Master students. This rewarding opportunity was made possible thanks to the researchers and teachers of the acoustic department (DAUM) to whom I am grateful, for their availability and their help in preparing myself for such a new role. I am thus really grateful to Bruno Gazengel, Christophe Ayrault, Olivier Richoux, Philippe Béquin, Sylvie Houlbert, Cyril Desjouy, Jean Pierre Dalmont, Samuel Raetz and Laurent Simon.
The rigorous Ph.D. thesis management from the pole doctoral is acknowledged here, with particular thanks to Geoffroy Martin and Virgine Froger.

Maintenant que les acteurs les "plus sérieux" ont été remerciés, je m'autorise à terminer ces remerciements dans ma langue natale, afin de m'adresser aux différentes personnes qui m'ont permis de réaliser ce travail de thèse de 3 ans en gardant quotidiennement le sourire et la motivation nécessaire.
Dans un premier temps, je souhaite remercier mes colloques du bureau 81 (passé et présent): Théo, Robin, Thomas, Jean, Tang, Yuzhou, Yeng, Louise et Eric. De nombreuses discussions resteront sous silence pour le bien de l'humanité, cependant nos quelques échanges scientifiques auront été instructifs. Merci pour la bonne ambiance !
Les 3 années de thèses se vivent à plusieurs, dans le même bateau, et j'ai eu la chance d'avoir de nombreux compagnons d'infortune avec qui les pauses café et repas auront permis de garder le cap. Je pense en particulier aux doctorants de "ma génération", Gautier dit "Goutier"ou "l'homme qui murmurait à l'oreille des gouttes", Thomas et sa répartie tranchante, Colas dit "Commandant Cousteau", Erwan dit "Holo-man", Jean-Baptiste dit "Boulon-man", et le reste de la team Erwan, Meryem, Jules, et Guillaume. Je tairai les quelques occasions ou le bateau se mit à tanguer face à une importante houle, faisant alors honneur au poème de Rimbaud.
Nous avons eu la chance d'être précédés par des doctorants bienveillants, toujours disponibles pour échanger avec nous des procédures et de nos doutes, je tiens donc à remercier R. Matthieu Malléjac (pour comprendree le "R.", merci de lire les oeuvres de Asimov), Thibault Abily pour son aide précieuse au conseil du laboratoire et sa bonne humeur, Mathieu Gaborit, Elie, Samuel, et Charlotte et Valentin.
Je tiens aussi à remercier Florian Allein et Thibaut Devaux, avec qui j'ai eu l'occasion de bien réfléchir en amont au projet de thèse. Vos nombreux conseils se sont avérés très utiles, merci !
Ces derniers remerciements me permettent de faire la transition vers l'association RAmDAM que j'ai eu la chance et le privilège de présider pendant mes 2 premières années de thèse. Je souhaiterais ici remercier l'ensemble des personnes qui m'ont épaulé afin de rendre ces années mémorables. Parmi les personnes précédemment citées, je pense à Gautier, Matthieu, Elie, Erwan et Meryem. Parmi les non-cités, je remercie Antoine Sternberger et son dynamisme, Adrien, Constance, Felix, Lénaig (pense à manger !), Nicolas, Gaëlle et Jean-Pierre, Elliot, Joris, Raphaël, Valentin et Nina. Votre implication dans l'association a

permis d'organiser des évènements que je n'aurai pas imaginé organiser, le tout dans la bonne humeur. J'espère ne pas vous avoir traumatisés, et que vous en garderez d'aussi bons souvenirs que moi ! Je souhaite un bon vent à la prochaine équipe, menée par Guilhem et Elie, en sachant pertinemment que tout est sous contrôle en regard des super projets en approche... Enjoy !
Mention spéciale à Murielle dite "Mumu", de la cafet' des sciences, pour tous les cafés d'après permanence RAmDAM...!

Enfin, en sortant du périmètre géographique de l'Université, il me reste un certain nombre de personnes que je me dois de remercier pour leur présence et leur soutien durant ces différentes années.
Tout d'abord, j'ai la chance d'avoir franchit les différentes étapes de l'enseignement supérieur avec d'autres étudiants qui, au fil des années, sont devenus des amis puis comme une seconde famille. Je remercie donc ici Nina, Jane, Bertille, Nathalie, Justin, Thomas, Said, Vivien, Thibault, Matteo, Ewen, Hugo et Alexis. Nous avons beau être maintenant éparpillés partout en France (voire en Europe), nos différentes vacances de groupes ont permis de remettre les compteurs à zéro et reprendre le travail dans les meilleures conditions. Ainsi, que ce soit lors de nos voyages à Bordeaux, à Oléron, au Mont-Saint-Michel, et même au Mans (!), ou bien lors de la coupure de la rédaction de thèse pour aller cracher mes poumons dans la montée de Valbuche, nos fourberies et escapades auront été de vraies bouffées d'oxygène. Merci pour tous, les amis ! On me dit dans l'oreillette qu'en plus, c'est loin d'être terminé..!
Pour terminer, je ne serai jamais arrivé jusqu'ici sans les efforts de mes parents, Christine et Didier, ainsi que le soutien de mes frères et leurs conjointes, Loann et Pauline, Julien et Hyacinthe. Merci d'avoir toujours été là pour moi. En plus, obtenir le grade de docteur l'année ou "The Doctor" part à la retraite c'est un signe, une page qui se tourne !
Bien entendu, ces remerciements ne peuvent être complets sans que je ne remercie Meryem. C'était un vrai pari que de commencer nos thèses le même jour, cela s'est transformé en défi lorsque nous nous sommes retrouvés confinés à mi-parcourt. À aucun moment je n'ai ressenti de faiblesse et tu en es la première raison. Merci pour tout.

«The most exciting phrase to hear in science, the one that heralds new discoveries, is not 'Eureka!' but 'That's funny...'»

Isaac Asimov
1920 - 1992

TABLE OF CONTENTS

List of Figures

List of Tables

NOMENCLATURE

a	Scale parameter of the CWT
$a_{CAP,t}$	Projection of the transmitted CAP beam radius on the x-axis
A_{mod}	Amplitude parameter of the Gaussian and exponential model
a_r	Zener ratio
a_{pump}, a_{probe}, a_{CAP}	Radius of the intensity distribution (at the $1/e^2$ level) of the pump, probe lasers and CAP beams
$\bar{a}_{probe}$	Normalized a_{probe}, or probe by CAP beam radii ratio
$a_{overlap}$	Radius at the $1/e^2$ of the overlap between the Gaussian distributions of the probe light and the incident CAP beams
$a_{overlap,\alpha}$	Radius at the $1/e^2$ of the overlap between the Gaussian distributions of the probe light and the reflected CAP beams
$a_{overlap,t,\alpha}$	Radius at the $1/e^2$ of the overlap between the Gaussian distributions of the probe light and the transmitted CAP beams
$A(t)$	Amplitude of the acoustic signal model
B	Bulk modulus
b	Translational parameter of the CWT
C_{ij}	Elastic constants of a material
c_j	Speed of light in material (j)
C_v	Specific heat per unit volume
c_{vacuum}	Speed of light in vacuum
d	Thickness (of the metallic film used as an OAT)
D_B	Directivity pattern of the TDBS detection
D_{B0}	Directivity pattern of the TDBS detection with $l_{CAP} = 0$
$\mathbf{E^{(j)}}(t,x,y,z)$	Electric field vector in material (j)
$E^{(j)}(t,x,y,z)$	Electric field amplitude in material (j)
f_{BO}	Brillouin oscillation frequency
f_{BO}^m	Brillouin oscillation frequency of mode m
f_{pump}	Pulse repetition frequency of the pump laser
g	Electron-phonon coupling constant
$G_r(\theta)$	Spatio-temporal factor describing the dynamic of the reflected CAP

$G_t(\theta)$	Spatio-temporal factor describing the dynamic of the transmitted CAP
$G(z,t)$	Spatio-temporal thermal source function
$\mathbf{H}^{(\mathbf{j})}(t,x,y,z)$	Magnetic field vector in material j
$H(t)$	Time window used to compute the STFT (Hann window)
i	Imaginary number
$I_f(t)$	Optical pulse intensity variation
$I_{gaussian}$	Gaussian model of the intensity distribution at the laser beam waist
$I^{(j)}(x,y,z)$	Intensity of the electric field amplitude in material (j)
K	Thermal conductivity
k_a	Acoustic wavenumber
k_j	Optical wavenumber in material (j)
l_B	Overlap volume length of the probe light and CAP beams
l_{CAP}	Half-length of the unipolar Gaussian strain pulse (at $1/e^2$ level)
$l_{CAP,t}$	Scaled l_{CAP} after transmission of the CAP at the material interface
$L_{coherence}^{probe}$	Coherence length of the probe laser pulse
L_R	Diffraction length (Gaussian beams)
$\mathbf{n}$	Propagation direction vector
$\tilde{n}_j$	Optical refractive index (complex) in material (j)
n_j	Real part of the refractive index $\tilde{n}_j$
$P(t,x,y,z)$	Acoustically-induced nonlinear optical polarization
p_j	Photoelastic constant in material (j)
R	Optical intensity reflection coefficient
r_{jl}	Optical amplitude reflection coefficient between material (j) and (l)
r_{jl}^{ac}	Acoustic amplitude reflection coefficient between material (j) and (l)
Q	Energy of the incident pump laser pulse
q	Laser fluence
$s(t)$	Acoustic signal model
t	Time variable
t_{jl}	Optical amplitude transmission coefficient between material (j) and (l)
t_{jl}^{ac}	Acoustic amplitude transmission coefficient between material (j) and (l)

T_m^{min}	Period associated to the slowest mode m in ceria
$\mathbf{u}(t,x,y,z)$	Displacement vector
u_z	Displacement component along the z direction
$\mathbf{v}(t,x,y,z)$	Velocity vector
v_m	Phase velocity of the acoustic mode m
$W^{detected}$	Optical energy collected at the photodetector (TDBS in reflection configuration)
$W^{heterodyned}$	Optical probe energy contribution from the heterodyned probe light at the photodetector
$W^{reflected}$	Optical energy contribution from the reflected probe light at the photodetector
$W^{scattered}$	Optical energy contribution from the scattered probe light by the CAP at the photodetector
$WSST_s(\omega,b)$	Wavelet synchrosqueezed transform (WSST) of $s(t)$
$W_s(a,b)$	Continuous wavelet transform (CWT) of signal $s(t)$
x	Spatial variable along the x-axis
x_A	x-coordinate of point A
y	Spatial variable along the y-axis
z	Spatial variable along the z-axis (depth)
z_0	Coordinate of the rays center intersection of the probe light and CAP beams (on the z-axis)
$z_a(t)$	Position along the z-axis of the CAP strain at time t
α	Inclination angle between the probe light and CAP beams propagation directions
α_{1/e^2}	Critical inclination angle for which D_B reaches the $1/e^2$ level
α_{ac}	Acoustic absorption coefficient
$\underline{\underline{\alpha}}^T$	Thermal expansion tensor
α^{max}	angle α associated to the maximal $\omega_B(\alpha)$ value
α^{shape}	Radius of the sphere in the 3-D alphashape algorithm
$\alpha^\star$	Effective thermal expansion coefficient
α^T	Thermal expansion coefficient (linear)
$\bar{\beta}$	Normalized β variable (β being any defined variable)
γ	Gruneisen parameter
$\underline{\underline{\Gamma}}$	Christoffel's tensor
$\delta(t)$	Dirac delta function
$\underline{\underline{\delta}}$	Identity tensor
δ_{ij}	Kronecker symbol

Δf	Beating frequency between the ASOPS laser cavities
Δf_{BO}^{m}	Non-dimensionnal parameter accounting for BF shifting of mode m
$\Delta R/R$	Relative transient reflectivity
ΔT	Thermal field distribution
$\Delta\epsilon$	Weak permittivity variations induced by the CAP
$\Delta\Omega_B$	Spectral full width of Ω_B
ϵ_{vacuum}	Electric permittivity in free space
ϵ_j	Relative electric permittivity in material (j)
ζ	Optical penetration depth
$\eta(t,x,y,z)$	CAP strain field
η_0	Strain amplitude
η_{zz}	Only non-zero component of the strain tensor in 1-D assumption (propagation along z-axis)
θ	Inclination angle of the material interface relative to the free surface $z=0$
θ_{FF}^{CAP}	CAP half angle of divergence in the far field
θ_{FF}^{probe}	Probe half angle of divergence in the far field
$\theta^{incident}$	Incidence angle of the probe laser beam on the sample surface
θ_t	Angle of CAP transmission / refraction at a material interface
κ_j	Absorption coefficient of light in material (j)
λ	Optical wavelength in vacuum
λ_{BO}	Wavelength at the BO frequency
$\lambda_{pump}, \lambda_{probe}$	Optical wavelength of the pump/probe laser in vacuum
μ	Poisson's ratio
μ_{vacuum}	Magnetic permeability in free space
μ_j	Relative magnetic permeability in material (j)
$\tilde{\xi}_j$	Electric susceptibility in material (j) (complex)
ρ	Density
$\underline{\underline{\sigma}}^T$	Thermoelastic stress tensor
σ^T	Spherical thermoelastic stress tensor
σ_{zz}	Only non-zero component of the stress tensor in 1-D assumption (propagation along z-axis)
$\bar{\tau}$	Characteristic time combining τ_r and τ_B
τ_B	TDBS wave packet duration
τ_c	Coherence time of the probe laser pulse

τ_i	Time taken by the incident CAP to be reflected / transmitted by the interface, as it is monitored by TDBS
τ_{probe}	Duration of the probe laser pulse
τ_r	Time taken by the reflected CAP to be reflected / transmitted by the interface, as it is monitored by TDBS
$\phi(t, x, y, z)$	Scalar potential of the velocity vector $\mathbf{v}$
ϕ_{mod}	Phase term of the Gaussian exponential model
$\phi(t)$	Phase of the acoustic signal model
$\tilde{\chi}_j$	Electric susceptibility (complex) in material (j)
χ_j	Real part of the electric susceptibility in material (j)
Ψ	Mother wavelet of the CWT
$\boldsymbol{\psi}(t, x, y, z)$	Vector potential of the velocity vector $\mathbf{v}$
Ψ_{bump}	Bump wavelet
$\psi(t)$	Rapidly varying part of the phase $\phi(t)$ of the acoustic signal model
ω	Angular frequency of light
ω_B	Acoustic angular frequency
$\omega_{B,t}$	Scaled ω_B after CAP transmission at a material interface
Ω_B	Monochromatic carrier frequency in the TDBS wave packet
Ω_B^{max}	Maximal $\omega_B(\alpha)$ value
Ω_{B0}	Monochromatic carrier frequency in the TDBS wave packet with $l_{CAP} = 0$
$\omega_s(a, b)$	Instantaneous frequency in $W_s(a, b)$ (candidate)
$\mathbb{1}$	Indicator function
erf	Error function
erfc	Complementary error function
sign	sign function (or *signum*)

List of Acronyms

AFM Atomic force microscope
ASOPS Asynchronous optical sampling
BBO Beta barium borate (crystal)
BF Brillouin frequency
BO Brillouin oscillations
CAP Coherent acoustic pulse
CWT Continuous wavelet transform
DAC Diamond anvil cell
EBSD Electron backscattering diffraction
FDBS Frequency-domain Brillouin scattering
FIR Finite impulse response
fQTA "Fast" quasi-transversal acoustic (mode)
FT Fourier transform
fTA "fast" transversal acoustic (mode)
IR Infra-red
IWSST Inverse wavelet synchrosqueezed transform
LA Longitudinal acoustic (mode)
LUI Laser ultrasonic imaging
MRI Magnetic resonance imaging
NDT Non-destructive testing
OAT Opto-acoustic transducer
PAI Photoacoustic imaging
PAT Photoacoustic tomography
QLA Quasi-longitudinal acoustic (mode)
QTA Quasi-transversal acoustic (mode)
SDT Synchronous detection technique
SEM Scanning electron microscope
SNR Signal-to-noise ratio
SPM Scanning probe microscopy
sQTA "Slow" quasi-transversal acoustic (mode)
sTA "slow" transversal acoustic (mode)
STFT Short-time Fourier transform
STM Scanning tunnelling microscope (or microscopy)
TA Transversal acoustic (mode)
TDBS Time-domain Brillouin scattering
TEM Transmission electron microscope
UV Ultra-violet
WSST Wavelet synchrosqueezed transform

GENERAL INTRODUCTION

It is at the end of the 19th century that the possibility of an interaction between light (an electromagnetic wave) and sound (an elastic wave) was experimentally evidenced for the first time, owing to "The Photophone" of A. G. Bell, assisted by S. Tainter [1]. In its 1880's communication published in Nature, Bell reported that "when a vibratory beam of light falls upon these substances[1] they emit sounds", a pioneer statement of the light-sound interaction known as the photoacoustic effect. However, it is only in the beginning of the 1960's that the photoacoustic effect was propelled one step forward, with the creation of the laser (Light Amplification by Stimulated Emission of Radiation) by T. H. Maiman [2]. The laser ultrasonic discipline was born, and it took only three years for R. M. White to evidence the generation of elastic waves in matter using lasers [3].

The photoacoustic effect (also referred as optoacoustic effect) designate the conversion of the laser light into acoustic (elastic) waves, via the absorption of the light energy by a material. Once an acoustic wave is launched in a sample via the optoacoustic effect, the monitoring of its propagation can also be realised with a laser light, since the acoustic wave can change locally the optical properties of the material. This acousto-optic interaction can thus be combined with the optoacoustic generation to create an all-optical, non-contact technique to characterise materials, at scales typically unreachable by conventional ultrasound techniques (using transducers). The characterisation of materials and, to a further extent, material imaging, was not new when the laser technology was introduced. In fact, the discovery by L. Brillouin and L. I. Mandelstam of the scattering of light by an elastic (acoustic) disturbance, is approaching its 100 years anniversary [4, 5].
However, it is with the shortening of the laser pulse durations, down to hundreds of femtosecond (fs, 10^{-15} s) that the generation of elastic waves in the GHz (10^9 - 10^{12} Hz) frequency range was made possible. More exactly, it is in 1984 that H. J. Maris and his team [6], have established the first picosecond acoustic experiment, drastically enhancing the frequency band and the spatial resolution of such laser ultrasonic techniques.
It is finally with recent technical developments in laser technology that the extension from single point measurements to raster scan, and thus 3-D characterisation, was made possible with picosecond acoustic techniques.

[1] The word "substances" referred here to the different metals they studied: Au, Ag, Zn, Pt ...
The photophone is an ingenious selenium-(Se)-based apparel capable of carrying a conversation via light transport between two individuals up to 231 (!) meters apart.

In this thesis, we present our contribution to the development of a non-contact, non-destructive method to study the structure of materials, in three-dimensions (3-D), at the micrometer to the nanometer scales, by means of an opto-acousto-optic experimental method, using the time-domain Brillouin scattering (TDBS) detection technique and a dedicated processing of the data. The development of a step-by-step signal processing procedure led to the complete 3-D reconstruction of the structure of transparent polycrystals. The multiple-grains structure of the samples was evidenced along with interesting features in the frame of imaging. Imaging contrast has been enhanced with the complementary use of transversal waves, in addition to the longitudinal ones. Grain boundaries, inclined relative to the propagation direction of sound and light, were also evidenced and characterized, requiring the extension of the TDBS theory to the situation where an inclined interface is present. A theory is thus developed to account for the non-collinear propagation between the optical and acoustical fields, induced by the refraction of the latter at the interface.
Part of this manuscript has been published in *Journal of Applied Physics* [7], *Photoacoustics* [8] and provided on the ArXive platefrom [9].

This manuscript is composed of four Chapters. In the state of the art Chapter, a non-exhaustive review of the imaging techniques allowing micrometric to nanometric spatial resolutions is proposed. First, surface imaging techniques are presented for their very high spatial (lateral) resolution, but limited to the vicinity of the sample surface. Sub-surface techniques are then discussed with a focus on both spatial resolutions (lateral and axial). Finally, the acoustic-based nanoscale imaging techniques are introduced, divided in three categories based on their physical principles. After discussing the photoacoustic effect, each imaging technique is presented to finally arrive to the TDBS technique employed in this thesis. The aim of this first Chapter is to position the TDBS in the family of nanoscale imaging techniques.
A second Chapter spotlight the theoretical background needed for the comprehension of the pump-probe technique employed for the transient reflectivity measurements realised in this thesis. The physics of the optoacoustic generation by the pump laser beam of a coherent acoustic pulse (CAP) via thermoelasticity is detailed. The TDBS detection of the acoustic pulse propagating in a transparent sample explains the expected acoustic signature (Brillouin oscillations) in the transient reflectivity signals recorded with a photodetector. The Chapter is concluded on the theoretical and experimental possibility to generate and detect transversal acoustic waves with such method, that will prove to be of the highest importance in the frame of complete 3-D imaging of samples.
In the third Chapter, a step-by-step signal processing method is proposed for the treatment of the raw transient reflectivity data from raster-scans obtained with the ultrafast imaging setup. The processing procedure aims to reconstruct the 3-D shapes of the grains forming the polycrystalline samples studied. The first step consists in extracting the acoustic content from the raw transient reflectivity signals. The second step intend to evaluate the instantaneous frequency of the step-one-obtained "acoustic signals". Two methods relying on time-frequency tools are presented, a first one uses a classical short-time Fourier

transform combined with a synchronous detection technique, while the second one takes advantage of the powerful wavelet synchrosqueezed transform. The acoustic content of the scan brings a preliminary insight on the sample structure, that is enhanced with the last step. In the third step, the results of step 2 are segmented to assess the number of grains in the sample and their respective limits (boundaries), before the reconstruction of their 3-D volumetric shapes using the alphashape algorithm. The processing procedure is finally applied to the study of two different transparent polycrystalline materials: a high pressure water ice sample obtained in a diamond anvil cell, and a cerium dioxyde (or ceria) polycrystal. 3-D images of both structures are discussed and more particularly the case of buried inclined boundaries leads to the opportunity of extending the TDBS theory in Chapter 4.

The fourth and final Chapter present the extension of the time-domain Brillouin scattering theory, applied for many years to study homogeneous samples and/or materials with interfaces parallel to the free surface of the samples where the acoustic pulses are generated normally to the surface. This theory is extended to the case of light and sound beams propagating with non-collinear directions, a situation that is justified by the observation of 3-D inclined interfaces between two materials using the processing procedure of Chapter 3. Indeed when the light and sound beam reach the interface between two materials with different elastic and optical properties, reflection and refraction occur and, as a result, the non-collinear propagation between the light and sound beams affects the TDBS signal recorded, in both its amplitude and phase. Thus comprehension of the phenomena at the interface would ultimately allow a better localisation of it, as well as estimating its inclination.

Chapter 1

State of the art - Nanoscale imaging

Contents

1.1 Introduction

The word "image" etymologically comes from the latin *imago*, interpreted as the representation, the portrait of something. Therefore "imaging" is defined as the operation of recreating the image, the representation of an object. One meaningful criteria to discuss the precision level of an image is the resolution: the smallest perceived distance between two points close to each other. For example, the bare human eye can achieve a resolution of hundreds of micrometers (µm) given good light conditions. Through the use of an assembly of optical lenses (a microscope), the resolution of the image perceived is importantly improved. With the most efficient microscopes, the resolution limit can be defined as half the wavelength of the light (optical diffraction limit) [10], *e.g.*, for white light centred at 500 nm, the best-achievable resolution is close to 250 nm. To achieve imaging of objects below this resolution, a variety of techniques have been developed, ingeniously harnessing different physical mechanisms, some of them being discussed in the following first chapter. Ultimately, one should keep in mind that image quality is also connected to the contrast (capacity to distinguish two objects with close intensity/contrasting properties) and the signal-to-noise ratio (SNR), or how well the object to image is emerging from noise, *i.e.*, non meaningful data.

In physical sciences, imaging covers areas as different as: recoverying the structure of comets, like in the case of Hale-Bopp grain structure study at different epochs via infra-red (IR) polmarimetry [11], or identify the first signs of breast cancer, the survival rate being directly linked to early detection [12]. In medical and biomedical imaging, the aim is usually to reproduce the image of the body, or part of it, in order to visually review it and establish a diagnostic based on the observations. Image quality is understandably a major point of concern, the race toward spatial resolution enhancement, *i.e.*, being able to image smaller objects, or bigger objects but with a higher resolution, being driven by the hope of better, earlier diagnostics. For example, magnetic resonance imaging (MRI) is nowadays a common imaging system accessible in hospital, reaching spatial resolutions of the millimeter (mm) order, down to hundreds of micrometer (µm) in advanced research applications [13]. However, imaging results, assessing the state of the target at a given time with a given sensitivity, are sometime still too late in the frame of pathology detection. For example, the detection of osteoarthritis (especially relevant in aging and/or obese populations) with MRI detects cartilage deteriorations only when it is in advanced stages. The proposed solutions implies the development of quantitative MRI imaging, *i.e.*, extraction of quantifiable features from images, to enhance the sensitivity of the imaging technique to subtle changes, like here biomedical changes, markers of early stages of the disease [14].

Sundry imaging methods, well-known in the medical field such as echography, have been transfered to the material imaging field, where it is the internal structure of materials that is imaged, as for structural defects or bonding quality control, or grain agregates visualisation. Sonograms (acoustic images) are obtained by sending ultrasound pulses inside the tested sample (a patient or a concrete wall), using a

transducer to launch and record the pulses. When propagating in the sample, pulses are reflected by the different interfaces (tissues and organs of a patient, or cracks and voids in concrete). Recording the amplitude of the reflected pulses and/or the transit time between the pulse echoes gives information on the internal structure below the surface of probe scanning. Such ultrasonic inspection methods are commonly referred as non-destructive testing (NDT) techniques, and are common for structural mechanic inspections [15].

Imaging at the nanoscale is motivated by the possibility of understanding material properties at a larger scale by studying its nano-structure. Transducers used in the echography scheme detailed hitherto are usually sending pulses in the megahertz (MHz) range with acoustic oscillation wavelengths of the µm scale, hence precluding nanometer (nm) scale imaging. To overcome this limit, laser pulses can be used to generate high frequency acoustic pulses of the gigahertz (GHz) range and thus pave the way to nanoscale imaging. By accessing nm structures, such as inter-grain boundaries in polycrystalline aggregates, it is for example possible to explain the dynamics driving the ionic conductivity of a sample. Inspired by these perspectives, and by curiosity, scientists have developed an extended variety of methods to image materials or biological cells to smaller and smaller scales, ingeniously taking advantage of different physical mechanisms to investigate samples. The aim of Chap. 1 is to introduce the reader to some of these nanoscale imaging techniques, to discuss the advantages and drawbacks of each introduced method in order to, finally, compare them with the time-domain Brillouin scattering (TDBS) method employed in this thesis work.

In this way, Sec. 1.2 presents the non acoustic-based methods that have been widely used to image the surface of samples down to an incredible precision, achieving atom-to-atom resolution, and then switch to the method achieving three dimensional (3-D) imaging. In Sec. 1.3, the photoacoustic effect (conversion of light energy into acoustic waves) is introduced with the definition of phonons, and the family of techniques based on this effect are presented in three sections, the last one being the TDBS method.

1.2 Imaging at the nanoscale: non acoustic-based techniques

The first section of this state of the art Chapter is dedicated to the presentation of imaging techniques suited to surface and sub-surface mapping of samples with the best possible resolution. The aim is to briefly present existing nanoscale imaging techniques relying on different physical mechanisms, before focusing on the subject of this manuscript, *i.e.*, acoustic imaging.
In this respect, in the following sections we try to spotlight the most relevant techniques and do not claim to give an exhaustive list of all available methods. Moreover, these introductions might appear as "not deep enough" to experienced readers since they are mainly oriented to readers not familiar with such small scale imaging techniques.
Firstly, nanoscale surface imaging techniques are presented, allowing the reconstruction of the sample surface or of the few nm below it. Secondly, when the purpose of the imaging is to evaluate the content of the sample beneath its surface, *i.e.* below $\sim$ 1 µm, different techniques are employed to access the in-depth structure of the sample.

1.2.1 Surface imaging techniques

As an introduction to advanced imaging techniques, two different methodologies of surface mapping are presented. In the first approach, the scanning electron microscope (SEM), uses beam of accelerated electrons focused onto the surface of the sample to study and imaging is performed by collecting the outgoing electrons resulting from the interaction with the sample. The second strategy relies on measuring a physical quantity using a nanometric probe. Scanning probe microscopy (SPM) techniques resolve atom-to-atom precision but are limited to two dimensional (2-D) scans. These two methodologies are bounded to 2-D surface imaging, the thickness (third dimension) of the sample is not characterised or only along few nm.

Scanning electron microscope (SEM)

Electronic microscopy relies on beams of accelerated electrons to scan the surface of samples: the story of the invention of the electron microscope, motivated by the expectation of outperforming the resolution of light microscopes, is inspiringly narrated by Ernst Ruska in its "Nobel lecture" [16]. Indeed, when typical light wavelengths range from UV to IR [200 - 1000] nm, electrons acceleration allows to reach drastically shorter wavelengths, below the nm scale. A scanning electron microscope (SEM) gives access to different aspects of a sample surface, like its geometry or topography (shape and size of materials composing the surface) and other properties (crystallographic orientations or physical/chemical properties) [17].
The first element of a SEM is the electron source. It is usually divided into two categories: thermionic (heating of a filament) and field emission (strong electrostatic field applied to a tip) sources. For the electrons to be emitted along a common direction, *i.e.*, to obtain an electron beam, electrostatic and electromagnetic lenses are used to control the energy of the electrons and the beam diameter. Small electron

beam diameters (nm radius) allows high spatial resolution, at the expense of low contrast due to low beam current. Increased beam currents allows imaging with better contrast but increases consequently the beam size. There is thus a compromise to be found between spatial (lateral) resolution and contrast. One of the main constraints in SEM is that all the components, from the electron beam source to the sample chamber, needs to be placed under high vacuum to avoid electrons to collide with an element that is not the sample. The electron beam is directed onto the surface of the material to be studied, and the interaction of the electrons with the material (scattering and deflection by the electric fields of the atoms) will produce two types of outgoing electrons to be detected.

First, the backscattered electrons corresponds to the electrons experiencing sufficient scattering and deflections to be redirected back in the half space where they were emitted from. The other type of electrons that can be detected are called secondary electrons and arise from the inelastic scattering of weakly-bonded material electrons [17].
At normal incidence of the electron beam, the backscattered electrons are usually predominant and their detection offers strong signals with information on the topography (surface height) and crystallography (crystalline orientations) of the surface. The maximum depth, *i.e.*, the distance from the surface of beam focusing, reached by a backscattered electron is shorter than 1 µm for most of the combination setup / materials. For example, in Ref. [17], Monte-Carlo simulation in copper (Cu) for electrons at 20 keV shows that backscattered electrons penetrate a distance shorter than 400 nm, at normal incidence of the electron beam. Thus, SEM is restrained as "surface imaging", the third dimension being resolved on too short distances.

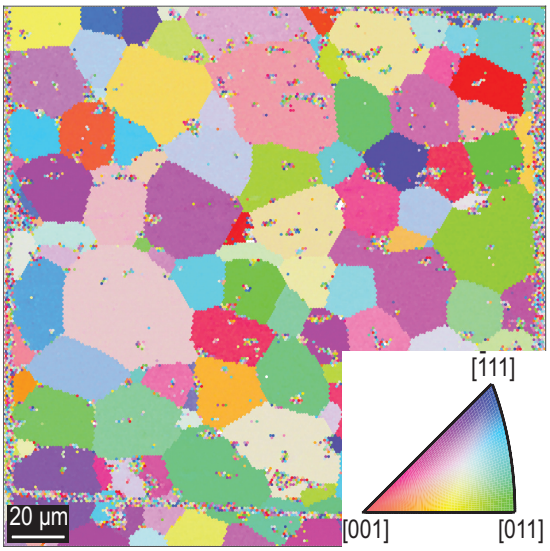

Figure 1.1 – Electron backscattering diffraction (EBSD) pattern of the surface of a polycrystalline cerium dioxyde (CeO_2) sample. The grain boundaries are precisely determined at the micrometric scale, as well as the crystalline orientation of each individual grains (or crystallites). Measurements and data courtesy to Dr. Z. Hua and Dr. D. H. Hurley, Idaho national laboratory.

When studying polycrystalline materials, electron backscattering diffraction (EBSD) patterns are obtained in the frame of identifying (among other characteristics) the different grains (or crystallites) orientations [18], like presented in the case of a polycrystalline cerium dioxyde CeO_2 sample, that will be studied in Chap. 3 [Fig. 1.1]. Colors are linked to the crystalline orientations of the different grains and the color shades allows to estimate visually the orientation deviation from grain to grain, knowing that each orientations can be precisely determined.

Scanning probe microscopy (SPM)

To evaluate the structural, mechanical, optical, electronical and magnetic properties of the surface of a material, a family of common-base techniques are regrouped under the term "scanning probe microscopy" (and/or nanoscopy). The very first one, scanning tunnelling microscopy (STM), was developed in 1981 [19] functioning via the tunnelling effect induced between a sharp metallic tip (referred as the probe) and the surface of a conductive material [Fig. 1.2 (a)]. The atomic-scale tip is approached near (few angstrom (Å) above) the surface of the conducting material, and when a voltage is induced between the tip and the surface, a very localized tunnelling effect may occur. The probability of electrons tunnelling through the potential barrier between the tip and the surface is directly linked to the tip/sample surface distance. It is then possible to do a scan (raster scan), *i.e.*, measuring the current passing through the tip for different positions (but a fixed height) over the sample surface, allowing to map it as precisely as resolving the location of each atom [Fig. 1.2 (a)]. The lateral resolution is controlled by the size of the tip at the apex, going down to a single atom in the most precise setups. Only two years after the first experiments conducted with the tunnelling effect, the atomic force microscope (AFM) was developed, using the same principle but functioning with a different interaction between the tip and the sample.

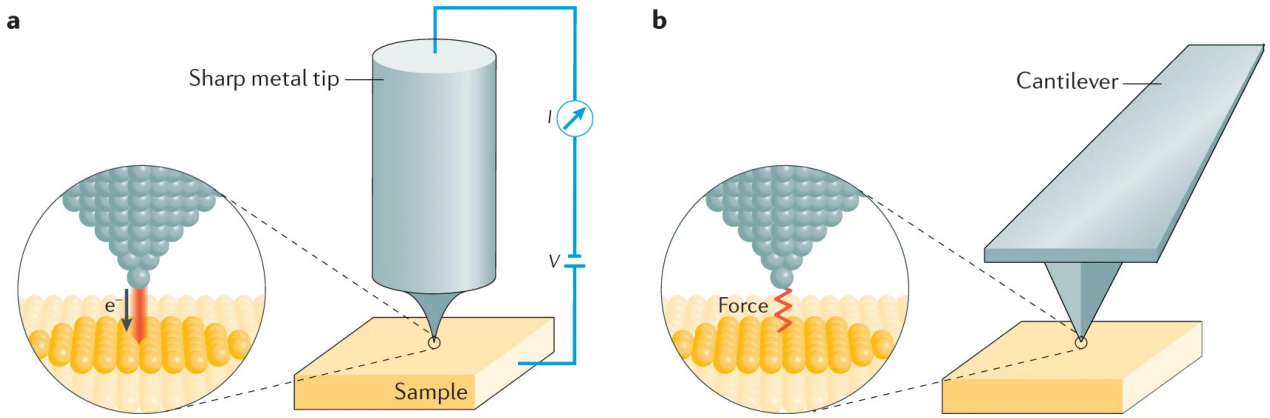

Figure 1.2 – Schematic representation of the basics of scanning tunnelling microscope (STM) and atomic force microscope (AFM) sensing techniques [20]. (a) In the STM configuration, a sharp metallic tip is used to probe the surface of a conducting material by measuring the tunnelling current induced between the tip of the probe and the sample surface. (b) In the AFM case, the sharp tip is mounted on a cantilever and it is the atomic forces that are measured via the deflections of the cantilever. In both cases imaging of the sample surface is obtained by raster-scanning and nm lateral resolutions are achieved.

In the AFM, the tunnelling current is replaced by the measurement of the atomic forces between the tip and the sample surface [21]. The tip is placed at the free end of a cantilever, the deflection of the later (changing the tip-surface distance) is fixed with the force applied to the cantilever. Raster scanning with the AFM consist in measuring the deflections (displacements along the tip-surface axis) of the cantilever due to the atomic forces perceived at the apex of the tip [Fig. 1.2 (b)]. Measure of the cantilever's small-scale displacements are usually done with laser sensing. The advantages of scanning atomic forces

over tunnelling are that measurements are doable even with non-conducting materials, and under less restrictive environmental conditions (low/high temperature/pressure).
Finally, many techniques have been developed from AFM, like dynamical AFM where the cantilever is used as an oscillating device that allows measuring (and fixing) either its frequency or its amplitude changes when scanning the surface. For a recent review on SPM, please refer to Ref. [20].
The limitations of the SPM family of techniques is found in the third spatial dimension: SPM is an extremely precise and reliable 2-D imaging of atomically flat surfaces, but does not permit mapping of below-the-surface features. When it comes to 3-D rendering of the surface topography, like in the case of nano-structured samples and large bio-molecules, the resolution and the quality of the imaging is diminished, and such experiments could often depend on previous topographic measurements, obtained with other methods, to adapt the tip-surface distance in order to avoid damaging the tip and/or the sample surface [22].
An AFM-based method was employed for the atomic-scale 3-D imaging of the step-edges of a pentacene molecule absorbed on the surface of a natural single crystal of anatase mineral (Titanium dioxyde). The resolution achieved with this method correspond to the height difference induced by the pentacene molecule over the atomically flat surface of the titanium dioxyde, and corresponds to the order 0.24 nm [22].

In Sec. 1.2.1, two different approaches to nanoscale imaging have been presented, but it is important to keep in mind that, in this manuscript, we are interested in the 3-D imaging of material, *i.e.*, accessing to the evolution of the sample properties in its volume beneath its surface. Corresponding 3-D imaging techniques suited to, *e.g.*, evaluate the evolution of the grain boundaries beneath the free surface of the CeO_2 sample in Fig. 1.1, are presented in the next section.

1.2.2 Sub-surface imaging techniques

In general, the imaging techniques that permits evaluation of the third dimension of a sample are relying on the interaction between a penetrating beam and the volume of the sample being probed. Such probe beams might be composed of electrons like presented in electron microscopy and used here in transmission, or x-ray radiations leading to x-ray microscopy. The 3-D imaging requires the definition of a new term. 2-D "flat" representations are composed of elementary surfaces named pixels, it is thus straightforward to define an elementary volume of a 3-D image by adding the thickness dimension to a pixel, giving a voxel.

Transmission electron microscope (TEM)

The transmission electron microscope (TEM) was invented in 1931 by Knoll and Ruska [23], and is directly related to the SEM since it shares the same electron source principle. Indeed, as in SEM, the sample is placed in a vacuum chamber and a precisely shaped electron beam is directed onto the sample

surface. However, the main difference is found in the fact that TEM acquires images via the detection of the transmitted electrons, *i.e.*, electrons entering the sample from the surface where the electron beam is focused and passing through the sample. Moreover, SEM provides surface imaging by raster-scan of the sample, while usually TEM uses a beam to illuminate the complete area of the sample to image. It is then easy to understand that the information obtained via the detection of such transmitted electrons are tied to the volumetric structure of the sample, thus enquiring possible deviations compared to the surface structure.

During their transmission trough the material, the electrons are scattered by the atoms and the electrons forming it. There are two type of scattering depending on the conservation of the kinetic energy and/or momentum: elastic scattering mostly occur when electrons are scattered by heavier objects such as atoms nucleus, while inelastic scattering can lead to radiation emission during electron-electron interactions. It is the elastic scattering of electrons that provides high resolution information due to the nature of the interaction [24]. When the electron beam is tightly focused and the 3-D imaging requires to raster-scan the sample, it is referred as scanning transmission electron microscope (STEM) [17].

The main drawback arising from TEM is the sample preparation, as ultra-thin samples ($\sim$ 150 nm) with calibrated surface flatness are required for the electrons to be efficiently transmitted. Moreover, the material under observation needs to be resistive to the electron beam and not get degraded or even react under electron radiation during the time scale of the imaging.

Nonetheless, when these sample conditions are granted, TEM can perform incredibly high spatial (lateral) resolution of about 0.1 nm (1 Å) [24]. Some of these techniques might be refered to as high resolution TEM (HRTEM) [25]. Axial resolution below 10 nm was achieved using specific deconvolution of the STEM dataset recorded on gold nanoparticles, at the expense of the lateral resolution [26].

X-ray microscopy

A second group of methods used for the nm-to-µm scale sub-surface imaging of samples is based on x-ray radiation, and are especially suited to examine the texture of polycrystalline solids, with a spatial resolution adapted to the grain scale. X-ray-based probes possess the capacity to interact with the sample, non-destructively, bringing information on internal structure (inhomogeneities), magnetism, chemical bonding and orbital orientation [27]. The main advantages of x-ray microscopy over electron microscopy are that x-rays interact weakly with the structure studied and thus it does not require so restrictive sample preparation, as in SEM and TEM, to avoid its degradation.

X-rays are obtained via the acceleration of electrons, either by using an x-ray tube (compact, low-cost and with limited x-ray flux) or a synchrotron storage ring (large scale, expensive infrastructures and with x-ray flux order of magnitudes higher than tubes). The x-ray flux informs on the number of x-ray photons in the incident beam, per second per unit area, and thus, the higher the flux, the higher the scan sensitivity due to a greater number of transmitted x-rays for a same time of exposure. Thus, synchrotron sources are preferred when a very high spatial resolutions is aimed, as well as suited to real-time imaging,

e.g., to acquire thousands of projections per second at µm resolution of a sample structure evolving with time.

The contrast in the images obtained via x-ray scans comes from the variations recorded in the refractive index of the sample, either by its imaginary part (attenuation contrast) or by its real part (phase contrast). Most of the x-ray acquisitions techniques provide 2-D slices of the sample (referred as radiographs), and the 3-D rendering is computed from a collection of radiographs obtained from multiple acquisitions in 360°, *i.e.*, by computed tomography (CT) [28]. The final output of such dataset treatment is often referred as a tomogram, *i.e.*, a 3-D greyscale rendering of the internal structure of the sample [Fig. 1.3 (d)].

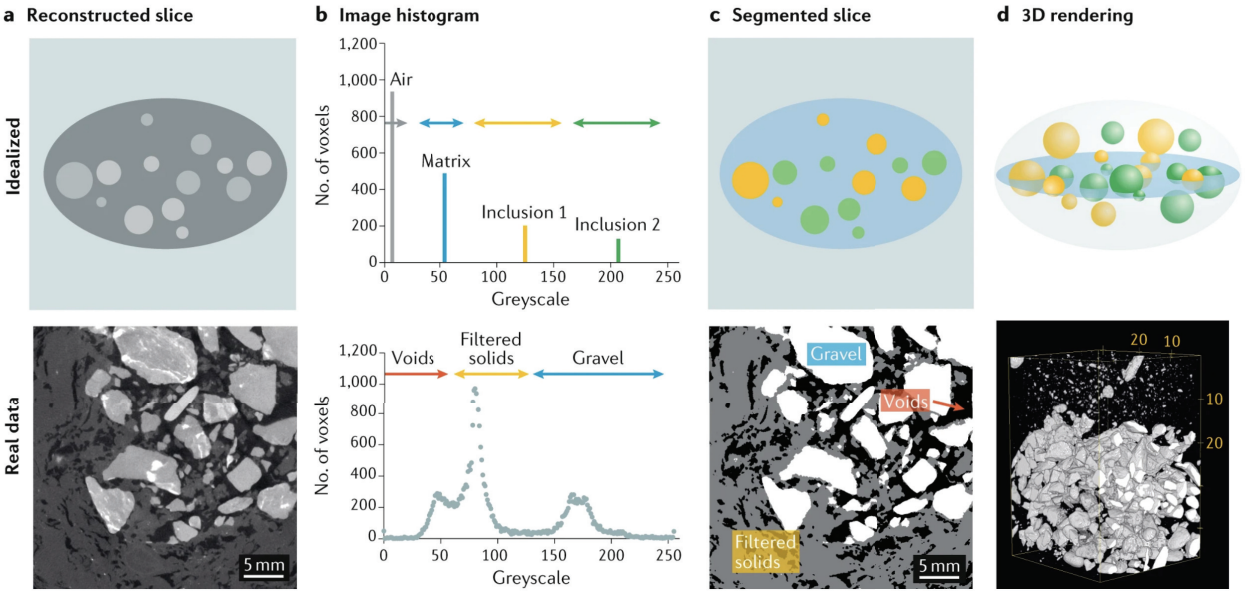

Figure 1.3 – Segmentation signal processing steps of x-ray computed tomography in the case of an idealized envisioned sample (upper row) and a real example of gravel filter pack (lower row), imaged by tube-source microtomography [28]. (a) The raw data obtained from the scan permits reconstruction of a 2-D "averaged" image of the sample. (b) The histogram repartition of the number of voxel per greyscale unit contains peaks, depicting group of voxels that can be regrouped as common elements: the histogram is segmented into intervals of greyscale depicting common contents. (c) Voxels belonging to common segmented greyscale intervals are regrouped by colors on the 2-D map of (a). (d) Final 3-D rendering after segmentation and computed tomography (CT): the sample is reconstructed in 3-D and the segmentation allowed identification of the different elements of the sample obtained by the scan.

The aforementioned signal processing steps are illustrated in Fig. 1.3, in the case of an idealized envisioned sample and a real example of gravel filter pack. In this example, the 10 cm-thick gravel pack samples were imaged using an x-ray tube source, leading to a final voxel in the µm scale (35 μm^3).

The necessity to acquire radiographs over 360° requires the sample to be accessible along, at least, 2 spatial directions, and restrains the preferable shape of the sample, *e.g.*, excluding thin films with thick-

ness shorter than the lateral dimensions of the sample. However, such limitations are addressed in other implementations of x-ray imaging like in x-ray reflectivity [29]. Interestingly, comparable processing steps as in Fig. 1.3 have been developed during this thesis with segmentation of the experimental dataset with the use of an histogram repartition of the content of interest.
X-ray CT is employed for many different imaging scales: sub-mm spatial resolution are usually enough in the medical or industry context, while close to nm resolutions have been achieved with either very bright synchrotrons, or by dedicated reconstruction techniques such as ptychographic x-ray CT [30]. In this example, bone structure with 100 nm resolution was imaged via the processing of phase contrast data containing meaningful physical properties, as opposed to "only" greyscale images deduced from absorption contrast.
There exists an important variety of elaborated x-ray imaging methods and part of them push forward the limits of nanoscale imaging of materials like in the review Ref. [27], that focuses on synchrotron sources. However, imaging quality and spatial resolution of the final results are strongly linked to the sample studied and more specifically to the size of the resolved object aimed. Close to nanometric spatial resolutions can be achieved, but induce a small field of view (hence small areas of the sample will be imaged) for the detection, and a small x-ray beam radius thus higher dose of radiation that could lead to damaging, especially in the frame of biological samples. Thus, even if extremely high spatial resolution might be achieved, some sample configurations require distinct care reducing the achievable resolution.
A final remark concerning issues arising in x-ray imaging, that can be generalized to future issues encountered in this manuscript, is the data volume augmentation with increasing resolution. To scan a sample with nm resolution, the x-ray beam size is reduced along with the field of view, thus multiple scans (in the same frame as raster-scanning with previously described methods) would be required to cover the entirety of the sample. Such stacking of measurements leads inevitably to computational costs due to large experimental dataset. Along with large data volume, segmentation issues might arise from the computed tomography processing when imaging low-contrast samples, and segmentation adjustments dedicated to each sample might limit its "automatic" aspects. Perspectives of solutions exist in the domain of artificial intelligence (A.I.) supervision of the segmentation and, more generally, on the detection of common patterns in such large datasets.

Different methods have been presented for the imaging of surface (2-D) and sub-surface (3-D) of materials by taking advantage of multiple physical mechanisms, from the mm to the nm scale, with a focus on the techniques allowing the best resolutions.
Surface imaging methods rely on electron beams or atomic forces to map the properties at the surface of the sample, with a spatial resolution reaching atom-to-atom precision. The main limitation is found in the fact that the properties in the volume beneath the surface are not obtained.
Sub-surface imaging methods employ penetrating beams to probe the sample properties beneath the surface ($\sim$ 1 µm beneath). Such probe beams can be composed of accelerated electrons or x-rays and

offer 3-D reconstructions of samples at the mm to the nm scales. However, constraints on the sample preparation (shape, size, accessibility or resistance to the probe), as well as complex and costly infrastructures used as probe beams sources (synchrotron) might appears as a hindrance to the use of these methods.

Other approaches based on the ability to optically monitor the propagation of an acoustic wave launched in the sample are presented in the next section, with a final focus on the method employed in this thesis for the 3-D imaging of transparent materials.

1.3 Imaging at the nanoscale: acoustic-based techniques

Ultrasound imaging is nowadays commonly used in many domains including medical imaging [31] and non-destructive testing of industrial components [15]. Numerous applications are based on the echography scheme, *i.e.*, sending an ultrasound pulse (using various transducer types) and measuring, in reflection or transmission, the amplitude and/or time of propagation of the pulse. The typical bandwidth in medical imaging extends up to the MHz range with corresponding axial (in depth) resolution of the µm scale, corresponding to the "Ultrasound" part of the acoustic spectrum [green in Fig. 1.4 (a)].
The limiting factors to reach nm resolutions with these ultrasound techniques are found in the acoustic absorption at higher frequencies, reducing the attainable depth of imaging, as well as the bandwidth capacity of the instruments. Nanoscale acoustic imaging techniques are employing higher frequency acoustic pulses, in the "Hypersound" part of the acoustic spectrum [red in Fig. 1.4 (a)]. Consequently, the second section of this state of the art Chapter on nanoscale imaging focuses on the introduction to the photoacoustic imaging techniques that uses short laser pulses to generate acoustic disturbances (pulses) in materials, and detect them using transducers or via non-contact optical detection.
In a first part, the type of "acoustic disturbance" used for nanoscale imaging is defined by introducing the phonons, and the photoacoustic effect is briefly introduced. Extended discussion on the physical mechanisms for the generation of acoustic pulses in materials, as well as their detection with TDBS, is given in Chap. 2. Different imaging techniques using laser-generated acoustic waves are discussed, grouped according to their physical principles into three categories: (i) laser ultrasonic imaging (LUI), (ii) photoacoustic imaging (PAI) and (iii) time-domain Brillouin scattering (TDBS).

1.3.1 Phonons and photoacoustics

Inside a material, at the atomic scale, atoms are linked together by atomic forces and, as a simplification for studying elastic waves propagation, the crystalline structure can be conceived as a 3-D arrangement of masses (atoms) linked to their neighbours by springs (atomic forces). Unless the material is frozen to the absolute zero temperature (0° K), this arrangement of atoms is in an incoherent state of vibrations, each atom vibrating around its equilibrium position, that is linked to the thermal state of the material. A temperature change could modify this motion state, hence the "Heat" part of the acoustic spectrum [orange in Fig. 1.4 (a)].
The two high frequency (GHz to THz) states of motion in Fig. 1.4 (a) are described in quantum mechanics as particles, named phonons (thermal phonons when referring to the incoherent state of motion), in analogy with the electromagnetic particles, the photons. These phonons corresponds to a collective motion of the atoms, and can be understood as being the normal modes that can propagate in the crystalline structure of the material. For example, if we simplify the complex 3-D atomic structure down to a 1-D diatomic lattice, *i.e.*, an array of two alternated atoms (one heavier than the other), then the dispersion relation of such lattice can be computed and expresses what are the phonons oscillations

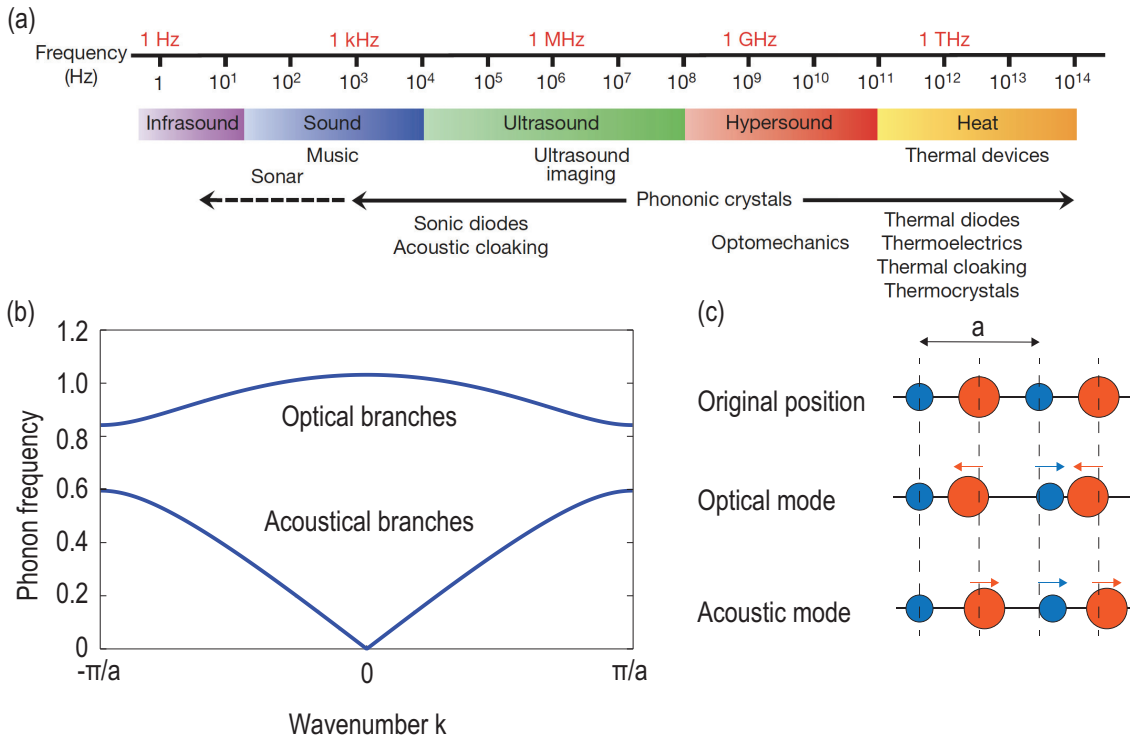

Figure 1.4 – (a) Acoustic spectrum [32]. (b) Dispersion relation (in the first Brillouin zone, frequencies normalized by the maximum value) giving the normal modes (or phonons) in a lattice composed of two different atoms (diatomic by the masses, $M_2 = 2 \times M_1$). For a fixed wavenumber k, and considering a single mode, *i.e.* compressional waves (LA waves), it exists two types of phonons: the lower branch correspond to the acoustic phonons and the upper one to the optical phonons. (c) Illustration of the fundamental displacements difference between the acoustic (in-phase motion) and optical (out-of-phase motion) phonons.

frequencies permitted to propagate in the lattice, as illustrated for the case of compressive motions (longitudinal waves: compression-dilatation) in Fig. 1.4 (b-c).

The dispersion relation of the diatomic lattice [Fig. 1.4 (b)] shows that for a fixed wavenumber k, *i.e.*, a fixed wavelength, two phonons (or normal modes) are expected: the lower branch, starting from zero frequency, contains the acoustic phonons (with a lower frequency), while the upper one contains the optical phonons (higher frequency). Theses acoustic/optical phonons corresponds to coherent motions of the atoms, in opposition to thermal phonons being an incoherent motion. Keeping in mind that transversal motions (shear/transversal modes) can be observed too, the dispersion relation of a lattice containing p atoms will have $3p$ branches, the acoustic phonons being limited to the 3 acoustic branches linked to the longitudinal acoustic (LA) mode and the two orthogonally polarized transversal acoustic (TA) modes. Finally, coming back to the 3-D atom arrangements of the crystalline structure of materials, phonon properties (oscillation frequency, velocity) will depend on the orientation of its propagation direction in this 3-D structure, consequently complicating the dispersion relation.

It is in the 1920s that the light scattering effect, or acousto-optic effect, of the phonons was discovered, by L. Brillouin and L. Mandelstam [4, 5] for the acoustic branch, and by C. V. Raman [33] for the optical branch. An incident light beam, *e.g.*, from a laser source, is reflected with a shifted optical frequency due to the photon-phonon interaction. This effect is designated as Brillouin or Raman frequency shifting pending on the type of phonon (acoustic or optical).

Henceforth, the use of this effect to probe the optical, acoustical and acousto-optical properties of a sample is termed frequency-domain Brillouin scattering (FDBS) when the frequency shift (or Doppler effect [34]) is measured directly from the scattering of light by incoherent [35–37] or coherent phonons [38]. On the other hand, the technique used in this thesis, the time-domain Brillouin scattering (TDBS), relies on the mixing between the light that is scattered by the coherent phonons, and the light that is reflected at the different interfaces composing the structure of the sample, to reveal the presence of phonons.

The chosen denomination is such that when the photon-phonon interaction happens with phonon from the acoustic branch, the scattering is named Brillouin (or Brillouin-Mandelstam) scattering, while when the phonon is from the optical branch, it is Raman scattering [39]. The only difference resides in the frequency shift orders, being superior in the Raman process and thus requiring different detection techniques, as well as the corresponding atom motions in the lattice [Fig. 1.4 (c)].

To induce a coherent motion of the phonons, the optoacoustic process, *i.e.*, converting the laser light energy, carried by the photons, into coherent motions of the lattices atoms, or coherent acoustic pulses (CAPs), is usually employed under the "photoacoustic" denomination. This is the effect discovered by A. G. Bell in 1880 that led him to the creation of the photophone [1].

In the case of photoacoustic techniques, photo-excited CAPs are launched in the sample thanks to the pump laser beam. The conversion of the pump laser light energy into CAPs can be accomplished via various physical mechanisms, like electron-acoustic phonon deformation potential, inverse piezoelectric effect or electrostriction [40, 41]. Among them, it is the thermoelastic effect that is detailed in Sec. 2.2., as it is the most commonly used in TDBS. The pump laser beam is focused on the surface of a light-absorbing material, either the studied sample itself or a semi-transparent metallic film dedicatedly deposited on the sample surface, and named the optoacoustic transducer (OAT). Upon absorption of laser light energy, the light-absorbing volume temperature will abruptly increase and thermal expansion of the material will act like the source of thermal stresses, inducing coherent motions in the crystalline structure: CAPs.

The detection of the CAPs is achieved either by the use of piezoelectric transducers, or via optical detection [42, 43]. The surface motions can be detected with interferometers, or the detection can be achieved like in FDBS/TDBS by monitoring, with the probe laser beam, the propagation of the CAP in the material, owing to the acousto-optic effect that scatters the probe light field. The amplitude of the detected CAP depends on various material parameters such as the light absorption and reflection coefficients, the thermal expansion coefficient and the material elastic moduli. The lateral resolution in this photoacoustic spectroscopy (studying light absorption) is controlled by the focusing of the laser radiation [44] leading

to µm lateral resolution [45]. The lateral resolution may reach the nm scale with the use of near-field optics [46]. To complete, the contrast in photoacoustic microscopy/nanoscopy involves the variations in optical, elastic, thermal and thermoelastic (controlling the thermal expansion due to light absorption) parameters of the material.

In conclusion, photoacoustic 3-D imaging techniques have been developed, owing to the capacity to generate and detect phonons propagating in materials, with the use of laser light. Its capacity to investigate the samples non-destructively and without contact, using less restrictive sample preparation and excitation sources than x-ray radiation or electron beams, makes it attractive to study complex, nanostructured materials. The family of imaging techniques based on laser-generated CAPs are presented into the three following categories: (i) laser ultrasonic imaging (LUI), (ii) photoacoustic imaging (PAI) and (iii) time-domain Brillouin scattering (TDBS).

1.3.2 Laser ultrasonic imaging (LUI) and photoacoustic imaging (PAI)

In the first category, LUI, imaging is achieved like in traditional pulse-echo ultrasound measurements, by launching the CAPs from the sample surface into its volume, and detecting the acoustic modes transmitted/scattered by the sample inhomogeneities, defects and interfaces [47–50]. Since it is the scattered/transmitted acoustic modes that carry the information on the distribution of the acoustic inhomogeneities in the sample, the contrast in LUI is acoustical, and thus the axial resolution is controlled by the duration (length) of the laser-generated CAPs [51]. The axial resolution degrades with increasing distance between the transducer (OAT) and the inhomogeneity to image, since the acoustic absorption commonly broadens the CAPs during its propagation. LUI can provide nm scale axial resolution by application of picosecond (ps) or femtosecond (fs) laser pulses both for the generation and the detection of ps duration CAPs [6, 52, 53].
Among a rich variety of applications, LUI has been employed for the evaluation of the internal structure of biological objects [48–51], of stresses distribution [54, 55], and accurate measurements of the surface profile in various materials [56, 57]. The inherent compromise to achieve nanoscale axial resolution being the reduction of the depth of imaging, down to a dozen of µm, then ps LUI is particularly adapted to microelectronics applications. In this context, LUI has been developed from its first application to the single and multi-layered film-thickness characterisation [58] (with the less relevant but amusing creation of the first "nanoxylophone"), to the commercial MetaPULSE G (or simply PULSE^{TM} technology) in-line metrology system used for wafer metrology [59]. With such technology, film thickness from 50 Å to few µm are resolved, but the samples studied are made of parallel stacked materials.

In the second category, the local absorption of pump light photons penetrating in the material generates CAPs, profiled with the encoded information on the inhomogeneity of light absorption coefficient spatial distribution. The temporal shape of pulsed-laser-generated PA signal was evidenced in the 1970's to de-

pend on the magnitude of the light absorption coefficient [60], leading the way to measure experimentally the light absorption coefficient spatial distribution from the shape of the detected CAPs (Sec. 2.2 in Ref. [40]) and applied later for biological tissues study [61, 62]. The photo-generated acoustic waves deliver the encoded information to the detection region near or on the sample surface.
The advances in PAI have been principally driven by biomedical applications, relying on the attainable spatial resolution and field of imaging, limited either by acoustics or by optics. Applications includes in-vivo, pre-clinical and clinical PAI [63–72]. PAI performs 3-D imaging at cm to µm spatial scales, combining optical and acoustic imaging benefits, the first one giving high contrast and the second one high spatio-temporal resolution.
In optical-resolution PAI (3-D photoacoustic microscopy), the pump laser radiation is tightly focused and co-aligned with the focal region of an ultrasonic transducer. The lateral spatial resolution is thus controlled by the optical focal region and the imaging depth is limited by the optical penetration depth ($\sim$ 1 mm), even though better resolution ($\sim$ 0.1 µm) can be achieved in PA nanoscopy [73] but is limited to a few hundreds nm of light penetration depth.
In acoustic-resolution PAI, the unfocused pump light is delivered around the acoustic receiver focal region to create a uniform illumination. Both lateral and axial resolutions are controlled by the acoustic focal region [74]. The lateral spatial resolution is determined by loose acoustic focusing, and the penetration depth resolve deeper tissues, reaching several cm deep even in the highly light-scattering media that are biological tissues.
In the acoustic-resolution imaging technique called photoacoustic tomography (PAT), neither the light nor the sound are tightly focused. Different implementations of PAT allow the spatial resolution to be scaled with the desired imaging depth in tissue while a high depth-to-resolution ratio is maintained [75]. PAT can achieve sub-millimeter lateral and axial resolutions at depths up to several cm [75, 76].

1.3.3 Time-domain Brillouin scattering (TDBS)

The third category is fundamentally different compared to both LUI and PAI techniques. This approach, known under the names of picosecond ultrasonic interferometry [52, 77–79] and time-domain (or time-resolved) Brillouin scattering (TDBS) [79], is based on the interaction of the probe light with CAPs propagating inside media that are transparent or semi-transparent at the probe wavelength. TDBS and frequency-domain Brillouin scattering (FDBS) differ by the way the frequency shifting of the light is resolved. Unlike FDBS, which involves direct detection of the frequency shifting induced by light scattering and its evolution (with time or under new material constraints), TDBS involves detection of the frequency shifting from the difference between the reflected probe light at the sample surface (non-shifted) and the scattered probe light by the CAP.
The parameters of the CAP beam, such as its frequency spectrum and the directivity pattern, can be controlled like in LUI, via the design of the optoacoustic transducers (OAT) and the choice of the pump light characteristics and optical focusing [40, 79–81] .

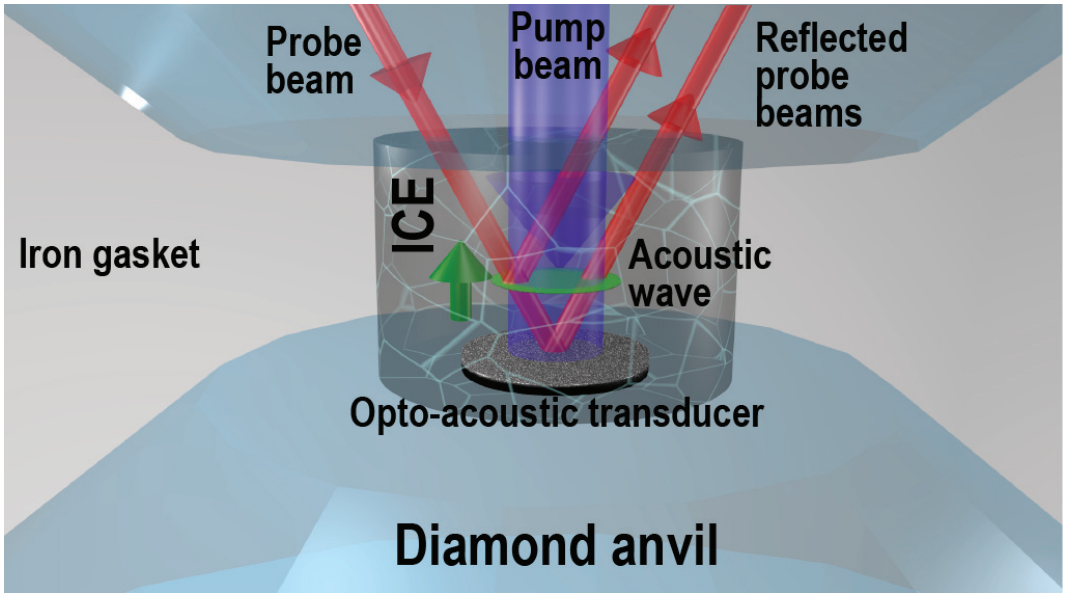

Figure 1.5 – Schematic of the time-domain Brillouin scattering (TDBS) interaction, schematized in the case of a compressed water ice sample in a diamond anvil cell (DAC) [82]. The probe laser beam is shown at an angle for clarity. Ultrashort laser pulses are used to (i) generate a CAP in the optoacoustic transducer (OAT) via thermo-elasticity (pump laser beam) and (ii) monitor the propagation of the CAP launched in the transparent-to-the-wavelength water ice sample (probe laser beam). The detection is realised via heterodyning between the strong reflections on the spatially-fixed sample interfaces, and the weak probe light intensity backscattered by the moving CAP. Hence oscillations in the transient reflectivity signals are induced by interferences due to the phase changes between the probe light scattered by the propagating CAP and the fixed reflections on the sample. The time-domain Brillouin oscillations observed in such signals reveal, by the changes in their frequency, variations in the acoustic velocity of the CAP and or in the refractive index. In a similar way, amplitude variations, different from expected decays due to such phenomena as acoustic and optic attenuation, or optical coherence length, inquire about inhomogeneities and possible interfaces encountered by the CAP in the sample. 3-D images are obtained by raster-scanning the co-focused pump and probe beam over the sample.

Application of ultrashort laser pulses, of ps duration or shorter, provides opportunity to launch CAPs in the GHz frequency range, a condition to obtain the most efficient scattering situation in the backscattering TDBS configuration (up to now, 3-D TDBS imaging has been conducted only in this configuration). Indeed, efficient scattering is obtained in this configuration when the photons and phonons momenta are comparable in magnitude, ensuring the respect of the momentum conservation law in the photon-phonon interaction (or Brillouin scattering condition) [35, 83]. The nm to sub-µm length CAPs are obtained when the laser pulses are incident on either strongly absorbing materials (like metal or semiconductors with light penetration depths shorter than several tens of nm) or just nm-thick absorbing films/coatings on the transparent substrate [Fig. 1.5]. This length scale controls the axial (depth) dimension of the probe light scattering volume, *i.e.*, the dimension along the propagation direction of the CAP. The lateral dimensions of the scattering volume are controlled by the focusing of the pump light, because it determines the lateral dimensions of the launched CAP and the angular spectrum of the emitted CAPs

[40, 84].

Detection of the CAPs is ensured by time-delayed (relative to the pump arrival time) ultrashort laser pulses referred to as the probe, commonly provided by the same laser as the pump (by splitting it into two beams) or by a similar laser source. The probe beam is mainly reflected on the motionless surfaces/interfaces of the sample under study, and weakly scattered (in a backscattered configuration like depicted in Fig. 1.5) by the propagating CAPs. Indeed, upon propagating in the sample, the acoustic compression-dilatation disturbance is locally changing the reflectivity of the sample, and thus acts like a weakly efficient, moving mirror. Hence when collected on a photodetector, the strong reflection and the weak scattering are interfering constructively/destructively pending on their phase difference. Heterodyning between these two contributions gives access to Brillouin oscillations (BO) in the recorded transient reflectivity signals, proportional to the product of the electric fields of the two light fields in a first order approximation. Therefore, when the CAP is launched in a homogeneous sample, the frequency associated to the BO, *i.e.*, the Brillouin frequency (BF), is constant since the velocity of the CAP is constant. In fact, in the collinear backscattering geometry, the BF is linearly proportional to the product between the CAP velocity and the refractive index of the sample at the probe light wavelength [79].

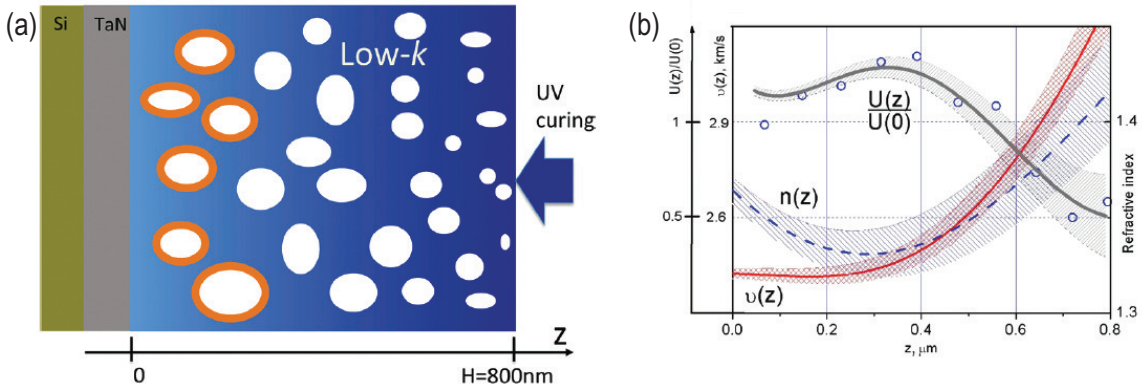

Figure 1.6 – (a-b) First TDBS experiments conducted on continuously spatially-distributed elactic inhomogeneity in the depth of a transparent nanoporous organosilicate film (SiCOH) [85]. (a) Representation of the inhomogeneity distribution in the sample, white disks being nanopores, varying in dimensions from the surface to the 30 nm TaN OAT film. Blue gradient indicates that the deeper (lighter) shade is the region of higher (smaller) elastic modulus. (b) Evolution of the depth profile of the refractive index $n(z)$, the sound velocity $\nu_s(z)$ and the normalized photoelastic coefficient $P(z)/P(0) \sim U(z)/U(0)$ obtained via TDBS.

3-D imaging by TDBS is achieved by raster-scanning the co-focused pump and probe laser beams over the sample. The lateral resolution is controlled by the overlapping pump and probe focii. TDBS was first successfully applied to imaging in transparent media with spatially localized inhomogeneities [88–92]. Following these seminal studies, the TDBS technique has been extended to 2-D and 3-D imaging of the

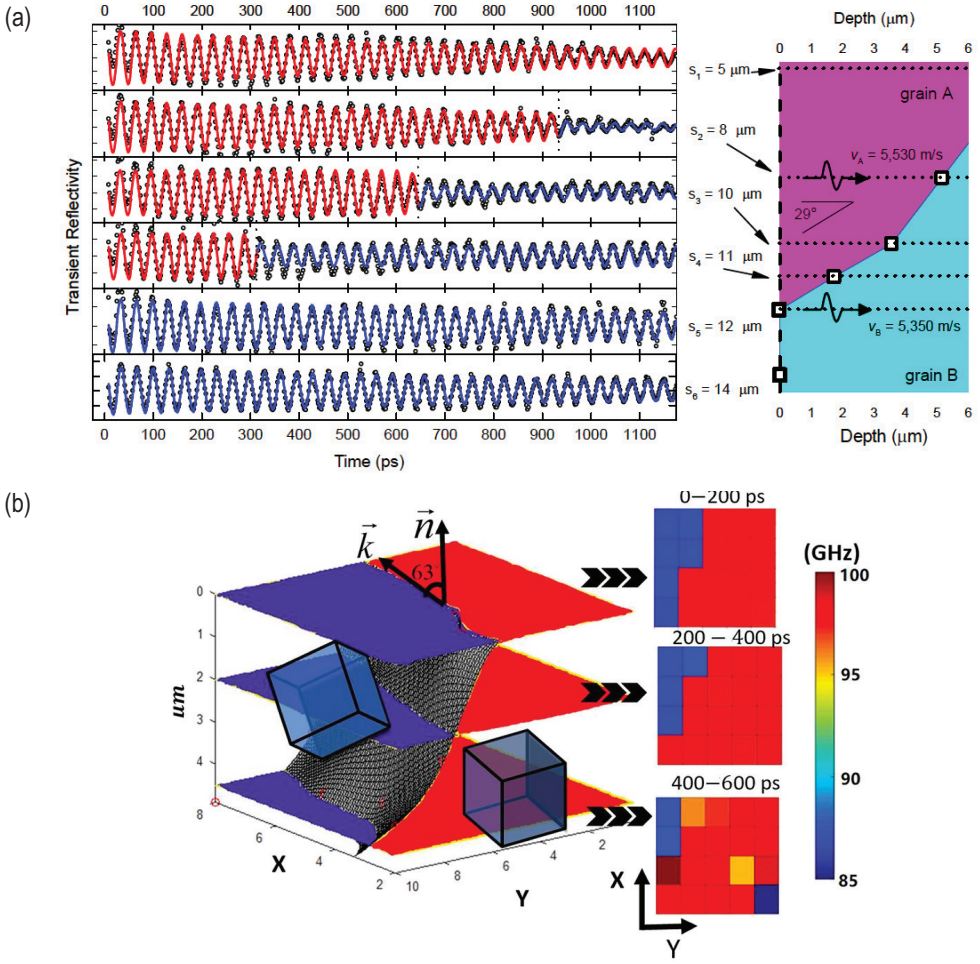

Figure 1.7 – (a) Sub-surface grain boundary evidenced via BF shifts in the transient reflectivity signal recorded via TDBS, in a polycrystalline UO_2 sample [86]. (left) Brillouin oscillations (BO) observed in the vicinity of the grain boundary: red and blue solid lines correspond to the experimental data best fits with oscillation frequency corresponding to grain A and B respectively. (right) Illustration produced from the analysis of the BO evidencing the sub-surface boundary between grain A and B. (b) Inclined grain boundary evidenced in a polycrystalline CeO_2 sample via TDBS with on the right the Brillouin frequency content of "slices" of the sample obtained at different time in the acoustic part of the transient reflectivity signals and on the left the "extrapolated" surface passing through the boundary evidenced in the sample "slices". Rotated cubes present the grain crystalline orientation and the $\vec{n}$ and $\vec{k}$ vectors present the normal to the sample surface and the normal to the inclined grain boundary, respectively [87].

continuously-distributed inhomogeneities in nanoporous materials [85, 93] with a stated axial resolution of $\sim$ 80 nm and allowing the evaluation of the continuously-varying refractive index, acoustic velocity and photoelastic constants [Fig. 1.6]. Other applications include ion-implanted semiconductors and dielectrics [94–96], texture in polycrystalline materials [82, 97] or inside vegetable and animal cells [98–100], and temperature profiles in liquids [101].

All these experiments confirmed that, when the CAP is reflected/transmitted by an interface between

two transparent media, the TDBS signal can change both in periodicity and amplitude. Changes in periodicity are due to different acoustical and different optical properties in each medium. Amplitude changes are additionally due to different acousto-optical parameters in each medium as well as acoustical and optical impedance mismatches across interfaces. The characterization of the spatial orientation of plane interfaces or, more generally, imaging of complex non-plane interfaces by TDBS in the bulk of a medium, has emerged quite recently in relation to polycrystalline materials with application in the energy industry [86, 87, 102], following earlier experiments where the surface acoustic waves generated and detected by ultrafast lasers were applied for the imaging of grain boundaries on the surface of a medium [103].

In Ref. [86], a 2-D image of a subsurface grain boundary in a polycrystalline UO_2 sample was obtained due to the variations of both the frequency and the amplitude of a monochromatic Brillouin oscillation, when the CAP was crossing the boundary [Fig. 1.7 (a)]. In Ref. [87], the 3-D TDBS imaging was applied to the evaluation of the elastic constants of a CeO_2 sample and determination of the crystallographic orientation of the grains on the surface of the sample. It was demonstrated that TDBS imaging with a quasi-transverse acoustic (QTA) pulse can be more sensitive to grain orientation than TDBS imaging with quasi-longitudinal acoustic (QLA) pulse. 3-D orientation of the subsurface boundary by TDBS imaging with LA mode was also reported. More precisely, the "extrapolated" reconstruction of the inclined surface between two grains of different crystalline orientation was achieved [Fig. 1.7 (b)]. The interface between the grains was extrapolated from the surface down to $\sim$ 5 µm deep into the sample, via BF "slices" of the sample obtained by extracting the frequency (BF) associated to the strongest frequency peak in the Fourier transform of the acoustic part of the transient reflectivity signals of the scan [Fig. 1.7 (b)]. The lateral and axial resolutions were of the same order, 2 µm, leading to an estimated 63° inclination of the grains interface with respect to the free surface of the sample. Finally, it has been demonstrated very recently [102] that complete orientation of the surface grains can be obtained by measuring how the polarization of the probe beam influences the detected signal amplitude in the TDBS imaging.

These recent studies on imaging of grain microstructure with TDBS lead to the ability of 3-D imaging of grains and grain boundaries in large volumes of polycrystalline materials. Yet, the complete 3-D imaging in a large volume remains to be addressed, due to the current lack of a dedicated and robust signal processing analysis routine and image reconstruction procedures. One of the aim of this thesis is to develop a step-by-step signal processing procedure to achieve complete 3-D shape reconstruction of grains and/or microstructures, the results will be detailed in Chap. 3.

1.4 Conclusion

Ernst Ruska, Gerd Binning and Heinrich Rohrer obtained the Nobel prize of physics in 1986 [104], the first one for the "design of the first electron microscope" and the two others for "their design of the scanning tunnelling microscope", historically acknowledging how the development of these imaging techniques was a major achievement in physics, but also benefiting to all science communities. The ability to image nanometric structures allowed to resolve long awaited questions, an example among other being the first evidence of finite length synaptic structure in the cerebral cortex permitted by the use of electronic microscopy. It is thus understandable that, the enhancement of existing techniques, as well as the development of different, complementary ressources to access the nanometric scale, is of major interest.
It is nowadays common, if not required, to compare the results of different imaging techniques to corroborate their veracity. In this context, Chap. 1 aimed at putting into perspective the currently developed time-domain Brillouin scattering technique, by positioning it among the abundant available nanoscale imaging techniques.
The surface imaging techniques described in Sec. 1.2 proved to be amazingly precise, resolving atom-to-atom location, while extracting fundamental properties such as crystalline orientation of surface grains [Fig. 1.1], but being limited to 2-D mapping. TDBS will appear as a suitable tool to investigate the evolution of this grains in the third dimension while, in the best conditions, *i.e.*, if detecting the three possible acoustic modes in one grain, could also extract orientation information.
On the other hand, non acoustic-based techniques permit 3-D evaluation too, with spatial resolution reaching the nanometer scale or close to it, like in TEM and in x-ray microscopy, even though important sample preparation limits the type of sample that can be studied.
Photoacoustic techniques, requiring a laser light source, appear as a technically simpler method to implement, and the wealthy amount of methods taking advantage of it in bio-medical and material sciences, is a good indication of its interest.

In this Chapter, we have reviewed a part of the nanoscale imaging techniques commonly employed in bio-medical and material science fields, with a distinction between methods involving acoustics or not. Non-acoustics techniques have been introduced, suited to surface and sub-surface imaging, via a variety of physical mechanism used to map/scan the samples properties. In the section dedicated to acoustic-based imaging techniques, the concept of phonon has been introduced along with the definition of photoacoustics. The nanoscale imaging techniques using photoacoustics have been presented, split into three categories: laser ultrasonic imaging (LUI), photoacoustic imaging (PAI) and time-domain Brillouin scattering (TDBS).
The purpose of Chap. 2 is to concentrate on the theoretical aspects hidden behind the thermoelastic generation of CAPs and the way TDBS allows to monitor their propagation.

Chapter 2

Theory of thermoelastic generation of CAPs and their detection via time-domain Brillouin scattering (TDBS)

Contents

2.1 Introduction

A variety of techniques have been developed since the eighties, relying on different physical mechanisms, for the generation of coherent acoustic pulses (CAPs) using ultrafast light pulses [41]. Accordingly, various methods to detect the surface movements induced by, or to monitor the propagation of, these CAPs are available [42]. The combination of both generation and detection techniques in a common experimental setup is permitted by the all-optical pump-probe scheme, where both pump and probe laser beams are directed onto the sample to generate and detect the CAPs. Pioneer experiments employing ps, or shorter, light pulse durations were realised in the 1980s [52, 77, 78, 105] with metals and semi-conductors, the CAPs being generated by the pump pulse in the sample through the optoacoustic effect and detected by the time-delayed (compared to the pump time of arrival) probe pulse via the acousto-optic effect.
The role of the pump laser pulse is to ensure the generation of the CAP, directly in the sample, or in a thin film called the optoacoustic transducer (OAT) in contact with the sample, as long as these materials are absorbing the pump light. When deposited on the surface from which the probe light is entering the sample, the OAT is transparent or semi-transparent to the probe light [52, 78, 89–91, 105].
In the first section, we consider the thermoelastic regime for the optoacoustic conversion of the pump laser light energy into a propagating (strain) CAP. The heating of the pump light absorbing material induces thermoelastic stresses via the thermal expansion of the material. This thermoelastic source launches a CAP in the absorbing material (OAT) that can be then transmitted to the transparent sample we aim to image. The second section details how monitoring the propagation of the CAP inside the transparent sample is accomplished using the time-domain Brillouin scattering technique, relying on the scattering of the probe light by the propagating CAP. Typical oscillations in the recorded TDBS signals (Brillouin oscillations) allows to monitor the velocity changes of the CAP via the changes in the frequency of the oscillations. The final section focuses on the possibility to generate and detect transversal acoustic modes along with the longitudinal ones, providing results obtained in a carbon-diamond (C) / tungsten (W) sample.

2.2 Acoustic modes generation with ultrashort laser pulses via thermoelasticity

The absorption of the pump electromagnetic radiation, focused on the surface of a pump-light-absorbing material, converts light energy into heat and generates, via thermoelastic stresses, an acoustic strain pulse, or CAP, containing a broad frequency range of phonons. Depending on the power density of the pump laser light, two CAP generation regimes exist: ablation and thermoelastic, as depicted in Fig. 2.1 [106]. If the power density is high enough, part of the illuminated surface is vaporized, creating forces normal to the surface but damaging the studied material [Fig. 2.1 (a)]. On the other hand, if the power density of the laser is below the level of ablation regime, the sample is heated without damaging it, and thermal stresses arise as the source of strain (CAP) [Fig. 2.1 (b)]. In the following, it is the thermoelastic regime that is considered, since it is suited to the non-destructive testing of samples, like the ones studied in Chaps. 3 and 4.
In a first part, the thermal field distribution inside the material, induced by the absorption of the pump laser light, is determined. As a first approximation, this thermal distribution is considered fixed in time, and acts as the source of thermal stresses, allowing to determine the shape of the CAP launched in the absorbing material. In the second part of this section, the consideration of thermal diffusion in the sample will modify the derived CAP shape to a more experimentally relevant one.

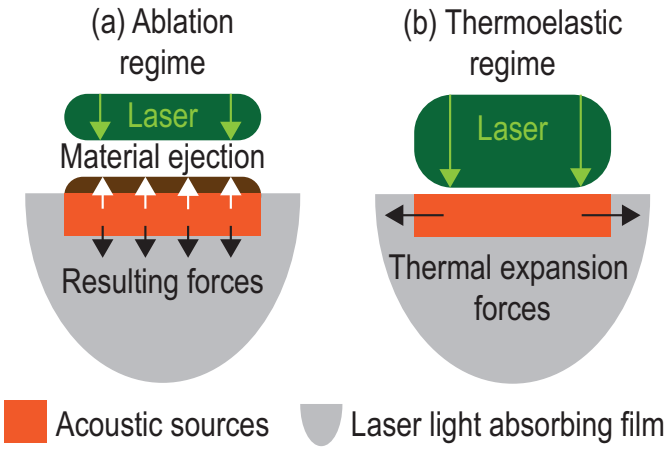

Figure 2.1 – Schematic of the two possible CAP generation regimes, ablation and thermoelastic, when the pump laser light pulse is absorbed by a metallic film, adapted from [106].

2.2.1 CAP generation by stationary temperature distribution induced by an instantaneous laser action

In the thermoelastic regime [Fig. 2.1 (b)], the pump optical pulse is incident on the surface of the pump-light absorbing material (OAT film), heating the sample due to the absorption of a part of its energy. In a first approximation, the conversion process from optical energy into heat is considered instantaneous, *i.e.*, governed by a delta function ($\delta(t)$) centred on the time of arrival of the pump to the surface of the film. The effect of thermal diffusion can be neglected until the characteristic diffusion time of the temperature (or thermal) field over the penetration depth [Eq. (2.1)] becomes shorter than the characteristic time of acoustic pulse propagation across the penetration depth [107]. Finally the heat is considered restricted inside a spatial region (below the free surface of the film) equal to the optical penetration depth (or absorption length) ζ of the pump laser. In metallic films, the penetration depth is generally of tens of nm.

In order to determine the shape of the CAP pulse generated via thermoelasticity, it is first required to anticipate the thermal field distribution ΔT induced by the pump light absorption. In the following theoretical developments, we are assuming an experimentally relevant situation, where the following assumptions are considered:

- the pump light pulse, of picoseconds (ps) to femtoseconds (fs) duration (ultrashort pulse), is instantly absorbed ($\delta(t)$ function),
- thermal diffusion is neglected (long time of diffusion compared to pulse propagation time),
- the laser light spot radius a_{pump}, reduced to $\sim$ µm size via its focus on the surface of the film using an objective lens, is larger than the nm-scale film thickness d and the light penetration depth ζ. Moreover, the film is considered elastically isotropic (1-D problem).
- The energy Q delivered by the light pulse, and the film thickness d, are set accordingly to the introduction of this chapter, so that Q is below the ablation regime and $\zeta < d$ (thermoelastic regime).

As it will be discussed in Sec. 3.4.2, different physical factors limiting the imaging depth of the technique exist, and the optical absorption of the probe laser beam is one of them. This effect can be introduced via the definition of a complex-valued electric susceptibility [53]: $\tilde{\chi}_1 = \chi_1 - i\chi''$, with the subsequent complex-valued optical refractive index $\tilde{n}_1 = n_1 - i\kappa_1$, where i stands for the imaginary number $i^2 = -1$ and κ_1 stands for the absorption coefficient of the light in material (1).

Hence, for an electromagnetic plane wave propagating alont the z-axis in a medium with such complex-valued optical properties, the complex exponential part of the electric field $\mathbf{E}$ reads: $e^{-i\left(\tilde{k}_1 z - \omega t\right)} = e^{-i[k_0(n_1 - i\kappa_1)z - \omega t]} = e^{-i(k_0 n_1 z - \omega t)} e^{-k_0 \kappa_1 z}$, where $\tilde{k}_1$ is the complex-valued wavenumber of the electromagnetic wave in the medium and is equal to $\tilde{k}_1 = k_0 \tilde{n}_1$ with k_0 the real-valued wavenumber in vacuum, ω is the angular frequency of light, and t stands for the time variable. Hence the energy distribution, which

depends on E^2, is decaying exponentially with z as $e^{-2k_0\kappa_1 z} = e^{-z/\zeta}$ with the optical penetration depth (or absorption length / skin depth) of the light intensity at the wavelength λ in vacuum:

$$\zeta = \frac{1}{2k_0\kappa_1} = \frac{\lambda}{4\pi\kappa_1}. \tag{2.1}$$

Note that the expression of the optical penetration depth stands for both pump and probe laser light.
Taking into account these assumptions, the distribution of the temperature rise distribution, induced by the pump laser light absorption, along the depth axis of the film (z-axis, with $z = 0$ the free surface and $+z$ directed inside the film), is given by [105]:

$$\Delta T\,(z) = \frac{(1-R)\;Q}{\pi\;a_{pump}^2\;\zeta\;C_v} e^{-z/\zeta}, \tag{2.2}$$

with R the optical intensity reflection coefficient and C_v the specific heat per unit volume of the material.
The exponential decay profile of this temperature rise is illustrated in the case of pump light absorption by three different metallic films in Fig. 2.2 (a).
The temperature elevation inside the film (compared to its initial temperature) [Eq. (2.2)], causes the heated part of the sample to expand with a characteristic linear (isotropic film) thermal expansion coefficient α^T, giving rise to a thermoelastic stress. The associated thermoelastic stress tensor $\underline{\underline{\sigma}}^T$ is thus spherical [108]: $\underline{\underline{\sigma}}^T \sim \delta_{ij}$ denoted for simplicity σ^T, where δ_{ij} is the Kronecker symbol.
Following the 1-D assumption that sets the problem along the z direction, the resulting stresses depend on z and the only allowed motion is parallel to z, thus the stress and strain tensors are described by their only non-zero component: σ_{zz} and η_{zz}, respectively. In addition, the isotropic-film assumption reduces the possible acoustic generated mode, in the 1-D problem, to longitudinal motion (LA mode).
Accordingly, the stress-strain relation in the presence of a thermal stress, is given (in 1-D) by [53]:

$$\sigma_{zz} = 3\left(\frac{1-\nu}{1+\nu}\right) B\eta_{zz} - \sigma^T = \rho v_{LA}^2 \eta_{zz} - 3B\alpha^T \Delta T(z), \tag{2.3}$$

with ν Poisson's ratio, B the bulk modulus, ρ the density and v_{LA} the velocity associated to the longitudinal acoustic (LA) mode (compression). In this configuration, most of the generating volume (thermoelastic source volume) is acting like a piston expanding normally to the surface [108].
The resolution of the equations of thermoelasticity, giving the displacement u_z along the z direction (with $\eta_{zz} = \partial u_z/\partial z$), leads to the wave equation for u_z [53, 105, 107, 109]

$$\frac{\partial^2 u_z}{\partial t^2} = v_{LA}^2 \frac{\partial^2 u_z}{\partial z^2} + \frac{v_{LA}^2 \eta_0}{\zeta} e^{-z/\zeta}, \tag{2.4}$$

with η_0 deduced from the boundary condition $\sigma_{zz} = 0$ at time $t = 0$ (non-expanded surface before the light pulse arrival) [53]:

$$\eta_0 = \frac{3B\alpha^T(1-R)Q}{\pi a_{pump}^2 C_v \zeta v_{LA}^2} = \frac{\gamma(1-R)Q}{\pi a_{pump}^2 \zeta v_{LA}^2}, \tag{2.5}$$

with $\gamma = 3B\alpha^T/C_v$ the Gruneisen parameter.
Finally, the shape of the CAP (strain) is given by the following equation [53, 105]:

$$\eta_{zz}(z,t) = \eta_0 e^{-z/\zeta} - \frac{\eta_0}{2}\left[e^{-\frac{z+v_{LA}t}{\zeta}} + e^{\frac{|z-v_{LA}t|}{\zeta}}\,\mathrm{sign}(z-v_{LA}t)\right], \tag{2.6}$$

where sign correspond to the sign (or *signum*) function. The strain in Eq. (2.6) is composed of a stationary strain (first term) illustrated by the constant decaying (from the film surface, distance $z = 0$) part in Fig. 2.2 (b). The two other terms under brackets in Eq. (2.6) account for the propagating strain pulse shape.

The strain profile [Fig. 2.2 (b)] obtained with Eq. (2.6) highlights two distinct regions: a progressive

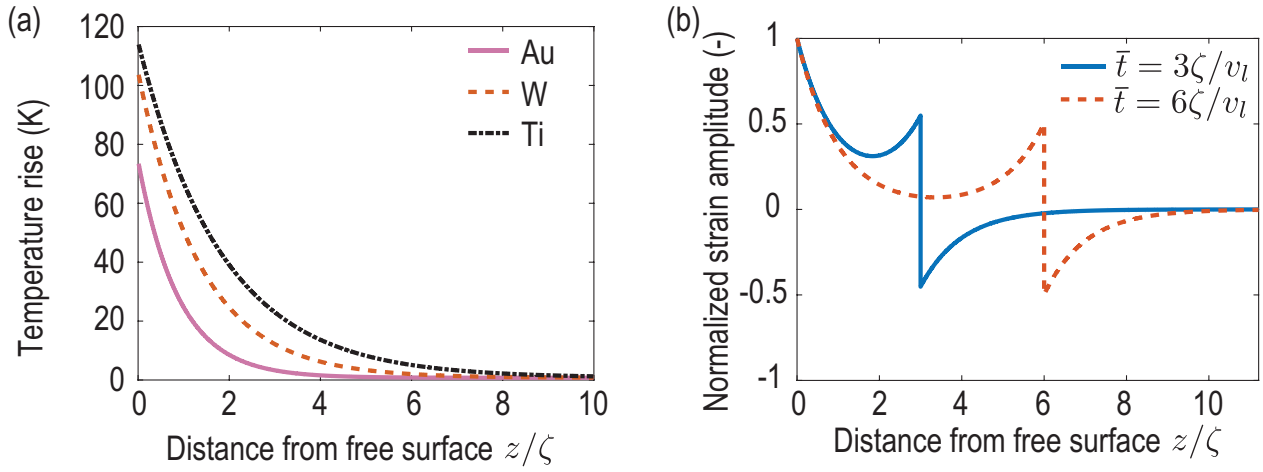

Figure 2.2 – (a) Temperature rise distribution, below the free surface of the film $z = 0$ nm, obtained from Eq. (2.2), for three different metallic films: gold (Au), tungsten (W) and titanium (Ti). The parameters used to compute these distributions are given in the table of Appendix 1. (b) CAP (strain) pulse shape [Eq. (2.6)] computed in gold (Au) with the associated time-fixed temperature gradient [Eq. (2.2)] at two different normalized times $\bar{t}$.

decay in the vicinity of the free surface of the film (near $z = 0$), and a bipolar pulse. The first one is time-independent and corresponds to the strain induced by the thermoelastic stresses. The second one is a bipolar pulse with a width twice the penetration depth ζ of the pump light and propagating at the velocity v_{LA}. Its bipolar shape comes from the fact that the reflection coefficient for the strain at the free surface is -1. The thermoelastic source acts as a volumetric source, below the film surface, of two exponentially decaying strains pulses, initially propagating in the $+z$ and $-z$ opposite directions, the

later being reflected "upside down" when reaching the free surface of the film and then also propagating in the $+z$ direction, which justifies the bipolar shape of the pulse. These exponentially decaying strain pulses are replicating the initial exponential temperature distribution in the material [Fig. 2.2 (b)] [110].

As a first approach, the shape of the CAP, generated by the absorption of an ultrashort optical pulse in a metallic film has been obtained under specific assumptions. Among them, the absorption of the laser pulse energy has been considered instantaneous, and the thermal diffusion processes were neglected. The second part of this section aims to consider the influence of the thermal processes on the shape of the generated CAP.

2.2.2 CAP shape and thermal diffusion

In the previous section, the CAP (strain) shape has been derived and represented [Fig. 2.2 (b)] when considering the generation of CAPs by a stationary temperature distribution [Eq. (2.2)] induced by the instantaneous pump laser absorption. This definition of the temperature distribution prevents from taking into account the possible thermal diffusion processes of ΔT. Taking into account these effects modifies the shape of the launched pulse. First, the shape of the CAP is derived and represented far (in both time ans space) from the generation area, and then the effect of thermal diffusion processes is discussed.
To include the effect of thermal diffusion, the wave equation for the displacement u_z [Eq. (2.4)] is slightly modified [107]:

$$\rho\frac{\partial^2 u_z}{\partial t^2} = \rho v_{LA}^2\frac{\partial^2 u_z}{\partial z^2} - \frac{\partial G(z,t)}{\partial z}, \tag{2.7}$$

to include $G(z,t)$ the thermal source function varying with both space z and time t.
The temperature distribution in the film is now consider to depend on both time and space: $\Delta T(z,t)$, and the contribution to the stress is defined in the thermal source function by [107]:

$$\delta G = \gamma C_v \Delta T(z,t). \tag{2.8}$$

The stress field is then obtained by taking the sum over the source terms δG. Doing so, the shape of the strain pulse propagating in the $+z$ direction, *i.e.*, away from its generation volume, is given by [107]:

$$\eta_{zz}(z,t) = -\frac{1}{2\rho v^2}\int_{-\infty}^{+\infty} \text{sign}\left[z - v_{LA}\left(t-t'\right)\right]\left.\frac{\partial G}{\partial t}\right|_{(|z-v_{LA}(t-t')|,t')} dt', \tag{2.9}$$

with the following stress-free surface boundary condition:

$$\rho v_{LA}^2\left.\frac{\partial u}{\partial z}\right|_{z=0} - G(0,t) = 0. \tag{2.10}$$

Like in Eq. (2.6), the sign function in Eq. (2.9) is a result of accounting for the sign change of the part of the strain that is reflected on the free surface of the film. Equation (2.9) describes the strain pulse shape when the pulse has left the optical penetration depth ζ, *i.e.*, at times $\bar{t} \gg \zeta/v_{LA}$, in order not to account for the time-independent part of the strain discussed in Fig. 2.2 (b).
The temperature distribution in the film can be first modelled with Fourier's 1-D diffusion law [107]:

$$C_v \frac{\partial T}{\partial t} = \frac{\partial}{\partial z}\left(K \frac{\partial T}{\partial z}\right) + \frac{(1-R)}{\zeta} I_f(t) e^{-z/\zeta}, \tag{2.11}$$

with K the thermal conductivity and $I_f(t)$ the intensity variation of the optical pulse, and the two following boundary conditions: $\partial T/\partial z = 0$ at $z = 0$ and $\Delta T = 0$ at $z = \infty$.
First, the shape of the CAP can be derived analytically from Eqs. (2.8)-(2.11) in the same situation as previously [Sec. 2.2.1], *i.e.*, neglecting the thermal diffusion, by setting $K = 0$ in Eq. (2.11). From this assumption, and keeping in mind the instantaneous absorption of the pump light pulse (instantaneous heating) that sets here $f(t) \equiv \delta(t)$, the CAP shape is given by [107]:

$$\eta_{zz} = \eta_0 \text{sign}\left(v_{LA}t - z\right) e^{-\frac{|z - v_{LA}t|}{\zeta}}, \tag{2.12}$$

with a new definition of the strain amplitude $\eta_0 = \gamma(1-R)q/\left(2\zeta\rho v_{LA}^2\right)$, q being the laser fluence (energy per unit area per pulse).

In Fig. 2.3 (a), the same bipolar shape of the pulse as the one obtained in Fig. 2.2 (b) is showed in the case of copper (Cu), without the progressive thermally generated strain amplitude decay in the vicinity of the free surface of film, as expected. The two exponentially decaying strains composing the bipolar pulse are again replicating the thermal source distribution.
However, the effect of Fourier thermal diffusion needs to be taken into account, *i.e.*, with a non-zero value for K in Eq. (2.11), when the thermal diffusion time is smaller than the time $\bar{t} = \zeta/v_{LA}$ for the pulse to exit the optical penetration depth ζ of the pump laser. The result of taking into account the Fourier diffusion in the example of copper (Cu) [Fig. 2.3 (b)] shows the broadening of the CAP shape due to the extension of the thermal source, in both time and space, during the generation of the CAP. It is no more possible to approximate the generation of the CAP as instantaneous compared to the CAP duration, and as a consequence the shape of the CAP is no more a replica of the initial temperature distribution in the film.
More specifically, the CAP bipolar symmetry is broken: the exponentially decaying strain that directly propagates in the $+z$ direction seems to be more importantly influenced compared to the one that is reflected at the film free surface. The reason is that the first strain, that propagates from the beginning away from the film free surface, is affected by the strongly diffused temperature distribution, while the second one, that is first propagating to the free surface of the film, is delayed and thus affected by an already less diffusive temperature distribution.

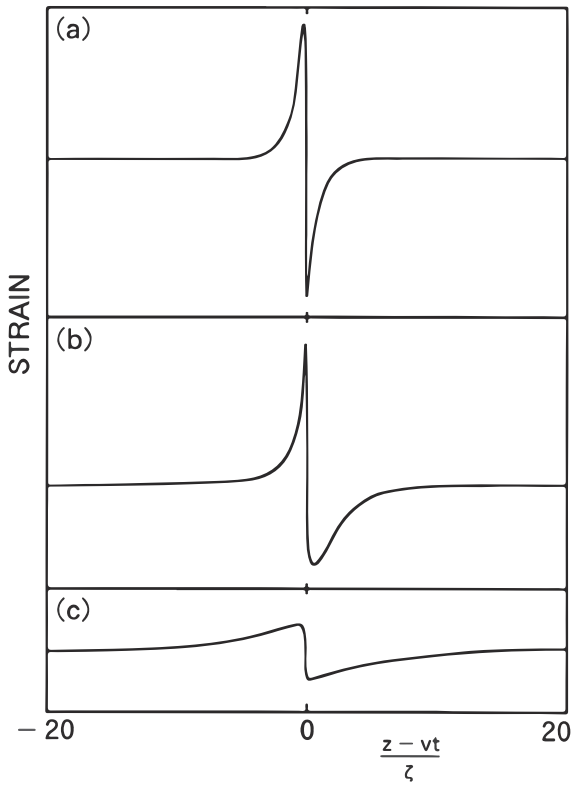

Figure 2.3 – CAP strain shape changes when accounting for thermal diffusion in a copper (Cu) film [107]. (a) Thermoelasticaly generated CAP strain shape without thermal diffusion ($K = 0$, $g \to +\infty$) and caused by instantaneous heating [Eq. (2.12)]. (b) Thermoelasticaly generated CAP strain shape with Fourier thermal diffusion [Eq. (2.11)] and instantaneous heating ($g \to +\infty$, meaning instantaneous heating of the electrons and instantaneous equilibrium of the electron and lattice temperature in the two temperature model). (c) Thermoelasticaly generated CAP strain shape accounting for electronic diffusion. The scales in (a-c) are the same [107].

Finally, in metallic films, another diffusive effect needs to be accounted for the ultrashort time scales of pump light absorption. At the atomic scale, the electrons are absorbing the pump light energy in an instantaneous time compared to the CAP duration. However, it is the energy transfer from these electrons to the lattice (the atomic structure of the material) via electron-phonon collisions that is not necessarily instantaneous. As a consequence, the effective thermoelastic stress distribution becomes longer than the optical penetration depth ζ and thus the effect of considering the electron thermal diffusion is the increase of the CAP broadening [Fig. 2.3 (c)].

More precisely, to derived the pulse shape in Fig. 2.3 (c), it has been considered that the electrons and the lattice are decoupled, with each of them remaining in a pseudo-equilibrium with a specific temperature. The electron temperature will first increase drastically from its initial "rest" state, under pump light exposure, and then these overheated electrons will transfer their energy to the lattice until reaching a thermal equilibrium, *i.e.*, when both electrons and lattice temperature are equal. Hence the time for the

electrons to diffuse and transfer their energy to the lattice, known as the relaxation time, increases the effective distance from the surface where the generation of the CAP is influenced by thermal processes. The duration of the relaxation time is mainly driven by the electron-phonon coupling constant g: the larger g, the smaller the relaxation time. Typically, in metals exhibiting high electrical conductivity, this relaxation time is of the order of ~ 1 ps. In the case of the simulation presented in Fig. 2.3 (c), it is the two temperatures model that has been used to account for the electronic diffusion.

Ultimately, the shape of the generated CAP will not be extensively discussed in the frame of TDBS detection, and the non-diffusive CAP shape, replicating the thermal distribution one, obtained in Eq. (2.9) [Fig. 2.3 (a)] is a sufficiently good approximation to discuss the physics behind TDBS detection. The shape of the CAP thermoelastically generated by the absorption of the pump light energy in a metallic film has been obtained. The effect of taking into account the diffusion processes, via the 1-D Fourier law and the electronic diffusion, have been discussed. The second step of the pump-probe experiments can thus be addressed: the detection of the CAP when propagating inside a transparent material, relying on the time-domain Brillouin scattering (TDBS) technique.

2.3 TDBS detection of CAPs propagating in transparent materials

The generation of a coherent acoustic pulse (CAP), by the absorption of the ultrashort pump light pulse, has been discussed in Sec. 2.2. As already mentioned, the imaging technique employed throughout this Ph.D. thesis is a pump-probe technique, relying on a second time-delayed light pulse, the probe, to monitor the propagation of the pump-generated CAP.

More specifically, the detection technique employed is the time-domain Brillouin scattering (TDBS) technique. This technique permits the structural imaging of transparent-to-the-probe-wavelength materials, thanks to its capacity to monitor the CAP while it is propagating in the (complex) structured transparent sample. TDBS imaging has been used up to now in reflection configuration, meaning that the heterodyne detection is realised with the reflected part of the probe light. In our experiments, both pump and probe laser beams are focused on the same side of the sample, on the surface of the OAT.

Then, a portion of the probe light, scattered by the propagating CAP, is measured via heterodyning with the portion of the probe light reflected from the surface/interfaces of the sample. This Brillouin scattering of the probe light contributes to the total variations of the transient energy of the reflected probe beam, collected by a photodiode, and gives rise to an oscillating component in time, due to the interferences with stationary reflected light, as illustrated in Fig. 2.4.

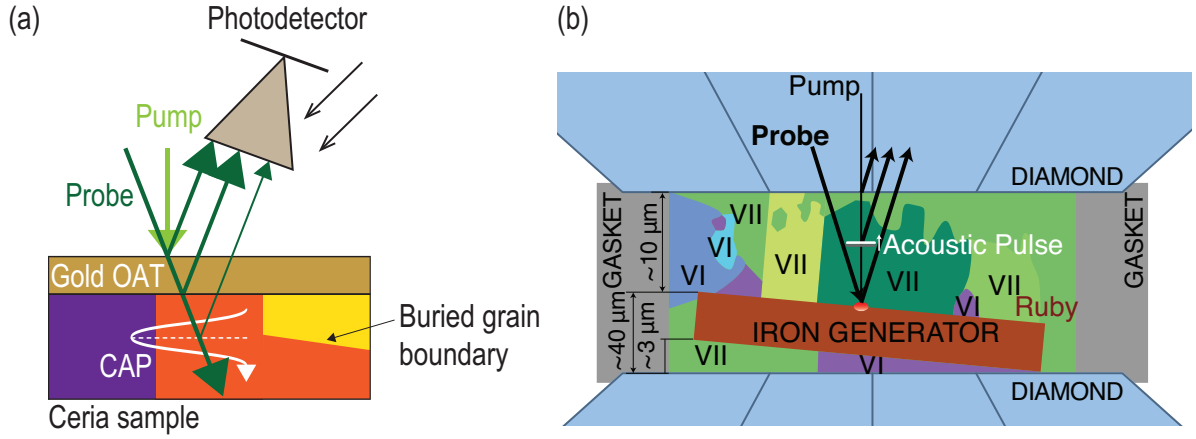

Figure 2.4 – (a) TDBS configuration where the OAT, a gold (Au) film, is deposited on the transparent sample surface at which the probe light is entering the sample, here a polycrystalline CeO_2 sample. This situation corresponds to the forward propagating CAP, where both the probe and CAP are propagating in the same direction [8]. (b) TDBS configuration where the OAT is below the transparent sample surface at which the probe light is entering the sample, here for studying a high pressure polycrystalline water ice sample using an iron (Fe) OAT. The Fe film is reached by the pump and probe laser beams after propagating through the transparent ice sample. This situation corresponds to the backward propagating CAP, where the CAP is propagating in the opposite direction relative to the incident probe propagation direction [7].

Two typical geometries are presented in Fig. 2.4, where the pump-absorbing film is in contact with the transparent material to image, and is used as an optoacoustic transducer (OAT) in order to thermoelastically generate the CAPs and then transmit them in the transparent material. Both cases studied

in Fig. 2.4 are transparent polycrystalline materials, but with a slightly different configuration. In Fig. 2.4 (a), the gold (Au) OAT is deposited on the free surface of a cerium dioxyde (CeO_2) transparent polycrystal to image, and thus the CAP to monitor with TDBS is propagating away from the probe beam focal spot, in the same direction as the probe light propagation direction. In Fig. 2.4 (b), the iron (Fe) OAT is deposited beneath the water ice crystal (obtained at ambient temperature in a high pressure environment) to image. Hence in this configuration, both pump and probe beams propagates through the ice sample to image, and are focused on the OAT surface. Thus, the CAP to monitor is propagating in the opposite direction compared to the propagation direction of the probe laser beam.
Both situations depicted in Fig 2.4 have in common the fact that the probe light and the CAP are propagating collinearly (or quasi-collinearly), which is the typical situation studied theoretically in this section. Chapter 4 of this Ph.D. thesis will consider the situation where these light and sound beams are propagating non-collinearly, following refraction of the CAP at an inclined interface during its propagation in a transparent material.

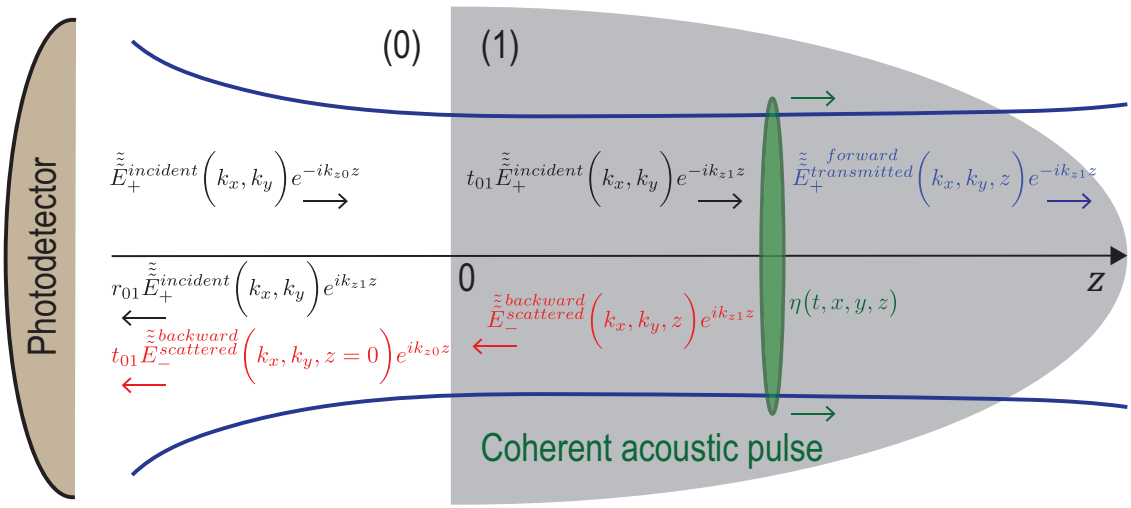

Figure 2.5 – Schematic representation of the probe light and the CAP contributing to the time-domain Brillouin scattering signal detection. The initial probe light field, that exists even in the absence of the CAP, is due to the laser pulses incident, from the semi-infinite light-transparent material denoted by (0) ($z < 0$), on the sample surface ($z = 0$). These incident pulses induce the laser pulses transmitted inside the semi-infinite material denoted by (1) ($z > 0$) and the laser pulses reflected from the sample surface. The strain CAP $\eta(t, x, y, z)$ is launched in the transparent material (1) due to the absorption, near the surface, of the pump laser beam (not represented), co-focused on the surface $z = 0$ with the probe laser beam. Either the material (1) is highly absorbing for pump laser pulses or a semi-transparent metallic layer (not represented) is deposited on the surface. When the pump laser pulses are incident on the sample before the probe laser pulses, the acousto-optic interaction between the coherent acoustic pulses and the initial probe light field creates the optical polarization sources of the scattered light. The time-domain Brillouin scattering signal is a result of the heterodyne detection of the acoustically scattered probe light by the reflected-by-the-surface ($z = 0$) probe light, both collected by the same photodetector.

Therefore, the most typical TDBS configuration is presented in Fig. 2.5, the probe light beam being focused through a transparent media (denoted by (0) in the half space $z < 0$) on the surface ($z = 0$) of the transparent sample (denoted by (1) in the half space $z > 0$).

At first, both materials are considered homogeneous and isotropic from the optical point of view, thus the electric field vector $\mathbf{E^{(j)}}(t,x,y,z)$ and magnetic field strength vector $\mathbf{H^{(j)}}(t,x,y,z)$ in medium j, for $j=\{0,1\}$, are varying according to Maxwell's equations [53]:

$$\begin{aligned}
&\nabla\cdot\mathbf{E^{(j)}}(t,x,y,z)=0,\\
&\nabla\cdot\mathbf{H^{(j)}}(t,x,y,z)=0,\\
&\nabla\times\mathbf{E^{(j)}}(t,x,y,z)=-\mu_{vacuum}\frac{\partial\mathbf{H^{(j)}}(t,x,y,z)}{\partial t},\\
&\nabla\times\mathbf{H^{(j)}}(t,x,y,z)=\epsilon_j\epsilon_{vacuum}\frac{\partial\mathbf{E^{(j)}}(t,x,y,z)}{\partial t},
\end{aligned} \tag{2.13}$$

where $\nabla\cdot$ and $\nabla\times$ denote respectively the divergence and curl operators, the quantity in bold denotes, here and in the remaining of the manuscript, a vector, and with μ_{vacuum} and ϵ_{vacuum} the magnetic permeability and electric permittivity of free space, and $\epsilon_j=1+\chi_j$ the relative electric permittivity in medium (j) with χ_j the real part of the electric susceptibility.
From Eqs. (2.13), the wave equation for the electric field amplitude $E^{(j)}(t,x,y,z)$ (the same standing for the magnetic field amplitude) is obtained:

$$\nabla^2E^{(j)}\left(t,x,y,z\right)=\frac{1}{c_j^2}\frac{\partial^2E^{(j)}\left(t,x,y,z\right)}{\partial t^2}, \tag{2.14}$$

with c_j the speed of light in the associated material that writes: $c_j=c_{vacuum}/\sqrt{\mu_j\epsilon_j}$ with μ_j the associated relative magnetic permeability and c_{vacuum} the speed of light in vacuum.
In Fig. 2.5, a superposition of the incident, transmitted and reflected probe light beams composes the initial light field distribution in the absence of the CAPs. All light beams at optical frequency ω satisfy the Helmholtz equation for the electrical field amplitude of the laser radiation $E(t,x,y,z)\equiv\tilde{E}(x,y,z)e^{i\omega t}$,

$$\left[\left(\frac{\partial^2}{\partial x^2}+\frac{\partial^2}{\partial y^2}+\frac{\partial^2}{\partial z^2}\right)+k_j^2\right]\tilde{E}^{(j)}(x,y,z)=0, \tag{2.15}$$

with $k_j(\omega)\equiv\omega/c_j$ the optical wave number in material (j). The solutions of the wave equation [Eq. (2.15)] can be obtained via decomposition of the three dimensional wave fields into propagating plane waves:

$$\tilde{E}^{(j)}\left(x,y,z\right)=\frac{1}{2\pi}\int\int_{-\infty}^{\infty}\tilde{\tilde{E}}^{(j)}\left(k_x,k_y,z\right)e^{-i(k_xx+k_yy)}\mathrm{d}k_x\mathrm{d}k_y, \tag{2.16}$$

and,

$$\tilde{\tilde{E}}^{(j)}\left(k_x,k_y,z\right)=\int\int_{-\infty}^{\infty}\tilde{E}^{(j)}\left(x,y,z\right)e^{i(k_xx+k_yy)}\mathrm{d}x\mathrm{d}y, \tag{2.17}$$

with the wavevector components k_x and k_y that set $k_{zj}=\sqrt{k_j^2-k_x^2-k_y^2}$.

These wave fields satisfy the following equation:

$$\left[\frac{\partial^2}{\partial z^2} + k_{zj}^2\right] \tilde{\tilde{E}}^{(j)}(k_x, k_y, z) = 0. \tag{2.18}$$

The transverse distributions of the plane wave amplitudes of the transmitted and reflected light in Fig. 2.5 are related at $z = 0$ to the transverse distribution of the incident probe beam $\tilde{\tilde{E}}_+^{incident}(k_x, k_y)$ via $\tilde{\tilde{E}}_+^{transmitted}(k_x, k_y) = t_{01}\tilde{\tilde{E}}_+^{incident}(k_x, k_y)$, $\tilde{\tilde{E}}_-^{reflected}(k_x, k_y) = r_{01}\tilde{\tilde{E}}_+^{incident}(k_x, k_y)$, where the transmission and reflection coefficients of the incident probe light at the surface $z = 0$ are denoted by t_{01} and r_{01}, respectively. The solution of Eq. (2.18) for the initial probe light field in Fig. 2.5 is:

$$\begin{cases} \tilde{\tilde{E}}_+^{incident}(k_x, k_y, z) & = \tilde{\tilde{E}}_+^{incident}(k_x, k_y)\, e^{-ik_{z0}z}, \\ \tilde{\tilde{E}}_+^{transmitted}(k_x, k_y, z) & = t_{01}\tilde{\tilde{E}}_+^{incident}(k_x, k_y)\, e^{-ik_{z1}z}, \\ \tilde{\tilde{E}}_-^{reflected}(k_x, k_y, z) & = r_{01}\tilde{\tilde{E}}_+^{incident}(k_x, k_y)\, e^{ik_{z0}z}. \end{cases} \tag{2.19}$$

Here the indices "0" and "1" indicate the difference in the probe light velocities in the materials (0), which is air typically, and (1) which is usually the transparent material of interest.
The presence of the CAP in material (1) induces (via its strain) a spatially-localised weak variation of the permittivity: $\Delta\epsilon_1(t, z) \cong \dfrac{\partial\epsilon_1(t, z)}{\partial\eta}\eta(t, z) \ll \epsilon_1$, that is varying in both time and space (propagating along the z-axis), consequently changing the optical wavenumber [Eq. (2.15)] in the transparent material (1) (since $k_1^2 = \omega^2\mu_1\epsilon_1$):

$$\begin{aligned} \epsilon_1 = n_1^2 \rightarrow \epsilon_1 + \Delta\epsilon_1(t, z) &= (n_1 + \Delta n_1(t, z))^2 \\ &\simeq n_1^2 + 2n_1\Delta n_1(t, z), \end{aligned} \tag{2.20}$$

leading to:

$$\Delta\epsilon_1(t, z) \simeq 2n_1\Delta n_1(t, z). \tag{2.21}$$

Introducing $\Delta\epsilon^{-1}(t, z) = p_1\eta(t, x, y, z)$, with p_1 the photoelastic constant of material (1), defined as the derivative over the strain of the inverse of the permittivity, one can obtain the following relation:

$$\Delta\epsilon_1(t, z) \simeq -p_1 n_1^4\eta(t, x, y, z). \tag{2.22}$$

The effect of probe light absorption has been neglected ($\kappa_1 \rightarrow 0$).
In Fig. 2.5, the diffracting CAP $\eta\,(t, x, y, z)$ launched in the material ($z > 0$) is symbolically sketched for the case when the initial acoustic pulse radius, controlled by the pump laser focusing, is larger than the radius of the probe light focus. The presence of the CAP in material (1) induces, via the acousto-optic interaction (or, as it will be henceforth referred, the photo-elastic effect) [34, 111], the nonlinear optical

polarization [112], and modifies Eq. (2.15) in material (1):

$$\left[\left(\frac{\partial^2}{\partial x^2}+\frac{\partial^2}{\partial y^2}+\frac{\partial^2}{\partial z^2}\right)+k_1^2\right]\tilde{E}^{(1)}(t,x,y,z)=k_1^2n_1^2p_1\eta(t,x,y,z)\tilde{E}^{(1)}(t,x,y,z). \tag{2.23}$$

In Eq. (2.23), $n_1^2p_1\eta(t,x,y,z)\tilde{E}^{(1)}(t,x,y,z)\equiv\tilde{P}(t,x,y,z)$ is the acoustically-induced nonlinear optical polarization [112]. Since the photo-elastic interaction is weak, Eq. (2.23) can be solved in the single-scattering approximation [105, 113], where the initial "strong" light field, $\tilde{\tilde{E}}_+^{transmitted}(k_x,k_y,z)$, creates a nonlinear polarization that emits additional much weaker light waves in material (1):

$$\begin{aligned}\left[\left(\frac{\partial^2}{\partial x^2}+\frac{\partial^2}{\partial y^2}+\frac{\partial^2}{\partial z^2}\right)+k_1^2\right]\tilde{E}^{scattered}(t,x,y,z)&=k_1^2\tilde{P}^{initial}(t,x,y,z)\\&\equiv k_1^2n_1^2p_1\eta(t,x,y,z)\tilde{E}_+^{transmitted}(t,x,y,z).\end{aligned} \tag{2.24}$$

The light waves scattered by the CAP are symbolically represented in Fig. 2.5, both just after the scattering inside material (1) and after the transmission from material (1) to material (0). The parameter t_{10} denotes the transmission coefficient from material (1) to (0). The equation for the transverse distribution of the scattered light, derived from Eq. (2.24), is:

$$\begin{aligned}\left(\frac{\partial^2}{\partial z^2}+k_{z1}^2\right)\tilde{\tilde{E}}^{scattered}(t,k_x,k_y,z)&=k_1^2\int\int_{-\infty}^{\infty}\tilde{P}^{initial}(t,x,y,z)e^{i(k_xx+k_yy)}\mathrm{d}x\mathrm{d}y\\&\equiv k_1^2\tilde{\tilde{P}}^{initial}(t,k_x,k_y,z).\end{aligned} \tag{2.25}$$

The solution of Eq. (2.25) for the angular amplitude of the scattered light propagating in the negative direction of the z-axis, is:

$$\tilde{\tilde{E}}_-^{scattered}(t,k_x,k_y,0\le z<z_a(t))=\frac{1}{2ik_{z1}}(k_1^2)\int_{-\infty}^{\infty}\tilde{\tilde{P}}^{initial}(t,k_x,k_y,z')e^{-ik_{z1}z'}\mathrm{d}z', \tag{2.26}$$

with $z_a(t)$ the distance of the CAP penetration at the observation time t.

In the derivation of Eq. (2.26), it was assumed that the CAP is completely launched in the material ($z>0$), *i.e.*, that at time t of the observation, the interface $z=0$ is not strained: $\eta(t,x,y,z=0)=0$ and hence $\tilde{P}^{initial}(t,x,y,z\le0)=0$. The scattered field in Eq. (2.26) is evaluated at distances $z<z_a(t)$, not exceeding the distance $z_a(t)$, which leads to $\tilde{P}^{initial}(t,x,y,z>z_a(t))=0$. These two conditions provide the explanation for the integration limits over the spatial coordinate in Eq. (2.26) [114].

In TDBS measurements, we are interested in measuring the evolution of the light field scattered along the propagation of the CAP, and the possible changes in its evolution induced by the structure of the transparent sample studied (here material (1)). The scattered light, in Eq. (2.26), transmitted from material (1) to the surrounding material (0) is of much smaller amplitude than the reflected light. The information carried by the scattered light is revealed via optical heterodyne detection, through

the mixing of the acoustically scattered light with the probe light reflected by the surface ($z = 0$) at the photodetector, whose response is linearly proportional to the absorbed light energy and hence is quadratic in the light field amplitude. Since the photodetector collects all the light from the acoustically scattered and reflected beams, the energy at the photodetector is found from the angular distributions of the scattered and reflected light as follows [114]:

$$\begin{aligned} W^{detected} &= W^{reflected} + W^{heterodyned} + W^{scattered} \\ &\sim \int\int_{-\infty}^{\infty} r_{01}\tilde{\tilde{E}}_{+}^{incident}(k_x,k_y)\left(r_{01}\tilde{\tilde{E}}_{+}^{incident}(k_x,k_y)\right)^{*}\mathrm{d}k_x\mathrm{d}k_y \\ &+ 2\Re\left\{\int\int_{-\infty}^{\infty} t_{10}\tilde{\tilde{E}}_{-}^{scattered}(k_x,k_y)\left(r_{01}\tilde{\tilde{E}}_{+}^{incident}(k_x,k_y)\right)^{*}\mathrm{d}k_x\mathrm{d}k_y\right\} \\ &+ \int\int_{-\infty}^{\infty} t_{10}\tilde{\tilde{E}}_{+}^{scattered}(k_x,k_y)\left(t_{10}\tilde{\tilde{E}}_{-}^{scattered}(k_x,k_y)\right)^{*}\mathrm{d}k_x\mathrm{d}k_y, \end{aligned} \tag{2.27}$$

with $\Re$ the real part, and the "$*$" denoting the complex conjugation.
It is the second term of Eq. (2.27) that is relevant to the TDBS technique, as it provides the frequency mixing of the reflected and scattered light. The change in the transient optical reflectivity, *i.e.*, the so-called TDBS reflectivity signal, is given by:

$$\frac{\Delta R}{R} \equiv \frac{W^{heterodyned}}{W^{reflected}}, \tag{2.28}$$

with $W^{reflected}$ the energy measured by the photodetector in the unperturbed (no CAP) reflectivity case. When the plane wave decomposition of the transmitted light field,

$$\tilde{E}^{transmitted}(x,y,z) = \frac{1}{(2\pi)^2}\int\int_{-\infty}^{\infty} t_{01}\tilde{\tilde{E}}_{+}^{incident}(k'_x,k'_y)e^{-i(k'_x x+k'_y y)}e^{-ik'_{z1}z}\mathrm{d}k'_x\mathrm{d}k'_y, \tag{2.29}$$

with $k'_{z1} = \sqrt{k_1^2 - k_x'^2 - k_y'^2}$, is substituted in the polarization $\tilde{P}^{initial}(t,x,y,z)$ [Eq. (2.24)], the scattered field can be evaluated with Eq. (2.26) and, finally, a rather general presentation of the heterodyned contribution to the light energy on the photodetector is derived:

$$\begin{aligned} W^{heterodyned} \sim -\frac{k_1^2 n_1^2 p_1}{(2\pi)^2}\Im\Bigg\{&\int\int_{-\infty}^{\infty}\mathrm{d}k_x\mathrm{d}k_y\left(r_{01}\tilde{\tilde{E}}_{+}^{incident}(k_x,k_y)\right)^{*}\frac{t_{10}}{k_{1z}}\int\int\int_{-\infty}^{\infty}\mathrm{d}x\mathrm{d}y\mathrm{d}z\eta(t,x,y,z) \\ &\times\int\int_{-\infty}^{\infty}\mathrm{d}k'_x\mathrm{d}k'_y t_{01}\tilde{\tilde{E}}_{+}^{incident}\left(k'_x,k'_y\right)e^{i(k_x-k'_x)x+i\left(k_y-k'_y\right)y}e^{-i\left(k_{z1}+k'_{z1}\right)z}\Bigg\}, \end{aligned} \tag{2.30}$$

with $\Im$ designating the imaginary part.
The only assumptions to get the solution in Eq. (2.30) are the perfect transparency of the material (1), leading to real-valued k_1, n_1 and p_1, and the opportunity to describe the photo-elastic interaction by a single constant p_1.

In the paraxial approximation of the diffraction theory [115], the projections of the entire light wave vectors on the z direction are approximated, in the description of the wave amplitude, by the full wave vectors, *i.e.*, the transverse wave vector components are neglected ($k_{1z} \rightarrow k_1$). Simultaneously, the possible dependences of all transmission/reflection coefficients on the transverse wave vector components are neglected and they are treated as constants. In the description of the phases, the first order corrections, proportional to the square of the transverse-to-axial component ratio, is taken into account:

$$e^{-i(k_{1z}+k_{1z'})} = e^{-i\left(\sqrt{1-\frac{k_x^2+k_y^2}{k_1^2}}+\sqrt{1-\frac{k_x'^2+k_y'^2}{k_1^2}}\right)} \rightarrow e^{-i2k_1} e^{[i/(2k_1)](k_x^2+k_x'^2+k_y^2+k_y'^2)}. \tag{2.31}$$

Under the listed assumptions, Eq. (2.30) takes the following simplified form:

$$\begin{aligned} W^{heterodyned} \sim & -\frac{k_1^2 n_1^2 p_1}{(2\pi)^2} r_{01}\left(1-r_{01}^2\right) \\ & \times \Im\left\{\int\int\int_{-\infty}^{\infty} \mathrm{d}x\mathrm{d}y\mathrm{d}z\eta(t,x,y,z) e^{-2ik_1 z} \int\int_{-\infty}^{\infty} \mathrm{d}k_x \mathrm{d}k_y \left(\tilde{\tilde{E}}_+^{incident}\left(k_x,k_y\right)\right)^* \right. \\ & \left. \times \int\int_{-\infty}^{\infty} \mathrm{d}k_x' \mathrm{d}k_y' \tilde{\tilde{E}}_+^{incident}\left(k_x',k_y'\right) e^{i(k_x-k_x')x+i\left(k_y-k_y'\right)y} e^{[i/(2k_1)]\left(k_x^2+k_y^2+k_x'^2+k_y'^2\right)z}\right\}. \end{aligned} \tag{2.32}$$

A final assumption, experimentally relevant, discussed hereafter is the TDBS configuration where the probe laser beam is non-diffracting. Omitting the phase factor $\left\{[i/(2k_1)]\left(k_x^2+k_y^2+k_x'^2+k_y'^2\right)z\right\}$ responsible for the diffraction of the paraxial light beam in Eq. (2.32), the description of the TDBS signal takes an extremely insightful form:

$$\begin{aligned} & W^{heterodyned} \\ & \sim -\frac{k_1^2 n_1^2 p_1}{(2\pi)^2} r_{01}(1-r_{01}^2)\Im\left\{\int\int\int_{-\infty}^{\infty} \mathrm{d}x\mathrm{d}y\mathrm{d}z\eta\left(t,x,y,z\right)\tilde{E}_+^{incident}(x,y,0)\left(\tilde{E}_+^{incident}(x,y,0)\right)^* e^{-2ik_1 z}\right\} \\ & \sim -\frac{k_1^2 n_1^2 p_1}{(2\pi)^2} r_{01}\left(1-r_{01}^2\right)\int\int\int_{-\infty}^{\infty} \mathrm{d}x\mathrm{d}y\mathrm{d}z\eta\left(t,x,y,z\right) I_+^{incident}(x,y,0)\sin(2k_1 z), \end{aligned} \tag{2.33}$$

with $I_+^{incident}(x,y,z)$ the probe light intensity field amplitude.
In the classical configuration of plane probe light pulse and plane CAP both propagating along the z-axis, Eq. (2.33) reproduces the well-known result of the one-dimensional theory [105]:

$$W^{heterodyned} \sim -\frac{k_1^2 n_1^2 p_1}{(2\pi)^2} r_{01}\left(1-r_{01}^2\right) I_+^{incident}\left(z=0\right)\int_{-\infty}^{\infty} \mathrm{d}z\eta\left(t,z\right)\sin\left(2k_1 z\right). \tag{2.34}$$

In Eq. (2.34) the CAP (strain) derived in Sec. 2.2 has been abbreviated: $\eta_{zz} \equiv \eta\left(t,z\right)$.
In accordance with Eq. (2.33), the TDBS signal is equal to the $2k_1$ spatial Fourier component, along the

propagation direction of the probe light, of the three-dimensional spatial overlap between the cylindrical probe light intensity column, $I_{+}^{incident}(x, y, 0)$, and the 3-D acoustic strain CAP. Stated differently, the $\sin(2k_1 z)$ term in Eq. (2.33) corresponds to the sensitivity function, *i.e.*, accounting for the spatial evolution along the z-axis of the CAP strain contribution to the change in reflectivity [Eq. (2.28)].
From the definition of the sensitivity function, it appears that the expected heterodyned energy contribution $W^{heterodyned}$, in the situation described to obtain Eq. (2.34), would correspond to an oscillating contribution, function of the relative time delay between the pump laser pulse and the probe laser pulse arrivals. As an illustrative example, lets consider the most simplest CAP model, an unipolar strain pulse with an infinitely small length (or at least shorter than the period of the sensitivity function in Eq. (2.34)): $\eta_{zz} \simeq \delta(z - v_{LA}t)$. The integration of this delta-localized strain pulse in Eq. (2.34) leads to an expected heterodyned energy contribution proportional to:

$$W^{heterodyned}(t, z) \propto \sin(2k_1 v_{LA} t)\,. \tag{2.35}$$

Crucially, the frequency of the oscillations in the heterodyned contribution Eq. (2.35), termed Brillouin oscillations (BO), are preferably linked to the specific acoustic modes, in the CAP, of wavenumber:

$$k_a = 2k_1 \rightarrow \omega_B = 2k_0 n_1 v_{LA} \rightarrow \boxed{f_{BO} = \frac{2n_1 v_{LA}}{\lambda_{probe}}}, \tag{2.36}$$

with k_a and $\omega_B = 2k_1 v_{LA}$ the acoustic wavenumber and pulsation (or angular frequency), f_{BO} the Brillouin oscillations (BO) frequency and reminded here n_1, v_{LA} and λ_{probe} the optical refractive index, the LA acoustic velocity and the optical probe wavelength in vacuum, respectively. Thus, if the optical refractive index at the probe wavelength is known hitherto, measurements of the BO frequency permits to deduce the velocity of the propagating CAP, and vice-versa.
Equation 2.34 could of course be extended to the case where the material (1) is absorbing the probe light by making use of its complex refractive index and its complex photo-elastic constant.

In this section, the detection of a CAP propagating inside a transparent material has been discussed, and the expected TDBS signal, in terms of energy measured by the photodiode, has been expressed in the 1-D approximation [Eq. (2.34)]. This results led us to the fundamental results expressing the expected frequency of the Brillouin oscillations that would be observed in typical TDBS signals [Eq. (2.36)].
In the next and final section, an introduction to the different strategies employed to thermoelastically generate transverse acoustic (TA) modes, and the process of detecting them by TDBS, is given. Results obtained in a carbon-diamond (C) / tungsten (W) sample are presented to illustrate the discussion.

2.4 Transverse acoustic modes generation and detection: theory and experiments

Sections 2.2 and 2.3 were focused on the thermoelastic generation of CAPs composed of LA modes and their detection with TDBS. However, different acoustic wave polarizations can be generated and detected, *i.e.*, transverse acoustic (TA) modes, with the potential of extracting complementary information to the ones obtained by the LA mode.
Indeed, the generation and detection of TA modes opens the possibility for assessing the shear viscosity of fluids and the rigidity of solids, by accessing complementary elastic constants compared to LA [116, 117]. TA modes detection, besides the LA ones, proved to be necessary to obtain the first two Euler angles for the crystalline orientation of grains in polycrystalline materials [87, 102]. In addition, understandings of the detection process of these TA modes can provide information about grain microstructure [118].
The final section of Chap. 2 introduces briefly the theoretical aspects lying behind the existing strategies to thermoelastically generate TA modes and the mechanisms allowing their detection. Extended discussions on these two subjects can be found in the work of T. Pezeril *et. al.* [117, 119]. Finally, this section is concluded by the experimental detection of transverse acoustic modes in a carbon diamond (C) / tungsten (W) sample.

2.4.1 Transverse acoustic modes generation strategies and detection mechanisms

When defining the phonons, in the first chapter of this Ph.D. thesis, it has been mentioned that the atoms displacements are not only restricted to longitudinal motions (compressional modes), but may exhibit transversal motions (shear modes), *i.e.*, the polarization of the wave may vary. The atomic forces being possibly different for each of the three orthogonal polarizations of the acoustic modes, up to three modes propagating at different velocities might be exited in a material, pending on the propagation direction, defined by the vector $\mathbf{n}$ inside the crystalline structure of the material.
Thus, the displacement vector $\mathbf{u}$ being not necessarily collinear nor perpendicular to $\mathbf{n}$ when propagating out of the principal axis of symmetry of the crystalline structure, it is by convention the mode with the closest polarisation to the direction of $\mathbf{n}$ that is defined as the quasi-longitudinal acoustic (QLA) mode, while the quasi-transversal acoustic (QTA) modes are differentiated by their relative velocity: the "fast" quasi-transversal acoustic (fQTA) mode propagates faster than the "slow" quasi-transversal acoustic (sQTA) one.
In summary, when a CAP is propagating along a principal axis in the crystalline structure of an isotropic (or an anisotropic) material, it is composed of pure longitudinal (LA) and pure transversal (TA) modes, composed only of compression or shear motions. In contrast, when a CAP is propagating in specific orientations of anisotropic materials that is not a principal axis, then it can be composed of up to three contributions from the three acoustic modes defined: QLA and QTA (fQTA and sQTA). Since these modes are not "pure" modes, they are composed of a weighted distribution of longitudinal and

transversal motions, hence in such situation the CAPs are a weighted compressional and shear straining perturbation propagating in the material structure.
The modes velocities v_m (with m = QLA, fQTA or sQTA or, in the specific situation where $\mathbf{n}$ is oriented along a principal axis of symmetry m = LA or TA) in any direction is obtained by solving Christoffel's equation and are given by the roots of the secular equation [120]:

$$\left|\underline{\underline{\Gamma}} - \rho v_m \underline{\underline{\delta}}\right| = 0, \tag{2.37}$$

with $\underline{\underline{\Gamma}}$ the Christoffel's tensor and $\underline{\underline{\delta}}$ the identity tensor. The representation of the 3-D slowness (inverse of the phase velocity) curves are illustrated in Chap. 3 for the case of the ice and CeO_2 samples.
In Sec. 2.2, the thermoelastic stress tensor $\underline{\underline{\sigma}}^T$ has been considered as spherical following the isotropic material assumption, and the wave equation [Eq. (2.4)] for the displacement u_z along the z-axis was obtained. Now, if we consider a 3-D displacement vector $\mathbf{u}(t,x,y,z)$, still in an isotropic film, and define its associated velocity vector $\mathbf{v}(t,x,y,z) = \partial\mathbf{u}(t,x,y,z)/\partial t$ in terms of a scalar $\phi(t,x,y,z)$ and a vector $\boldsymbol{\psi}(t,x,y,z)$ potentials, then $\mathbf{v}(t,x,y,z)$ writes:

$$\mathbf{v}(t,x,y,z) = \frac{\partial\mathbf{u}(t,x,y,z)}{\partial t} = \boldsymbol{\nabla}\phi(t,x,y,z) + \boldsymbol{\nabla}\times\boldsymbol{\psi}(t,x,y,z). \tag{2.38}$$

The wave equation is accordingly split in two parts [40, 117]:

$$\begin{aligned} &\frac{\partial^2\phi}{\partial t^2} - v_{LA}^2\nabla^2\phi = -\alpha^\star v_{LA}^2\frac{\partial\Delta T}{\partial t}, \\ &\frac{\partial^2\boldsymbol{\psi}}{\partial t^2} - v_{TA}^2\nabla^2\boldsymbol{\psi} = \mathbf{0}, \end{aligned} \tag{2.39}$$

with ∇^2 the Laplace operator and $\alpha^\star = \alpha^T B/\rho v_{LA}^2$ the effective thermal expansion coefficient.
In Eqs. (2.39), the scalar potential part of the velocity is associated to the LA modes, while the vector potential one is associated to the TA modes. It is thus straightforward that the TA modes can not directly be generated via the thermoelastic source in the isotropic film. However, a strategy to generate TA modes is found in the coupling of the two potentials (hence coupling of the LA and TA modes) at the boundary. Indeed, generation of TA modes implies to break the symmetry at the level of the CAP generation or at the level of its propagation, like depicted in Fig. 2.6.

In fact, three main categories of thermoelastic generation of TA modes are defined here, based on either mode conversion at the interface between two different materials (breaking the symmetry at the scale of the elastic boundary conditions) or by direct thermoelastic generation (breaking the symmetry at the scale of the thermoelastic forces), as depicted in Fig. 2.6.
A first solution has been proposed in the 1990s to convert LA into TA modes by the use of a prism: the LA mode generated on one of the prism faces is obliquely incident on the prism's hypotenuse (or to an extent, a buried interface inclined relative to the incident LA pulse direction [Fig. 2.6 (a)]) and generate, via

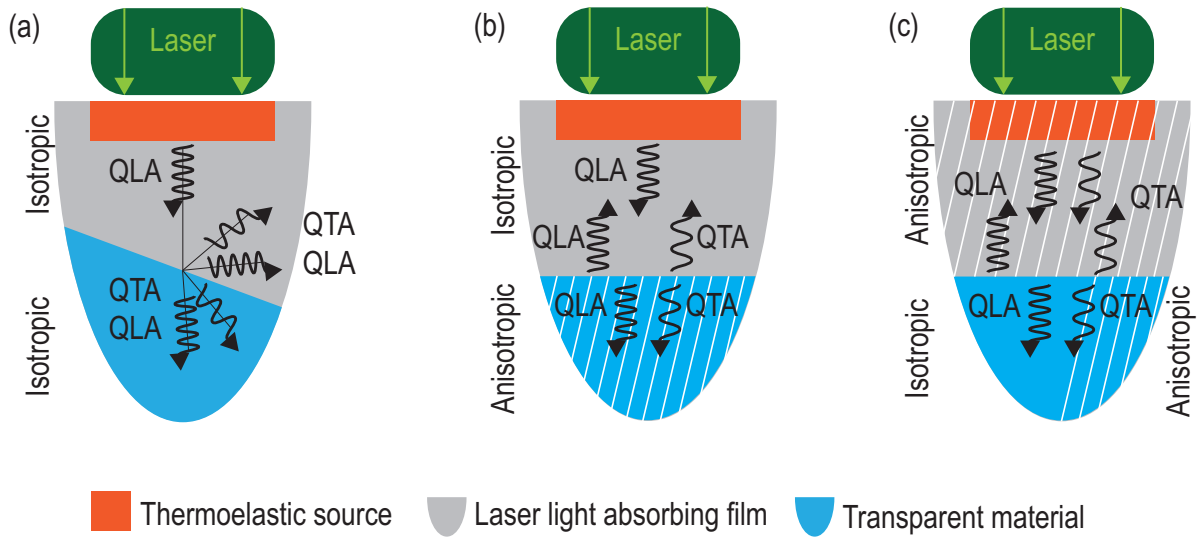

Figure 2.6 – Schematic of the three main strategies employed to generate TA modes via thermoelasticity. (a) Both the film (OAT) and the substrate (transparent material) are isotropic. LA modes are generated via thermoelasticity in the film, and TA modes are generated via mode conversion at the interface between the film and the substrate, in reflection and transmission, since the LA modes are obliquely incident to the interface [121]. (b) The film (OAT) is isotropic and the substrate is anisotropic. In this situation mode conversion from the LA modes generated in the film to TA modes is achieved owing to the anisotropy of the substrate in the case where no symmetry axis of the anisotropic medium is collinear with the normal to the interface. Examples of substrates are crystallites with the principal axis of symmetry deviating from the direction of the incident LA wave [122]. (c) The film (OAT) is anisotropic and the substrate can either be isotropic or anisotropic. In this situation, the generation of TA modes is not linked to mode conversion. TA modes are generated directly via thermoelasticity owing to the excitation of all 3 acoustic modes and the asynchrony of their propagation velocities [117].

mode conversion, both in reflection and transmission, TA modes [121]. However such strategy appeared doable at the MHz frequency range but requires manufacturing prisms at µm to nm scales to ensure that the GHz LA modes generated by thermoelasticty reaches the hypotenuse. Indeed, propagation distances needs to be reduced with decreasing acoustic wavelength due to the increasing acoustic attenuation.
A second strategy carried out in the 2000s relied on the mode conversion at an isotropic film / anisotropic substrate interface. When the thermoelastically generated LA mode in the isotropic film is reaching the interface with the anisotropic substrate, TA modes are obtained via mode conversion and can be detected in reflection [116] or in transmission [122] from the interface, even at normal incidence of the LA mode to the interface. The reason for the mode conversion is that at the interface between the isotropic film and the anisotropic substrate, the displacement and the stress have to be matched. Since the CAP (strain) in an (elastically) anisotropic material usually includes transversal components, and since contrarily the incident LA-composed CAP does not include them, LA to TA mode conversion is required for continuity.
The third strategy does not rely on mode conversion to obtain propagating TA modes in the transparent material. Instead, direct thermoelastic generation in metals with crystal lattice symmetry being not aligned to the coordinate system related to the sample surface permit efficient generation of TA modes. For example, in Ref. [117] such situation was obtained in a Zn single crystal with the C_6 axis oriented at

an angle $\sim 36°$ relative to the surface of the pump focus. Obtaining such disoriented OAT requires either cutting the metallic film in a specific orientation, or special growing process control of canted metal films, as it has been used to obtain disoriented iron (Fe) crystals in Ref. [123] for example.
Hence, in agreement with Sec. 2.2, we consider a CAP strain η_{zz} propagating along the z-axis, incident on an isotropic film / anisotropic substrate interface [124]. It reduces the reflected and transmitted CAP strain components to the z-dependent ones only, *i.e.*, η_{zz}, either given by Eq. (2.6) [Fig. 2.2 (b)] without thermal diffusion or Eq. (2.9) [Fig. 2.3] with thermal processes, η_{zx} and η_{zy}, the last two forming the expected TA modes. This situation is different compared to the one that led to Eq. (2.23) where the spatially-localised variation in the permittivity $\Delta\epsilon\,(t,z)$, induced by the CAP strain, was given with a photoelastic tensor reduced to a single value: p_1 in Eq. (2.21): $\Delta\epsilon = -n_1^4 p_1 \eta(t,x,y,z)$.
Instead, the weak permittivity changes due to the reflected CAP strain propagating in the isotropic film, denoted material (0), is expressed as [124]:

$$\underline{\underline{\Delta\epsilon_0^{-1}}}(t,z) = \begin{pmatrix} p_2\eta_{zz} & 0 & 2p_3\eta_{zx} \\ 0 & p_2\eta_{zz} & 2p_3\eta_{zy} \\ 2p_3\eta_{zx} & 2p_3\eta_{zy} & p_1\eta_{zz} \end{pmatrix}, \tag{2.40}$$

with $p_3 = (p_1 - p_2)/2$, while the weak permittivity changes due to the transmitted CAP strain propagating in the anisotropic transparent substrate (where TDBS should be applicable), denoted material (1), is more complicated [125]:

$$\underline{\underline{\Delta\epsilon_1^{-1}}}(t,z) = \begin{pmatrix} p_{1q}\eta_q & p_{56}\eta_5 & p_{55}\eta_5 \\ p_{56}\eta_5 & p_{2q}\eta_q & p_{q4}\eta_q \\ p_{55}\eta_5 & p_{q4}\eta_q & p_{3q}\eta_q \end{pmatrix}, \tag{2.41}$$

with $q = 3{,}4$ a summation index and where the equivalence with this manuscript notations are: $\eta_3 \to \eta_{zz}$, $\eta_4 \to 2\eta_{zy}$ and $\eta_5 \to 2\eta_{zx}$.

The permittivity changes in the isotropic film [Eq. (2.40)] is coupled to transverse strain components via its off-diagonal terms and requires thus specific polarization and oblique incidence of the probe laser light to be detected [125]. On the other hand, the permittivity changes in the anisotropic substrate [Eq. (2.41)] highlights coupling of the transverse strain components with the diagonal of $\underline{\underline{\Delta\epsilon^{-1}}}$. There is, *a priori*, no particular conditions upon the detectability of the corresponding QTA components of the CAP. However, pending on the magnitude of the longitudinal (compression) component in the QTA modes in the CAP, optimisation of the detection might be required for probe light to be efficiently scattered.
The efficiency of QTA modes generation in this specific strategy has been discussed recently in [126], underlining the fact that the orientation of the grain (crystallite) in contact with the film (OAT) plays a major role on the efficiency. It was demonstrated that the efficiency of QTA mode generation was tied to the magnitude of the longitudinal component, as well as materials with large elastic anisotropy favor strong QTA mode generations. Conversion efficiency in reflection and transmission were derived in both

[122, 126].
The anisotropic substrates studied in Refs. [116, 122] are composed of isotropic aluminium (Al) OAT films, deposited on the surface of a zinc (Zn) substrate, thus with an hexagonal crystalline structure [116], and deposited on tetragonal paratellurite crystal (TeO_2). The first configuration was chosen to reduce the reflection coefficient of the strain pulse at the interface, while the second crystal was selected for its strong anisotropy. Detection of these TA modes were achieved either by monitoring the surface motion induced by the TA modes when reaching back the free surface of the film [116], as well as by TDBS [116, 122]. The main advantages of this strategy is that it should work even for normal incidence of the LA modes at the interface.
Finally, the third strategy employed to generate QTA modes directly via thermoelasticity implies the use of an anisotropic film which is characterised by an anisotropic thermal expansion tensor $\underline{\underline{\alpha}}^T$. It means that the laser-induced thermal stress tensor $\underline{\underline{\sigma}}^T$ will no more be spherical, allowing direct generation of QTA modes via thermoelasticity like in Ref. [125] where they used an hexagonal crystal, *i.e.*, with anisotropic thermal expansion. Nonetheless, to achieve QTA modes emission, different symmetry of the crystal axis orientation relative to the incient CAP to the interface, was required. A more detailed study on the thermoelastic generation of QTA modes in anisotropic materials can be found in Ref. [117] that has been used in this section, as well as T. Pezeril Ph.D. thesis [119].

To conclude, the generation of TA components in the propagating CAPs has been discussed in a situation limited to the thermoelsatic regime of CAP generation. In this situation, breaking of the symmetry is required to generate QTA modes either via mode conversion at an interface, or by direct thermoelastic generation in an anisotropic film. It has to be noted that other generation mechanisms exist that could generate TA wave components, such as electrostriction [127] and inverse piezoelectric effect [128].
The detection of the transverse components in the CAP strain thereby obtained is ensured by the coupling between the permittivity changes and the transverse components of the CAP strain, requiring specific probe polarization and oblique incidence for isotropic media. In the case of anisotropic media, the detection can be enhanced via different means including probe polarization and mode conversion optimisation. In the next section, experimental results discussing the detection of QTA modes in a "disoriented" transparent carbon-diamond (C) sample with a deposited tungsten (W) film as OAT, are presented.

2.4.2 Detection of a QTA mode in a disoriented carbon-diamond (C) / tungsten (W) sample with TDBS

Investigations on the possibility to generate, via thermoelasticity, and detect, via TDBS, QTA modes in a transparent carbon-diamond (C) sample were conducted in the preliminary stages of this Ph.D. thesis. The sample studied is composed of "disoriented" C transparent sample, "disoriented" meaning that its symmetry has been broken by cutting it 23° out of the [111] crystalline axis. An isotropic 34 nm thick tungsten (W) layer has been deposited (by physical vapor deposition, or PVD) on its surface to play the

role of the optoacoustic transducer (OAT), *i.e.*, to thermoelastically generate a CAP via the absorption of the pump laser beam [Fig. 2.7 (a)]. Originally, the cut was designed so that it would allow the maximum difference between the two propagation velocities of the TA modes, to ensure feasibility of their common/in parallel detection, and it was chosen to cut far from any symmetry axes of the diamond.
The disoriented C should allow the generation of TA modes via mode conversion at the isotropic film/anisotropic disoriented C interface, following the discussion of Sec. 2.4.1. The aim of these experiments is to observe the Brillouin oscillations (BO) in the TDBS signal, and more specifically the Brillouin frequency of these oscillations, associated to the propagation of QLA and QTA modes [Eq. (2.36)]. The TDBS signals are obtained with a classical picosecond acoustic setup [Fig. 2.7 (b)], where both pump and probe laser beams originate from a common Ti:Saphire laser source (Spectra-Physics, 2 W, 808 nm). To differentiate pump and probe beams, the laser is split in two parts with a polarizing cube. The first part is used as the pump: it is frequency-doubled using a 1-cm long non-linear BBO (beta barium borate) crystal. The use of an acousto-optic modulator [AOM in Fig. 2.7], working at a frequency of 161 kHz, allows to perform a synchronous detection of the probe light scattered by the sample, with a lock-in amplifier, in the aim of enhancing the signal-to-noise ratio. The second part of the laser beam is used as the probe and time-delayed relative to the pump beam using a mechanical delay line. Both laser beams are focused on the surface of the OAT using a 50× objective lens and the reflected/scattered light fields are collected using a photodetector.

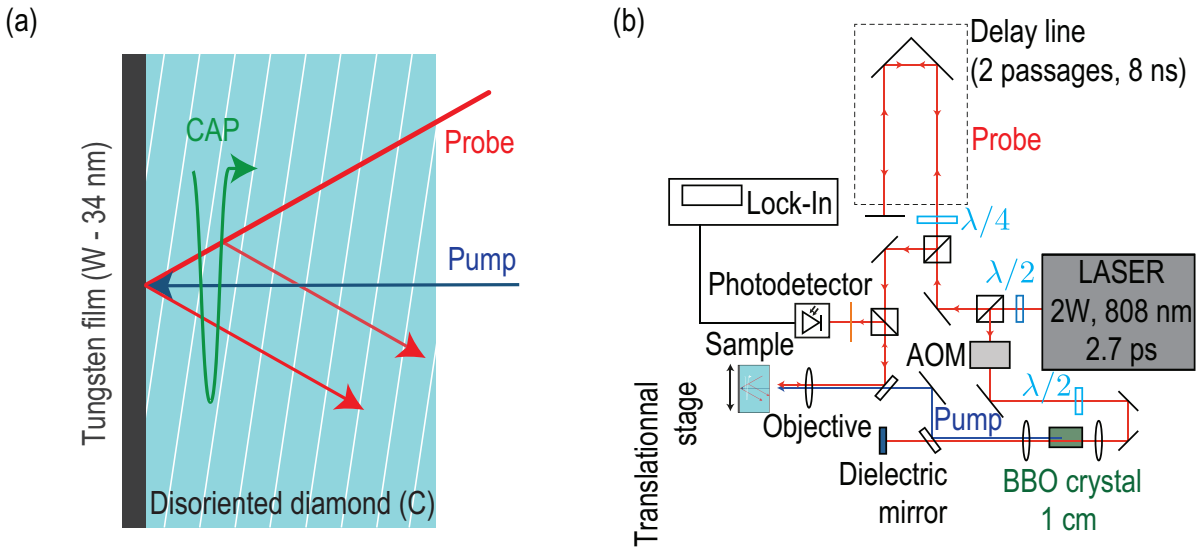

Figure 2.7 – (a) Schematic of the disoriented carbon-diamond transparent sample (C) with a thin layer (34 nm) of tungsten (W) deposited on it to play the role of the OAT. The TDBS configuration of these experiments corresponds to the situation described in Fig. 2.4 (b) where both pump and probe laser beams are focused at the OAT/diamond interface, passing through the transparent diamond sample. (b) Experimental picosecond acoustic setup. The blue pump beam is frequency doubled in a BBO crystal from the source laser beam wavelength, also used as the red probe $\lambda_{probe} = 808$ nm (adapted from [97]).

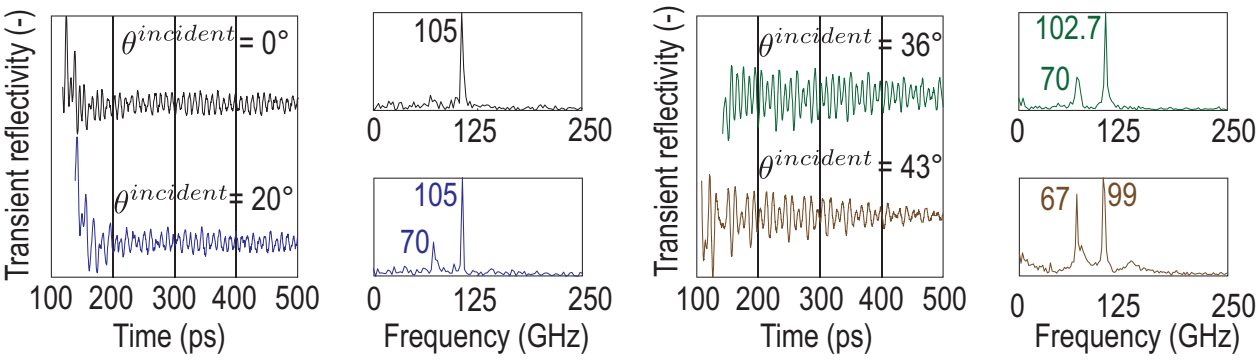

Figure 2.8 – Experimental TDBS signals obtained in the disoriented carbon-diamond (C) / tungsten (W) thin layer used as the OAT, for four different incidence angles of the probe laser beam. The associated Fourier transforms of the signals highlight the detection of both the LA mode (in the four situations) and one of the TA modes (in all situations except normal incidence of the probe) in the disoriented carbon-diamond.

Figure 2.8 presents the transient reflectivity signals obtained via TDBS in the disoriented (C) / (W) sample for four different incidence angles $\theta^{incident}$ of the probe laser beam to the disoriented (C) / (W) interface, with their associated Fourier transform. The raw transient reflectivity signal typically contains a decaying thermal contribution that have been subtracted here. An extended discussion on the processing of the raw transient signals obtained via TDBS is given in Chap. 3.

The Fourier transform of the TDBS signals [Fig. 2.8] highlights the detection of a strong QLA mode in all the situations (around $\sim$ 100 GHz), while one of the QTA mode is clearly observed only when the probe light is inclined (around $\sim$ 70 GHz). The detection of the QTA mode is enhanced with increasing inclination of the probe, but the reasons why it is not clearly resolved (oscillation amplitude comparable to the noise level) for normally incident probe are unclear. The main reason might be that the out-of-axis cut is not realised as far from the [111] axis as expected and thus the detection of the TA modes is made more difficult.

The BO frequency is varying as a function of the incidence angle of the probe laser beam [129]:

$$f_{BO}^{m} = \frac{2v_m}{\lambda_{probe}}\sqrt{n_C^2 - \sin^2\left(\theta^{incident}\right)}, \tag{2.42}$$

with m = [QLA, sQTA, fQTA] the acoustic mode studied, v_m the velocity of the acoustic mode, λ_{probe} = 808 nm in this setup and n_C the optical refractive index of the disoriented carbon-diamond sample at 808 nm. Experimental results are compared with Eq. (2.42) in Fig. 2.9. In the results presented in Fig. 2.9 for the detection of BO associated to QLA and QTA modes propagating in the disoriented carbon-diamond, a theoretical interval of frequency has been displayed using Eq. (2.42). This interval, instead of a single line, comes from the fact that the possible acoustic velocities lie, in the 3-D velocity surfaces computed with Eq. (2.37), along the continuum of directions provided by a cone of 23 ° around the [111] axis. It means that the possible velocities of each acoustic mode are not unique but are distributed in an interval,

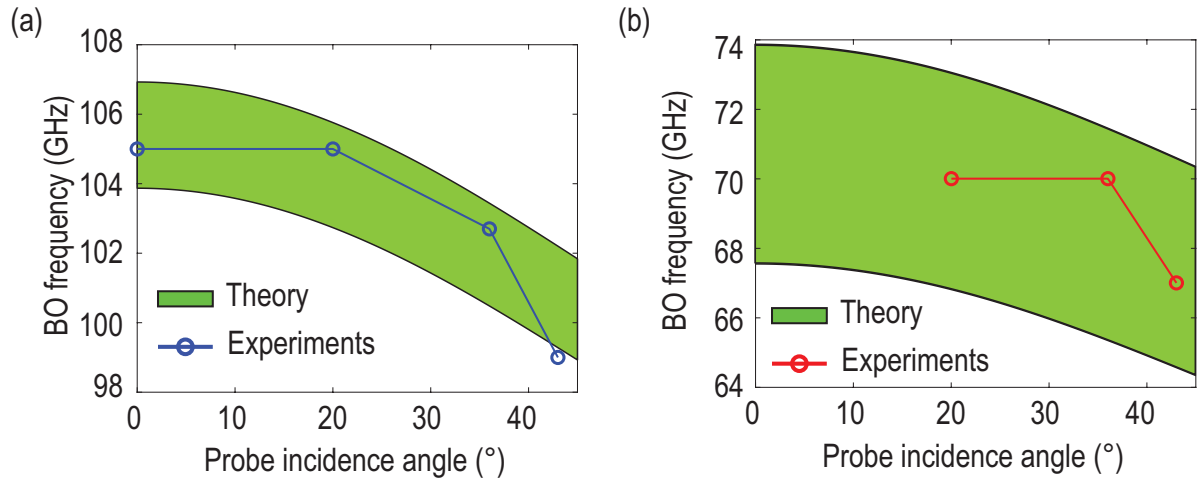

Figure 2.9 – (a) Frequency of the Brillouin oscillations (BO) associated to the QLA mode recorded via TDBS in the disoriented carbon-diamond (C) / tungsten (W) sample as a function of probe laser beam incidence angle. (b) Frequency of the Brillouin oscillations (BO) associated to the QTA mode recorded via TDBS in the disoriented carbon-diamond (C) / tungsten (W) sample as a function of probe laser beam incidence angle. The theoretical frequency interval are computed with Eq. (2.42) and taking into account the interval of acoustic mode velocity in the 23 ° cone around the [111] axis in the carbon diamond. Theoretical results are computed with the refractive index $n_C = 2.32$ and the density $\rho_C = 3.468\ \mathrm{g\,cm^{-3}}$ from Ref. [129] and the elastic constants of Ref. [130].

which means in return that the expected BO frequencies are in the displayed intervals in Fig. 2.9. In Fig. 2.9, the detected BO frequency associated to the QLA and QTA mode are found to be in the theoretical interval, with the same frequency downshift tendency. Unfortunately, complementary measurement, with the ultrafast scanning system NETA (presented in Chap. 3) evidenced the degradation of the bounding between the tungsten layer and the disoriented carbon diamond, especially under continuous laser light heating (even for low laser light powers). This bounding degradation has precluded the transmission of the CAP generated in the W to the transparent C sample.

In conclusion, TA modes have been generated via the mode conversion of LA mode at the interface between an isotropic W film and an anisotropic disoriented C transparent substrate, and detected using TDBS at oblique incidence of the probe laser beam. The reason for the too-weak-to-be-resolved detection of the TA mode at normal incidence of the probe are still to be found, but the reason is most likely linked to the precision of the out-of-axis cut of the diamond. The uncertainty of the cut ($\pm$ 2.5 °) provided by the Almax-easylab company [131] was estimated when cutting out of the [100] axis of the diamond sample. However here, it is out of the [111] axis that the cut is realised, which is the most common cleavage plane of the diamond crystalline structure, *i.e.*, most common orientation when diamond is fractured [132]. Hence the orientation uncertainty might be greater and the cut is very likely closer to the cleavage plane [111], which theoretically preclude the detection of the TA modes.

2.5 Conclusion

The main purpose of this second Chapter was to provide the theoretical basis on the thermoelastic generation of CAPs using ultrashort laser pulses, and the detection of their propagation in a transparent sample via TDBS. The thermoelastic regime of CAP generation has been, firstly, solved in the 1-D geometry allowing to derive a simple shape of the generated CAP strain, considering a time-fixed temperature distribution and, secondly, account for thermal diffusion processes at small and long time scales, consequently broadening the shape of the CAP.

Once the generated CAP is transmitted to a transparent material, monitoring of its propagation using TDBS is detailed, in the reflection configuration, by studying the electric field distribution of the probe in the material. The transient reflectivity signal (or TDBS signal) is defined as the ratio of (i) the heterodyned contribution arising from the mixing between the static surface/interface-reflected field with the propagating CAP-scattered field, by (ii) the energy collected with the photodiode in the absence of the propagating CAP. Periodic variations in the TDBS signals are found to be linked to a sensitivity function, in the 1-D solution, with theoretical Brillouin oscillation frequency linked to the velocity of the acoustic mode composing the CAP.

Transversal acoustic mode generation, and their detection by TDBS, is made possible via broken symmetry in the studied sample. Mode conversion of the longitudinal acoustic modes into transversal acoustic modes is obtained experimentally, at the interface between an isotropic OAT and an anisotropic transparent sample. The detection of the transversal modes is allowed since the propagating acoustic modes are not pure (not propagating along a symmetry axis of the crystalline structure). Experimental results obtained in a disoriented carbon-diamond / tungsten sample illustrate the possibility to detect the transversal modes in the discussed situation, but raises questions on the quality of the sample design/symmetry.

Chapter 3

Signal processing methods applied to the 3-D reconstruction of samples from TDBS scans

Contents

3.1 Introduction

In the first Chapter, the TDBS imaging method is compared to diverse micro-to-nano-meter imaging techniques relying on various physical mechanisms to evaluate the structure of samples. In particular, the capacity of TDBS to study the 3-D microstructure of grains (or crystallites) is mentioned with a spotlight on the remaining complete 3-D imaging of large sample volumes to be addressed.

Up to now, inhomogeneity in the sample has been evidenced along the axial direction (CAP propagation direction) in nanoporous [85, 93] and compressed water ice [82, 97, 133] materials, as well as in damaged/irradiated semiconductors [94, 95], and inside vegetable/animal cells [98–100].

Extension to investigate the 2-D and 3-D evolutions of the micrometric structure of polycrystalline samples emerged more recently with line-scans and raster-scan measurements. A 2-D sub-surface boundary between two UO_2 grains were observed in Ref. [86], followed by the 3-D imaging of grains microstructure in a CeO_2 (ceria) sample [87, 102].

Still, a dedicated procedure for the 3-D volumetric reconstruction of the complete grains in such polycrystalline samples, from TDBS scans, is missing. The aim of this third Chapter is to provide the complete method, developed during this Ph.D. thesis, for the 3-D image reconstruction of transparent sample from TDBS scans.

In a first section, the ultrafast imaging system, *i.e.*, compared to the conventional picosecond acoustic setup described in Sec. 2.4.2, developed by the company Neta [134] (France) is presented. The setup relies on an asynchronous optical sampling (ASOPS) technique to significantly accelerate the single point TDBS measurements, opening the way to TDBS scans.

The second section presents the step-by-step signal processing method developed in order to reconstruct the 3-D images of the samples from the raw transient reflectivity measurements (TDBS signals) obtained by scanning the sample with the ASOPS-based setup. Three main steps are considered: (i) extracting the acoustic component in the raw transient reflectivity signals, (ii) "slicing" the signals to estimate their amplitude and frequency evolutions with depth (time), and (iii) "shaping" the results of step (ii) relying on data segmentation and the alphashape algorithm.

The third section provides examples of applications of the processing methods in two different polycrystalline samples: a high pressure water ice sample obtained at ambient temperature in a diamond anvil cell (DAC) with an iron (Fe) OAT, and a cerium dioxyde, or ceria (CeO_2) sample with a gold OAT layer.

3.2 Ultrafast pump-probe experimental setup

In this first section, the experimental setup used to scan the sample, *i.e.*, record the TDBS signals on a defined area at the sample surface by raster-scanning it, is presented with a focus on its ultrafast data acquisition capacity compared to classical picosecond acoustic setups.

Measurements of the transient reflectivity signals are done using a pump-probe asynchronous optical sampling (ASOPS) system [135, 136]: the JAX-M1 commercialized by the french company NETA [134] [Figure 3.1]. In opposition to the classical picosecond acoustic setup described in Sec. 2.4.2, the ASOPS-

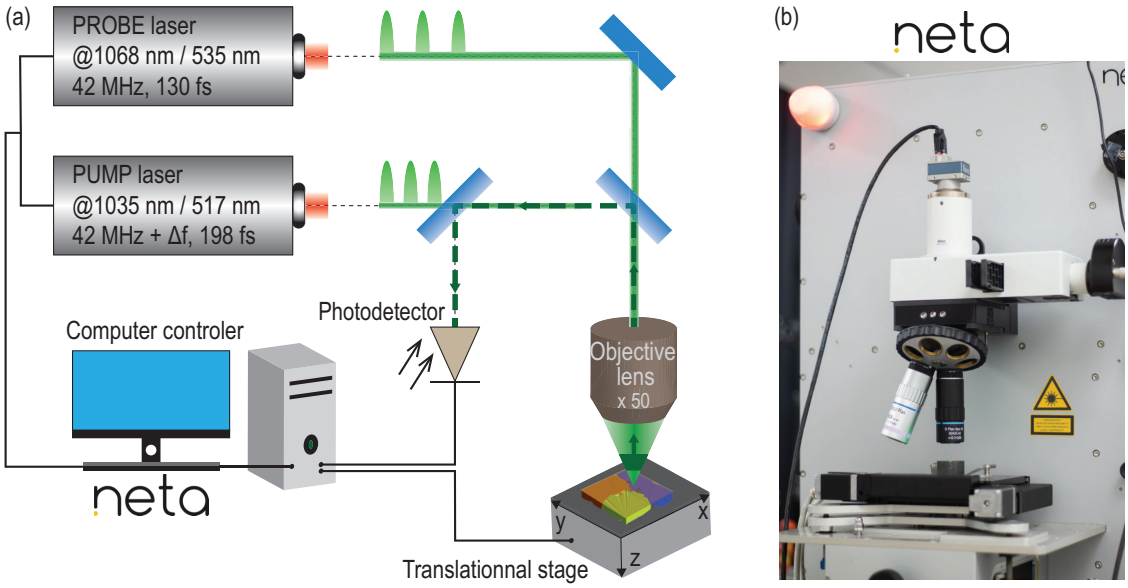

Figure 3.1 – Ultrafast ASOPS-based imaging system (JAX-M1 by NETA). (a) Schematic of the experimental TDBS imaging system (JAX-M1) commercialized by NETA [134] (France) [8]. (b) Photograph of the sample holder part of the JAX-M1 during a scan on the ceria sample.

based setup is composed of two Yb:KYW mode-locked laser cavities, emitting femtosecond laser pulses. The pulse delay between the two lasers is accomplished electronically by shifting the pulse repetition rate of the replica laser (source of the probe laser beam) compared to that of the source laser (source of the pump laser beam) that is fixed $f_{pump} = 42$ MHz [Fig. 3.2 (a)]. The difference in the frequency of repetition between the two lasers, or the beat frequency, is set to $\Delta f = 500$ Hz. Compared to the classically employed mechanical delay line, that is delaying the time arrival of the probe beam to the sample, relative to the fixed time arrival of the pump, by changing the probe's path length, the ASOPS system can be understood as a "virtual" delay-line.

Each time a pump laser pulse reaches the OAT, every $1/f_{pump} = 23.8$ ns (see first row in Fig. 3.2), the dynamic of the sample is excited (depicted in the second row of Fig. 3.2 by the simplified transient reflectivity signal, or transient process) and supposed repeatable/stable over at least a beating period. Since recording the high-frequency dynamic in a "single shot" manner is not achievable, the probe laser

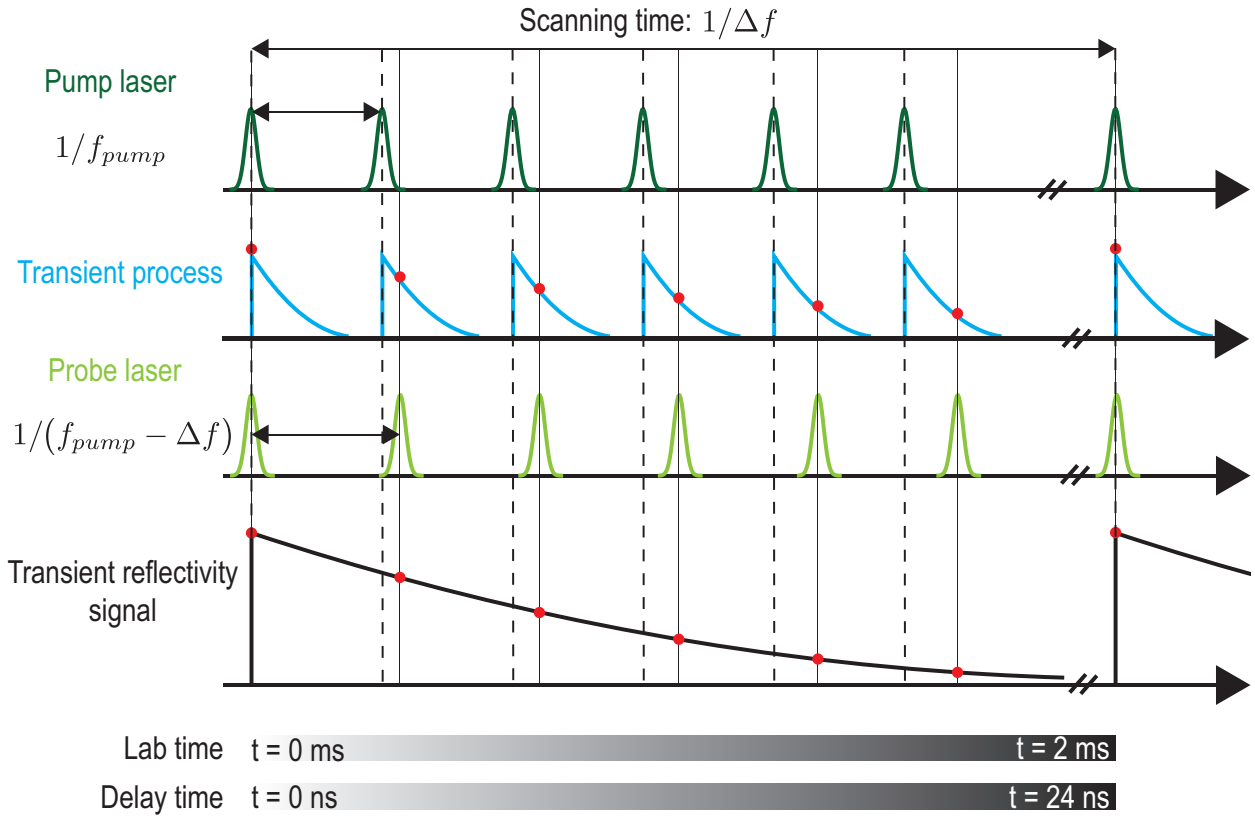

Figure 3.2 – Asynchronous optical sampling (ASOPS) operating principle: the pump laser pulse generates a CAP in the sample with a fixed repetition rate f_{pump} (top row, blue signals), while the probe laser beam is scattered by the CAP with a lower repetition rate, controlled by the beating frequency $f_{pump} - \Delta f$ (middle row, red signals). Thereby, the complete probing time window is monitored by the probe in an iterative way with a "virtual" delay line, requiring only the time $1/\Delta f = 2$ ms in our experiments. Illustration adapted from [137].

pulse is launched in the sample with a slightly lower repetition rate controlled by the beating frequency between the two laser cavities $t = 1/(f_{pump} - \Delta f)$, as shown in the third row of Fig. 3.2. Thus, the time between two probe pulses arrivals is slightly shifted compared to the pump pulse time arrivals, the time delay between each pulse being 0.28 ps in our configuration. The added delay between each probe laser pulses thus increases the relative time difference to each pump laser pulse, meaning that each probe pulse will probe the sample state at an iteratively different time, effectively sampling the propagation of the CAP in the sample for instance. This sampling over a larger time scale thanks to this stroboscopic effect is represented by the red dots in Fig. 3.2, the complete transient reflectivity signal [bottom row in Fig. 3.2] being measured in the characteristic time $1/\Delta f = 2$ ms.

Both pump and probe beams are focused, using a 50× microscope objective lens, usually on the surface of the OAT. The electric field distribution of both lasers at the focus spot are considered Gaussian and

equal, the distribution of the probe laser pulse being given by (following the notations of Sec. 2.3):

$$E_{+}^{incident}(x,y,0) = E_0 e^{\left[-\frac{(x+y)^2}{a_{probe}^2}\right]}, \tag{3.1}$$

with a_{probe} the radius of the electric field amplitude distribution at the $1/e^2$ level.

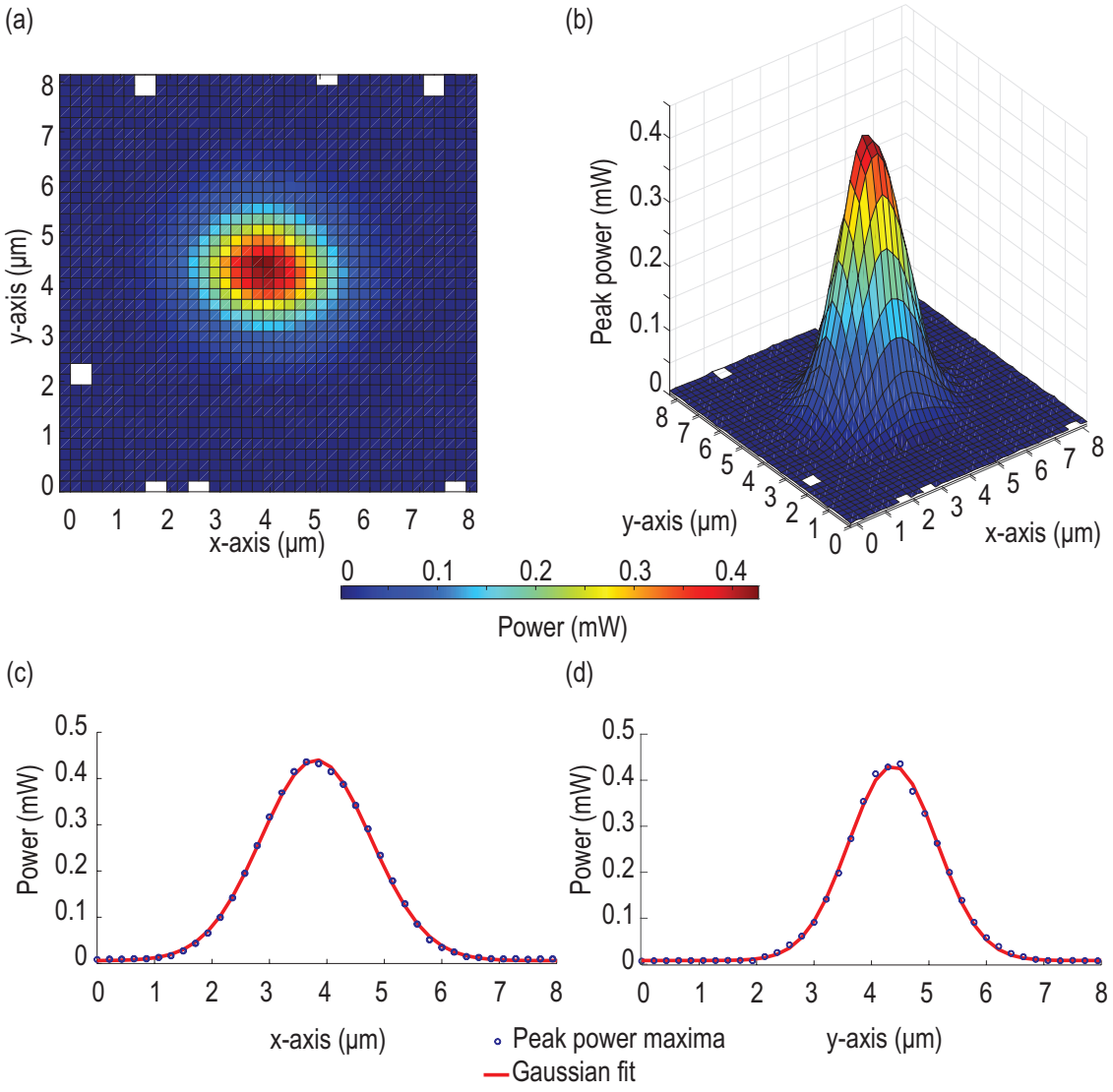

Figure 3.3 – Effective radius of the laser beam focii sizes determination by cross-correlation, obtained by a raster scan of the (fixed) probe beam by the pump beam on the surface of a titanium (Ti) OAT deposited on a sapphire (Al_2O_3) substrate. (a-b) 3-D map of the peak power measured by the photodiode in the TDBS signals in (a) top view and (b) side view. (c-d) Fits of the Gaussian model function Eq. (3.2) to the maxima of the 3-D peak power maps (a-b) along the (c) x-axis and (d) y-axis of the scan.

To determine the effective radius of the probe laser beam in our experimental configuration, a cross-correlation map of the pump and probe laser beams has been measured by scanning the pump laser beam around the position of the fixed probe laser beam [Fig. 3.3 (a-b)].
The scan has been made on a 8×8 µm^2 area with a step size of 0.2 µm, centred on the probe spot, on a titanium (Ti) OAT deposited on a sapphire (Al_2O_3) substrate.
The absolute maximum value of the electronic peak [for example observable in Fig. 3.4 (a) at time t $\sim$ 0.15 ns], compared to noise level, obtained by averaging the values before the electronic peak hence between time t = 0 ns and t $\sim$ 0.15 ns in Fig. 3.4 (a), has been determined in each signal, and converted into measured power using the photodiode datasheet (Thorlabs balanced amplified photodetectors PDB 440/450 series).
The 3-D peak power maps, showing the electronic peak maximum power as a function of the pump position in the raster scan, are given in Fig. 3.3 (a-b) respectively, giving reasonable results upon the Gaussian beam approximation of the spots.
To determine the beams spots radii, considering that both beams are Gaussian and of equal radii at the focal spot, a Gaussian model is fitted to the maxima of the peak power map along the x-axis [Fig 3.3 (c)], and correspondingly to the y-axis [Fig 3.3 (d)]:

$$I_{gaussian} = I_0 e^{-\frac{(x - x_0)^2}{a^2}} + d. \tag{3.2}$$

Fitted parameters	Value	95% confidence interval
x-axis		
I_0	0.4258	[0.4216, 0.4299]
x_0	4.024	[4.014, 4.034]
a	1.358	[1.341, 1.375]
d	0.006074	[0.003885, 0.008262]
y-axis		
I_0	0.4136	[0.4083, 0.4189]
y_0	4.159	[4.148, 4.169]
a	1.086	[1.069, 1.104]
d	0.009469	[0.007196, 0.01174]

Table 3.1 – Results of the Gaussian model [Eq. (3.2)] fitting to the maxima of the peak power map [Fig. 3.3 (a-b)] measured by scanning the probe beam with the pump beam. The fitting is done for the maxima along the x- and y-axes to consider a possible ellipticity of the beams.

In Eq. (3.2), the variables highlighted in blue corresponds to the fitted variables, the results being given in Tab. 3.1 for the fits along both x- and y-axes, and with the associated 95% confidence intervals.
The beam radius a is the radius at $1/e^2$ level of the intensity distribution. The latter being proportional to the square of the electric field distribution $I \propto |E|^2$, we can determine the probe (correspondingly pump) beam radius (or waist) for both axis by: $a_{probe} = \sqrt{2} \times a$.
The experimentally determined probe beam radius finally yield the following values:

$$\begin{aligned} a^x_{probe} &= 1.925 \text{ µm} \pm 0.05 \text{ µm}, \\ a^y_{probe} &= 1.5358 \text{ µm} \pm 0.05 \text{ µm}. \end{aligned} \tag{3.3}$$

Both beam radius will be considered henceforth circular with a radius $a_{probe} = a_{pump} = 1.5$ µm. Only the second harmonics of the laser sources are used. The wavelength of the probe laser beam is $\lambda_{\text{probe}} = 535$ nm, while that of the pump laser beam is $\lambda_{\text{pump}} = 517$ nm. To monitor the relative optical reflectivity changes ΔR/R caused by the propagating CAP, the backscattered probe light is directed to a photodiode where it interferes with static reflections of the probe beam on the sample surfaces, like described in Sec. 2.3. To achieve a precise raster scanning, the sample is mounted on two translationnal plates (ZABER ASR050B-T3) with a sub-micrometric accuracy. The automatic raster-scan and signal acquisitions are realized using NETA's built-in software. More details on the ASOPS-based setup can be found in Ref. [136].

3.3 Signal processing procedure: from TDBS scans to 3-D images

In this second section, the step-by-step processing of the raw transient reflectivity signals, acquired using the ASOPS-based imaging system described in Sec. 3.2, is presented. To illustrate each step of the processing, the signals obtained in a scan of the ceria sample are considered throughout this section, while a discussion on the results of the 3-D imaging is given in Sec. 3.4.2. The processing procedure is divided is three main steps, applied to every signals of the scans.

- Step 1: the filtering.
  The raw transient reflectivity signals are processed in order to access the acoustic part of the signal, *i.e*, filters are applied to extract the expected characteristic Brillouin oscillations (BO) from the other features of the signals (thermal background, electronic peak, noise). The output signals are designated as "acoustic signals".

- Step 2: the slicing.
  The aim of this step is to estimate the amplitude and frequency variations of the acoustic signals. A first strategy relied on applying a short-time Fourier transform (STFT) in a moving window and estimating the strongest frequency component, in the window, with a synchronous detection technique (SDT). A second strategy uses the wavelet synchrosqueezed transform (WSST) to compute a reassigned (refined) spectrogram and extract the time-frequency ridges linked to the different modes identified in the signals. The final output of this step gives access to a 4-D stacked representation of the sample structure composed of 3-D (spatial variables) voxels with colors associated to the detected Brillouin frequency (BF).

- Step 3: the shaping.
  The final step of the processing consist in gathering the voxels of the 4-D stacked representation belonging to common grains of the polycrystal, and shape the grains envelopes. To do so, segmentation methods are employed in order to gather the voxels in clouds of voxels of common BF, using an adaptation of Otsu's image segmentation method [138]. The clouds of voxels are finally given as an input to an alphashape algorithm used to compute a constrained envelope around the clouds, giving access to a final 3-D volumetric representation of the grains composing the sample.

3.3.1 Acoustic signal extraction from the raw data

The raw transient reflectivity measurements are composed of a multitude of elements, witness of the different physical phenomena arising during a TDBS measurement, superimposed together: electronic diffusion, thermal diffusion, BOs, noise. The purpose of the first processing step is to extract from the raw data the information we are interested in, *i.e.*, the BOs related to the propagation of the CAPs inside the transparent material.

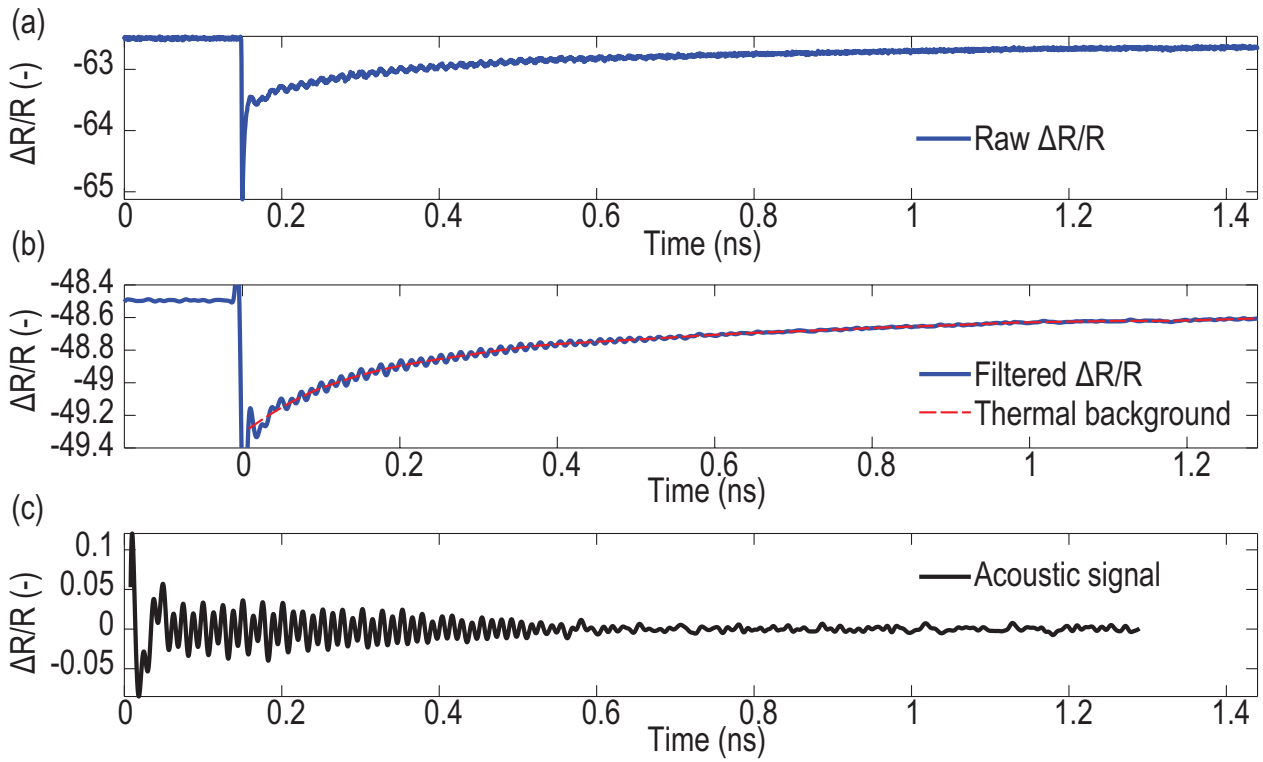

Figure 3.4 – Processing step 1: extraction of the acoustic content in the raw transient reflectivity signals. (a) Raw transient reflectivity signal recorded in the ceria sample at coordinates $x = 6.10$ µm and $y = 21.57$ µm. (b) Transient reflectivity signal filtered with a 48th order FIR bandpass filter with cut-off frequency set at 10 GHz below and above the expected BO frequencies in ceria (blue solid curve) [for a discussion on the BO frequencies, please refer to Sec. 3.4.2]. The time axis is shifted so that the time $t = 0$ is set at the electronic peak. The remaining background, estimated using an averaging moving window of length 238 ps is represented in the time scale associated to the final acoustic signal (red dashed curve). (c) Final acoustic signal obtained by subtracting the remaining background from the filtered transient reflectivity signal [blue solid curve minus red dashed curve in (b)].

The first step is illustrated for a single signal in Fig. 3.4 and is applied the same way to all the signals of the scan. First, the raw transient reflectivity signal [Fig. 3.4 (a)] is denoised using a 48th-order finite impulse response (FIR) bandpass filter, with a passband tuned to the frequency range where the BOs are predicted to be detected. For an extended discussion on the determination of the Brillouin frequency (BF) intervals, computed for each of the three possible acoustic mode launched in the sample, the reader is referred to the related sections of each sample studied [Secs. 3.4.1 and 3.4.2].

The time axis is shifted so that the time $t = 0$ ns is set at the electronic peak, *i.e.*, the common time of arrival of both pump and probe pulses [Fig. 3.4 (b)]. Then, the electronic peak, corresponding to the overlapping time of both pump and probe laser pulses, is avoided since it is not related to the acoustic contribution [Fig. 3.4 (b)]. The first few ps are cut to remove the electronic response near $t = 0$ ns, meaning that the first nm in contact with the OAT are not used (*i.e.* considered homogeneous) for the depth vector reconstruction (as it will be discussed in the next section [Sec. 3.3.2]) Finally, to estimate and

subtract the remaining contribution of the thermal processes, a local linear regression method (LOESS from MATLAB) is applied over a 0.24 ns window, corresponding to $\sim 1/6$ of the signal complete duration to avoid filtering of the local variations *i.e.*, the BO or acoustic content, to the filtered timer-shifted peak-free signal [Fig. 3.4 (b)].
The resulting signal of these three steps of filtering is referred as the "acoustic signal" [Fig. 3.4 (c)] and are considered to contain exclusively the acoustic contribution of the transient reflectivity signals.

A first insight on the structure of the scanned sample [Fig. 3.5 (a)] is achieved by estimating the strongest frequency component in the Fourier transform (FT) of the complete acoustic signals [Fig. 3.4 (c)], here in the frequency range of the BO associated to the QLA mode, in all the signals of the scan.
The 2-D map obtained in Fig. 3.5 (a) allows to identify the different grains, via the BF detected in the FT of the acoustic signals, thanks to the different pixels colours: one pixel being linked to the BF associated to one acoustic signal. The white pixels correspond to non-exploitable results, usually due to saturation of the photodiode induced by strong light scattering from defects/impurities on the sample surface.

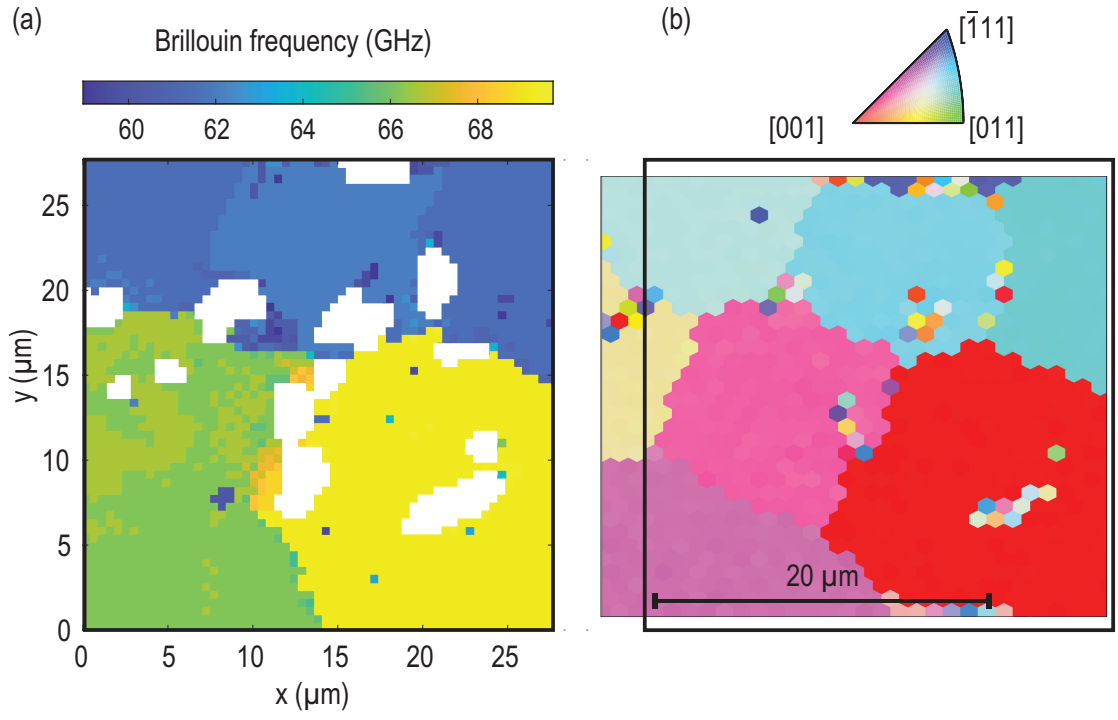

Figure 3.5 – First insight on the sample structure with the QLA mode 2-D maps of the BF repartition in the complete acoustic signals, compared to the EBSD pattern. (a) 2-D map of the strongest BF component in the complete acoustic signals of the ceria scan, when considering the detection of QLA mode. (b) EBSD pattern of the same ceria area as (a), the black square area denoting the TDBS scan area. White pixels correspond to absence of exploitable signal (usually induced by strong light scattering from defects/impurities at the surface of the sample saturating the photodiode).

The agreement between the QLA mode 2-D map and the EBSD pattern is sufficiently good to confirm the location of the TDBS scan in the EBSD pattern. However, not all the grains are resolved and some boundaries seems to be not perfectly located when compared to the surface image of the EBSD pattern, like in the middle of the scan (x = [10 - 15] µm, y = [7 - 17] µm) in the QLA mode 2-D map [Fig. 3.5 (a)].
Complementary study of the QTA modes will allow to locate all the grains, as it is discussed in Sec. 3.4.2, but the main point here is that the 2-D map gives an averaged view on the scanned sample. When considering the FT of the complete acoustic signals, we are collecting information along the full time of monitoring of the CAP, preventing us from obtaining the possible axial (depth) variations of the grains structure. The strongest frequency component is extracted, but the appearance/disappearance of a frequency component with time (hence with depth in the sample) are not resolved. Crucially, studying these variations in time will give an explanation [Sec. 3.4.2] for the not-perfectly located grain boundary mentioned before: since TDBS imaging resolves deeper structures than EBSD, this boundary is in fact buried and inclined relative to the OAT/sample surface. Next section [Sec. 3.3.2] presents the methods that allow to study the axial variations of the BF by using time-frequency tools.

3.3.2 The slicing: estimating the Brillouin oscillations frequency variations with depth

The acoustic signals obtained as an output of the first processing step [Sec. 3.3.1] are now subject to two different processing methods to analyze their amplitude and frequency variations with time, that is later converted into variations with depth (distance from CAP-launching surface in the sample).
The prime interest is to follow the variations of the BO frequency with time: following Eq. (2.36), if we know the probe laser wavelength λ_{probe} and the refractive index n of the assumed optically-isotropic sample at the wavelength of the probe, then a variation in the oscillations frequency means that the CAP propagation velocity v_{LA} (here in the case of QLA mode propagation) is varying too. Acceleration or deceleration of the CAP is an indication that the structure of the sample is changing, and that the CAP has encountered a grain of different orientation compared to the one it was originally launched in. Thus seeking for BO frequency shifting is equivalent to looking for grain transitions in the sample. In addition, transition from one grain to another can also be evidenced by amplitude modulations in the recorded signal. Accordingly, a first processing method rely on the short-time Fourier transform (STFT) applied in a moving (along the time axis) window in order to "slice" the acoustic signal and estimate its time frequency content. The second processing method relies on a wavelet synchrosqueezed transform (WSST) to extract the amplitude and frequency variations of the modes composing the signals. The capacity to perform these extraction for all the three modes at once with good time and frequency resolutions, compared to a mode-by-mode extraction with the STFT-based method, makes it interesting for faster, more general computations.

Short-time Fourier transform (STFT) and synchronous detection technique (SDT)

The 2-D map obtained in Fig 3.5 (a) shows the strongest frequency component of the complete acoustic signals in the BF interval associated to the propagation of the QLA mode. The averaged information that emerges from this map is incomplete since it does not inquire about the time associated to the disappearance / appearance / shifting of the BF. It is thus logical to turn toward time-frequency tools to overcome these limitations, and access the variations with time of the BF variations.
Each acoustic signal is processed following a mode-by-mode detection of the BF measured in a short-time window moving along the complete acoustic signal duration. We thus assume that a single frequency needs to be retrieved, and will need to apply the processing method three times to obtain the results for the three expected modes defined in Sec. 2.4.1.
The summary of the STFT-based processing is the following: the short-time Fourier transform (STFT) [139] is applied in each portion of the signal in a Hann moving window, which size is tuned depending on the mode processed, and the strongest frequency peak in the window is extracted and associated to the central time of the moving window.

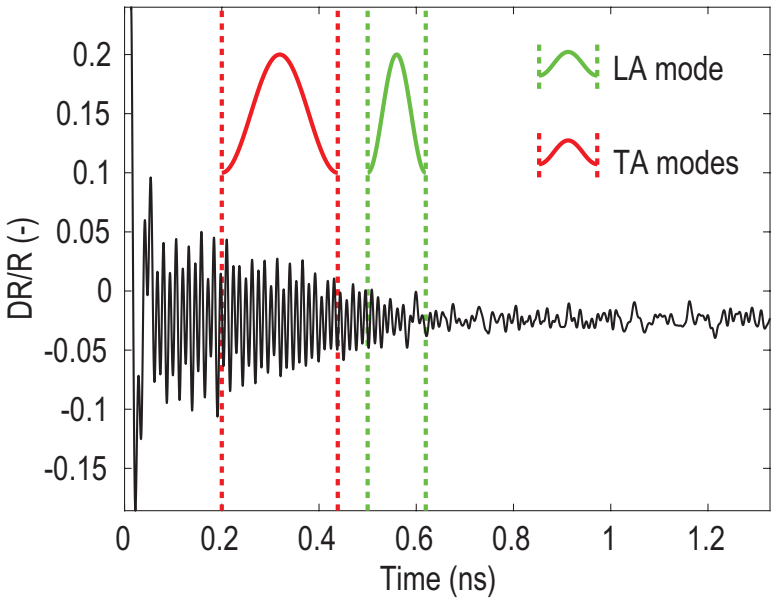

Figure 3.6 – Short-time Fourier transform (STFT) window sizes difference between QLA and QTA modes processing in ceria. The moving window used to process the QLA mode is twice shorter (251 points ≡ 119.5 ps) than the window used to process both QTA modes (501 points ≡ 238.6 ps). This choice is motivated by the aim to keep a comparable number of BO periods in all STFTs, the QLA mode velocities being twice as fast as the QTA modes, as well as obtaining reasonable time and frequency resolutions.

A representation of the Hann moving windows is given in Fig. 3.6 in comparison with the signal in Fig. 3.4 (b). The size of the window used for the detection of the oscillations associated to the QLA mode is

twice shorter than the one used for the detection of the oscillations associated to the QTA modes [Fig. 3.6]. This choice is justified by the will to have a comparable number of full oscillation periods in the window, since the QLA mode is propagating on average twice faster than the QTA modes.
With a window of 251 points $\equiv$ 119.5 ps, the slowest QLA mode can fit 7 full oscillations in the moving window, while with a 501 points $\equiv$ 238.6 ps window, the slowest QTA mode fits $\sim$ 6.4 oscillations. On another hand, the window size requires this 2 times ratio to ensure keeping good time and frequency resolutions, and avoid artefacts (oscillations in frequency or non-detection) in the time-frequency representation arising from badly dimensioned windows.
Finally, the shifting distance between two windows is set to 1/6 of the window size, *i.e.*, the time difference between two successive window central times is $\sim$ 19.9 ps for the QLA mode and $\sim$ 39.8 ps for the QTA mode.
Following the processing described in Ref. [133], the acoustic signals $s(t)$ are expressed with a simple model, in terms of a time-dependant amplitude $A(t)$ and a time-dependant phase $\phi(t)$ as follows:

$$s(t) = A(t)\cos\left[\phi(t)\right], \tag{3.4}$$

with the phase term composed of a slowly $\left(2\pi \int f_{BO}(t')dt'\right)$ and a rapidly $\left(\psi(t)\right)$ varying terms:

$$\phi(t) = 2\pi \int f_{BO}(t')dt' + \psi(t), \tag{3.5}$$

with, reminded here, f_{BO} the frequency of the Brillouin oscillations.
To find the strongest frequency component in the temporal window, a synchronous detection technique (SDT) is applied in order to overcome the limitation of the STFT temporal resolution, linked to both the signal-to-noise ratio (SNR) of the acoustic signal and the time window $H(t)$ duration. Indeed, for the signals with low SNR ratio, extraction of the peak frequency (or instantaneous frequency) may lead to large uncertainty/erroneous values that is increasing with short-duration windows with lower frequency resolutions. This issues are usually leading to the necessity of using a longer-duration Hann window to obtain reasonable results, decreasing consequently the temporal resolution.
The aim of the SDT technique is to find the value f_m that maximizes the norm of the integral I_{SD} in the time window $H(t)$:

$$I_{SD}(t) = \int_{-\infty}^{\infty} H(\tau - t)e^{i\phi(\tau)}e^{-i2\pi f_m \tau}d\tau \tag{3.6}$$

Assuming slow variations of the BF within the Hann moving window $H(t)$, the slowly-varying phase term in Eqs. (3.4) and (3.5) can be approximated: $2\pi \int f_{BO}(t')dt' \equiv 2\pi < f_{BO} > t$, where $< f_{BO} >$ is the mean BF within the time window, *i.e.*, our target. The BF is determined iteratively for each time window and associated to a corresponding detection time, the Hann window central time.
To avoid/remove wrongly attributed values of BF due to, *e.g.*, a non slowly-varying phase, a threshold criteria is implemented. In parallel to applying SDT, the STFT of the signal inside the window $H(t)$ is

computed in order to use the prominence of the frequency peak as a discriminant.
The topographic prominence of a peak was defined in the earth science field as a way to describe how a peak (like the summit or the pass of a mountain) stands-out relative to its surroundings environement (valley, other summits, cliffs) [140]. This criteria thus allows to estimate "how well-defined" is the detected BF relative to the frequency content of the signal in the window, and can be understood as a signal-to-noise (SNR) criteria. In the normalized (by its maximum value) STFT, the SDT-detected BF associated to a peak with a prominence below 0.6% in the QLA mode case, and below 2% in both QTA modes cases, are removed. Slices of the BF repartition in common central-time windows are obtained, where the white/empty pixels corresponds to the removed values [Fig. 3.7 (a-c)].
Knowledge of the BF of the acoustic mode for each time step allows the conversion from time to depth using the velocity calculated with Eq. (2.36). For each time step, the acoustic velocity associated with the extracted BF allows to estimate the depth travelled since the previous time step. The first time step, being different from zero due to efforts made to avoid the electronic peak influence (Sec. 3.3.1), defines the first depth step. The imaged material is thus approximated as homogeneous, with the properties of the BF detected at the first time step, in the first nanometers of the CAP propagation. Finally, the slices [Fig. 3.7 (a-c)] giving the BF repartition of all the acoustic signals for a common central time (but not a common depth due to the different CAP velocities in the different grains) are stacked in a 4-D representation (3-D spatial variables and 1-D for the colours associated to the BF) [Fig. 3.7 (d-e)]. Differently stated, once the time-instantaneous frequency vectors of a specific mode, for all the scan signals, are converted into depth(z-axis)-instantaneous frequency vectors, they are assembled into a 4-D stacked representation. The results obtained for the QLA mode are given in Fig. 3.7 (d-e) and the results for both QTA modes in Fig. 3.8.
One can imagine the processing as follows: the acoustic signal is a bread loaf we want to cut in regular slices in order to inspect the bread crumb. The size and the number of slices are controlled by the duration of the moving window $H(t)$ and the shifting time between two consecutive window central time position, and the BF determined by the STFT and SDT is the bread crumb "quality". Regrouping on a 2-D map the detected BF of all acoustic signals of the scan at a common central-time window gives a "slice" of bread at a certain time thus at a non-flat "slice" of bread at a certain depth. Stacking together all the bread slices brings back the original uncut bread loaf.
The lateral resolution is controlled with the translational plate on which the sample is mounted [Fig. 3.1], being 0.469 µm in the ceria scan case. The axial (from the sample surface to its depth) resolution is linked to the duration of the temporal window. In the QLA mode case, with a 119.5 ps duration window, the fastest expected mode (70.02 GHz thus 7 903 $\mathrm{m\,s^{-1}}$, see Tab. 3.4) yield a worst-case scenario resolution of 0.94 µm. In both QTA situations, the window is 238.6 ps long and leads to an axial resolution of 1.14 µm with the fastest fTA mode (42.48 GHz thus 4 794 $\mathrm{m\,s^{-1}}$, see Tab. 3.4), and of 1.02 µm with the fastest sTA mode (37.97 GHz thus 4 285 $\mathrm{m\,s^{-1}}$, see Tab. 3.4).

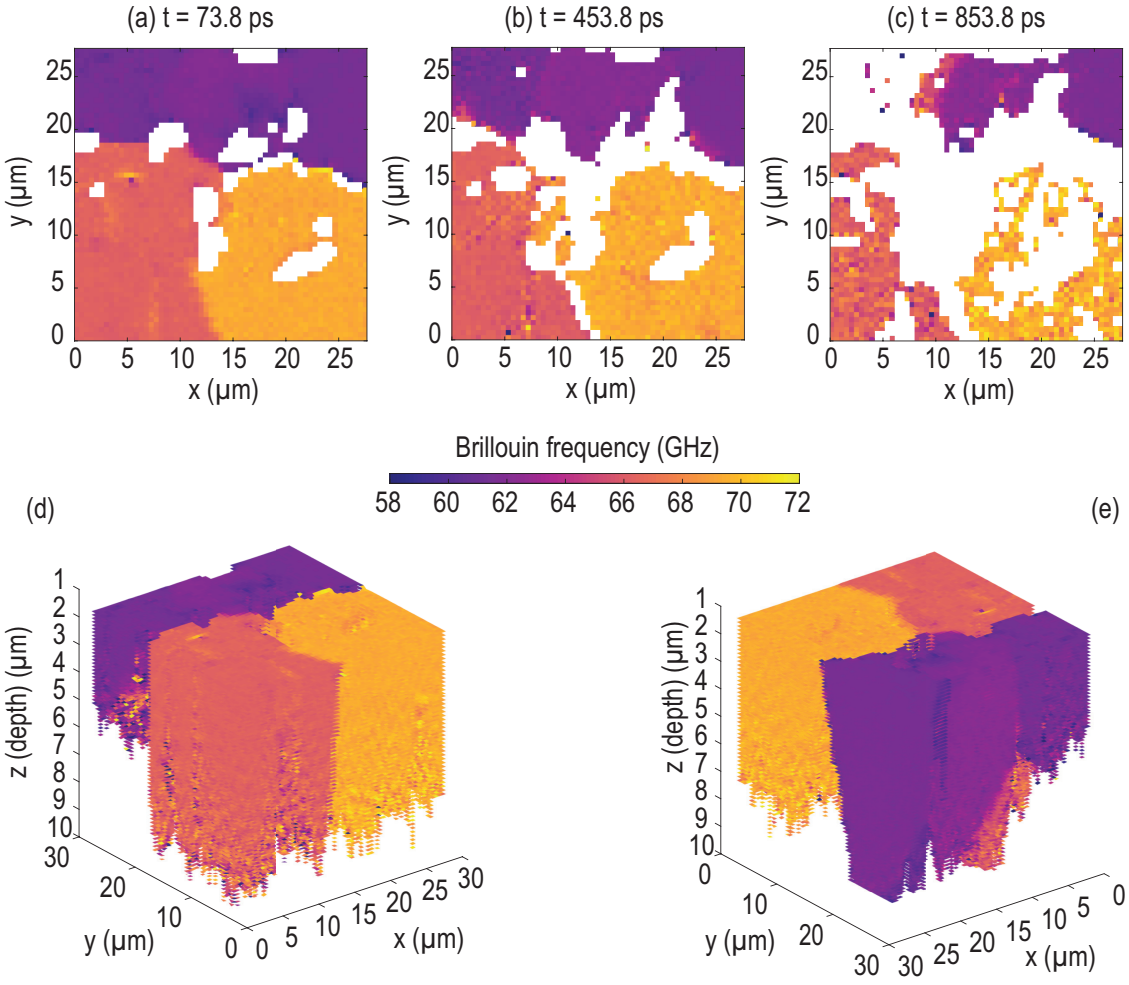

Figure 3.7 – 4-D stacked representation obtained with the STFT/SDT-based processing applied to the QLA mode in ceria. (a-c) Slices of the SDT-detected BF component, obtained in common moving window central times: (a) t = 73.8 ps, (b) t = 453.8 ps and (c) t = 853.8 ps. (d-e) 4-D (3-D for the spatial coordinates and 1-D for the color associated to the BF) stacked representations of the BF repartition in the sample scanned, obtained when all the slices of the sample are stacked/grouped.

Better (higher) axial resolution can be obtained with reduced window sizes but will lead ultimately to frequency resolution issues, as a decreased number of complete oscillations periods in the window will decrease the capacity of the SDT to resolve continuous BF detection from a moving window to another. Consider it like the quality of the STFT-based spectrogram being reduced due to a badly dimensioned window compared to the frequency content to resolve. A compromise must be found, as always, between frequency and time resolutions when computing the STFT.

This first STFT-based technique yield interesting and exploitable results but contains a principal disadvantage in the fact that it needs to be run (and parametrically tuned) independently for each acoustic mode, hence three times. Adding the compromise in frequency and time resolutions, this technique ap-

pears to be limited for 3-D imaging enhancements. Next section [Sec. 3.3.2] presents a second technique that proposes solutions to these issues.

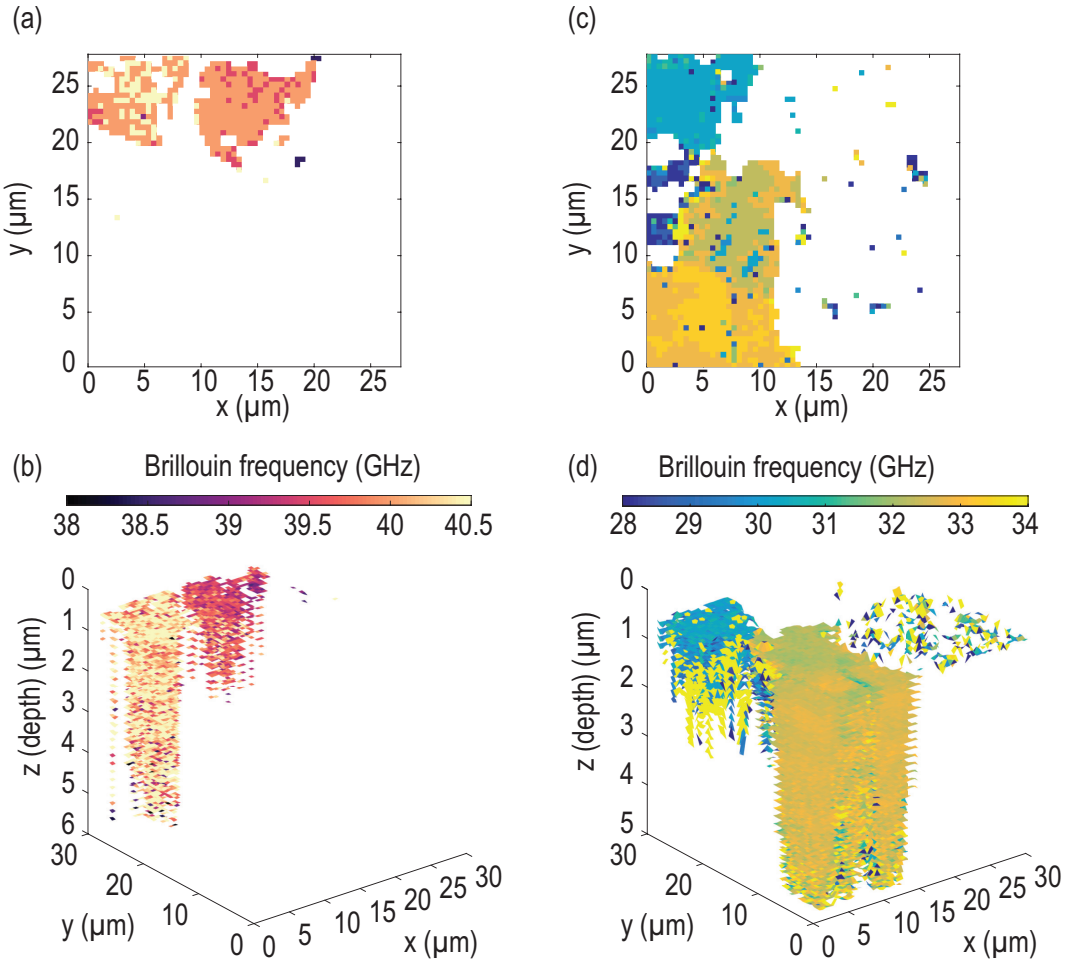

Figure 3.8 – Fourier transform of the complete acoustic signals and 4-D stacked representation obtained with the STFT/SDT-based processing, for both the sQTA and fQTA modes in ceria. (a) FT of the complete acoustic signals and (b) 4-D stacked representation in the [38 - 42.5] GHz interval, corresponding to the detection interval of fQTA mode. (c) FT of the complete acoustic signals and (d) 4-D stacked representation in the [26 - 38] GHz interval, corresponding to the detection interval of both QTA modes.

Wavelet synchrosqueezed transform (WSST)

When dealing with time-frequency representations, the ultimate goal is to achieve an ideal representation of a multi-component / multi-mode signal with a good resolution along both time and frequency axis. A multitude of processing techniques have been developed in the frame of reaching this goal, like the empirical mode decomposition (EMD) and the reassignment methods [141].
Among these methods, the synchrosqueezed transform stood from the rest: it is a good approximation

of the ideal time-frequency representation of a multi-mode signal, and enables mode reconstruction, *i.e.*, reconstruction of the amplitudes variations of a single mode with time, provided that the signal studied is composed of weakly modulated modes. This method, applied in combination with ridge extraction, has been successfully used for the reconstruction of the temporal behaviour of a superposition of AM/FM modes in a noisy signal [142, 143]

Synchrosqueezing of the continuous wavelet transform (CWT), henceforth refered as wavelet synchrosqueezed transform (WSST), was introduced by I. Daubechies and S. Maes in 1996 in the context of analysing audio signals with the aim of identifying the speakers in a recording [144]. The main essence of this tool is to narrow the time-frequency representation obtained with the CWT by re-allocating the spectrum energy of a time-frequency point (t,ω), depending on the local behaviour around this point [145].

Following the definitions given in Refs. [144, 145], the first step of the WSST is to compute the CWT, W_s, of the signal studied, hence here the acoustic signal $s(t)$ [Fig. 3.9 (a)] defined in Eq. (3.4) (or a sum of such signal $s(t)$ at different frequencies):

$$W_s(a,b) = \frac{1}{2\pi}\int s(t)a^{-1/2}\Psi\Big(\frac{t-b}{a}\Big)^* dt, \tag{3.7}$$

with Ψ the mother wavelet chosen to be scaled and compared with the acoustic signal, a and b the scale and translational parameters of the CWT, and the $*$ denoting the complex conjugate.

In the following, it is the bump wavelet (as defined in MATLAB) that is chosen to study the signals, since it provides shorter wavelet durations hence leading to better axial resolution compared to other common wavelets. The bump wavelet is given in the Fourier domain (ω denoting the angular frequency) by:

$$\Psi_{bump}(a\omega) = e^{\left(1-\frac{1}{1-(a\omega-\nu)^2/\xi^2)}\right)}\mathbb{1}_{[(\nu-\xi)/a,(\nu+\xi)/a]}, \tag{3.8}$$

with the default values $\nu = 5$ and $\xi = 0.6$, and $\mathbb{1}$ denoting the indicator (or characteristic) function. The parameter ξ controls the time/frequency spreading of the wavelet and thus the resolution.

The result of applying the CWT with the *bump* wavelet on the acoustic signal [Fig. 3.9 (a)] is given in Fig. 3.9 (b) in the form of a spectrogram in dB scales. Figure 3.9 (b) contains also the cone of influence of the CWT, *i.e.*, the area where the scaled wavelet extend beyond the signal edges, and thus where the CWT results may display non-physical artefacts (edges effects). This cone of influence being linked to the scaling factor of the wavelet, its influence on the signal will be more important for lower frequencies (longer duration scaled wavelets) and thus results in a longer layer of sample approximated (and thus reconstructed) as homogeneous, from the OAT/sample surface to the first point of the extracted ridge.

The CWT-based spectrogram [Fig. 3.9 (b)] shows two components in the acoustic signal, linked to the contribution to the TDBS signal of the QLA mode (around 65 GHz) and one of the possible QTA mode (around 30 GHz) in ceria.

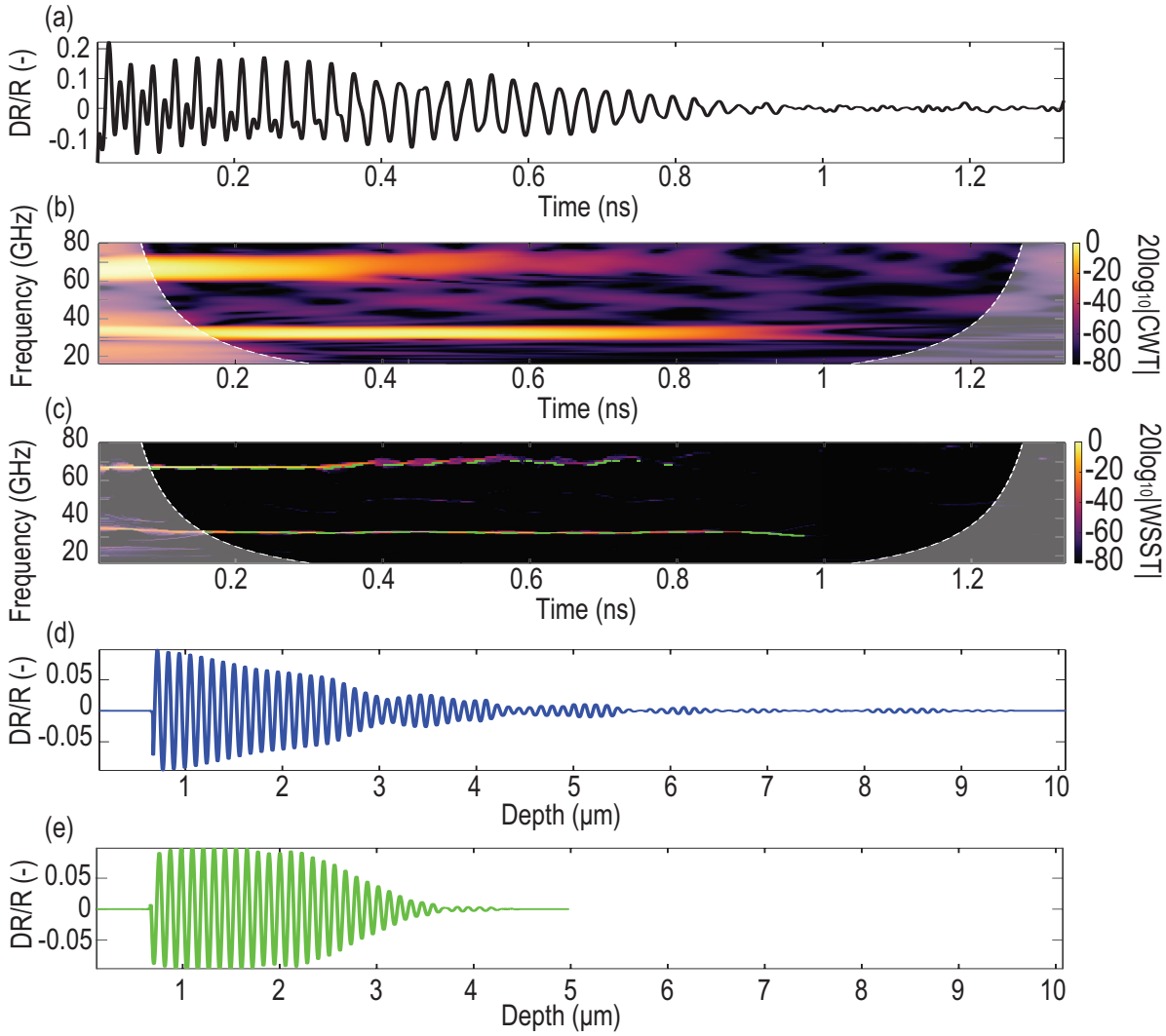

Figure 3.9 – Acoustic signal study using the WSST: spectrogram, ridge extraction and multi-mode reconstruction. (a) Acoustic signal located at coordinates $x = 9.37$ µm and $y = 11.72$ µm of the ceria scan. (b) CWT-based spectrogram $\left(20\log_{10}\left|\mathrm{CWT}\right|\right)$ of the acoustic signal (a), normalized by its maximum value. The cone of influence of the CWT is given by the white dashed curves and associated shadowed area from the edges of the signal. (c) Synchrosqueezed CWT-based spectrogram $\left(20\log_{10}\left|\mathrm{WSST}\right|\right)$ of the acoustic signal (a), normalized by its maximum value, and extracted ridges (green dashed lines). The same cone of influence as in the CWT is given by the white dashed curves and the shadowed area at the spectrogram edges. (d-e) Modes reconstructed from the extracted ridges using the IWSST: (d) mode reconstructed from the QLA mode (highest frequency component) contribution and (e) mode reconstructed from one QTA mode (lowest frequency component) contribution.

However, the instantaneous frequency of each mode, our ultimate goal, is not clearly defined and instead, the energy appears to be spread out along the aimed instantaneous frequency. The ingenious idea that led to the creation of the synchrosqueezing is to compute a candidate instantaneous frequency $\omega_s(a,b)$ for any (a,b) pair (hence everywhere in the signal spectrum) where $W_s(a,b) \neq 0$, defined by the product

of CWT^{-1} with its first derivative with respect to the translation parameter:

$$\omega_s(a,b) = -i\Big(W_s(a,b)\Big)^{-1}\frac{\partial}{\partial b}W_s(a,b). \tag{3.9}$$

Finally, the synchrosqueezing step consists in transferring the values of the time-scale plane (b,a) to the the time-frequency plane (b, $\omega_s(a,b)$), using the obtained instantaneous frequency Eq. (3.9). The CWT values are thus squeezed to the region close to the instantaneous frequency $\omega_s(a,b)$, the wavelet synchrosqueezed transform being given by [145]:

$$\mathrm{WSST}_s(\omega,b) = \int_{A(b)} W_s(a,b)a^{-3/2}\delta(\omega_s(a,b)-\omega)\mathrm{d}a, \tag{3.10}$$

with $A(b) = [a; W_s(a,b) \neq 0]$ and where $\delta()$ should be interpreted in the sense of distributions (see Ref [145], Sec. 3 for more details).

All the interest of the WSST of the acoustic signal is the capacity to extract the time-frequency ridges associated to the modes composing the signal, highlighted by horizontal dashed green lines in Fig. 3.9 (c). This ridge extraction, *i.e.*, extraction of the maximum-energy time-frequency ridges of the spectrum, offers the possibility to evaluate with precision the BF of the acoustic modes, exactly like obtained with the combination of the STFT and the SDT in Sec. 3.3.2. However, with the WSST, all three possible instantaneous frequency ridges can be extracted at once and with both good time and frequency resolutions (owing to the scaling of the CWT compared to the fixed window size of the STFT). Also, the synchrosqueezing step pushes further the SDT step by relying on the reassignment of the complete spectrum to locate with precision the time-frequency ridge of each mode.

Furthermore, when performing the ridge extraction, not only the time-frequency content is extracted, but also the associated spectrogram energy amplitude for a specific time-frequency point. It is thus straightforward to define a threshold using this energy amplitude, in order to define what part of the extracted ridge should be kept and what part should be considered as too low when compared to noise. In the ceria scan, the ridge points with amplitudes below -64 dB are removed hence explaining why the ridges in Fig. 3.9 (c) are not continuous along the complete time axis. One very useful property of the CWT that is kept even when applying the synchrosqueezing, is to apply the inverse CWT in order to reconstruct the original time-varying signal given as an input to CWT. More precisely, the interest of the inverse WSST (IWSST) is to reconstruct the amplitude variations in time of the modes, independently, by applying the IWSST to each extracted ridges [Fig. 3.9 (d-e)]. Doing so, applying the WSST to the signal, then extracting the ridges in the spectrogram and finally reconstructing the modes with IWSST permits visualisation of each modes, and acts like a very precise filtering that adapts in both time and frequency to the modes composing the signal. The conversion from time-frequency ridges to depth-frequency ridges is done exactly like in Sec. 3.3.2, making use of Eq. (2.36) to calculate the local velocity.

The depth-frequency ridges of a common mode and of all the scan signals are grouped leading to the 4-D stacked representation introduced in Sec. 3.3.2 [Fig. 3.10]. Even though it gives an interesting view of the sample structure, the 4-D stacked representations are not composed of precisely defined 3-D volumetric grains. The aim of the next and last step of processing is to shape the envelope of the grains.

Finally, concerning the axial (depth) resolution, its estimation depends on the acoustic mode studied, since it is linked to the temporal resolution of the corresponding wavelet in the wavelet filter bank of the WSST. However, in the case of the ceria scan, the acoustic velocity (and hence BF) ratio between the QTA mode and the QLA mode is close to two and leads to an approximately 0.75 µm resolution for both a 64 GHz QLA mode and a 34 GHz QTA mode, while the temporal resolution of the wavelet is such that it includes at least 6 full oscillations of the associated BF wavelength.

3.3.3 The shaping: 3-D reconstruction of samples

Third and final step of the developed signal processing method, the shaping aims to shape the best possible envelope around the grains in the 4-D stacked data sets [Fig. 3.10] obtained in Sec. 3.3.2. In these data sets [Fig. 3.10], one voxel is defined by its BF and its 3-D location (x,y,z), and thus a grain is defined by a group of adjacent voxels with common BF. Accordingly, the first step of the slicing consist in segmenting the data in order to determine which voxels belong to which grains. A foreword on image processing method is given to explain the origin of Otsu's segmentation technique, that is subsequently adapted to the 4-D

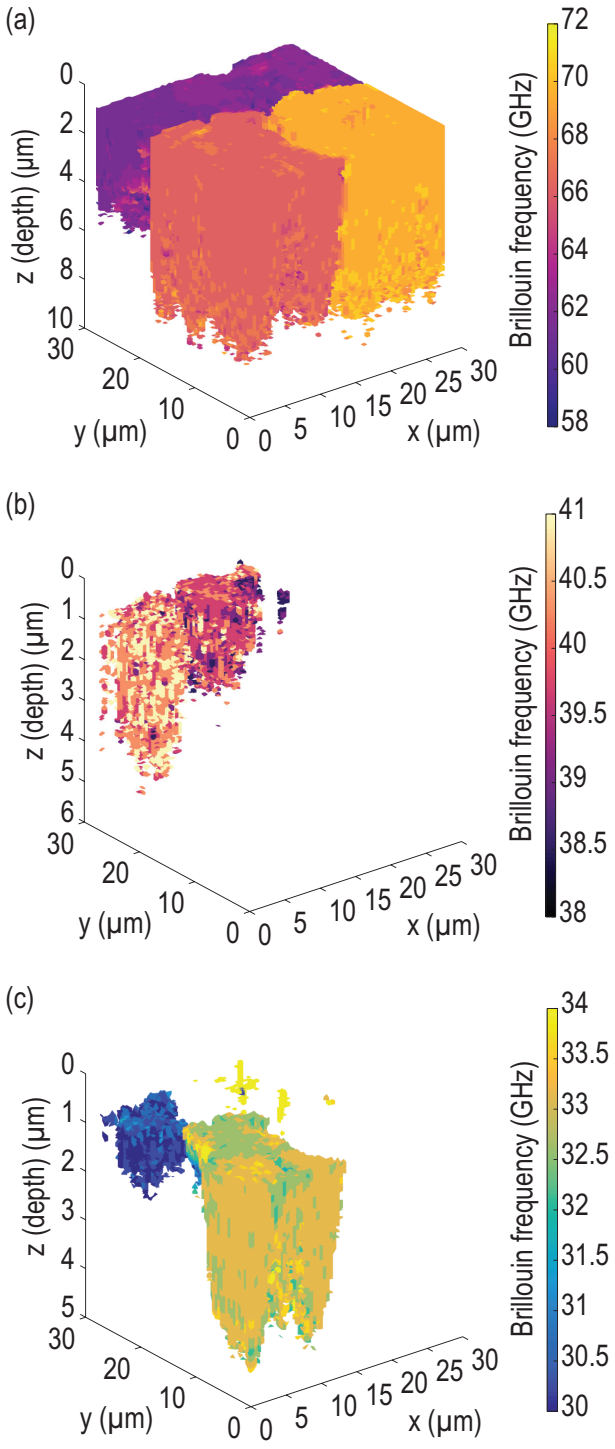

Figure 3.10 – 4-D stacked representations obtained with the WSST-based method applied to the ceria scan, for all three acoustic modes: (a) QLA mode, (b) fQTA mode and (c) both QTA modes (refer to Sec. 3.4.2 for a discussion on the BF intervals definition).

stacked cloud of voxels.
Once the segmentation is done, the clouds of voxels defining a grain are given as an input of an alphashape algorithm that computes the best constrained shape around and inside the cloud. The final output of this alphashape algorithm leads to the 3-D representations of the imaged grains in the sample.

Data segmentation methods

Foreword on image processing techniques.
In a first attempt to gather the 4-D stacked cloud of voxels parts that "visibly" belong to common grains, image segmentation methods were investigated in the results obtained with the STFT and SDT techniques [Fig. 3.7 (d-e)]. First, an interpolation of the cloud of voxels along the z-axis was done in order to obtain a "flat" 4-D stacked representation, *i.e.*, slices of the sample with common-depth voxels. Once this "flat" 4-D stacked representation was obtained, image processing tools were applicable on each flat sample slice. It is at this moment that Otsu's segmentation method [138] appeared as a suitable algorithm to separate the grains in each slices. In few words, Otsu's method is an histogram-based image segmentation: a 8 bits greyscale image can be defined in terms of its intensity distribution, *i.e.*, the number of pixels of common intensity in a 255 greyscale level / intervals [Fig. 3.11 (a-b)]. These values can thus be represented in an histogram with 255 intervals, or classes. Otsu's segmentation firstly aimed at finding the threshold dividing the histogram in two regions: the foreground and the background of the image, by computing the minimal variance between the intervals (minimal intraclass variance). The method has been then extended to multi-level thresholding and refered as multi-Otsu thresholding [146].
The step-by-step procedure is detailed in Fig. 3.11: from one frequency-coloured sample slice [Fig. 3.11 (a)], its greyscale image is computed [Fig. 3.11 (b)]. Then a multiple threshold Otsu's segmentation al-

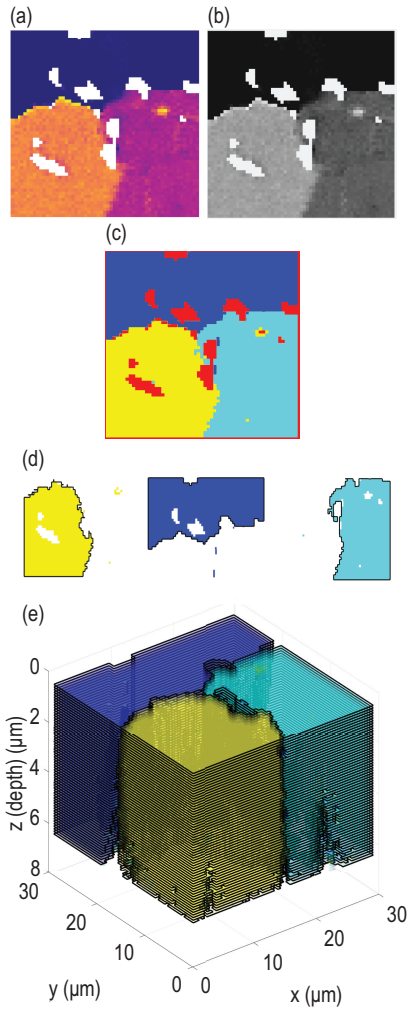

Figure 3.11 – Data segmentation using image processing techniques. (a) Original "common depth" slice of BF repartition to segment. (b) Greyscale of the original image in (a). (c) Segmented image (using a multi-Otsu thresholding image segmentation) with 3 grains and the background. (d) Representation of each independent grain of (c) and their associated contour lines (black solid lines). (e) Stacked representation of the segmented grains and their contour lines. These results were obtained with the QLA mode in the ceria scan.

gorithm is applied to separate a determined number of grains (here 3 thresholds for 3 grains and the background) [Fig. 3.11 (c)].
From Otsu's segmentation, the separated grains are obtained and a gradient operator is applied to locate the outer boundaries, or contour lines [black lines in Fig. 3.11 (d)]. Once this procedure is repeated on each slice, the final "flat" and segmented 4-D stacked representation is obtained [Fig. 3.11 (e)]. The output of this procedure are the points forming the contour lines of the grains [black lines in Fig. 3.11 (d-e)] that are fed as the input cloud of voxels to the alphashape algorithm.
It is easy to understand that this method is not the best since it relies on the interpolation of the original cloud of voxels, and gives only the outer boundaries as an input to the next step. However, it is the spirit of Otsu's segmentation method that led to the segmentation method that follows.
Note that this method is comparable to x-ray computed tomography segmentations presented in Sec. 1.2.2 [Fig. 1.3].

Adaptation of Otsu's segmentation method.

The histogram repartition of the voxels, *i.e.*, the number of voxels in a common BF interval of the 4-D stacked cloud of voxels, is plotted for each acoustic mode in Fig. 3.12. The number of bins (frequency intervals of the histogram, blue rectangles in Fig. 3.12) and their associated frequency edges are defined by the frequency resolution of the WSST, thus defined by the wavelet filter bank used to compute the CWT prior to synchrosqueezing. Such parameter is decided by the "number of voices per octave" defined in MATLAB's CWT function documentation.
In our version of histogram segmentation, we aim to locate the BF intervals containing a high number of voxels, an indicator of the presence of a grain. First, a threshold value is defined as a % of the total voxels number, the value chosen for the ceria scan here being 4% (solid red horizontal lines in Fig. 3.12). Then, local maxima are found in the occurrence curve, *i.e.*, the curve passing through all the bins values (solid black curve in Fig. 3.12). In this situation, the prominence criteria is used again and only maxima having prominence above half the 4% threshold are kept (red triangles in Fig. 3.12).

Depending on the bins distribution around the local maxima, two scenarios are possible. Note that, the BF intervals around a local maxima is chosen to be composed of at least three bins (a bin detected with a high number of voxels and its two surrounding bins) so that the frequency interval includes the voxels that could be detected on its outer boundary.
Hence, in the first scenario, if the occupancies of the two surrounding bins are below the 4% threshold, the associated BF interval includes exactly three bins, *i.e.*, the local maxima bin and the ones just before and after it. In the second scenario, if one or two bins surrounding the local maxima have a voxel number above the 4% threshold, then closer attention needs to be given to the voxels repartition.
If only one neighbouring bin is higher than the 4% threshold, the BF interval includes the three previously-defined bins around the local maxima, plus the second bin in the direction of the above-threshold bin

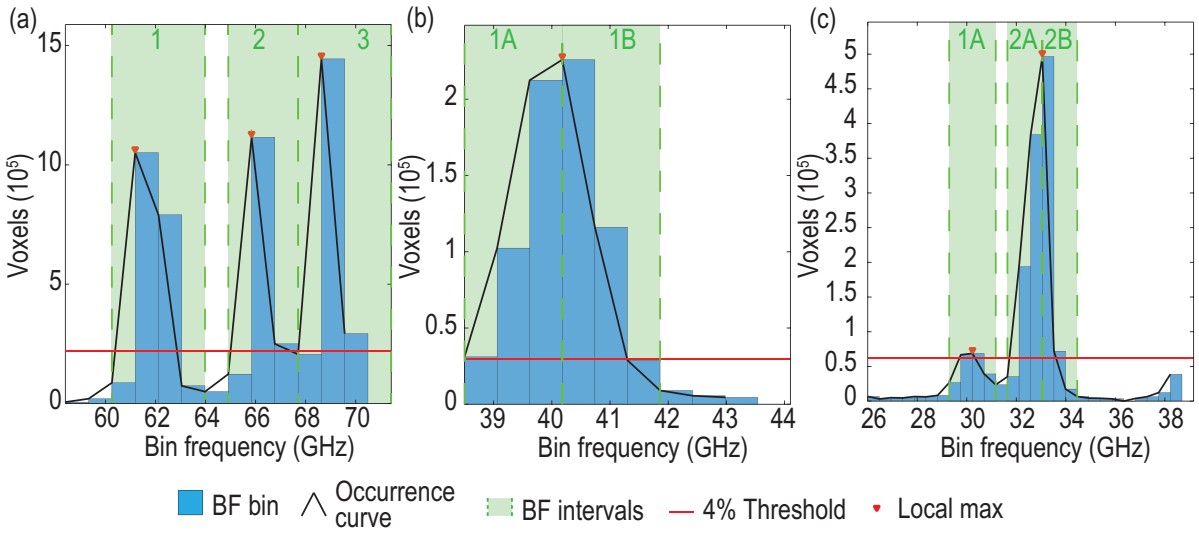

Figure 3.12 – Histogram-based segmentation of the voxels composing the WSST-based 4-D stacked cloud of voxels, for all three acoustic modes: (a) QLA mode, (b) fTA mode and (c) both QTA modes (refer to Sec. 3.4.2 for a discussion on BF intervals definition).

(extended to the left if it is the lower frequency bin and to the right if it is the upper frequency one). Such situation is seen in Fig. 3.12 (a) for all the BF intervals, the three intervals being extended to the right, as well as in Fig. 3.12 (c) where the BF interval associated to grain 1A has been extended to the left of the local maximum. It has to be noted that the BF intervals cannot overlap for obvious reasons (a voxel cannot belong to 2 grains), thus the interval defining grain 2 in Fig. 3.12 (a) is in fact not extended in the direction of the second bin over the threshold. Finally, if the occupancies of both the neighbouring bins are above the 4% threshold, the gradient of the occupancy curve is computed and is used to locally separate the two highest bins, and split the BF interval in two BF intervals, hence in two grains, like in Fig. 3.12 (b) to separate grains 1A and 1B, or in Fig. 3.12 (c) to separate grains 2A and 2B.

In summary, the BF intervals defining a grain are always bonded either by the interval edge of another grain, or a bin with a number of voxel below the 4% threshold. More precise results could be obtained by increasing the number of voices per octave (the number of wavelets per octaves in the filter bank), increasing in the same time the computation time. This option is made possible by the use of PYTHON instead of MATLAB, the CWT in the latter being limited to 48 voices per octaves, which is the value that has been used here.

This adaptation of Otsu's segmentation method allows to both estimate automatically the number of grains in the input cloud of voxels, as well as giving the BF intervals corresponding to each grains.

Gathered cloud of voxels, *i.e.*, the voxels in the obtained BF intervals, are then given as an input of the next and final step of the signal processing. It consists in shaping the best envelope around this cloud of voxels, using the alphashape algorithm.

Alphashape algorithm for the 3-D rendering

The alphashape algorithm, and more generally the concept of "shape" of a set of points, has been introduced by H. Edelsbrunner and his team, in the 1980's for the first time [147] and extended to 3-D in the 1990's [148]. Various definitions of the shape of a set of point, based on "visual" or geometrical criteria, such as Voronoi cells, appeared too weak to be implemented, providing motivation for the definition of the "shape".

Starting from the convex hull, *i.e.*, the smallest convex envelope that contains all the points of the cloud

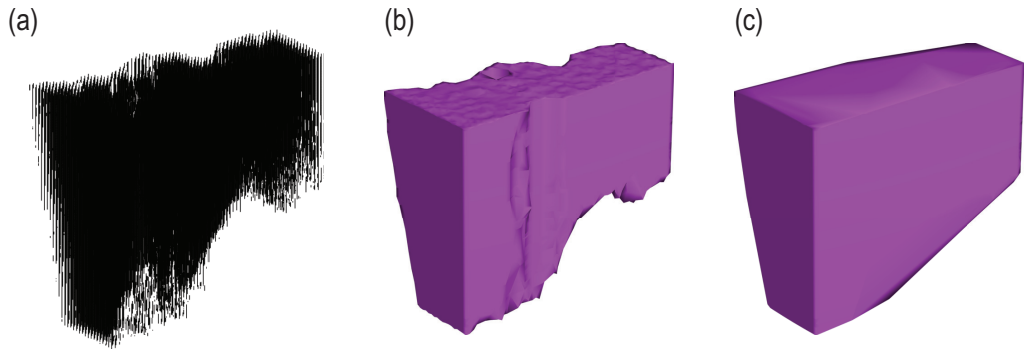

Figure 3.13 – Different alphashape results of one ceria grain imaged with the QLA mode: (a) the cloud of voxels itself (or set of points) of the grain obtained with a radius $\alpha^{shape} = 0$ µm, (b) alphashape of the grain obtained with a radius $\alpha^{shape} = 1$ µm, and (c) the convex hull of the grain obtained with a radius $\alpha^{shape} = \infty$.

of voxels, the family of alphashapes (also referred as α-shapes) of a set of points [Fig. 3.13] tries to give a possible definition and representation of the "shape".

The alphashape notion is conceptually and intuitively described in Ref. [148]. Conceptually, considering a finite set of points S in 3-D and a positive real number α^{shape}, the alphashape of S is defined as a "polytope" or here in 3-D a polyhedra, but not necessarily convex or connected. Intuitively, imagine the 3-D space ($\mathbb{R}^3$) being filled with ice-cream (or styrofoam like in [148]) and the set of points S being made of a solid chocolate pieces (or solid rocks in the styrofoam). A spherical tool, like the curved ice-cream spoon, of radius α^{shape} is used to carve out the ice-cream (styrofoam), everywhere it is possible without touching/reaching a chocolate piece (rock). This spoon carves both from the outside and from the inside of the set of point S. The resulting carved object is composed of circular edges and spherical caps, that are substituted for simplicity by straight lines and triangles. The final object is defined as one alphashape of the set of point S. The family of alphashape is defined by all the alphashapes obtained by changing the radius of the spoon α^{shape}. Thus, the limiting cases are obtained when $\alpha^{shape} = 0$, the final result is the set of points itself [Fig. 3.13 (a)], while when $\alpha^{shape} = \infty$ it is the convex hull of the set of point that is obtained [Fig. 3.13 (c)].

The alphashape algorithm is thus applied to the different voxels clouds defined by the BF intervals obtained with the segmentation method, *e.g.*, applied three times for the QLA case [Fig. 3.12 (a)] for the

three identified grains. The radius of the sphere used to "carve" the cloud of voxels is set to $\alpha^{shape} = 1$ µm, and objects, *i.e.*, 3-D group of adjacent voxels, smaller than 1/5 of the previously defined 4% threshold in these clouds of voxels are ignored to avoid reconstruction of small, uninformative features.
The final results of the alphashape algorithm are given in Fig. 3.14 (a), (c) and (e), for the three acoustic mode intervals, in comparison with their respective 4-D stacked representation [Fig. 3.14 (b), (d) and (f)].
The 4% threshold allows to denoise the final 3-D representation of the grains with the drawback of removing small grains from the resulting image. Typically, in the case of the QLA mode, the total volume occupied by the voxels after thresholding the ridge extraction in the slicing step of the WSST method [Sec. 3.3.2] reduces from 7 200 µm^3 to about 4 600 µm^3 [Tab. 3.7]. This means that grains with a volume less than approximately 184 µm^3 outside the segmented BF intervals are neglected in the QLA reconstruction, *i.e.*, no BF interval is defined, due to the 4% threshold. On the other hand, inside of each segmented BF interval, the smaller reconstructed object (3-D groups of adjacent voxels) has a volume of approximately 37 µm^3 (due to the final 1/5 threshold).

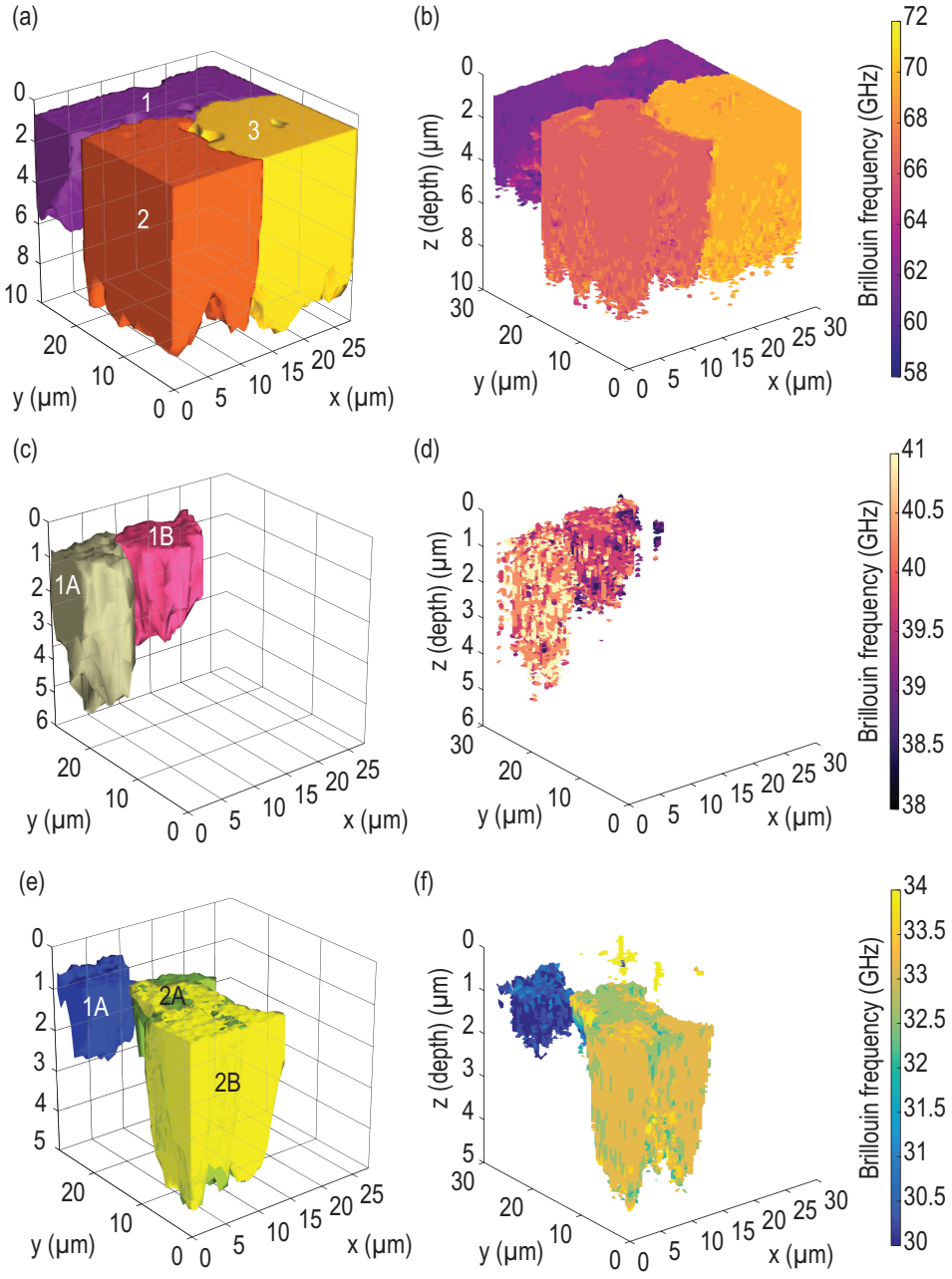

Figure 3.14 – 3-D representation obtained with the alphashape algorithm (a),(c) and (e) of the grains imaged in the ceria scan for all three acoustic mode intervals, compared to their 4-D stacked representations (b), (d) and (f) obtained with the WSST-based processing. (a-b) corresponds to the QLA mode results,(c-d) the fQTA and finally (e-f) the mixed QTA results. The alphashape results evidence the reconstitution of 3 grains (1/purple, 2/orange, and 3/yellow) with the QLA mode (a), 2 grains (1A/white and 1B/pink) with the fQTA mode (c) and 3 grains (1A/blue, 2A/green and 2B/yellow) with the QTA modes (e).

3.4 Application of the processing method to the 3-D reconstruction of transparent polycrystalline samples

The final section of Chap. 3 aims to present two experimental situations where transparent polycrystalline samples were scanned using the ultrafast experimental setup described in Sec. 3.2, and the results were processed with the method developed in Sec. 3.3.
The first scanned material is an ambient-temperature high-pressure polycrystalline water (H_2O) ice sample obtained in a diamond anvil cell (DAC). The integral/holistic 3-D image of the H_2O multi-grain ice sample is done in an approximative $100\times100\times10$ µm^3 volume, containing two different high-pressure phases (ice VI and ice VII). These results have been published in Ref. [7].
The second sample considered is a cerium dioxyde (CeO_2) polycrystal used as a processed example in Sec. 3.3. A multi-grain (crystallites with differently oriented crystalline structures) area of the sample was identified as a promising playground for 3-D imaging thanks to an EBSD measurement. The propagation of CAP is monitored down to 8 µm deep in a 30×30 µm^2 area. These results have been published in Ref. [8].
The first sample (compressed H_2O ice) proposes a first glimpse in 3-D imaging results obtained with the processing described in Sec. 3.3 using the STFT/SDT-based method, while the second sample (ceria) was used as a playground/test sample to improve the signal processing method and, ultimately, develop the WSST-based processing.

3.4.1 High pressure polycrystalline water ice (H_2O)

The opportunity to obtain an ambient-temperature water ice sample is owing to the use of a diamond anvil cell (DAC), in our case a Merril-Bassett type [149], used to compress a water droplet between two diamond culets up to GPa pressure levels. The DAC used is composed of unbevelled culets with diameters of $\sim$ 500 µm, the sample volume being controlled by a stainless steel gasket. A $\sim$ 180 µm-diameter hole was drilled in the center of the gasket, the latter being pre-indented to $\sim$ 60 µm [Fig. 3.15 (b)]. The hole in the gasket was filled with bi-distilled water that solidified upon compression, and the thermoelastic generation of CAP was allowed by a thin iron disk, playing the role of the OAT, launching CAPs in the ice sample. The iron disk was obtained by a gentle compression of a small iron spherule between the diamond anvils, whose surfaces are parallel to each other, until the desired surface was obtained. The disk was initially in contact with one of the anvils but lifted up on one side by a few micrometers when the sample volume was filled with water [Fig. 3.15 (b)]. Note that the shape and the orientation of the iron generator presented in Fig. 3.15 (b) are illustrative.
In the sample volume, few ruby grains of 1-5 µm in size were also distributed in between the iron disk and the gasket wall. These grains were used to measure the pressure using the calibrated shift of fluorescence emission frequency happening with the compression. Thanks to this, the H_2O ice sample was compressed to 2.15 ± 0.05 GPa, until the ice VI and ice VII phases were simultaneously present in the sample volume

[Fig. 3.15 (b)]. The pressure of 2.15 GPa is not choosen arbitrarily, since it corresponds to the expected transition at room temperature from the lower-pressure phase VI to the higher-pressure phase VII of H_2O ice.
The TDBS scan was obtained with the ultrafast setup described in Sec. 3.2, the lateral step was 1.25 µm along the x- and y-axes. The optical image of the H_2O ice polycrystal in the DAC shown in Fig. 3.15 (a) reveals some dark areas on the iron transducer corresponding to low local optical reflectivity of iron that could be due to some degradation processes, like the oxydation of the iron transducer (please refer to Ref. [150] and associated supplementary materials for more details).

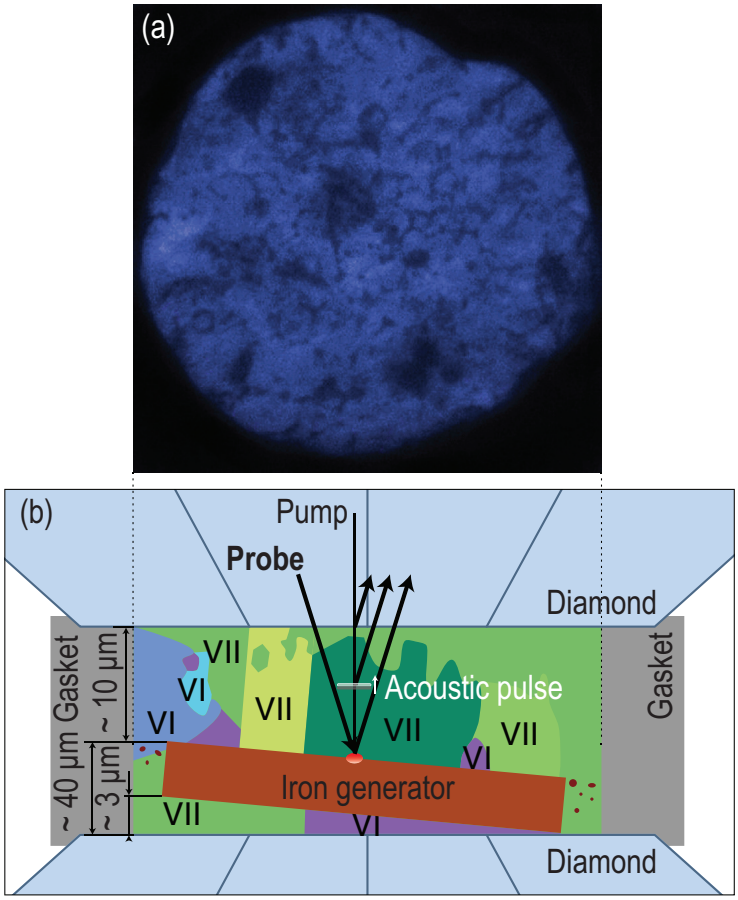

Figure 3.15 – Optical image and schematic representation of the H_2O ice polycrystal obtained in the DAC. (a) Optical image of the H_2O ice polycrystal in the DAC between the diamond anvil and the iron OAT. (b) Magnified cross-sectional side view of the DAC containing the two-phases ice sample. The disk-shape iron OAT inside the sample chamber has a diameter of about 100 µm, and touches the lower diamond anvil at its right end. Pump and probe laser beams are collinear in our experiments hence the probe laser beam is drawn inclined for a better visualization of its different reflections. Adapted from [7].

BF intervals expected in two different ice phases

The possibility to apply the signal processing methods [Sec. 3.3] requires first to compute the expected BF intervals to be detected in the scanned sample. Up to three acoustic quasi-modes can be generated in both ice phases. The determination of the associated BF intervals requires the estimation of the slowest and fastest acoustic velocities for each quasi-mode. To achieve this, the Christoffel equation is solved for each of the ice phases and the velocities v associated to any direction are given by the roots of the secular equation (following Ref. [120] notation):

$$\left|\underline{\underline{\Gamma}} - \rho v^2 \underline{\underline{\delta}}\right| = 0, \tag{3.11}$$

with $\underline{\underline{\Gamma}}$ Christoffel's tensor, ρ the material density and $\underline{\underline{\delta}}$ the identity tensor. The density and the elastic constants of each ice phase are given in Tab. 3.2.

Phases of H_2O ice (lattice system)	VI (tetragonal)	VII (cubic)
Density [151, 152] ($g\,cm^{-3}$)	$\rho = 1.419$	$\rho = 1.600$
	$C_{11} = 40.56$	
	$C_{12} = 13.75$	
Elastic constants [152] (GPa)	$C_{13} = 18.59$	$C_{11} = 37.61$
	$C_{33} = 34.43$	$C_{12} = 19.17$
	$C_{44} = 7.50$	$C_{44} = 21.59$
	$C_{66} = 6.39$	
Refractive index [151, 152] at 515 nm	$n = 1.468$	$n = 1.521$
BF intervals (GHz)	QLA: [26.71 - 29.37]	[27.58 - 33.09]
	fQTA: [12.63 - 16.89]	[16.46 - 20.90]
	sQTA: [11.66 - 12.80]	[13.66 - 20.90]

Table 3.2 – Properties of the high-pressure phases VI and VII of H_2O ice near the pressure of 2.15 GPa, and used to calculate the BF intervals for the three possible acoustic modes to be observed in the sample.

Then, the minimum and maximum velocity of each acoustic mode, in each phase of the H_2O ice, are determined and the BF intervals are deduced [Eq. (2.36)]. The associated BF intervals of both ice phases are given in Tab. (3.2).

The situation in the case of the two phases high-pressure H_2O ice sample is more complicated than single crystal samples like ceria, since a set of six BF intervals are deduced, one for each of the three possible acoustic modes in both phases. Since the acoustic velocities are known in any propagation direction of the CAPs, then the BF are known too, which allows to plot the surfaces of BF distribution of each acoustic mode as a function of the propagation direction. These surfaces are represented in Fig. 3.16 for

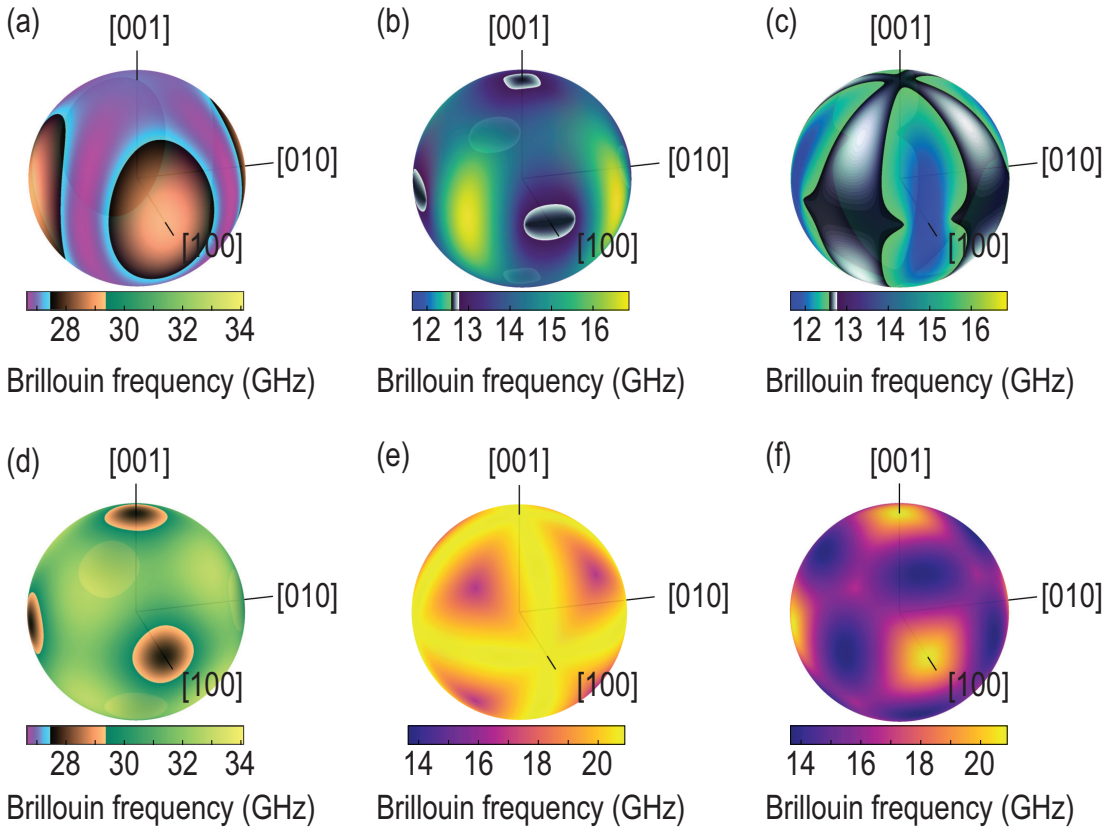

Figure 3.16 – Distribution of the BF of each acoustic mode for (top) the phase VI and (bottom) the phase VII of H_2O ice along the principal axes of the crystals as a function of the orientation of the normal to the iron/ice interface relative to the ice crystal principal axes. The results are presented separately for different modes: (a,d) for the QLA mode, (b,e) for the fQTA mode and (c,f) for the sTA mode. Adapted from [7].

(top line) the phase VI and (bottom line) the phase VII of H_2O ice, and separately presented for each mode: in (a,d) for the QLA mode, (b,e) for the fQTA mode and (c,f) for the sQTA mode. The different symmetries of both phases of water ice (tetragonal for phase VI and cubic for phase VII) are visible in Fig. 3.16 in the symmetries of the color distribution on the surface of the spheres. The color scale in Fig. 3.16 (a,d) has been designed to quickly depict whether the value of the BF of the QLA mode is lower than 27.5 GHz (magenta-to-cyan color scale), in which case it could be only attributed to phase VI. On another hand, if the BF value is higher than 29.4 GHz (greenish color scale), then it could be attributed to phase VII directly. Finally, when the frequency intervals overlaps between both phases, *i.e.*, in the BF interval [27.5 - 29.4] GHz, the color scale is copperish and indicates that complementary information, obtained by the detection of QTA modes, are required to recognise the phase. Similarly, the color scale of Fig. 3.16 (b,c) has been designed to show the direction of propagation in which the BF could be either attributed to the fQTA or the sQTA mode. Note that, obviously, the sQTA velocity should not exceed the fQTA one. Finally the color scales of Fig. 3.16 (e,f) and (b,c) are the same.

It is worth noting here that, potentially, in optically anisotropic ices, a single acoustic mode could produce up to three different BFs because of the birefringence phenomena, giving rise to Brillouin scattering with optical mode conversion [118, 153]. However, the phase VII of H_2O ice is cubic (and thus optically isotropic), while the birefringence of the tetragonal phase VI is too weak (less than 1% [151]) to be observed in our TDBS experiments, the latter explaining why a single value of the refractive index in ice VI has been listed in Tab. 3.2.

Grains identification with 2-D BF maps

Once the expected BF intervals of the scanned sample are known, a first look at the averaged information along the complete acoustic signals, of the imaged sample, is obtained in the 2-D BF maps [Fig. 3.17]. These 2-D maps present the contribution of the most prominent grains to the TDBS signal by evaluating the strongest frequency, in the first two nanoseconds of the acoustic signal, in the QLA mode interval [Fig. 3.17 (a)] or one of the QTA modes interval [Fig. 3.17 (b)]. The chosen time interval corresponds to the acoustic propagation time through $\sim$ 10 µm of the ice sample at a QLA mode velocity. The color

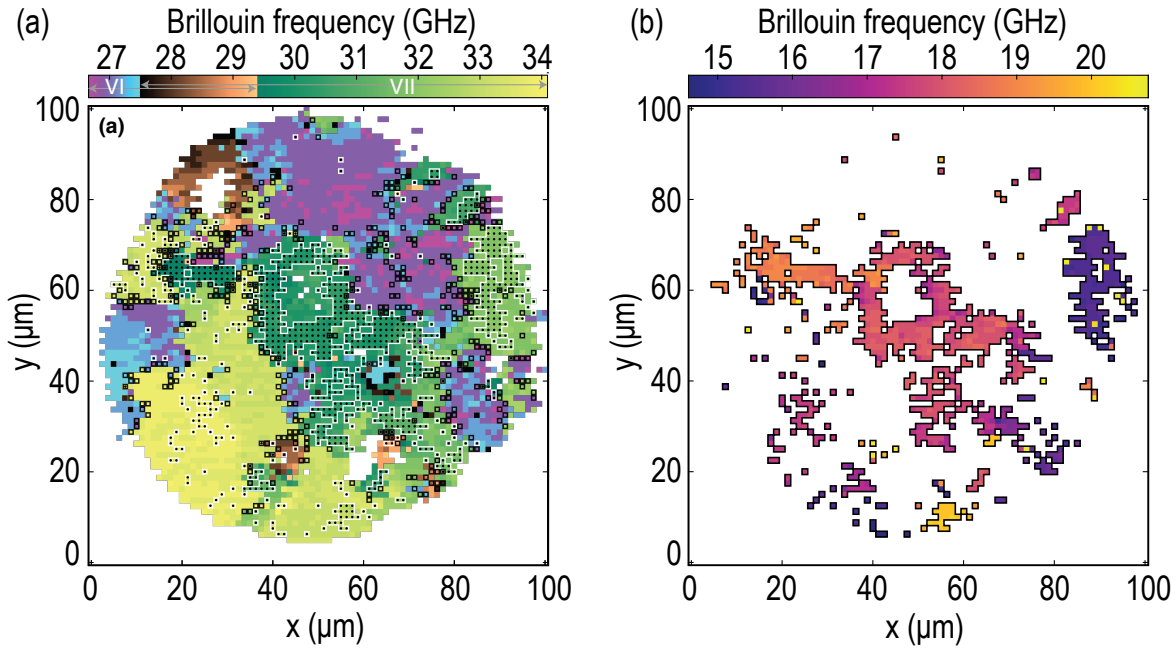

Figure 3.17 – 2-D maps of the dominant frequency in the BF intervals associated to (a) the QLA mode and (b) the QTA modes in the first two nanoseconds of the TDBS signals recorded in the high-pressure ice sample. The white solid lines in (a) delimit areas where the QTA modes shown in (b) have been detected. In (a), each pixel shown in (b) is marked with a central black dot. Adapted from [7].

scale in Fig. 3.17 (a) is matching the one in Fig. 3.16 (a,d), while the color scale in Fig. 3.17 (b) is

matching the one in Fig. 3.17 (e-f). As it will be discussed in the following, most of the detected QTA modes belong to the sQTA one in phase VII. The color scale thus allows in a glance to qualitatively inform about the orientation, relatively to the DAC axis, of the probed grains exhibiting QTA modes of particular frequency. Finally, the TDBS signals are not observed in the locations indicated by white pixels areas due to a poor SNR or a saturation of the photodetector (as for ceria). These white pixels zones [Fig. 3.17 (a)] are matching the dark tones of the optical image of the sample [Fig. 3.15 (a)]. In opposition to the optical image, the 2-D maps [Fig. 3.17] obtained by analysing the TDBS signals resolve the individual grains (or crystallites) in the sample.

The 2-D frequency map obtained for the QTA mode [Fig. 3.17 (b)] was obtained by extracting the most prominent peak in the frequency interval [10 - 22] GHz, *i.e.*, excluding the QLA modes (see Tab. 3.2). The QTA map is less complete than the QLA one since, usually, the amplitude of the contribution to the TDBS coming from the QTA modes is lower than that of the QLA one. The same observation is done in the ceria scan [Fig. 3.19 (b-c)] and has been theoretically explained in Chap. 2, Sec. 2.4.1.

Nevertheless, TDBS signals with good SNR containing signatures of the QTA modes, even weak, allowed to image part of the sample [Fig. 3.17 (b)]. The white solid lines in Fig. 3.17 (a) indicate areas where the QTA modes shown in Fig. 3.17 (b) have been detected. Complementary, each pixel shown in Fig. 3.17 (b) is marked with a black central dot in Fig. 3.17 (a).

Interestingly, most of the detected QTA modes are recorded in grains corresponding to the phase VII of H_2O ice, *i.e.*, in the greenish BF interval corresponding to frequencies higher than 29.4 GHz. On the contrary, almost no QTA modes are detected in the locations associated to the phase VI grains (magenta-to-cyan color scale), where the QLA mode frequencies are lower than 27.5 GHz. These observations suggest that the monitoring of QTA modes in the phase VI is very unlikely with the current state of the technique.

Another noticeable aspect is that in the center-right grain (around $x = 90$ µm and $y = 60$ µm) in Fig. 3.17 (b) with the lowest QTA frequencies, the color of some neighbouring pixels is occasionally switching from dark violet, *i.e.*, the lowest frequency of the color scale, to light yellow, *i.e.*, the highest frequency of the color scale. This is because the figure represents the dominant frequency content in the BF intervals associated to the QTA modes, and this particular grain contains the two detectable QTA modes. The amplitude of the sQTA mode is usually higher than that of the fQTA mode, except in some (light yellow) locations.

Finally, the area where identification of the main ice phase remains unclear from the first analysis of the dominant frequency content of the QLA signals, *i.e.*, where the frequency is greater than or equal to 27.5 GHz and lower than or equal to 29.4 GHz, are depicted with the copper color scale in Fig. 3.17 (a).

TDBS imaging with the QLA mode

To obtain the 3-D images of the H_2O ice sample by studying the QLA mode [Fig. 3.18], the TDBS signals of the scan have been processed using the STFT/SDT-based procedure, as described in Sec. 3.3.2. This method has been preferred to the more complex WSST-based one since we decided to focus the imaging to the QLA mode content of the signals, the processing with QTA modes results being too sparse to obtain informative images. The reason of the low-QTA content in the TDBS signals can be explained by the use of a very low power of both pump and probe laser beam during the scan, necessary to avoid thermal transformation of ice VII into ice VI.

The imaging results presented in Fig. 3.18 are obtained by computing the synchronous detection technique (SDT) and the STFT of the acoustic signals sliced with a Hann window of 0.23 ns (about seven period of oscillations of the QLA mode), which gives an axial resolution of ~ 1.2 µm. When reconstructing the depth axis (the same way as in Sec. 3.3.2) it has been decided to attribute only one optical refractive index to a given set of voxels with the same lateral (x, y) coordinates, even when it contains two phases, for the sake of simplicity. The attribution of the refractive index is based on the previous determination of the phases of each grain as discussed in the QLA 2-D map [Fig. 3.17 (a)]. The refractive index of the dominant phase has thus been used, and this assumption engender some distortions of the grains, that are here considered as minor. Additionally, for the pixels with unattributed phases (BF of the QLA mode in the interval [27.5 - 29.4] GHz), the refractive index is chosen to be the averaged index between that of phases VI and VII.

The 3-D imaging results presented in Fig. 3.18 (a-k) offer a different view on the 4-D stacked representations given in Secs. 3.3.2 and 3.4.2 on the ceria images, since it gives for each panel a slice of the polycrystalline H_2O ice sample at a particular coordinate along the z-axis (given in the right-bottom corner of each panel). In Fig. 3.18 (l), a 3-D representation of the complete probed volume is shown with the first and last slices, (a) and (k) xy planes, and the vertical slices through the sample middle (yz and xz planes) at $x = 50$ µm and $y = 50$ µm, respectively (red dashed rectangles). This representation has been preferred to the alphashape one for different reasons, the principal one being clarity/visualisation. The rectangles (shown with solid and dotted lines) and the circle mark in Fig. 3.18 indicate the sample regions/volumes with some interesting changes in the bulk revealed by this 3-D imaging that are discussed in the following.

The analysis of the 2-D QLA map [Fig. 3.17 (a)] seems to indicate that the volume zone pointed out by the circle in Fig. 3.18 (a-f) is composed of multiple small grains. This observation is confirmed in Fig. 3.18 since it can be seen that close to the iron OAT, the circled zone is composed of multiple and relatively small grains depicted by different colors. About half of the voxels within the circle depicted in the slice at $z = 0.89$ µm [Fig. 3.18 (a)] belong to ice VI grains. In the next slice at $z = 1.25$ µm [Fig. 3.18 (b)], it can be seen that in the place of the phase VI grains with high QLA velocity for that grain (cyan voxels, BF close to 27.5 GHz) the ice phase is now VII with low QLA velocity for that phase (green voxels, BF close to 31.1 GHz).

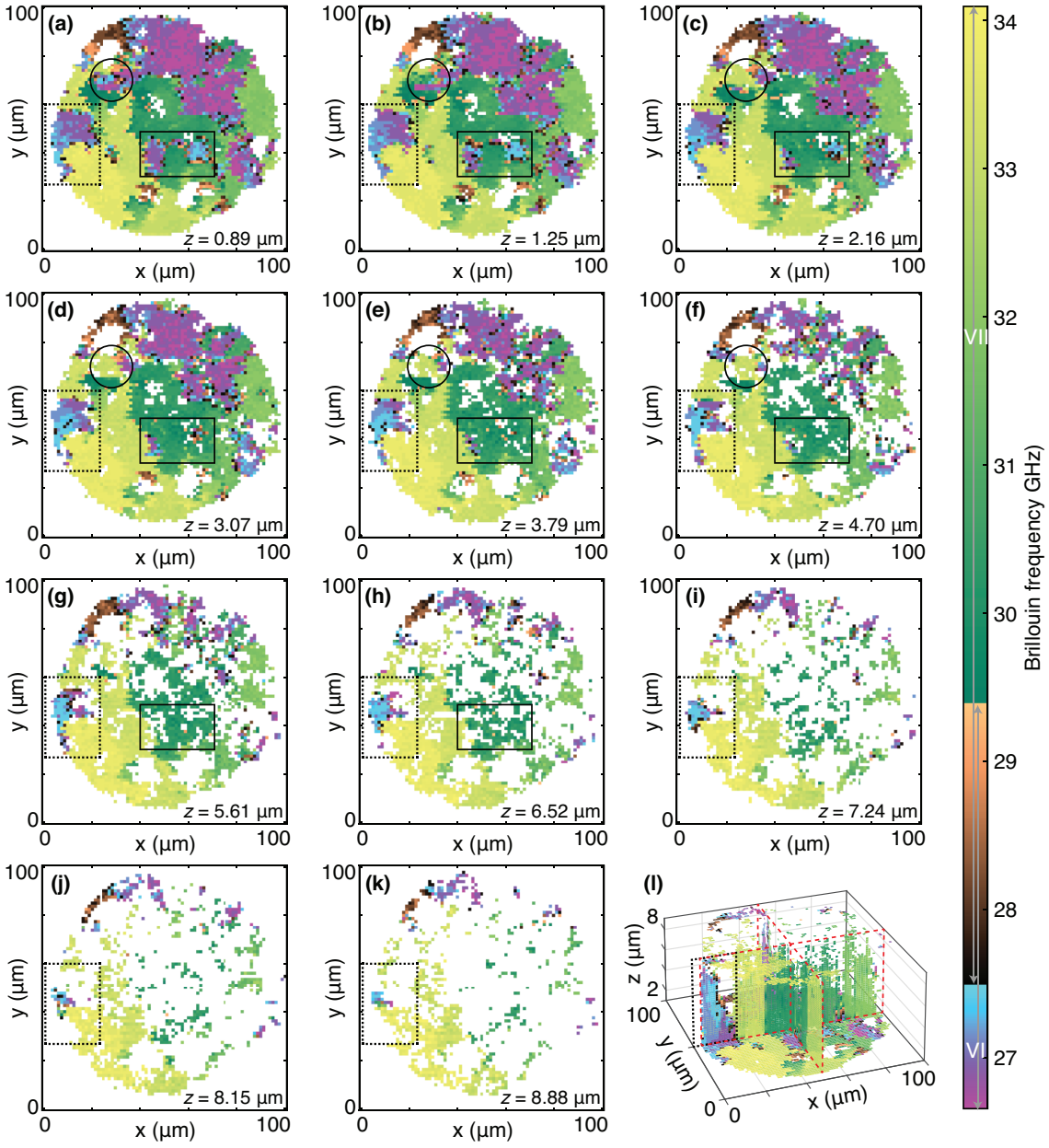

Figure 3.18 – 3-D TDBS imaging of the polycrystalline H_2O sample with QLA mode [7]. (a-k) The slices are shown at particular positions along the z-axis indicated in the right-bottom corner of each slice. In (a-f), the circles depict a volume zone composed of multiple small grains (crystallites). In (a-h), the solid-line rectangles depict the zones where crystallites of phase VI are seen between the OAT and the higher located grains of phase VII. In (a-l), the dotted line rectangles depict zones with oblique boundaries between several grains of phase VI. (l) 3-D representation of the complete probed volume with the first and last slices, (a) and (k) xy planes, and the middle slices (yz and xz planes) at $x = 50$ µm and $y = 50$ µm, respectively (red dashed rectangles). The color scale is common to all parts of the figure, and is the same as in Fig. 3.17 (a). It is important to note that, for the sake of visibility of 3-D textures, the scale of the vertical z-axis is enlarged compared to the x- and y-axes by a factor 12.

From that slice to the next one at $z = 2.16$ µm [Fig. 3.18 (c)], the voxel color slightly changes to lighter green, which could be temptatively attributed to a change from one phase VII grain to another one having a different crystallographic orientation. Yet, the resolution along the z-axis of about 1.2 µm controlled by the width of the Hann window means that the frequency/color attributed to those voxels in the slice in Fig. 3.18 (b) is indeed a weighted average of the frequency of the phase VI grains (close to the transducer) and that of phase VII [higher in the DAC, see Fig. 3.15 (b) for illustration]. The use of the WSST-based processing in the next section on ceria imaging will propose an alternative to these limitations. The rectangles shown by solid lines [Fig. 3.18 (a-h)] also depict the zones where grains of phase VI are seen between the OAT and the higher located grains of phase VII. Interestingly, the frequency (and color in Fig. 3.18) is not switching here from that of phase VI to that of phase VII at the same depth for all voxels. This is the clear sign of an oblique interface between the two grains composed of different phases of H_2O ice. Last but not least, rectangles shown with dotted lines [Fig. 3.18 (a-l)] surround other textural features demonstrating the 3-D imaging capability of the TDBS technique. In this case, oblique boundaries between several grains of phase VI having different crystallographic orientations extend up to the ice/diamond interface. In Fig. 3.18 (l), the inclined boundaries are clearly visible in the vertical slice (xz plane) at $y = 50$ µm.

Axial (depth) resolution and limitation

In the 3-D TDBS images shown in Fig. 3.18, shapes and coordinates of both H_2O ice phases, obtained using the QLA modes only, were measured with the spatial resolution similar to that achieved in the most recent x-ray diffraction based computed tomography (CT) measurements [154, 155]. The axial resolution of the TDBS scan is for this sample 1.2 µm, and the lateral one, defined by focusing of the laser beams to be 2.5 µm (using the technique described in Sec. 3.2), is approximately twice larger than the lateral step of the scans.

Technically, the lateral resolution of the TDBS scans could be improved to half the probe optical wavelength, down to 150 nm if UV-blue light lasers are used. On another hand, axial resolution of < 170 nm can be achieved with our probe laser if both QLA mode and QTA modes are used, since it is only limited by the probed acoustic wavelength $\lambda_{BO} = \dfrac{\lambda_{probe}}{2n}$.

Up to now, the axial resolution is controlled by the type of processing method used (either STFT/SDT-based or WSST-based). In the H_2O ice situation it is defined by the size/duration of the Hann window used in the STFT, balanced between time and frequency resolutions. Indeed, to keep a reasonable frequency resolution, and have a sufficient dynamic in the tight BF interval associated to the QLA mode of phase VI (spanning only over 2.7 GHz), a balance is necessary to disentangle two grains with different crystallographic orientations. For this reason, the temporal size of the Hann window is 0.23 ns, which is theoretically even a bit small since the 3 dB bandwidth of such a window function is 3.2 GHz. It will be seen in the next section on ceria imaging that such limitations are reduced with the WSST-based processing.

In addition, a polycrystalline aggregate under pressure in a DAC is usually subjected to stress inhomogeneity/nonhydrostaticity, which could lead to an induced optical anisotropy within the DAC and therefore could influence the obtained 3-D images if not accounted for. This effect in our case is negligible. Indeed, the uniaxial stress component parallel to the load axis of the DAC was estimated to 30 MPa, from the measured 0.15 GPa difference in pressure between the center and the edge of the sample. It is much smaller than in the case where the uniaxial stress component was estimated to be 1 GPa for a 4 GPa difference in pressure over 45 µm for which the induced optical anisotropy was reported to be negligible [82].

Concerning the limitation of the depth of imaging in the TDBS measurements, several factors are considered such as (i) the coherence length of the probe laser pulses, $L_{probe}^{coherence}$, in the transparent material, (ii) the diffraction length, L_R, of the probe laser radiation and of the acoustic waves composing the CAP, and (iii) by the absorption of the CAPs and probe light.

We estimated the coherence length in our measurements using the equation:

$$L_{coherence}^{probe} = \frac{c_{vacuum}\tau_{probe}}{2n} = 15 \text{ µm}, \tag{3.12}$$

where c_{vacuum} denotes the speed of light in vacuum, $\tau_{probe} = 150$ fs the duration of the laser pulses of the ASOPS-based setup [Sec. 3.2], and $n \sim 1.5$ the refractive index of ice at 2.15 GPa for $\lambda = 515$ nm (close to our probe wavelength $\lambda_{probe} = 535$ nm). The main limiting parameter is obviously τ_{probe} since the only type of laser cavities currently supporting the ASOPS synchronisation are fs laser cavities.

Because of the strict relation between λ_{probe} in the medium and the wavelength of the coherent acoustic phonon at the BF, *i.e.*, $\lambda_{BO} = \frac{\lambda_{probe}}{2n}$, the Rayleigh range (*i.e.*, the diffraction length) of both the probe light beam and the CAP beam at the BF can be described by the formula:

$$L_R = \frac{\pi a_{probe}}{\lambda_{probe}/n}, \tag{3.13}$$

where (reminded here) a_{probe} is the radius of the probe laser beam defined at $1/e^2$ level of the intensity distribution.

Because focusing of the pump laser beam controls the radius of the photo-generated CAPs, and the pump and probe laser beams were co-focused to the same spot, with $a_{probe} = 1.2$ µm, we obtained $L_R \simeq 14.3$ µm, very similar to $L_{coherence}^{probe}$. However, the signal amplitude drops by e^2 times at the coherence length, while it decreases by only $\sqrt{2}$ times at the Rayleigh range. Accordingly, the influence of the diffraction ($\sim 1/[1 + (v_{QLA}t/L_R)^2]^{1/2}$) on the depth of imaging was negligible.

Some experimental observations confirmed these considerations. In some lateral positions, the gaps between the OAT and the diamond anvil were filled by single crystals within the complete gaps. In one of these positions, the QLA wave with a BF of 26.85 GHz and $v_{LA} = 4\ 881$ m s^{-1} propagated from the OAT to the diamond anvil in 2.15 ns, thus providing the distance of 10.5 µm. During the propagation, the BO amplitude decreased by only 75%.

The observed Brillouin amplitude decay has been fitted by accounting for (i) the Gaussian temporal decay related to the coherence length of the probe laser pulses and (ii) the additional exponential temporal decay that could be potentially caused by unknown absorption of CAPs. The fitting method employed is detailed in the case of ceria imaging, thus to avoid repetition, the reader is referred to Sec. 3.4.2 for the details.
The optical absorption of the green probe light was not considered because it is known to be negligible at the evaluated coherence length. The fit results demonstrated that the contribution of the acoustic absorption in the observed decay of the Brillouin amplitude is negligible too and that the decay of the TDBS signal in single crystals of ice is controlled by the coherence length because we obtained the fitted values of $L_{probe}^{coherence} \simeq 13$ µm and $\tau_{probe} \simeq 125$ fs, consistent with the experimental pulse duration of the probe laser.
Thus, the depth of imaging was limited in our experiments by the sample thickness. We note that the application of lasers with pulses in the ps range, presently not commercially available for ASOPS although achievable from fs laser-based ASOPS systems with prisms or optical gratings, will allow a significant extension of the 3-D-imaging depth of the method, without any degradation of other imaging characteristics.

The 3-D imaging of the holistic H_2O ice sample using the STFT/SDT-based signal processing method allowed to identify the grains belonging to either phases of ice obtained at 2.15 GPa, at ambient temperature, in the DAC. Evolutions of the grains with depth were obtained with an axial resolution of 1.25 µm, and the complete ~ 10 µm thick sample was imaged with the QLA mode reconstruction.
In the next section, the WSST-based signal processing technique is applied to a cerium dioxyde polycrystalline sample, enhancing the axial resolution and thus allowing to resolve inclined boundaries between differently oriented grains.

3.4.2 Ceria: polycrystalline cerium dioxyde (CeO_2)

The sample studied is a cubic polycrystalline cerium dioxyde (or ceria) CeO_2 [3.20 (b)], with an optical refractive index $n = 2.37$ at the probe wavelength $\lambda_{probe} = 535$ nm. The refractive index has been estimated from the measurements (and is in good agreement with that reported in Ref. [156]) with a deduction based on the 3-D slowness surfaces of ceria. This material is optically isotropic and elastically anisotropic because of its cubic crystalline structure. Ceria thus provides a model material for demonstrating enhanced imaging using transverse acoustic waves, without the complication of optical birefringence.
In the case of birefringent materials, *i.e.*, optically anisotropic crystals, polarimetry measurements would be required to distinguish ordinary from extraordinary light contributions to the TDBS signal. Moreover, refraction of the probe light at the interface between differently oriented grains would modify the scattering efficiency in the deepest grain, while in the presented case there is no refraction of light at the interface. The refraction of probe light at inclined interfaces will be discussed in Chap. 4.

The sample was annealed at 1650 °C to promote grain growth (please refer to Ref. [87] and supplementary materials for details), the average grain size on the surface being ∼20 µm^2. The surface was coated by a 20 nm-thick gold layer to serve as an OAT. A focused ion beam was used to put down fiducial marks in order to locate specific area, for the TDBS scans to match the EBSD-characterised area [Fig. 3.19].

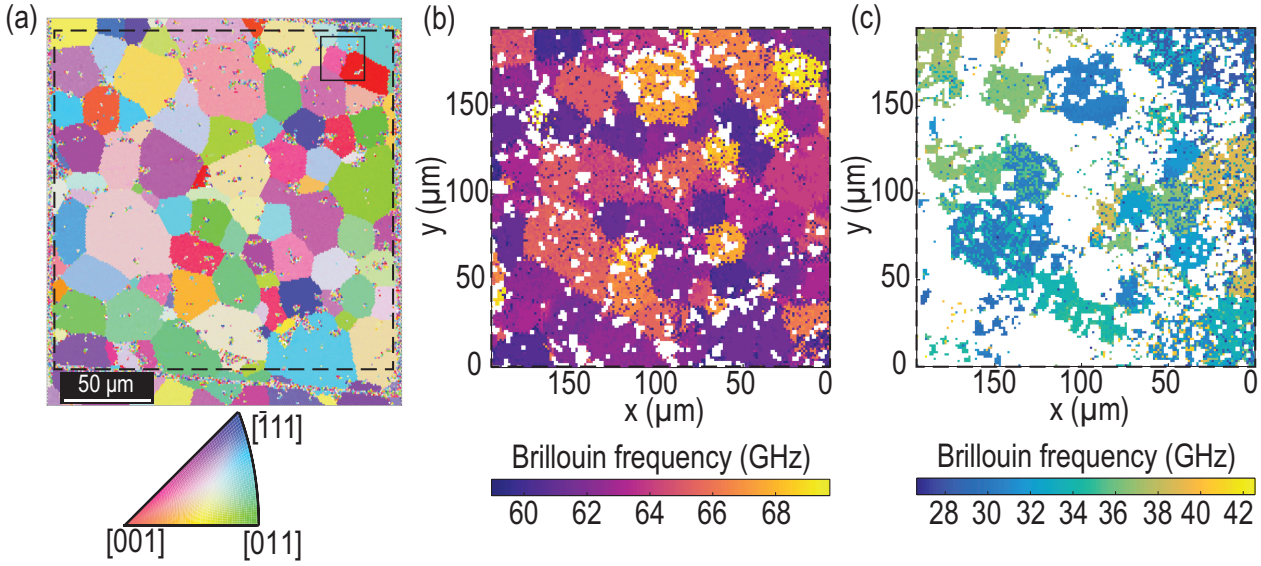

Figure 3.19 – Comparison of the EBSD pattern and the TDBS 2-D maps obtained on an identified area in ceria. (a) EBSD pattern of the surface of the ceria sample in an area identified with fiducial marks. The black squares highlights the nearly 200×200 µm^2 scan (dashed lines), and the 30×30 µm^2 more precise scan (solid lines) processed in Sec. 3.3. (b) TDBS scan of the same ceria area, obtained by looking at the strongest QLA frequency in the FT of the complete acoustic signals. (c) TDBS scan of the same ceria area, obtained by looking at the strongest QTA frequency in the FT of the complete acoustic signals.

To obtain the scans, the sample is placed on a translational stage and owing to the speed of a single-point measurements provided by NETA's ultrafast setup, a scan lasting less than five hours is realized on a 30×30 µm^2 zone, with a lateral resolution of 0.469 µm [Fig. 3.5]. A black solid line square in the EBSD pattern [Fig. 3.19 (a)] indicates the zone where this more precise scan was done. This ceria scan corresponds to the one used in Sec. 3.3 to illustrate the signal processing steps and from which the following discussed results have been obtained.

The grain (or crystallite) orientations can be obtained via the EBSD pattern, where the fiducial marks are visible [Fig. 3.19 (a)] and allows to locate specific grains. A good agreement is found between the 2-D maps of the TDBS scans, obtained by evaluating the strongest frequency peak in the BF intervals associated to the QLA mode [Fig. 3.19 (b)] and both QTA modes [Fig. 3.19 (c)]. White pixels area correspond to TDBS signals with too poor SNR to extract its frequency content, as explained in Sec. 3.3.1. Note that the QTA map [Fig. 3.19 (c)] contains less information compared to the QLA map since in general the QTA modes are harder to detect due to their lower amplitudes in the TDBS signals.

Slowness surfaces, expected BF intervals and refractive index determination

Similar to the study of the high-pressure ice sample (Sec. 3.4.1), the first step required for the interpretation of the imaging results is to determine the BF intervals expected in ceria. Hence, the same procedure is applied, *i.e.*, solving Christoffel's equation [Eq. (3.11)] using the density and the elastic constants of Tab. 3.3, in all possible propagation directions.

	ρ (g m^{-3})	C_{11} (GPa)	C_{12} (GPa)	C_{44} (GPa)
Ceria [87]	7.22	451	119	66

Table 3.3 – Elastic parameters of ceria [87] used to compute the 3-D slowness surfaces.

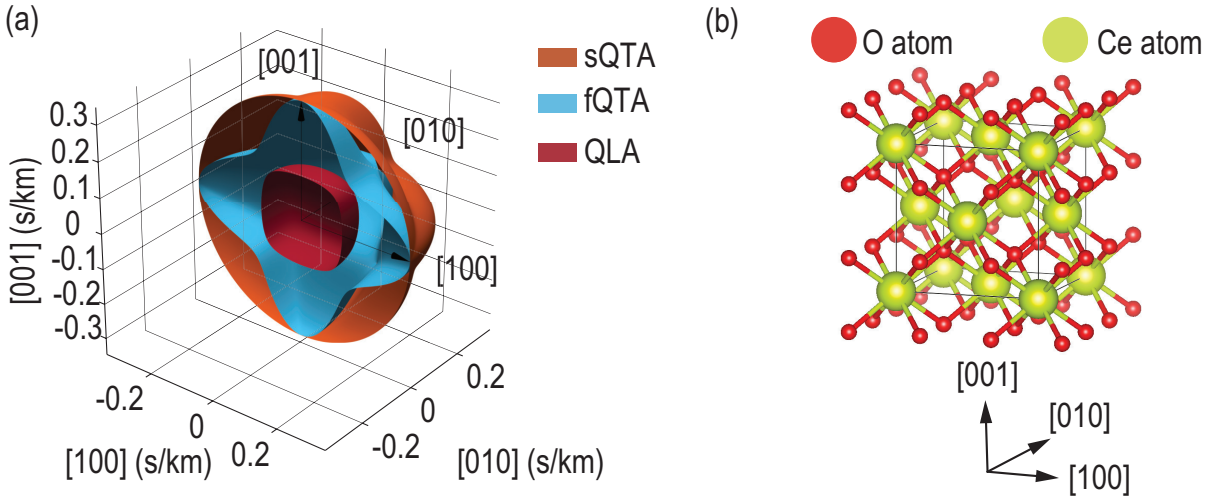

Figure 3.20 – Slowness surfaces and crystalline structure of the cerium dioxyde (CeO_2). (a) Slowness surfaces of the three possible acoustic modes in CeO_2. Half of the polar angles are represented to obtain the cross-sectional view. (b) Crystalline structure (cubic, space group m3m) obtained with Mercury 4.0 software [157].

The 3-D slowness (inverse of velocity) surfaces of the three modes are plotted in Fig. 3.20 (a), which shows how much faster the QLA mode (inside red surface) is, compared to both QTA ones. The slowness surfaces also depict that both QTA modes are more sensitive to changes in the propagation direction with respect to the crystal principal axes than the QLA mode. The expected BF for a specific orientation can then be deduced with Eq. (2.36), and the BF intervals in which each mode should be observed are obtained by applying Eq. (2.36) to their fastest and slowest velocities. These BF intervals of expected modes detection are given in Tab. 3.4. From the results of Tab. 3.4, transverse modes with frequencies falling in the common BF interval [26.79 - 37.97] GHz are labelled as QTA, while modes above this interval can be unambiguously labelled as fQTA modes. Determination of the optical refractive index n is made possible thanks to the detection of the three acoustic modes in a specific grain of the area

Acoustic mode	BF interval (GHz)
QLA	[58.77 - 70.02]
fQTA	[26.79 - 42.48]
sQTA	[26.79 - 37.97]

Table 3.4 – Expected BF intervals to be detected with TDBS in the case of ceria, for each acoustic mode.

scanned, located in the spatial interval x = [0, 5] µm, y = [20, 25] µm [grain 1/1A in Fig. 3.14 (a), (c) and (e)].

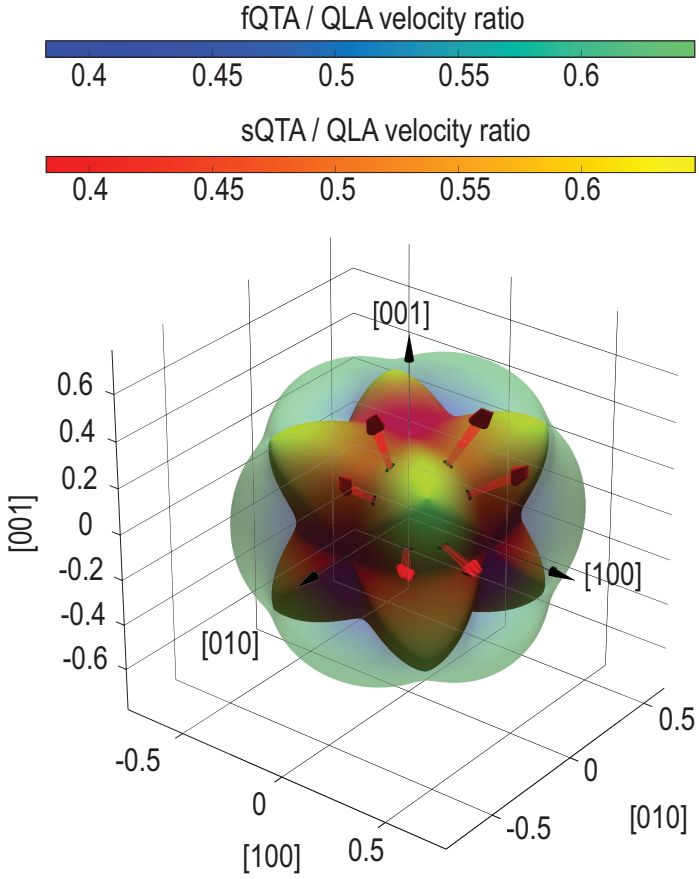

Figure 3.21 – 3-D "surfaces of transverse to longitudinal velocities ratio" in ceria for both QTA modes. The fQTA/QLA surface of velocity ratio is transparent for better visualization of the smaller-valued sQTA/QLA one. The possible orientations of grain 1A, in which the three acoustic modes are monitored, are represented by red arrows in one octant (1/8 of a sphere) of the surface. Due to symmetries in the cubic crystalline structure, six orientations with common velocity ratio are obtained, each of them composed of multiple arrows due to the uncertainties. Adapted from [8].

Indeed, from the slowness surfaces, it is possible to represent the two "surfaces of transverse to longitudinal velocities ratio" for both QTA modes [Fig. 3.21]. In Eq. (2.36), λ_{probe} and n are fixed, *i.e.*, they do

not vary with the propagation direction, thus the velocities ratio is equal to the BFs ratio. Therefore, it is possible to locate in the two "surface of transverse to longitudinal velocities ratio" the orientations associated to the BFs ratio obtained in the aforementioned grain 1/1A. Finally, by isolating n in Eq. (2.36) and assuming the mechanical properties reported in Tab. 3.3 to be good, the refractive index of our ceria sample can be estimated at the probe wavelength of the setup. The deduced refractive index values are given in Tab. 3.5, obtained with their associated uncertainties given by the frequency resolution of the WSST, as discussed in Sec. 3.3.3.

Acoustic mode	Frequency (GHz)	Ratio to QLA	Associated v ($\mathrm{m\,s^{-1}}$)	Deduced n
QLA	61.65 ± 0.47	/	6 958 ± 52	2.37 ± 0.04
fQTA	40.15 ± 0.3	0.6515 ± 0.01	4 537 ± 97	2.37 ± 0.07
sQTA	30.37 ± 0.23	0.4925 ± 0.008	3 428 ± 33	2.37 ± 0.03

Table 3.5 – Estimates of the optical refractive index n of the ceria sample.

Depth of imaging limitations

Grains 3-D imaging results obtained in Fig. 3.14 (a) appear to be imaged down to a depth of about 8 µm in the most favourable experimental situations. This limitation of the depth of imaging can be attributed to the coherence length of the probe laser beam, rather than other physical mechanisms such as the acoustic pulse attenuation or the probe laser beam diffraction. The part of the probe light that is scattered by the moving CAP looses progressively its coherence (it stops to overlap) with the part of the probe light being reflected by the stationary surfaces of the sample, as the scattering happens further away from the OAT/sample interface. To estimate the coherence length of the probe laser beam in our experimental configuration, one of the acoustic signal with the longest duration is selected (located at the position $x = 25.79$ µm and $y = 23.45$ µm of the scan) [Fig. 3.22 (a)]. The use of the WSST confirms the presence of a single, QLA mode in the WSST-based spectrogram of the signal, and permits the ridge extraction of this mode [Fig. 3.22 (b)]. Application of the IWSST to the extracted ridge reconstruct the QLA mode contribution (expect inside the cone of influence of the CWT) [black line in Fig. 3.22 (c)]. Finally, a sinusoid with Gaussian and exponential damping is fitted to it [red signal in Fig. 3.22 (c)]. The fitted model is given by:

$$A_{mod}\ \sin\left(2\pi\Delta f_{BO}^{LA} f_{BO}^{LA} t + \phi_{mod}\right) e^{-2\left(\frac{t}{\tau_c}\right)^2} e^{-\alpha_{ac} t}, \tag{3.14}$$

with A_{mod} the amplitude parameter, $f_{BO}^{LA} = 62.08$ GHz the BF of the QLA mode obtained with the mean value of the extracted ridge in the WSST of the signal [Fig. 3.22 (b)], Δf_{BO}^{LA} a non-dimensional parameter used in the fitting procedure to account for shifting of f_{BO}^{LA} due to the frequency resolution of the WSST, ϕ_{mod} the phase term, τ_c the coherence time of the probe laser pulse and α_{ac} the acoustic

Fitted parameters	Starting value	Lower bond	Upper bond	Value	95% confidence interval
A_{mod}	0.4	0	1	0.4060	[0.3976, 0.4144]
ϕ_{mod}	1	-π	π	1.7869	[1.7746, 1.7991]
τ_c	1	0	10	1.2405	[1.1982, 1.2828]
α_{ac}	1	0	10	0.0	[-0.0937, 0.0937]
Δf_{BO}^{LA}	1	0.8	1.2	0.9928	[0.9927, 0.9929]

Table 3.6 – Results of the sinusoid with Gaussian and exponential damping model [Eq. (3.14)] fitting to the long-lasting acoustic signal [Fig. 3.22 (c)].

absorption coefficient, of the signal. A nonlinear least-squares algorithm is used to estimate the best parameters to be fitted to the model of Eq. (3.14) (blue variables). The trust region reflective algorithm is used to fit the five parameters with constrained bounds, *i.e.*, maximum and minimum values to be looked at during the minimization process of the fitting. Doing so, reasonable values were obtained for all parameters except α_{ac} that converged to zero, its imposed lower bound. The results obtained with the starting values $A_{mod} = 0.2$, $\phi_{mod} = 1$, $\tau_c = 1$ are given in Tab. 3.6. From that, we can conclude that the damping effect is principally driven by the Gaussian damping, compared to the exponential one, and thus the coherence length effect is driving the amplitude decrease of the oscillations in the acoustic signal (and not the acoustic damping).

Estimation of the coherence time from the fitting gives $\tau_c = 1.24 \pm 0.042$ ns, the uncertainty being estimated with the 95% confidence interval of the fitting. Such a value can be checked from the relation between the coherence time and the duration of the probe laser pulse τ_{probe}:

$$\tau_{probe} = \frac{2 v_{LA} \tau_c}{c_0/n}, \tag{3.15}$$

with $v_{LA} = (f_{BO}^{LA} \Delta f_{BO} \lambda_{probe})/(2n) = 6\ 957\ \mathrm{m\,s^{-1}}$ the QLA mode velocity deduced from Eq. (2.36). The probe laser pulses duration is thus estimated as $\tau_{probe} = 136 \pm 4.6$ fs, close enough to the laser datasheet value $\tau_{probe} = 130$ fs. To finally estimate the coherence depth, one can either use the product of the coherence time τ_c by the QLA mode velocity v_{LA} used here for the fitting, giving $L_{coherence}^{probe} = 8.63 \pm 0.29$ µm, or use the estimated duration of the probe laser pulse τ_{probe} with:

$$L_{coherence}^{probe} = \frac{c_0 \tau_{probe}}{2n}. \tag{3.16}$$

From this second method, the estimated coherence penetration depth is $L_{coherence}^{probe} = 8.61 \pm 0.29$ µm, close to the previous estimate and in good agreement with the deepest reconstructed grains obtained in the 3-D images.

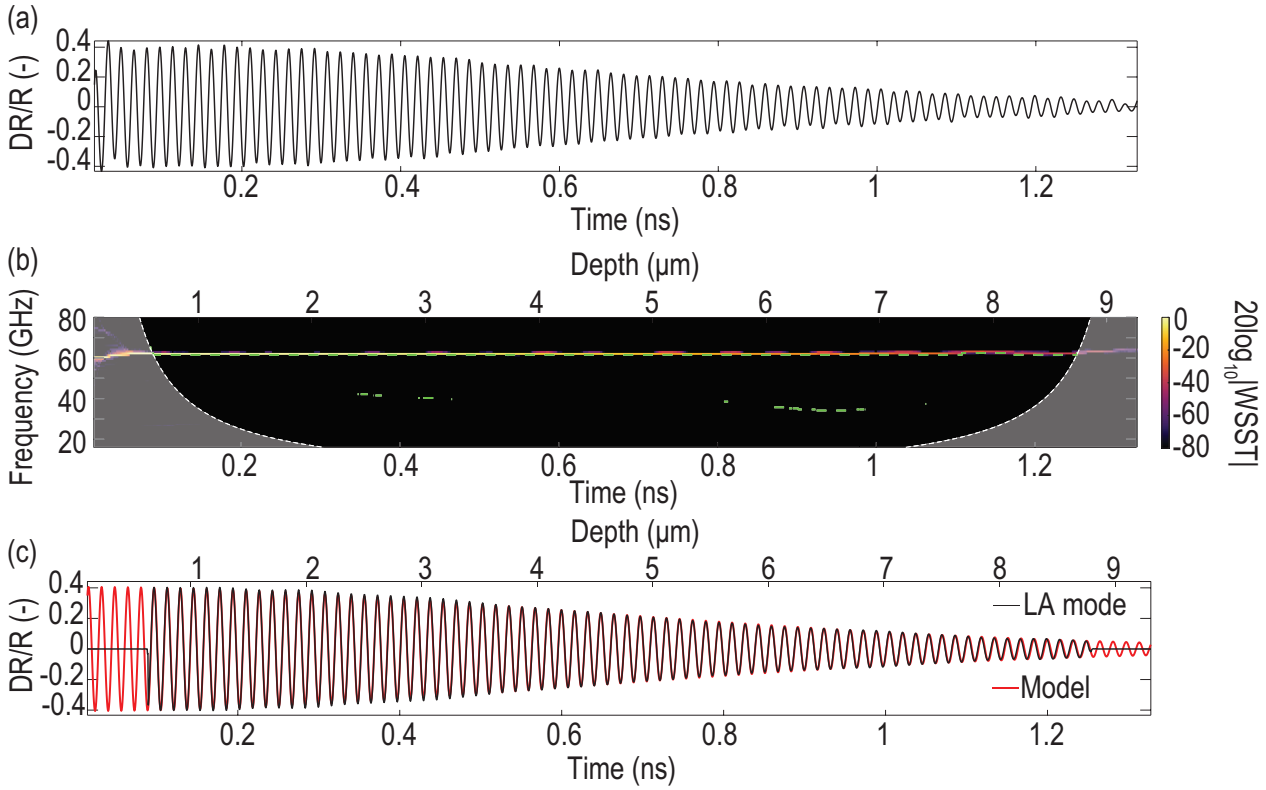

Figure 3.22 – (a) Acoustic signal located at coordinates $x = 25.79$ µm and $y = 23.45$ µm, studied for the depth of imaging estimates. (b) WSST-based spectrogram of the acoustic signal (a) with cone of influence (white dashed lines and shade) and extracted ridges (green dotted lines. A single mode is clearly evidenced here. (c) Comparison between the mode reconstructed by applying the IWSST to the QLA ridge extracted from the WSST-based spectrogram (b) (black solid line) and the results of the fitted model [Eq. (3.14)] (red solid line). Adapted from [8].

Imaging results enhanced with QTA modes detection

The signal shown in Fig. 3.9 offers insight into multi-component signals with BF in the QLA mode interval as well as in the QTA modes interval. The reconstruction of the temporal behavior [Fig. 3.9 (d) and (e)], and their changes with depth, associated to both acoustic modes gives the opportunity to extract complementary information used for the imaging. The boundary between two differently-oriented grains is evidenced by the two modes via two different physical mechanisms.

First, the QLA mode is subject to an upshifting of its BF [upper ridge in Fig. 3.9 (c), and Fig. 3.9 (d)] that can be attributed, following Eq. (2.36), to the increase of the QLA mode velocity due to its transmission to a differently-oriented grain.

In parallel, the QTA mode amplitude suddenly decreases to the noise level [lower ridge in Fig. 3.9 (c),

and Fig. 3.9 (e)] at the same corresponding depth ~ 3 µm at which the BF of the QLA mode is upshifted. This sudden drop in amplitude of the QTA mode after transmission into the second, subsurface grain is the signature of: either large angle, off-axis refraction of the QTA mode such that the interaction with the probe is vanishingly small, or small photoelastic coupling in the new grain with different orientation. In the specific case of the acoustic signal in Fig. 3.9 (e), the amplitude drop is associated with the

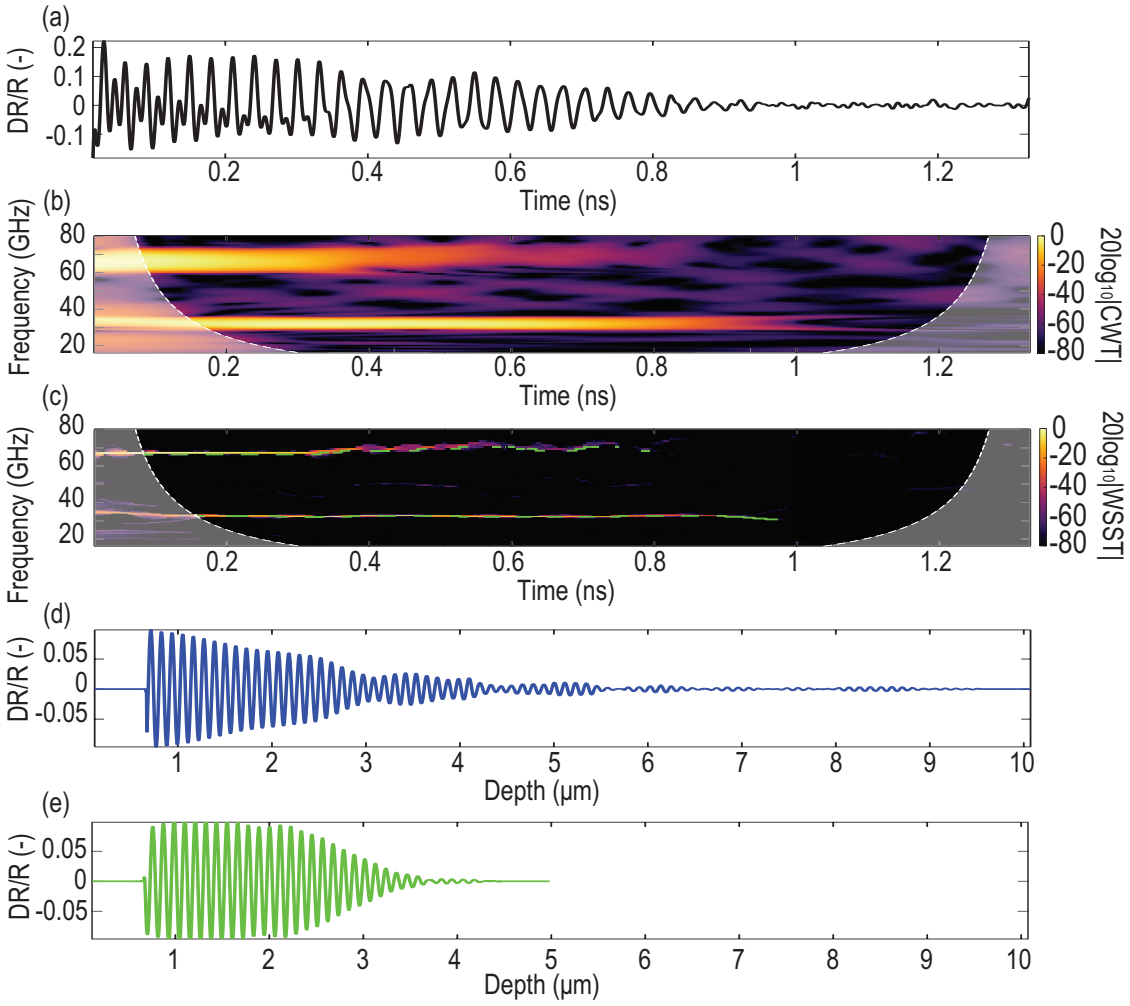

Figure 3.9 – **Note** that this figure is a reproduction of Fig. 3.9 brought back here for the comfort of the reader. Acoustic signal study using the WSST: spectrogram, ridge extraction and multi-mode reconstruction. (a) Acoustic signal located at coordinates $x = 9.37$ µm and $y = 11.72$ µm of the ceria scan. (b) CWT-based spectrogram $\left(20\log_{10}\left|\mathrm{CWT}\right|\right)$ of the acoustic signal (a), normalized by its maximum value. The cone of influence of the CWT is given by the white dashed curves and associated shadowed area from the edges of the signal. (c) Synchrosqueezed CWT-based spectrogram $\left(20\log_{10}\left|\mathrm{WSST}\right|\right)$ of the acoustic signal (a), normalized by its maximum value, and extracted ridges (green dashed lines). The same cone of influence as in the CWT is given by the white dashed curves and the shadowed area at the spectrogram edges. (d-e) Modes reconstructed from the extracted ridges using the IWSST: (d) mode reconstructed from the QLA mode (highest frequency component) contribution and (e) mode reconstructed from one QTA mode (lowest frequency component) contribution.

latter case, because the deepest grain has a [001] orientation and such an orientation preclude QTA mode detection.

The 4-D stacked, or slice-by-slice, representation [Fig. 3.10] obtained as an output of the slicing processing step [Sec. 3.3.2] offers a mode-by-mode view of the information of each extracted ridge, analagous to a loaf of slice bread. Looking to such representation from the top gives a view on the first few nanometers of the sample, *i.e.*, the gold-coated surface of the ceria sample [Fig. 3.23 (a-c)]. One can identify the different grains from their associated BF (colors), white zones being attributed to signals with no exploitable results (due to, as a reminder, photodiode saturation and/or amplitude of the associated WSST ridge below the -64 dB threshold defined previously).

The first layers of the reconstructed sample [Fig. 3.23 (a-c)] can be directly compared to the EBSD pattern of the same scanned area. The localization of the previously analyzed signals are represented, on this top views, as a green star [Fig. 3.22] and a red circle [Fig. 3.9].

Imaging results [Fig. 3.23 (e-g)], output of the shaping processing step [Sec. 3.3.3], reconstruct the 3-D boundaries of the grains detected by each modes: the QLA mode [Fig. 3.23 (e)] brings out three mains grains (1/purple, 2/orange and 3/yellow), while the fQTA and QTA mode intervals identifies smaller ones inside these main "QLA" grains. The fQTA mode [Fig. 3.23 (f)] dismantles the 1/purple grain into three smaller ones: 1A/white, 1B/pink and a third one, 1C, that is evidenced thanks to the absence of detection of the fQTA mode. The QTA modes [Fig. 3.23 (g)], similarly, dismantles the 2/orange grain into three smaller ones: 2A/green, 2B/yellow and a third one, 2C, depicted by the absence of QTA modes in it.

Moreover, part of the 1A grain is reconstructed also with the QTA mode as 1A/blue [Fig. 3.23 (g)]. This grain presents the peculiarity of being imaged by the three acoustic modes: QLA (a)-(e), fQTA (b)-(f) and sQTA (c)-(g) [Fig. 3.23]. This grain allowed to estimate, at the beginning of this section, the optical refractive index n of the ceria sample at our working probe wavelength λ_{probe}, and offers the possibility to estimate its crystalline orientation in the laboratory frame [158, 159]. The z-axis (depth) scales are enlarged for better visualization, the ratio between the z-axis and the x- and y-axes are 1/6 in Fig. 3.23 (e) and 1/12 in Fig. 3.23 (f-g).

The use of the alphashape algorithm [Sec. 3.3.3] offers the possibility to estimate the volume of the reconstructed grains [Tab. 3.7]. The uncertainties are obtained using the definition of the alphashape: the radius of the sphere used to shape the voxels clouds is $\alpha^{shape} = 1$ µm thus the volume uncertainty is linked to the volume of the corresponding sphere of radius 1 µm.

When detected, the stronger sensitivity to anisotropy of the QTA modes offers an imaging contrast that was not achieved by monitoring the QLA mode, as evidenced by the upper part of Fig. 3.23 (a-c). Looking to the first slices of the processing, the QLA mode results [Fig. 3.23 (a)] seem to indicate the presence of three main grains in the scanned area, at the gold OAT/CeO_2 interface. The same processing applied to the fQTA and QTA modes leads to a new interpretation of the QLA mode results, highlighting the presence of smaller grains: the QLA purple grain in Fig. 3.23 (a) is in fact composed of three grains,

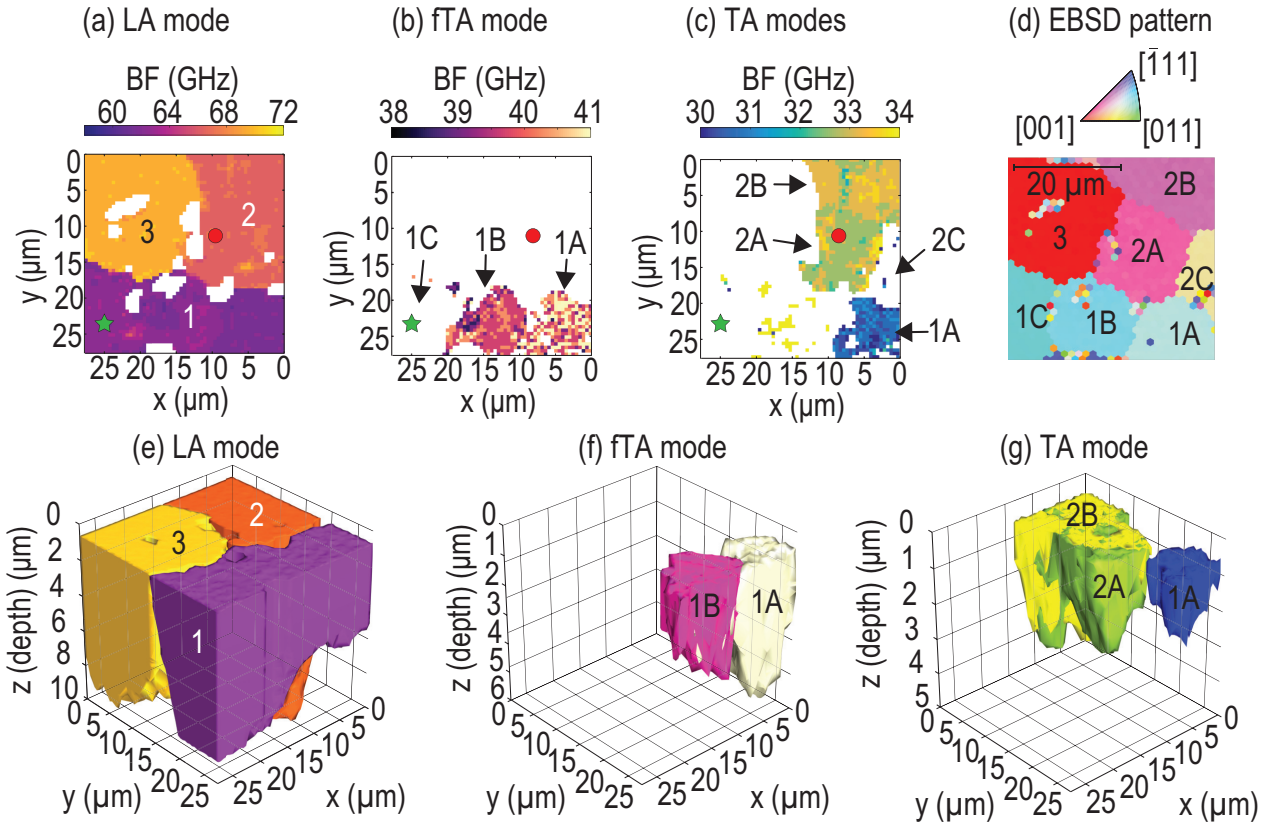

Figure 3.23 – Imaging results of the ceria scan. (a-c) Upper view (OAT/ceria interface) of the 4-D stacked representations (slicing step output) for each BF interval [Tab. 3.4]: (a) QLA mode, (b) fQTA mode and (c) QTA modes. (d) EBSD pattern of the same scanned area, showing good agreement with (a-c). The position of the previously analyzed signals are represented by a green star [Fig. 3.22] and a red circle [Fig. 3.9]. (e-g) 3-D alphashape representations of the associated (color and order) BF intervals (a-c). The alphashape results evidence the reconstitution of 3 grains (1/purple, 2/orange, 3/yellow) with the QLA mode (e), 2 grains (1A/white, 1B/pink) with the fQTA mode (f) and 3 grains (1A/blue, 2A/green and 2B/yellow) with the QTA modes (g). Adapted from [8].

two of them being evidenced by the fQTA mode results [Fig. 3.23 (b)], and one of the two being also imaged by monitoring the sQTA mode propagation [3.23 (c)].

Another example of the imaging enhancement permitted by QTA modes detection is given in Fig. 3.23 (c), where two grains, 2A and 2B, that were originally imaged as one grain on the QLA mode results [Fig. 3.23 (a)], with close, but different, BF of a QTA mode, are pictured in green and yellow. One can also deduce the presence of a third grain, 2C, located in the scan interval $x = [0, 5]$ µm and $y = [10, 20]$ µm, not detected in the QTA representation [white area in Fig. 3.23 (c)], and included in the 2/orange grain on the QLA mode results [Fig. 3.23 (a)].

Finally, thanks to the additional information obtained with the QTA modes, a complete view of the ceria polycrystal is achieved by TDBS and is in a very good agreement with the EBSD pattern measured on the surface of the sample [Fig. 3.23 (d)]. The imaging contrast provided by the QTA modes leads to the detection of the same number of grains as the EBSD pattern.

LA grains	Volume (± 4.2 µm^3)
1 (purple)	1 480
2 (orange)	1 267
3 (yellow)	1 807
fQTA grains	**Volume (± 4.2 µm^3)**
1A (white)	252
1B (pink)	173
TA grains	**Volume (± 4.2 µm^3)**
1A (blue)	77
2A (green)	252
2B (yellow)	292

Table 3.7 – Volume estimates of the alphashape-reconstructed grains.

The extension of these observations from the OAT vicinity to the depth of the grains, with the 3-D alphashape results shown in Fig. 3.23 (e-g), presents the evolution of the grains boundaries with depth. The 3-D representation obtained with the QLA mode sheds some light on a small grain appearing only in the depth of the sample (from 6 to 8 µm deep), below the 1/purple one, with a BF close to the interval of the 2/orange grain hence coloured in orange too [Fig. 3.23 (e)]. Such deep transition from one grain to another, not visible using electron microscopy without destructive serial section, highlights the capacity of the TDBS technique to image grain microstructure nondestructively in 3-D.

Buried inclined interface

The 3-D alphashape results [Fig. 3.23 (e-g)] appear as a suitable representation to locate buried inclined interfaces between differently oriented grains. One such surface is found to be between the orange (upper) and yellow (lower) grains of the QLA mode alphashape [Fig. 3.23 (e)], located in the center of the scanned area and between 2 to 3 µm deep. Evidenced by both the QLA and one QTA mode, the inclination of this interface can be assessed by following the behaviour of the TDBS signals in the vicinity of this area, one of the signal being represented and studied in Fig. 3.9. As already mentioned, such signals are sensitive to the crossing of the interface by the acoustic pulse and are evidenced by the frequency shifting of the QLA mode, and the amplitude drop to the noise level of the QTA mode.

A representation of the buried surface at which the frequency shifting in the QLA mode occurs is shown

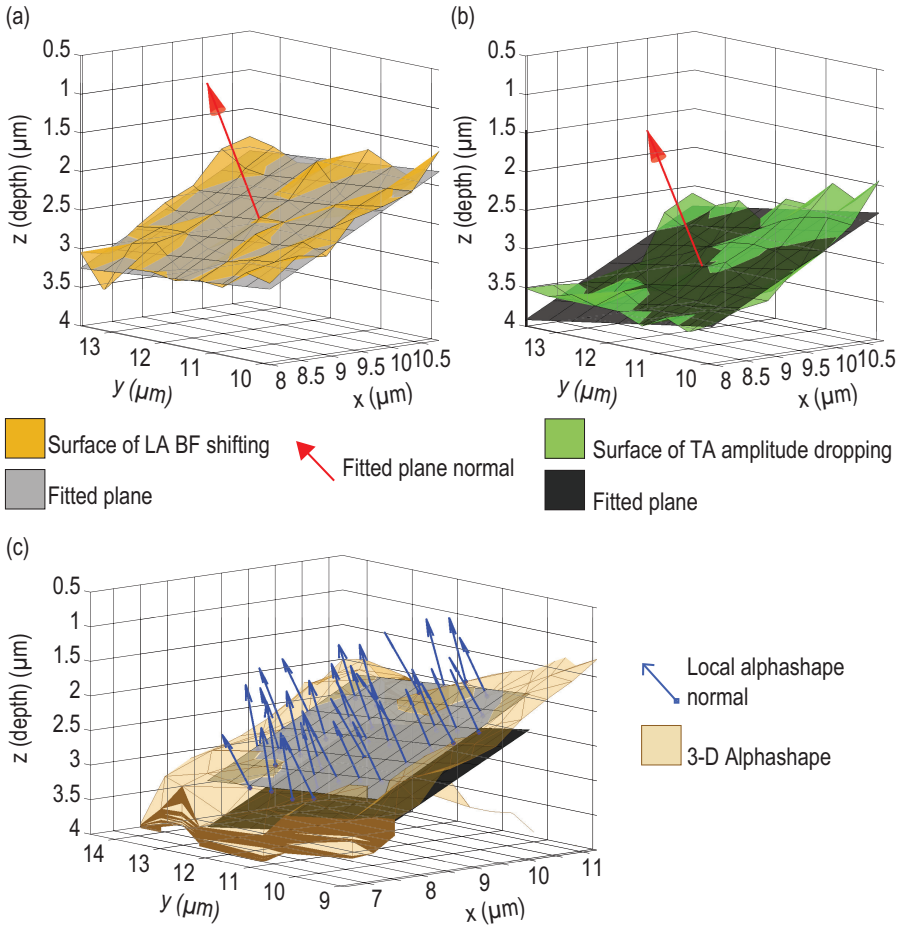

Figure 3.24 – Inclined buried interface between differently oriented grains [8]. (a) Surface of frequency shifting of the QLA mode (orange surface) and best (least mean square) fitted plane (grey plane). (b) Surface of amplitude drop below the -64 dB threshold of the QTA modes in the ridges extracted from the WSST-based spectrogram (green surface), and best (least mean square) fitted plane (black plane). The red arrows depict the outward normal of the fitted plane used to estimate the mean inclination angle of the surface. (c) Comparison of the alphashape results obtained with the QLA mode (yellow triangle mesh), and the two fitted planes of (a-b). The blue arrows, with a square base, highlights the local normals used to estimate the averaged angle over the alphashape region.

in Fig. 3.24 (a). Similarly, a representation of the buried surface at which the amplitude drops for the QTA mode is shown in Fig. 3.24 (b). Note that the absolute depth at which the buried surface is found from QLA and QTA modes are slightly shifted (of about 0.5 µm which is less than the axial resolution), due to the blind zone in the first ps of the temporal signals, while this is not influencing the inclination angle recovery. Fitting the least-mean-square plane to each surface gives access to a plane from which the mean inclination angle (with respect to the gold OAT, $z = 0$ µm plane) is estimated via its outward normal. Results obtained from the frequency shifting of the QLA mode [Fig. 3.24 (a)] gives an inclination angle of 23.3°, and from the amplitude drop of the QTA mode [Fig. 3.24 (b)] gives 23.2°.

Comparisons of the alphashape result of the lower grain of the interface, with the fitted planes shown in Figs. 3.24 (a-b) is shown in Fig. 3.24 (c). A good agreement between the inclinations of the fitted planes and the actual alphashape is obtained. The local normals of the alphashape-constructed triangle mesh of the same area are computed [blue arrows in Fig. 3.24 (c)] and the averaged angle between these local normals and the gold OAT gives a 23.8 ° inclined interface. Hence a good agreement between the fitted planes to the QLA and QTA modes surfaces, and the alphashape reconstruction, allows estimation of the inclination of this interface to be of about 23.5 ± 0.5 ° with respect to the $z = 0$ µm plane.
On a final note, the situation when a CAP is incident on an inclined boundary between differently oriented grains, leads to the reflection and transmission of the CAP (and not of the probe light due to the optical isotropy of ceria), and could lead to the mode-conversion of the incident CAP into up to three reflected and three transmitted CAPs with different polarizations [9] (see Chap. 4 for more details). However, for the interface inclinations observed in the ceria scan, the propagation directions of the reflected CAPs deviate more importantly than the directions of the transmitted CAPs, in comparison with the most efficient detection direction, *i.e.*, the propagation direction of the probe light. The reason of these detection reductions, studied in details in Chap. 4, is linked to the efficiency of the light scattering by the CAP (acousto-optic interaction, Sec. 2.3), being reduced due to the deviation from the momentum conservation law of the photon-phonon interaction. This deviation from the optimal scattering geometry results in the weakening of the scattering of the probe light and thus of the heterodyne detection, causing a diminution of the amplitude of the TDBS signal. Thus, an abrupt decrease to the noise level of the contribution to the TDBS signal from the reflected CAP is owing to its deviation (which is about 2θ in weakly elastically anisotropic crystals like ceria, where θ stands for the angle between the normal of the surface and the incident CAP propagation direction) from the propagation direction of the probe light. On the other hand, the contribution from the transmitted CAP is "only" weakened for the discussed small angles. Considering small angles results in significantly smaller refraction angles of the CAP in comparison with the reflection angles. Because of the low elastic anisotropy of ceria, its Zener ratio being $a_r = 2C_{44}/(C_{11} - C_{12}) = 0.4$ [87], the contribution to the TDBS signal of the mode-converted transmitted CAP is considered confined to the contribution of the transmitted QLA mode only. On one hand, low anisotropy could lead to weak mode-conversion and, on another hand, the resulting transmitted QTA waves would be composed in minority of a longitudinal component (which is the component efficiently scattering the probe light for the heterodyne detection), and in majority of transversal components, efficiently depolarizing the probe light (thus precluding it for being detected). It has been thus considered, for the results obtained in this ceria scan, that the contributions to the TDBS signal of the mode-converted reflected and the transmitted QTA waves, are too small to be accounted for, even though they are existing.
Extension of this work to the situations where more care is needed to consider the contribution from the incident, reflected and transmitted CAP at such an inclined interface, is presented in the final chapter of this manuscript, Chap. 4.

3.5 Conclusion

In conclusion, a step-by-step signal processing method has been developed to process the TDBS scans obtained with the ultrafast ASOPS-based experimental setup, in order to represent and study the 3-D geometry of transparent polycrystalline material. The imaging system allows fast raster-scan of the samples surface thanks to an electronic control of the laser sources repetition rates, with a lateral resolution of the micrometer scale, comparable with both pump and probe laser beam radii. The processing of the signals is done in three main steps: (i) the filtering allows to extract the acoustic content from the raw transient reflectivity signals recorded during the scan, (ii) the slicing permits the evaluation of the time-frequency content in the acoustic signals with precision, leading to 4-D representation of the frequency content of the scan for each acoustic mode, and (iii) the shaping takes the results of step (ii) and estimates the number of grains in the 4D dataset via segmentation methods before relying on the alphashape algorithm to recreate a final 3-D volumetric representation of the grains forming the sample. Two main slicing methods have been developed. A first one, based on the use of the short-time Fourier transform (STFT) and a synchronous detection technique (SDT) has been applied to a scan performed in a high pressure water ice sample. The H_2O ice sample was obtained at ambient temperature by compressing it to GPa pressure levels in a diamond anvil cell (DAC) where coexistence of two phases of ice was observed. The second slicing method, based on a powerful time-frequency reassignment algorithm, the wavelet synchrosqueezed transform (WSST), has been used to process a scan obtained in a transparent cerium dioxyde (CeO_2) polycrystal. An accurate 3-D image of the grains and their respective boundaries has been obtained down to 8 µm depth with an axial resolution of 0.75 µm. Grain boundaries identification has been enhanced by the detection of transverse acoustic modes, and the angle of a buried interface between two differently oriented grains has been estimated to be about 23.5° from the images obtained with the QLA and one QTA modes.

Yet, the study of the refraction of the CAP at the surface of a grain/material interface, inclined relative to the propagation direction of the probe laser beam, was reduced to the contribution of the quasi-longitudinal part of the transmitted CAP. The next and final chapter of this Ph.D. thesis aims to present ongoing work on the physics of TDBS detection at such interfaces, inclined relative to the propagation direction of the incident CAP, and the probe laser beam.

Chapter 4

Theory of TDBS scattering by CAPs near material interfaces

Contents

4.1 Introduction

In the second Chapter of this manuscript [Sec. 2.3], the theory of propagating CAPs detection with TDBS in transparent materials has been developed. The most typical situation is presented for the reflection configuration, where the probe light beam and the thermoelastically generated CAP are collinear and propagating in the same direction. The TDBS signal was shown to result from the heterodyne detection on a photodetector of the part of the probe light that is reflected by the (fixed) surfaces of the sample studied, and the part of the probe light that is scattered (via the acousto-optic interaction) by the (moving) volume of the CAP.

For most of the TDBS experiments (see Refs. [77, 79, 88] for examples), the theoretical descriptions obtained for collinear (anti-collinear) plane probe light and CAP propagations [Eq. (2.34)] are sufficient to interpret the experimental signals and extract the parameters of single-layer [like material (1) in Fig. 4.1] or multi-layered samples continuously structured or not along the propagation direction axis.

In the situation described in this final Chapter, the collinearity between the probe light beam propagation direction and the CAP propagation direction is broken, and the aim is to estimate theoretically the consequences of this non-collinear propagation in the resulting recorded TDBS signals. Such situation has been observed experimentally in recent TDBS imaging of transparent polycrystalline material [7, 86, 87, 102], and in the ceria scan [Sec. 3.4.2] [8], where a buried inclined interface, *i.e.*, non-parallel to the OAT surface where the CAP was launched, causes the reflection and refraction (upon transmission) of the CAP, but not of the probe laser beam (due to the optical isotropy of ceria).

The reflection and refraction of the CAPs at sub-surface boundaries is accompanied by characteristic changes in the TDBS signal amplitude and/or frequency. When the CAP encounter a material interface that is inclined relative to its propagation direction, the transmission and reflection at this interface induce a change in the CAP propagation direction. This extension of the TDBS theory aims to account for the interaction of probe light beam and CAP propagating with a relative angle between their propagation directions.

A first section is dedicated to the description of the expected TDBS signal when a CAP, regardless of its generation origin, is interacting with a classically oriented (normal to the OAT surface) probe light beam, with different propagation direction. The second section proposes a more experimentally-relevant configuration where both the probe light beam and the CAP are propagating collinearly until reaching an inclined interface between two elastically different materials (but optically equivalent, exactly like two differently oriented grains in ceria). The contribution to the TDBS signal arising from the incident, reflected and transmitted CAPs are evaluated as a function of the interface inclination angle. Finally, preliminary attempts in exploiting the developed theory to retrieve the inclination angle of a material interface with experimental TDBS measurements are presented.

4.2 Non-collinear interaction of CAP and light beams in free space

The situation studied in this first section is illustrated in Fig. 4.1 where the CAP is propagating in a direction inclined relative to the probe beam propagation direction, in a homogeneous isotropic material denoted (1), while the surrounding media (air) is denoted (0). Both probe light beam and CAP are propagating along the z and z' directions, respectively, while α denotes the relative angle between their propagation directions.

The results are derived under the highly relevant assumption of Gaussian pump and probe laser beams [160]. The Gaussian distribution of both light fields at the focus ($z = 0$) is defined by Eq. (3.1) (with their respectives radii: a_{probe} and a_{CAP}). The transverse distribution of strain in the CAP is assumed to be replicating the cross-sectionnal (xy plane) Gaussian distribution of the pump laser beam, at the focus on the OAT [40, 110]. Hence the associated strain pulse $\eta(t, x, y, z)$ takes the form of a directional Gaussian beam, considered in the distances shorter than the diffraction length, referred in the following as the CAP beam.

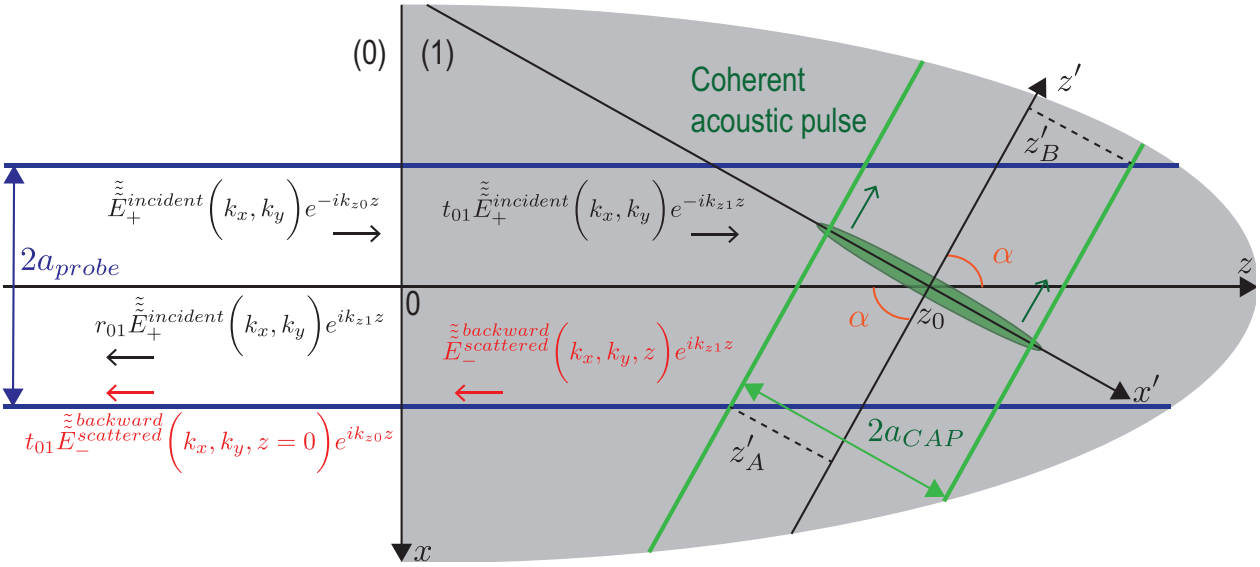

Figure 4.1 – Schematic of the TDBS monitoring by the probe light beam (radius a_{probe}) of the CAP beam (radius a_{cap}) propagating at an angle α relatively to the probe light path direction. The axes of these two Gaussian beams are in the figure plane and intersect at the point of coordinates ($x = 0$, $y = 0$, $z = z_0$).

In agreement with the notations introduced in Fig. 4.1, the description of the CAP beam in the (x', y', z') and the (x, y, z) coordinate systems are:

$$\eta\left(t, x', y', z'\right) = \eta_0 e^{-2\frac{x'^2+y'^2}{a_{CAP}^2}-2\frac{(z'-v_1 t)^2}{l_{CAP}^2}}, \tag{4.1}$$

and

$$\eta(t,x,y,z)=\eta_0 e^{-2\frac{[x\cos\alpha+(z-z_0)\sin\alpha]^2+y'^2}{a_{CAP}^2}-2\frac{[(z-z_0)\cos\alpha-x\sin\alpha-v_1 t]^2}{l_{CAP}^2}}, \tag{4.2}$$

respectively. In Eqs. (4.1) and (4.2), a_{CAP} and l_{CAP} denote the radius of the Gaussian CAP beam and the half-length of the unipolar Gaussian strain pulse, both defined at the $1/e^2$ level, η_0 is the magnitude of the strain pulse, v_1 stands for the velocity of the longitudinal acoustic wave in material (1), and z_0 denotes the z coordinate of the central rays intersection of the probe light beam and the CAP beam.
In Sec. 2.3, the three dimensional probe light electrical field was decomposed into plane waves [Eqs. (2.16) and (2.17)], and the energy of the light collected by the photodetector was considered to be composed of three components [Eq. (2.27)]: $W^{reflected}$ the energy of the light reflected by the sample (even in the absence of propagating CAP), $W^{scattered}$ the energy of the probe light scattered by the CAP and $W^{heterodyned}$ the energy of the mixing between the reflected and scattered light components. The heterodyned contribution has been derived, under experimentally relevant assumptions (transparency of material (1), paraxial and non-diffracting probe laser beam) leading to Eq. (2.33). Inside the Rayleigh range of the probe light field, the theoretical formula Eq. (2.33) is valid for an arbitrary strain CAP $\eta(t,x,y,z)$ localized inside the material (1), without straining the surface $z=0$. Since the TDBS reflectivity signal has been defined as the ratio between the heterodyned [Eq. (2.34)] and the reflected [deduced from Eqs. (2.17) and (2.27)] contributions on the photodetector, then the TDBS signal writes:

$$\frac{\Delta R}{R}=P\frac{\int\int\int_{-\infty}^{+\infty}\mathrm{d}x\mathrm{d}y\mathrm{d}z\eta(t,x,y,z)\,I_+^{incident}(x,y,0)\sin(2k_1 z)}{\int\int_{-\infty}^{+\infty}\mathrm{d}x\mathrm{d}y I_+^{incident}(x,y,0)}, \tag{4.3}$$

with the following compact notation: $P\equiv\dfrac{k_1 n_1^2 p_1}{(2\pi)^2}r_{01}(1-r_{01}^2)$.
From the definition of the probe light electrical field Gaussian distribution [Eq. (3.1)], Eq. (4.3) takes the form:

$$\frac{\Delta R}{R}=\left(\frac{2}{\pi a_{probe}^2}\right)P\int\int\int_{-\infty}^{+\infty}\mathrm{d}x\mathrm{d}y\mathrm{d}z e^{-2\frac{x^2+y^2}{a_{probe}^2}}\eta(t,x,y,z)\sin(2k_1 z). \tag{4.4}$$

Finally, the description of the CAP beam [Eq. (4.2)] is included in Eq. (4.4) and the integrations are

done [161]:

$$\frac{\Delta R}{R} = \sqrt{\frac{\pi}{2}} P \left[\frac{\eta_0 a_{CAP}^2 l_{CAP}}{\sqrt{a_{probe}^2 + a_{CAP}^2} + \sqrt{a_{probe}^2 + a_{CAP}^2 \cos^2\alpha + l_{CAP}^2 \sin^2\alpha}} \right] \left[e^{\frac{-k_1^2}{2} \frac{\left(a_{CAP}^2 l_{CAP}^2 + a_{probe}^2 l_{CAP}^2 \cos^2\alpha + a_{probe}^2 a_{CAP}^2 \sin^2\alpha\right)}{\left(a_{probe}^2 + a_{CAP}^2 \cos^2\alpha + l_{CAP}^2 \sin^2\alpha\right)}} \right]$$

$$\times\ e^{-2 \frac{\sin^2\alpha (v_1 t)^2}{\left(a_{probe}^2 + a_{CAP}^2 \cos^2\alpha + l_{CAP}^2 \sin^2\alpha\right)}} \sin\left(\omega_B \left[\frac{\left(a_{probe}^2 + a_{CAP}^2\right)\cos\alpha}{\left(a_{probe}^2 + a_{CAP}^2 \cos^2\alpha + l_{CAP}^2 \sin^2\alpha\right)} t + \frac{z_0}{v_1} \right] \right), \tag{4.5}$$

with, reminded here from Eq. (2.36): $\omega_B = 2k_1 v_1$.

The resulting Eq. (4.5) predicts the TDBS signal to take a wave packet form with an envelope described by $\exp\left[\left(-t^2\right)/\tau_B^2\right]$, where τ_B is the wave packet duration. This duration corresponds to the propagation time of the CAP at velocity v_1 across the overlap volume length l_B of the probe light and the CAP along the z' direction. Hence, $\tau_B = l_B/v_1$ with:

$$l_B = \sqrt{\left(\frac{a_{probe}}{\sin\alpha}\right)^2 + \left(\frac{a_{CAP}}{\tan\alpha}\right)^2 + l_{CAP}^2}. \tag{4.6}$$

In Eq. (4.6), the third term under the square root is related to the CAP half-length, while the first two terms arise from the contribution of the probe light and CAP beams cross-sections to the projection of the overlap volume length on the z' axis, with z'_A and z'_B in Fig. 4.1 defined as:

$$\frac{1}{2}(z'_B - z'_A) = \frac{a_{probe}}{\sin\alpha} + \frac{a_{CAP}}{\tan\alpha}. \tag{4.7}$$

The monochromatic sinusoidal carrier in the TDBS wave packet [Eq. (4.5)] oscillates at the frequency:

$$\Omega_B = \omega_B \frac{\left(a_{probe}^2 + a_{CAP}^2\right)\cos\alpha}{\left(a_{probe}^2 + a_{CAP}^2 \cos^2\alpha + l_{CAP}^2 \sin^2\alpha\right)} = \omega_B \frac{\left(a_{probe}^2 + a_{CAP}^2\right)\cos\alpha}{l_B^2 \sin^2\alpha}, \tag{4.8}$$

deviating from the 180° backward-scattering Brillouin frequency case derived in Sec. 2.3 [Eq. (2.36)], where $\Omega_B(\alpha = 0) = \omega_B = 2k_1 v_1$.

If we consider a plane probe light wave and a plane CAP ($a_{probe} = +\infty$, $a_{CAP} = +\infty$), the carrier frequency Ω_B is equal to $\Omega_B = \omega_B \cos\alpha$, *i.e.*, the Brillouin frequency shift that is expected from the momentum conservation law in the photon-phonon interaction, in backward non-collinear light scattering [85, 129, 162].

When considering finite cross sections probe light and CAP, the carrier frequency is different from this expected Brillouin frequency shift. The frequency Ω_B of the TDBS signal wave packet [Eq. (4.5)] depends on the optical and acoustical beams interaction angle α, the widths of the beams, and even the length of

the CAP. The reason of this difference is found in two facts (in the geometry considered here): (i) the plane acoustic and light waves composing the corresponding beams are propagating in various directions, and (ii) the heterodyning detection is potentially sensitive to the light scattered in various directions by the multiple-direction plane waves composing the CAP beam. Thus, the revealed carrier frequency is a result of an averaging over all possible interactions between these acoustic and light planes waves providing gatherable light for the photodetector.

In the following, a normalization by the CAP beam radius a_{CAP} of the different spatial variable is introduced. The evolution of the normalized overlap volume length

$$\bar{l}_B = \sqrt{\left(\frac{\bar{a}_{probe}}{\sin\alpha}\right)^2 + \left(\frac{1}{\tan\alpha}\right)^2 + \bar{l}_{CAP}^2}, \tag{4.9}$$

and the normalized carrier frequency

$$\bar{\Omega}_B = \frac{(1+\bar{a}_{probe})\cos\alpha}{\cos^2\alpha + \bar{l}_{CAP}^2\sin^2\alpha + \bar{a}_{probe}^2}, \tag{4.10}$$

of the TDBS signal [Eq. (4.5)] are represented in Figs. 4.2 and 4.3 as a function of the interaction angle α and the normalized probe light beam radius (or also mentioned as radii ratio) $\bar{a}_{probe} = a_{probe}/a_{CAP}$, for three different normalized CAP half-length values $\bar{l}_{CAP} = l_{CAP}/a_{CAP}$.

Taking into account a finite CAP half-length results in the diminishing of the overlap volume length $\bar{l}_B$, down to zero for $\alpha = \pi/2$ and small radii ratio [Fig. 4.2 (a-b)], as well as the diminishing of the maximal carrier frequency Ω_B^{max} [Fig. 4.2 (c-e)]. Coherently, the overlap volume length $\bar{l}_B$ grows with increasing radii ratio $\bar{a}_{probe}$ and decreasing interaction angle α.

The most interesting result comes from the evolution of the carrier frequency $\bar{\Omega}_B$: two regimes are evidenced [Fig. 4.3 (a-b)], split by a line (the geometric separator) obtained for $\bar{a}_{probe}^2 + 2\bar{l}_{CAP}^2 = 1$ [blue line in Fig. 4.2 (c-e)].

The analysis demonstrates that for $\bar{a}_{probe}^2 + 2\bar{l}_{CAP}^2 > 1$ [Fig. 4.3 (a)], the normalized (by its non-shifted value ω_B in the collinear probe and CAP situation $\alpha = 0°$) carrier frequency $\bar{\Omega}_B(\alpha) = \Omega_B(\alpha)/\omega_B$ is only decreasing. In Fig. 4.2 (e), $\bar{l}_{CAP} = 1$, the asymptotic case when $a_{CAP} \ll a_{probe}$ (common in picosecond acoustic experiments) is obtained: $\bar{\Omega}_B = \omega_B \cos\alpha$, independently from the value of the beam radii ratio $\bar{a}_{probe}$.

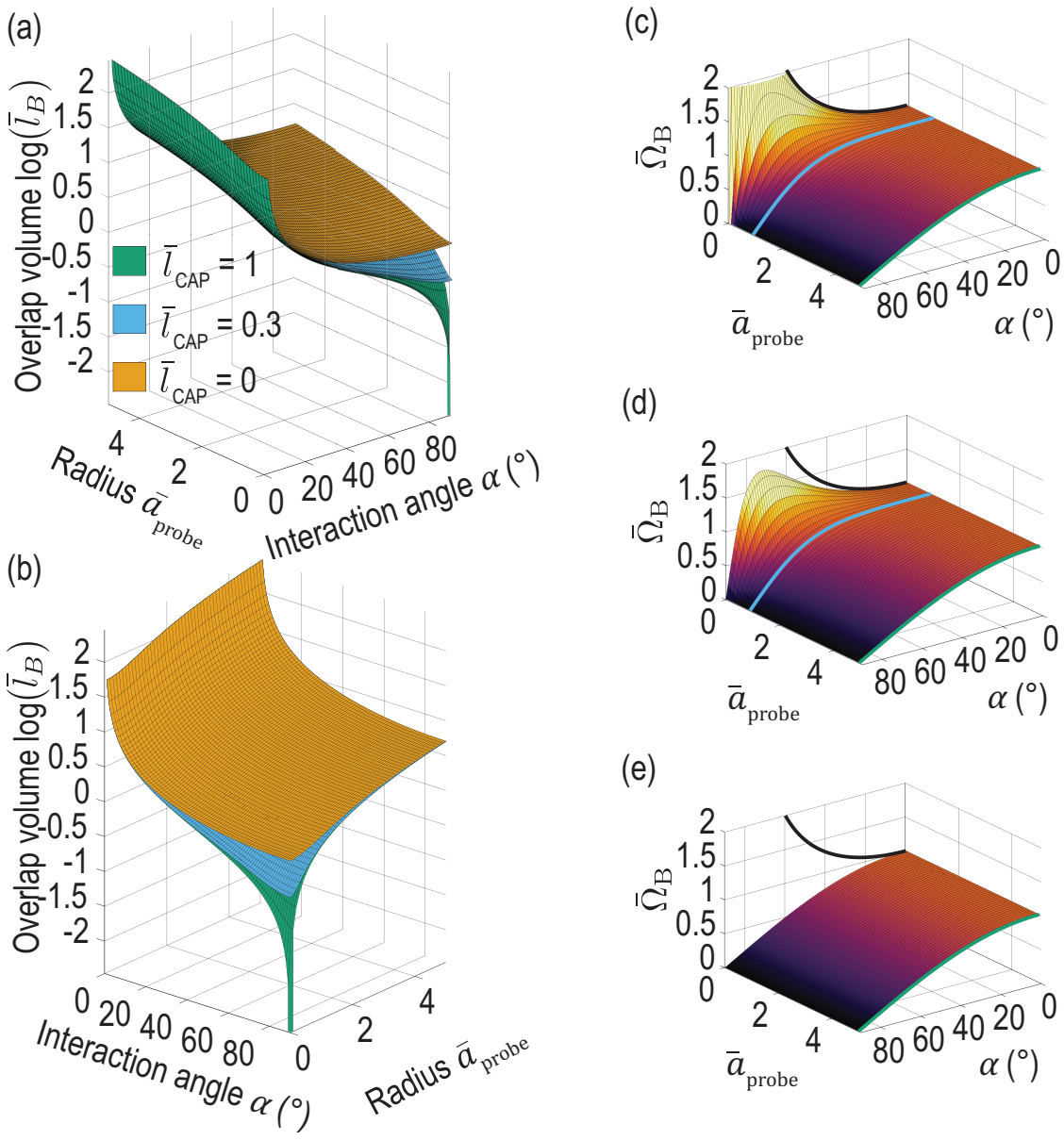

Figure 4.2 – Variations of the normalized overlap volume length $\bar{l}_B$ and carrier frequency $\bar{\Omega}_B$ as a function of the radii ratio $\bar{a}_{probe}$ and the interaction angle α. (a-b) Two views of the normalized overlap volume length $\bar{l}_B$ of the probe light and CAP beams along the propagation direction of the CAP, as a function of the normalized light beam radius $\bar{a}_{probe} = a_{probe}/a_{CAP}$ and the interaction angle α, for three values of the normalized CAP half-length $\bar{l}_{CAP} = l_{CAP}/a_{CAP}$. The logarithmic scale of $\bar{l}_B$ is presented to better appreciate the asymptotic evolutions. (c-e) Normalized carrier frequency $\bar{\Omega}_B$ of the wave packet as a function of $\bar{a}_{probe}$ and the interaction angle α, for the three same values of $\bar{l}_{CAP}$ as in (a-b): (c) $\bar{l}_{CAP} = 0$, (d) $\bar{l}_{CAP} = 0.3$ and (e) $\bar{l}_{CAP} = 1$. In each plot, the asymptotic frequency curves in Eq. (4.13) are represented: in black for the case $a_{CAP} \gg a_{probe}$ and in green for $a_{CAP} \ll a_{probe}$. The blue line indicates the splitting line (geometric separator), obtained for $\bar{a}^2_{probe} + 2\bar{l}^2_{CAP} = 1$, indicating the boundary between the two regimes presented in Fig. 4.3.

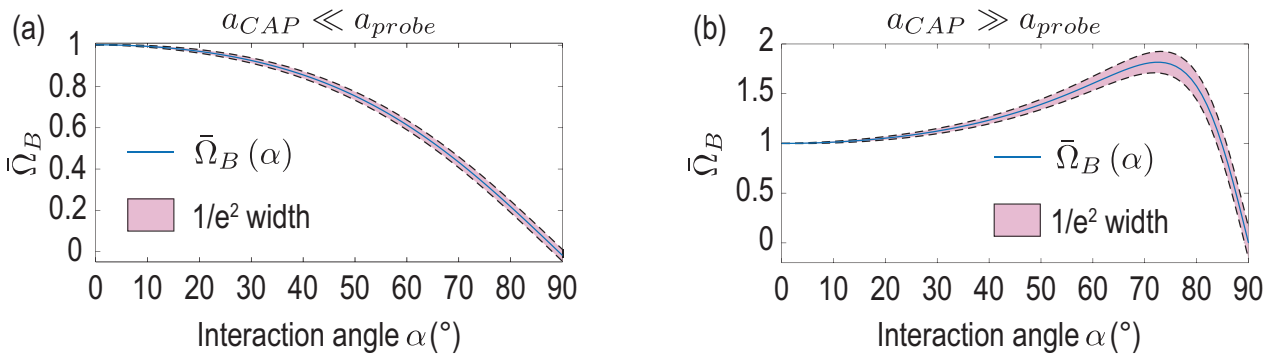

Figure 4.3 – Variations of the normalized carrier frequency as a function of the interaction angle for two different regimes. (a-b) Normalized carrier frequency $\bar{\Omega}_B$ and associated normalized spectral (full) width $\Delta\Omega_B/\omega_B$ at the $1/e^2$ level evolution with the interaction angle α with (a) $\bar{a}_{probe} = 1.7$, $\bar{l}_{CAP} = 0$ and (b) $\bar{a}_{probe} = 0.3$, $\bar{l}_{CAP} = 0$. The full width of the spectral line is related to the wave packet duration via $\Delta\Omega_B = 8/\tau_B$. The two different regimes highlighted in Fig. 4.2 (c-e) correspond to (a) for $a_{CAP} \ll a_{probe}$ and (b) for $a_{CAP} \gg a_{probe}$.

In the second condition, for $\bar{a}^2_{probe} + 2\bar{l}^2_{CAP} < 1$ [Fig. 4.3 (b)], the normalized carrier frequency $\bar{\Omega}_B$ increases compared to the value obtained at $\alpha = 0°$ $\left(\text{here } \bar{\Omega}_B(\alpha = 0) = 1\right)$, before decreasing to 0 for $\alpha = \pi/2$. The maximal carrier frequency value is given by:

$$\Omega_B^{max} = \frac{1}{2}\left(\sqrt{\frac{a^2_{probe} + l^2_{CAP}}{a^2_{CAP} - l^2_{CAP}}} + \sqrt{\frac{a^2_{CAP} - l^2_{CAP}}{a^2_{probe} + l^2_{CAP}}}\right)\omega_B \geq \omega_B, \tag{4.11}$$

obtained for:

$$\bar{\alpha}^{max} = \sin^{-1}\sqrt{1 - \frac{\bar{a}^2_{probe} + \bar{l}^2_{CAP}}{1 - \bar{l}^2_{CAP}}} \leq \frac{\pi}{2}. \tag{4.12}$$

Particularly, if the CAPs satisfies the condition $l^2_{CAP} \ll a^2_{probe} \ll a^2_{CAP}$, the carrier frequency Ω_B can reach much higher values than the (collinear) Brillouin frequency ω_B.

The physical sense of the different characteristic frequencies contributing to Ω_B can be revealed through the analysis of the different limiting cases. It is instructive to analyze the closest situation to most of the experiments reported until nowadays where the CAP half-length is negligible compared to both beams radii: $l^2_{CAP} \ll a^2_{probe}, a^2_{CAP}$. In this configuration, the biasing influence of the CAPs frequency spectrum on the carrier frequency is negligible:

$$\Omega_B(l_{CAP} = 0) \equiv \Omega_{B0} = \omega_B \frac{\left(a^2_{probe} + a^2_{CAP}\right)\cos\alpha}{\left(a^2_{probe} + a^2_{CAP}\cos^2\alpha\right)} \cong \begin{cases} \omega_B \cos\alpha & \text{if } a_{probe} \gg a_{CAP}, \\ \dfrac{\omega_B}{\cos\alpha} & \text{if } a_{probe} \ll a_{CAP}. \end{cases} \tag{4.13}$$

Both characteristic/asymptotic frequencies in Eq. (4.13) can be understood by evaluating the temporal periodicity of the photo-elastic interaction process in the considered limiting cases, as illustrated in Fig. 4.4.

In Fig. 4.4, the vertical gratings represented in blue lines introduce schematically the sensitivity function $\sin(2k_1 z)$ of the probe light to the CAP. The spacing between the lines depicts the periodicity of the sensitivity function along the z-axis that is $\pi/k_1 = \lambda_1/2$, with λ_1 the optical wavelength of the probe laser beam in medium (1). In Fig. 4.4 (a), it is clear that the period of the interaction process is equal to the time of flight of the CAP propagating between two blue (vertical) lines inside the probe light beam. The distance between the blue grating lines along the CAP propagation direction [red dashed arrow along the z'-axis in Fig. 4.4 (a)] is longer than the period $\pi/k_1 = \lambda_1/2$, and is equal to $\pi/(k_1 \cos\alpha)$. Thus, the period of the process is $\mathrm{T}(a_{CAP} \ll a_{probe}) = \pi/(k_1 v_1 \cos\alpha)$, while the characteristic frequency is $\Omega_{B0}(a_{CAP} \ll a_{probe}) = 2k_1 v_1 \cos\alpha = \omega_B \cos\alpha$. It corresponds to the momentum conservation in non-collinear backward scattering of photon by phonon.

However, in the opposite limiting case $a_{CAP} \gg a_{probe}$, the shortest distance between the grating lines along the CAP propagation direction is shorter than the grating period $\pi/k_1 = \lambda_1/2$. It is equal to $\pi\cos\alpha/k_1$ [red dashed arrow in Fig. 4.4 (b)]. Thus, the period of the process is $\mathrm{T}(a_{CAP} \gg a_{probe}) = \pi\cos\alpha/(k_1 v_1)$, while the characteristic frequency is $\Omega_{B0}(a_{CAP} \gg a_{probe}) = \dfrac{2k_1 v_1}{\cos\alpha} = \dfrac{\omega_B}{\cos\alpha}$. For all non-zero interaction angles, this characteristic frequency is higher than the "maximal" frequency of the 180° backward Brillouin scattering ω_B.

The physical reasons for the difference in the carrier frequencies predicted in the two limiting situations [Fig. 4.4] can be additionally appreciated using slightly different wording. In Fig. 4.4 (a) case, the different transverse parts of the probe light beam are reflected in the backward direction by the complete CAP beam, which has a phase velocity $v_1 \cos\alpha$ along the direction of the probe light beam. Contrastingly, in Fig. 4.4 (b) case, the complete probe light beam is reflected in the backward direction by the different transverse parts of the CAP beam, which are constituting an effective acoustic mirror moving at the

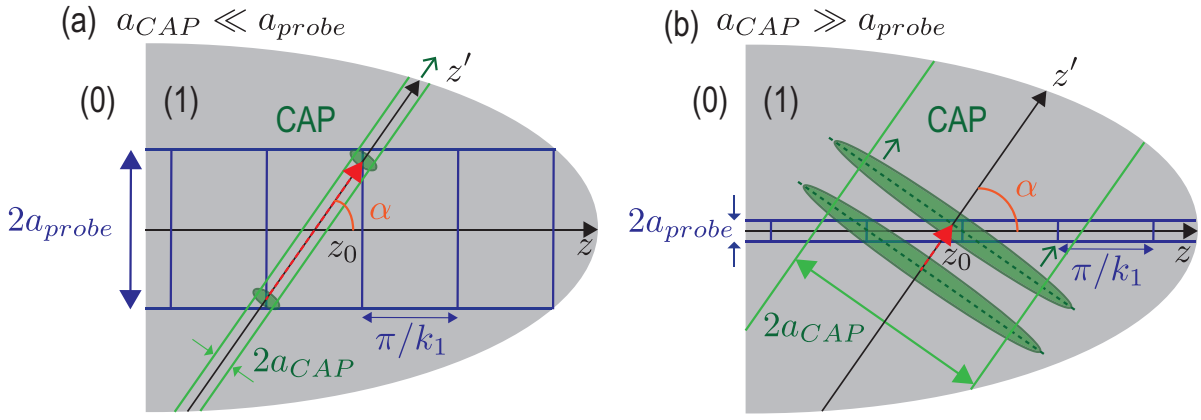

Figure 4.4 – Schemes illustrating the different temporal periodicity of the TDBS processes for two asymptotic relations between the probe light beam radius a_{probe} and the CAP beam radius a_{CAP}: (a) $a_{CAP} \ll a_{probe}$, and (b) $a_{CAP} \gg a_{probe}$. The propagating CAPs are represented by green ellipses.

phase velocity $v_1/\cos\alpha$ along the direction of the probe light beam. Thus, the asymptotic frequencies revealed in Eq. (4.13) can be interpreted as resulting from the Doppler effect [34], *i.e.*, arising from the probe light frequency shift induced by the probe light reflection on the moving acoustic "mirror" that is the CAP beam.

In the general case of Gaussian probe light and CAP beams of arbitrary radii, these two asymptotic characteristic frequencies are contributing to the carrier frequency of the TDBS wave packet via the following formal rule:

$$\frac{a_{probe}^2 + a_{CAP}^2}{\Omega_{B0}} = \frac{a_{probe}^2}{\Omega_B\left(a_{CAP} \ll a_{probe}\right)} + \frac{a_{CAP}^2}{\Omega_B\left(a_{CAP} \gg a_{probe}\right)}. \tag{4.14}$$

The amplitude factor of the TDBS wave packet [the terms in the two square brackets in Eq. (4.5)] is proportional to the characteristic volume of the CAP, $a_{CAP}^2 l_{CAP}$ and the strain pulse magnitude, η_0. The normalized (by the previously mentioned CAP volume, strain pulse magnitude, and the probe light and CAP beam areas) angular dependent part of this factor can be called the directivity pattern D_B of the TDBS detection (in the assumption of Gaussian probe light and CAP beams), and is given by:

$$D_B = \frac{\sqrt{a_{probe}^2 + a_{CAP}^2}}{\sqrt{a_{probe}^2 + a_{CAP}^2\cos^2\alpha + l_{CAP}^2\sin^2\alpha}} e^{-\frac{k_1^2}{2}\frac{\left(a_{CAP}^2 l_{CAP}^2 + a_{probe}^2 l_{CAP}^2\cos^2\alpha + a_{probe}^2 a_{CAP}^2\sin^2\alpha\right)}{\left(a_{probe}^2 + a_{CAP}^2\cos^2\alpha + l_{CAP}^2\sin^2\alpha\right)}}. \tag{4.15}$$

The directivity D_B has an extremum at $\alpha = 0°$, minimum for $l_{CAP} > a_{CAP}$ and maximum for $l_{CAP} < a_{CAP}$. In the common condition $l_{CAP} \ll a_{probe}, a_{CAP}$, the directivity pattern takes a more compact form:

$$D_B\left(l_{CAP} = 0\right) \equiv D_{B0} = \frac{\sqrt{a_{CAP}^2 + a_{probe}^2}}{\sqrt{a_{probe}^2 + a_{CAP}^2\cos^2\alpha}} e^{-\frac{k_1^2}{2}\frac{\left(a_{probe} a_{CAP}\sin^2\alpha\right)}{\left(a_{probe}^2 + a_{CAP}^2\cos^2\alpha\right)}}. \tag{4.16}$$

It is worth mentioning that in comparison with the carrier frequency Ω_{B0} [Eq. (4.13)], the directivity pattern D_{B0} [Eq. (4.16)] is always maximum at $\alpha = 0°$, independently of the radii ratio $\bar{a}_{probe}$.

In the aforementioned condition ($l_{CAP} \ll a_{probe}, a_{CAP}$), the strongest dependence on the inclination angle α comes from the Gaussian factor:

$$e^{-\frac{k_1^2}{2}\frac{\left(a_{probe}^2 a_{CAP}^2\sin^2\alpha\right)}{a_{probe}^2 + a_{CAP}^2\cos^2\alpha}} = e^{-\frac{k_1^2}{2}\left(\frac{a_{probe}^2 a_{CAP}^2}{l_B^2}\right)} = e^{-2\left(\frac{\pi a_{probe} a_{CAP}}{\lambda_1 l_B}\right)^2}. \tag{4.17}$$

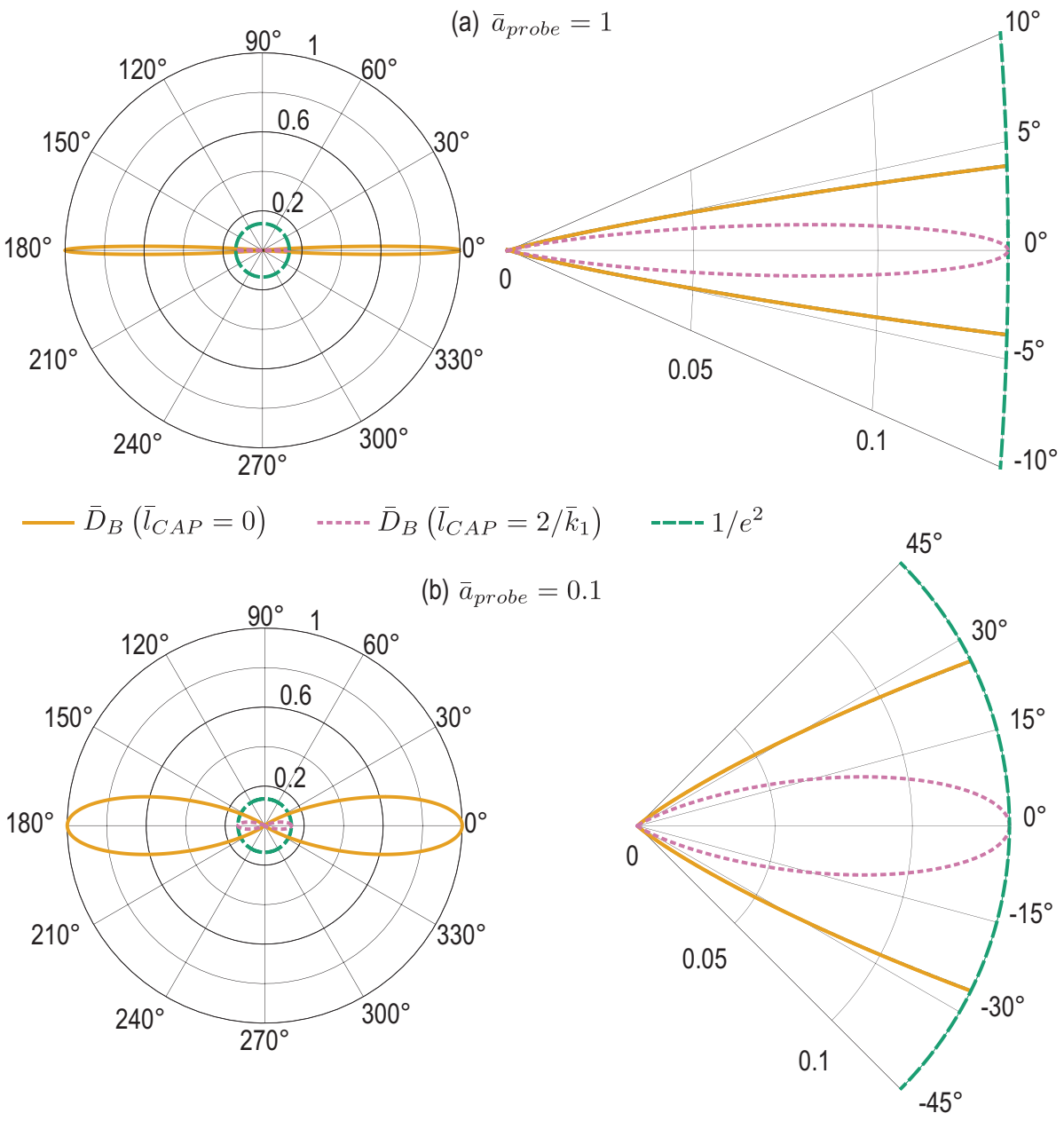

Figure 4.5 – Directivity pattern of the TDBS detection $\bar{D}_B$ (in the approximation of propagating light and CAP beams) for two different values of beam radii ratio $\bar{a}_{probe}$ and normalized CAP half length $\bar{l}_{CAP}$. (a) Directivity pattern (left) and zoom-in (right) for $\bar{a}_{probe} = 1$, $\bar{l}_{CAP} = 0$ (yellow solid line) and for $\bar{l}_{CAP} = 2/\bar{k}_1$ (pink dashed line). (b) Directivity pattern (left) and zoom-in (right) for $\bar{a}_{probe} = 0.1$, $\bar{l}_{CAP} = 0$ (yellow solid line) and for $\bar{l}_{CAP} = 2/\bar{k}_1$ (pink dashed line). In all the figures the $1/e^2$ level is represented by a green dashed line.

Following Eq. (4.17), three directivity regimes exist depending on the beams radii ratio. In the case of 3-D TDBS imaging, like discussed in Sec. 3.4, both pump and probe beam radii are of the same order: $\bar{a}_{probe} = 1$ [Fig. 4.5 (a)] since they are strongly co-focused in order to increase the lateral spatial

resolution. In this situation, the Gaussian amplitude factor [Eq. (4.17)] is simplified to:

$$e^{-\frac{k_1^2}{2}\frac{a_{CAP}^2 \sin^2\alpha}{(1+\cos^2\alpha)}}. \tag{4.18}$$

This situation is represented in Fig. 4.5 (a) where the normalized (by a_{CAP}) directivity pattern [Eq. (4.15)] is represented for two values of $\bar{l}_B$ in the $\bar{a}_{probe} = 1$ situation.
In the TDBS experiments where the condition $\bar{a}_{probe} \ll 1$ holds [Fig. 4.5 (b)], the Gaussian amplitude factor [Eq. (4.17)] is reduced to:

$$e^{-\frac{k_1^2}{2}a_{probe}^2 \tan^2\alpha}, \tag{4.19}$$

as far as α is not approaching $\pi/2$. In this situation, the critical inclination angle for which the signal amplitude is expected to drop at the $1/e^2$ level is obtained for:

$$\alpha_{1/e^2} = \tan^{-1}\left(\frac{\lambda_1}{\pi a_{probe}}\right). \tag{4.20}$$

For example, if we consider the condition $\lambda_1 \leq a_{probe}$ to hold, like in a typical material with an optical refractive index in material (1) $n_1 \geq 1.5$, the estimate predicts a small critical angle: $\alpha_{1/e^2} \cong \frac{1}{\pi n_1}$. Fig. 4.5 (b) emphasizes this strongly directive nature of the TDBS detection, where the $1/e^2$ level is attained for the interaction angles $\alpha > 30°$. The effect of taking into account a finite CAP half length $\bar{l}_{CAP}$ is the decreasing of the overall directivity amplitude, *e.g.*, if $\bar{l}_{CAP} = 0$ then $\bar{D}_B(\alpha = 0°) = 1$ thus one can obtain from the normalized Eq. (4.15) that the Gaussian factor in $\bar{D}_B$ diminishes e^2 times at $\alpha = 0°$ when $\bar{l}_{CAP} = 2/\bar{k}_1$ [pink dashed lines in Fig. 4.5], with $\bar{k}_1 = 2\pi a_{CAP}/\lambda_1$ the normalized optical wavenumber. In the $\bar{a}_{probe} = 1$ situation [Fig. 4.5 (a)], the TDBS detection is even more directive, the critical angle reducing to $\alpha_{1/e^2} \cong 7.8°$.
The third situation, where $\bar{a}_{probe} \gg 1$ gives a Gaussian amplitude factor [Eq. (4.17)] of the form:

$$e^{-\frac{k_1^2}{2}a_{CAP}^2 \sin^2\alpha}, \tag{4.21}$$

and leads thus to the following critical angle:

$$\alpha_{1/e^2} = \sin^{-1}\left(\frac{\lambda_1}{\pi a_{CAP}}\right). \tag{4.22}$$

In this case the angular peak in the directivity could be potentially broadened if the condition $\lambda_1 > a_{CAP}$ is achieved by using strongly focused pump laser radiation with a wavelength shorter than the probe light wavelength.
The abrupt drop in the directivity pattern of the TDBS detection when the interaction angle α is

increased, especially visible in the experimental situation of 3-D TDBS scans [Fig. 4.5 (a)] where the probe and CAP beam radii are of the same size, can be explained with the evolution of the scattering efficiency with the inclination angle. The abrupt diminishing of the scattering efficiency with increasing inclination angle is due to the abrupt diminishing of the number of quasi-collinearly propagating photons and phonons in the probe light and CAP beams, that could satisfy the momentum conservation law in the 180° backward Brillouin scattering. This momentum conservation law is a prerequisite of an efficient photo-elastic interaction in the experimental reflection configuration, where the heterodyning allows to detect the light that is acoustically scattered in the opposite direction compared to the incident probe light direction.

The existence of a critical angle α_{1/e^2} for the photo-elastic interaction efficiency can be straightforwardly understood from the qualitative analysis of the probe light and CAP beams scattering in the wave vectors space, *i.e.*, via the decomposition of the beams into rays (plane waves). A 2-D representation of the rays' cones associated to the Gaussian probe light and CAP beams [160] intersecting at an angle α is schematically drawn in Fig. 4.6. The probe half angle of divergence obtained in the far field

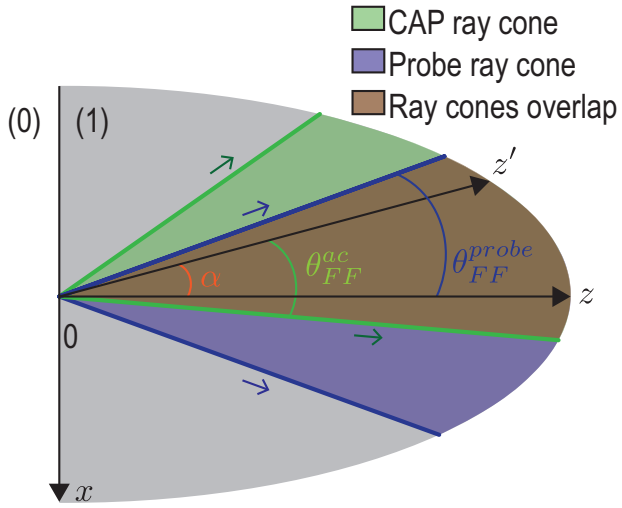

Figure 4.6 – 2-D illustration of the probe light and CAP ray distributions (represented as bounded inside cones), highlighting the existence of a critical angle resulting in a strong drop (disappearance) of the TDBS signal amplitude when the collimated probe light and CAP beams are propagating non-collinearly, inclined with an angle α. At a critical angle α_{1/e^2}, the CAP and probe light ray cones stop to overlap.

$\theta_{FF}^{probe} \equiv \dfrac{\lambda_1}{\pi a_{probe}}$ [160], is equal to the critical angle revealed previously in the situation $\bar{a}_{probe} \ll 1$ [Eq. (4.20)]. On the other hand, $\theta_{FF}^{ac} \equiv \dfrac{\lambda_{ac}}{\pi a_{CAP}}$ is the far field half angle of divergence of the monochromatic CAP beam with the acoustical wavelength λ_{ac} and the beam radius a_{CAP}.

The scheme in Fig. 4.6 illustrates that, as far as there is an overlap between the probe light ray cone and the acoustic ray cone, there will always be plane wave components of the probe light beam to be efficiently scattered by plane wave components of the CAP beam, in the quasi-collinear 180° backward Brillouin

scattering configuration, corresponding to $\lambda_{ac} \cong \lambda_1/2$. The overlap between the cones disappears at the interaction angle α satisfying the geometrical condition $\alpha - \theta_{FF}^{ac} = \theta_{FF}^{probe}$. This last relation takes the form:

$$\alpha = \theta_{FF}^{probe} + \theta_{FF}^{ac} = \frac{\lambda_1}{\pi a_{probe}} + \frac{\lambda_{ac}}{\pi a_{CAP}}, \tag{4.23}$$

under the 180° backscattering condition. It provides qualitatively correct estimates of the critical angles, in Gaussian beams, for all three earlier examined asymptotic situations. Thus, the analysis based on Fig. 6 confirms that the angular directivity in the interaction of probe light and CAP beams is due to the directional selectivity in the efficiency of the TDBS detection.

The results obtained in this section suggest that if a CAP, incident on an inclined material interface, is refracted (reflected and transmitted) with an inherent change in its propagation direction inducing non-collinear propagation with the probe light beam, then the amplitude and Brillouin frequency of the recorded TDBS signal will be importantly changed. This situation is studied in the next section.

4.3 Contributions to the TDBS signal from the incident and refracted CAPs at a material interface

The configuration studied theoretically in this section is close to the initial configuration of TDBS described in Sec. 2.3 and the associated Fig. 2.5 where the incident probe light beam and the generated CAP beam are propagating in the same direction and collinearly, but the difference is that these beams will face/reach an inclined material interface between material (1) and material (2) in their path [Fig. 4.7].
The initial thermoelastic generation of the CAP is considered confined to material (1) to ensure no "premature" detection of CAPs propagating in material (2) before the reflection and refraction of the CAP at the interface happen. Materials (1) and (2) are considered homogeneous and isotropic with the same optical, but different acoustical and acousto-optical, properties (exactly like ceria, Sec. 3.4.2). In this way, contrary to the CAP beam, the probe light beam is not reflected nor refracted by the material interface. Note that the possible reflected/transmitted transversal CAP, that could emerge as a result of the mode conversion of the longitudinal CAP incident to the inclined material interface, is not presented in Fig. 4.7 and later in Fig. 4.10. Moreover, in the development of the theory in Sec. 4.2, the possible multi-mode nature of the acoustical and optical fields is persistently neglected. These different points will be discussed as perspectives of this work.

4.3.1 TDBS monitoring of the CAP reflection at an inclined interface: incident CAP

In Fig. 4.7, the CAP, launched in material (1) via absorption of the pump beam by the OAT (not represented), is represented before and after the reflection from the material interface of its central part, displayed by the cylinders of diameter $2a_{CAP}$. To evaluate the transient processes, it is required to take explicitly into account that the acoustic field of the CAP is distributed through its complete radially infinite Gaussian beam, and is non-zero outside the cross section of the cylinders. For this purpose, the reflection of the CAP from the interface is sketched in Fig. 4.7 (b) with more details. Instead of being shown before and after reflection like in Fig. 4.7 (a), the CAP is given at a fixed instant when a part of the beam has already been reflected from the interface, while another part has not yet encountered the interface. In the following developments, it is assumed that the CAP can be modelled as a delta-localized strain (along its propagation direction). This situation is close to typical picosecond acoustic experiments [84] and should be sufficient to reveal the essential aspects of the Brillouin scattering.
Then from the geometry of the CAP reflection in Fig. 4.7 (b), it appears that both the incident and reflected CAPs exist only in the spatial region below the x-coordinate of the point labelled A. This point corresponds to the position of the incident CAP center at the material interface at a given time. Note that Fig. 4.7 is prepared for interfaces inclined with an angle $\theta > \pi/4$ relatively to the free surface of material (1) ($z = 0$). For smaller inclinations, the reflected CAP is localized in the half-plane above the x-coordinate of point A [Fig. 4.9 (b)]. The strain fields in the incident and reflected CAPs are described

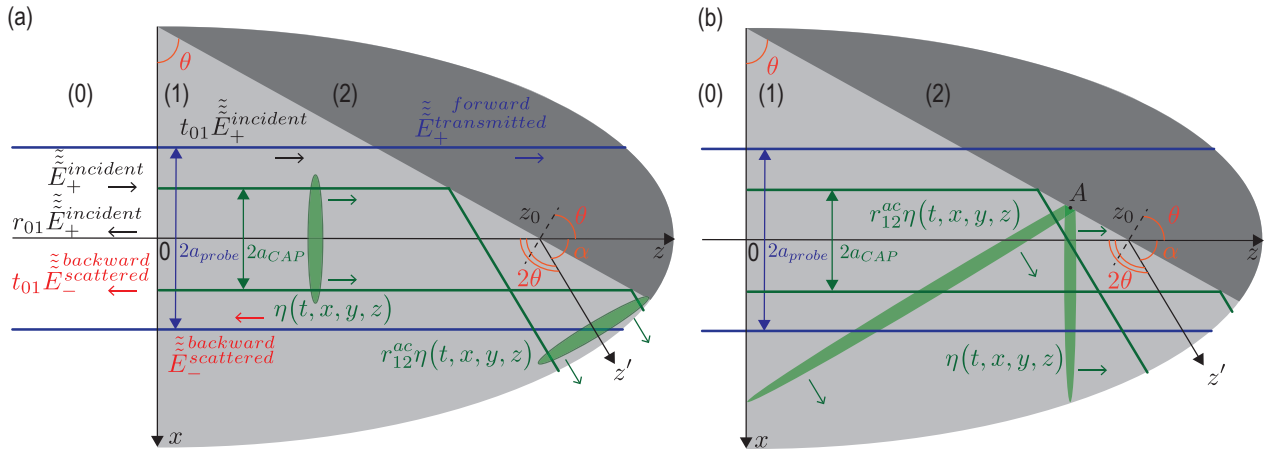

Figure 4.7 – (a) Simplified and (b) detailed sketches of TDBS monitoring of the CAP reflection at the interface between two materials inclined at an angle $\pi/4 \leq \theta < \pi/2$ relatively to the free surface ($z = 0$) of material (1) ($z > 0$). The deviation angle, with which the central ray of the CAP beam deviates from its initial propagation direction, is equal to 2θ. The probe light beam is not refracted nor reflected by the material interface since both materials have the same optical properties. Continuous green and blue lines present, inside their Rayleigh ranges, the CAP and laser beams respectively. The CAPs are additionally presented by (green) ellipses to illustrate their strong localization along the propagation direction caused by their ultrashort duration. In (b), the simplified CAP beam representation of finite $2a_{cap}$ lateral distribution shown in (a) is made more accurate to account for the infinite lateral dimension of the Gaussian CAP beam.

by:

$$\eta_{incident}(t,x,y,z) = \eta_0\,(2l_{CAP})\,e^{-2\frac{x^2+y^2}{a_{CAP}^2}}\,\delta\,(z - v_1 t)\,, \tag{4.24}$$

and

$$\begin{aligned}\eta_{reflected}\,(t,x',y',z') &= r_{12}^{ac}(v_1,v_2,\theta)\eta_0\,(2l_{CAP})\,e^{-2\frac{x'^2+y'^2}{a_{CAP}^2}}\,\delta(z' - v_1 t),\\ &= r_{12}^{ac}(v_1,v_2,\theta)\eta_0\,(2l_{CAP})\,e^{-2\frac{[x\cos\alpha-(z-z_0)\sin\alpha]^2+y^2}{a_{CAP}^2}}\\ &\times\ \delta\Big[(z-z_0)\cos\alpha + x\sin\alpha - v_1 t\Big].\end{aligned} \tag{4.25}$$

In Eqs. (4.24) and (4.25), $2l_{CAP}$ stands for the length of the ultrashort CAP, and $r_{12}^{ac}(v_1,v_2,\theta)$ denotes the acoustic reflection coefficient at the interface. Note here that for compactness, the dependencies of the acoustic reflection and transmission coefficients on the densities and the velocities of the transversal acoustic waves are not written but should be taken into account.

The angle between the incident and reflected CAPs propagation directions defined in Fig. 4.7 is $\alpha = \pi - 2\theta$, while the zero instant of time is associated to the arrival of the delta-CAP central ray at $z = z_0$. The x coordinate of point A is thus described by $x_A(t,v_1,\theta) = (v_1 t)\,/\,\tan\theta$.

Finally, the theoretical integral formula giving the TDBS signal at the photodetector [Eq. (4.4)] applied in Sec. 4.2 is only valid for a strain CAP localized inside material (1), without straining the surface $z =$

0. In order to consider that there is a strain field on the surface $z = 0$, the integration limits in Eq. (4.4) needs to be modified:

$$\frac{\Delta R}{R} = \frac{2}{\pi a_{probe}^2} P \int\int_{-\infty}^{+\infty} \mathrm{d}x\mathrm{d}y e^{-2\dfrac{x^2+y^2}{a_{probe}^2}} \int_0^{+\infty} \mathrm{d}z \eta(t,x,y,z) \sin(2k_1 z). \tag{4.26}$$

Similar to the reasoning of Sec. 4.2, Eq. (4.26) is applied for the strain field associated to the incident CAP [Eq. (4.24)] [161][1], with the integration over the x coordinate limited to $x_A(t, v_1, \theta) \leq x \leq +\infty$. The result leads to the description of the contribution to the TDBS signal collected from scattering of the incident CAP in material (1) [Fig. 4.1]:

$$\left(\frac{\Delta R}{R}\right)_{incident} = P \left[\frac{\eta_0 a_{CAP} l_{CAP}}{\sqrt{a_{probe}^2 + a_{CAP}^2}}\right] \left[1 - \mathrm{erf}\left(\sqrt{2}\frac{x_A(t)}{a_{overlap}}\right)\right] \sin\left(\omega_B \left[t + \frac{z_0}{v_1}\right]\right), \tag{4.27}$$

where a compact notation $a_{overlap}$ is introduced for the characteristic spatial scale defined by the following "summation" rule :

$$\frac{1}{a_{overlap}^2} \equiv \frac{1}{a_{probe}^2} + \frac{1}{a_{CAP}^2}.$$

This characteristic spatial scale corresponds to the radius at $1/e^2$ of the overlap between the Gaussian distributions of the probe light intensity and the CAP amplitude.
The incident CAP is collinear to the probe light ($\alpha = 0°$) and the Gaussian amplitude factor [Eq. (4.17)] is thus equal to 1, while the carrier frequency [Eq. (4.8)] is reduced to ω_B in Eq. (4.27). The wave packet envelope in Eq. (4.5), associated to the overlap volume length l_B [Eq. (4.6)], is not found in Eq. (4.27). The reason comes from the fact that the overlap volume length l_B diverges for $\alpha = 0°$ [Fig. 4.4 (a-b)].
The time decay of the incident CAP contribution to the TDBS signal is described by the erf function term under brackets in Eq. (4.27), and account for the "disappearance" of the incident CAP via its progressive transformation into reflected and transmitted CAPs:

$$\left[1 - \mathrm{erf}\left(\sqrt{2}\frac{x_A(t)}{a_{overlap}}\right)\right] = \left[1 - \mathrm{erf}\left(\sqrt{2}\frac{v_1 t}{a_{overlap}\tan\theta}\right)\right] \equiv \left[1 - \mathrm{erf}\left(\sqrt{2}\frac{t}{\tau_i}\right)\right]. \tag{4.28}$$

From the previous definition of $a_{overlap}$, the term $a_{overlap}\tan\theta$ can de defined as the characteristic distance along the CAP propagation direction, of the cylindrical volume where the delta-CAP, the probe light and the interface could coexist during the reflection of the CAP by the interface. In other words, this is an estimate of the distance that the CAP should travel between the moment it reaches the interface

[1] Page 455, Eq. 8: $\int_0^{+\infty} e^{-ax^2-cx}\sin(bx)\mathrm{d}x = \frac{i}{4}\sqrt{\frac{\pi}{a}}\left[e^{\frac{(c+ib)^2}{4a}}\mathrm{erfc}\left(\frac{c+ib}{2\sqrt{a}}\right) - e^{\frac{(c-ib)^2}{4a}}\mathrm{erfc}\left(\frac{c-ib}{2\sqrt{a}}\right)\right]$,
with erfc(z) = 1 - erf(z) the complementary error function.

for the first time and the moment it looses the contact with it, as it is monitored by TDBS of the probe light beam. The physical sense of the characteristic time τ_i defined in Eq. (4.28) can be understood as the time taken by the incident CAP to be reflected / transmitted by the interface, as it is monitored by TDBS.

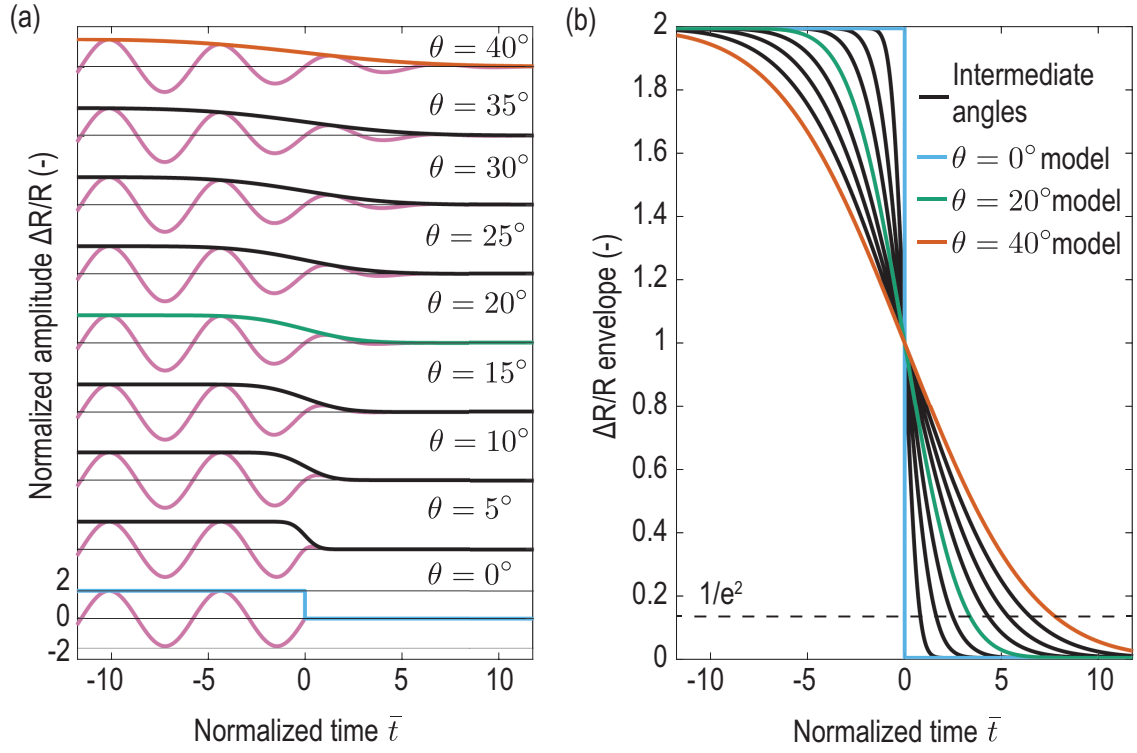

Figure 4.8 – Contribution to the TDBS signal from the incident CAP [Eq. (4.27)] as a function of the interface inclination angle θ, using the material properties of ceria as an example. (a) Normalized contribution of the incident CAP to the TDBS (solid oscillating pink curves) for $\theta \in [0°, 40°]$ with 5° steps, and associated envelopes (in solid black lines + 3 colored lines). The contributions are upshifted for better visualization. (b) Normalized contribution of the incident CAP to the TDBS envelopes (in solid black lines + 3 colored lines) for $\theta \in [0°, 40°]$ with 5° steps. The spatial variables in Eq. (4.27) are normalized by the CAP beam radius a_{CAP}, while the carrier (Brillouin) oscillations frequency Ω_B, the CAP velocity v_1 in material (1) and the time t are normalized by the oscillation frequency, the velocity and the period T_{LA}^{min} associated to the slowest LA mode in ceria [Tab. 3.4].

To illustrate the previous discussion, Fig. 4.8 (a) provides the contributions of the incident CAP to the TDBS signal [Eq. (4.27)] (solid oscillating pink curves) along with their envelope amplitudes, as a function of the inclination θ of the interface, normalized with the parameters associated to ceria, the material studied in Sec. 3.4.2. Therefore the considered interface is the boundary between two ceria grains of different crystalline orientations, analogous to the interface between materials (1) and (2) [Fig. 4.7]. Only the propagation of a longitudinal CAP (LA mode) is considered for the computation of Eq. (4.27) here. In Fig. 4.8 (b), the envelopes of Eq. (4.27) are presented separately for better appreciation, three of them being highlighted in both figures, with colors instead of using black solid lines, corresponding to

the cases $\theta = 0°$ (blue), $\theta = 20°$ (green) and $\theta = 40°$ (orange).
In the case of an interface parallel to the free surface of material (1), *i.e.*, parallel to the $z = 0$ plane and with $\theta = 0°$, the contribution of the incident CAP to the full TDBS signal is stopped/ended when the CAP reaches the interface [blue envelope in Fig. 4.8], as it is reflected and transmitted at the interface. For small interface inclination angles θ, the contribution of the incident CAP to the TDBS signal decreases abruptly, *e.g.*, when the boundary is inclined with an angle $\theta = 20°$, the amplitude of the envelope reaches the $1/e^2$ level before the normalized time reaches the value $\bar{t}(1/e^2) = t/T_{LA}^{min} = 5$ [green envelope in Fig. 4.8], *i.e.*, before 5 periods T_{LA}^{min} of the slowest LA mode that could be monitored in ceria. This contribution broadens with increasing inclination of the interface as expressed by the process of reflection/transmission of the pulse in Fig. 4.8 (b), the envelope decreasing progressively, starting before the arrival of the delta-CAP central ray at $z = z_0$ (before $\bar{t} = 0$), but reaching the $1/e^2$ level multiple periods T_{LA}^{min} later.

4.3.2 TDBS monitoring of the CAP reflection at an inclined interface: reflected CAP

Similarly to the description of the contribution to the TDBS signal from the incident CAP, the contribution to the TDBS signal from the reflected CAP, in the case of an angle $\pi/4 \leq \theta < \pi/2$, is obtained from Eqs. (4.4) and (4.25):

$$\left(\frac{\Delta R}{R}\right)_{reflected} = r_{12}^{ac} P \left[\frac{\eta_0 a_{CAP} l_{CAP}}{\sqrt{a_{probe}^2 + a_{CAP}^2 \cos^2\alpha}}\right] e^{-\frac{k_1^2}{2}\frac{\left(a_{probe}^2 a_{CAP}^2 \sin^2\alpha\right)}{\left(a_{probe}^2 + a_{CAP}^2 \cos^2\alpha\right)}} e^{-2\frac{\sin^2\alpha}{\left(a_{probe}^2 + a_{CAP}^2 \cos^2\alpha\right)}(v_1 t)^2}$$
$$\times \Im\left\{ e^{i\omega_B\left[\frac{\left(a_{probe}^2 + a_{CAP}^2\right)\cos\alpha}{\left(a_{probe}^2 + a_{CAP}^2 \cos^2\alpha\right)} t + \frac{z_0}{v_1}\right]} \left[1 - \mathrm{erf}\left(\sqrt{2}\frac{x_A(t)}{a_{overlap,\alpha}} - \sqrt{2}\frac{v_1 t \sin\alpha}{a_{CAP}^2 \cos^2\alpha} a_{overlap,\alpha} + i\sqrt{\frac{k_1^2}{2}\frac{\left(a_{probe}^2 a_{CAP}^2 \sin^2\alpha\right)}{\left(a_{probe}^2 + a_{CAP}^2 \cos^2\alpha\right)}}\right)\right]\right\}, \tag{4.29}$$

where a compact notation $a_{overlap,\alpha}$ similar to that in Eq. (4.27), introduces the characteristic scale defined by the following "summation" rule:

$$\frac{1}{a_{overlap,\alpha}^2} \equiv \frac{1}{a_{probe}^2} + \frac{1}{a_{CAP}^2 \cos^2\alpha}.$$

The similarity between Eqs. (4.27) and (4.29) means that most of the terms in the latter have been already discussed in Sec. 4.3.1. We can immediately recognize in Eq. (4.29) the Gaussian envelope of the wave packet (first exponential of the first line), the oscillation (carrier) frequency (first exponential in the imaginary part) and the angle-dependent constant in the time-dependent Gaussian amplitude factor already observed in Eq. (4.5) of Sec. 4.2.

The contribution from the reflected CAP to the TDBS signal [Eq. (4.29)] differs from Eq. (4.5) via the addition of spatio-temporal scales, regrouped in the factor G_r:

$$G_r\left(\theta > \frac{\pi}{4}\right) \equiv \left[1 - \mathrm{erf}\left(\sqrt{2}\frac{x_A(t)}{a_{overlap,\alpha}} - \sqrt{2}\frac{v_1 t \sin\alpha}{a_{CAP}^2 \cos^2\alpha} a_{overlap,\alpha} + i\sqrt{\frac{k_1^2}{2}\frac{\left(a_{probe}^2 a_{CAP}^2 \sin^2\alpha\right)}{\left(a_{probe}^2 + a_{CAP}^2 \cos^2\alpha\right)}}\right)\right]. \tag{4.30}$$

This factor contributes to the description of the dynamics of "generation" of the reflected CAP by the incident one, when monitored by TDBS. The first term in the argument of the error (erf) function contributes to the description of the appearance/disappearance dynamics of the reflected pulse in the characteristic volume of the probe light field near the inclined interface. The definition of $a_{overlap,\alpha}$ indicates that it corresponds to the radius at $1/e^2$ level of the overlap between the Gaussian distributions of the probe light intensity and the CAP amplitude along the x-axis. $a_{overlap,\alpha}$ differs from $a_{overlap}$ only by replacing the incident CAP beam radius with the reflected CAP beam radius, both projected on the

x-axis.
Thus, the sense of the characteristic time $\tau_r = (a_{overlap,\alpha} \tan\alpha)/v_1$ in the first term of the erf function argument [Eq. (4.30)] is similar to the already discussed sense of τ_i, *i.e.*, the time taken by the CAP to be reflected, as it is monitored by TDBS . The second time-dependent term in the argument of the erf function could be associated with the time $\tau_B(l_{CAP} = 0)$ of the CAP propagation across the overlap region between the probe light intensity and the reflected CAP, via the following relation:

$$\frac{v_1 t \sin\alpha}{a_{CAP}^2 \cos^2\alpha} a_{overlap,\alpha} = \frac{a_{probe}}{a_{CAP}} \left(\frac{v_1 t}{l_B(l_{CAP} = 0)} \right) = \frac{a_{probe}}{a_{CAP}} \left(\frac{t}{\tau_B(l_{CAP} = 0)} \right), \tag{4.31}$$

where $l_B(l_{CAP} = 0) = \sqrt{\left(\frac{a_{probe}}{\sin\alpha}\right)^2 + \left(\frac{a_{CAP}}{\tan\alpha}\right)^2}$ from Eq. (4.6). The dynamics of the G_r factor described by Eq. (4.30) drastically depends on the sign of the combined characteristic time $\bar{\tau}$ in the argument of the erf function:

$$\frac{x_A(t)}{a_{overlap,\alpha}} - \frac{v_1 t \sin\alpha}{a_{CAP}^2 \cos^2\alpha} a_{overlap,\alpha} \equiv \frac{t}{\tau_r} - \frac{a_{probe}}{a_{CAP}} \left(\frac{t}{\tau_B(l_{CAP=0})} \right) = \frac{t}{\bar{\tau}}. \tag{4.32}$$

If $\bar{\tau} < 0$, then the amplitude of $G_r\left(\theta > \frac{\pi}{4}\right)$ is growing from 0 at $t = -\infty$ to 2 at $t = +\infty$, while if $\bar{\tau} > 0$, then its dynamics is reversed: it is decreasing from 2 at $t = -\infty$ to 0 at $t = +\infty$.
It has to be reminded here that Fig. 4.7 and the solution for the reflected pulse contribution to the TDBS signal are relevant to the case where $\theta > \pi/4$, while the angle between the incident probe light and the reflected CAP propagation directions is defined as $\alpha = \pi - 2\theta$. The reflection of the CAP in the case $0 < \theta \leq \pi/4$ is illustrated in Fig. 4.9.

Based on the comparison of the sketches in Figs. 4.7 (b) and 4.9 (b), it appears that the only difference is that the integration over the x coordinate should be held in the region $-\infty \leq x \leq x_A(t, v_1, \theta)$, while the relation $\alpha = \pi - 2\theta$ still holds. In this case, the expected contribution from the reflected CAP to the TDBS signal differs from Eq. (4.29) in the description of the G_r function, which takes the form:

$$G_r\left(0 < \theta \leq \frac{\pi}{4}\right) \equiv \left[1 + \mathrm{erf}\left(\sqrt{2} \frac{x_A(t)}{a_{overlap,\alpha}} - \sqrt{2} \frac{v_1 t \sin\alpha}{a_{CAP}^2 \cos^2\alpha} a_{overlap,\alpha} + i \sqrt{\frac{k_1^2}{2} \frac{\left(a_{probe}^2 a_{CAP}^2 \sin^2\alpha\right)}{\left(a_{probe}^2 + a_{CAP}^2 \cos^2\alpha\right)}} \right) \right]. \tag{4.33}$$

The dynamics of $G_r\left(0 < \theta \leq \frac{\pi}{4}\right)$ is just the opposite to that of $G_r\left(\theta > \frac{\pi}{4}\right)$ with respect to the sign of $\bar{\tau}$. If $\bar{\tau} < 0$, the amplitude of $G_r\left(0 < \theta \leq \frac{\pi}{4}\right)$ is diminishing from 2 at $t = -\infty$ to 0 at $t = +\infty$, while if $\bar{\tau} > 0$, it is growing from 0 at $t = -\infty$ to 2 at $t = +\infty$.
Again, to illustrate the discussion, Fig. 4.10 (a) provides the contribution of the reflected CAP to the TDBS signal (solid oscillating pink curves) along with their envelopes amplitude, in function of the inclination θ of the interface, normalized with the parameters associated to ceria. Two different time scales

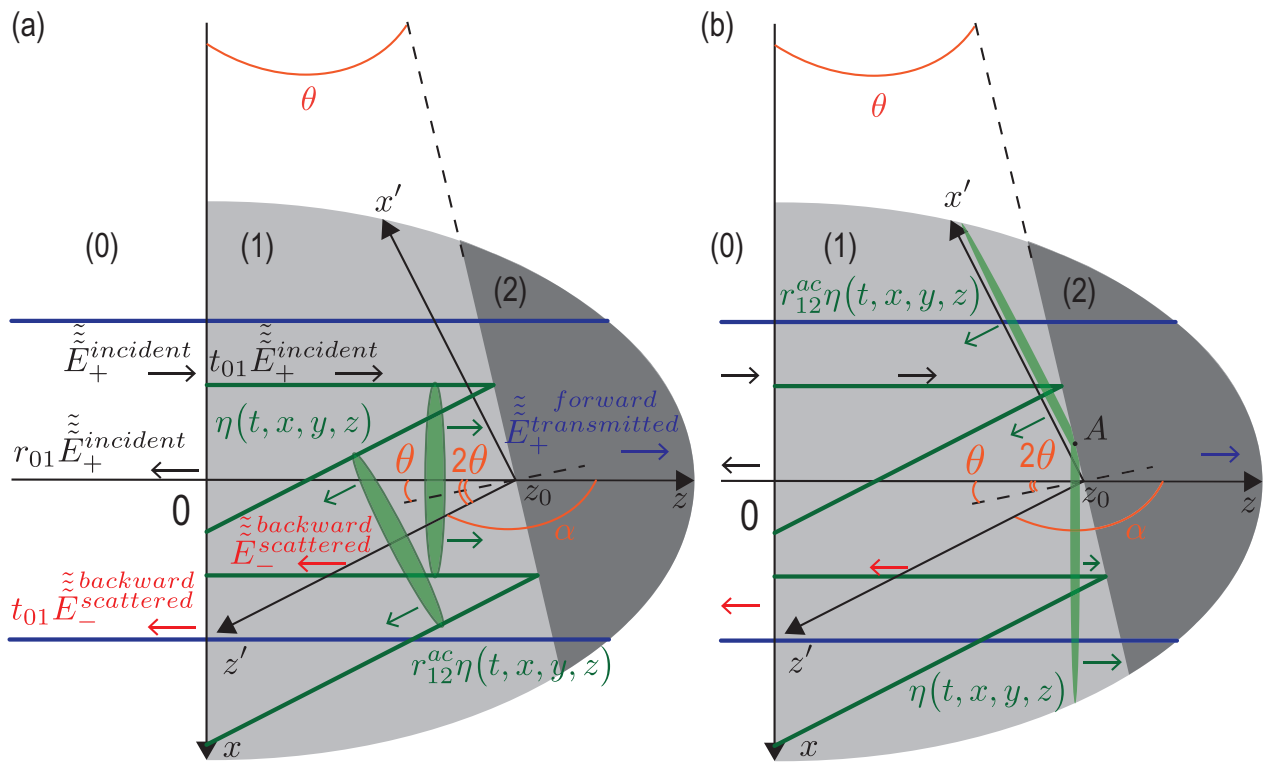

Figure 4.9 – (a) Simplified and (b) detailed sketches of TDBS monitoring of the CAP reflection at the interface between two materials inclined at an angle $0 \leq \theta < \pi/4$ relatively to the free surface ($z = 0$) of material (1) ($z > 0$). The deviation angle, with which the central ray of the CAP beam deviates from its initial propagation direction, is equal to 2θ. The probe light beam is not refracted nor reflected by the material interface since both materials have the same optical properties. Continuous green and blue lines present, inside their Rayleigh ranges, the CAP and laser beams respectively. The CAPs are additionally presented by (green) ellipses to illustrate their strong localization along the propagation direction caused by their ultrashort duration. In (b), the simplified CAP beam representation of finite $2a_{cap}$ lateral distribution shown in (a) is made more accurate to account for the infinite lateral dimension of the Gaussian CAP beam.

are presented in Fig. 4.10 , the $\theta = 0°$ model being 8 times longer than the 2 other models computed. In Fig. 4.10 (b) the envelopes of the reflected CAP contribution to the TDBS signal are presented separately, at different amplitude scales for better appreciation. Three specific cases are presented in Fig. 4.10, corresponding to the inclination angles $\theta = 0°$ (blue), $\theta = 3°$ (green) and $\theta = 6°$ (orange).

In agreement with Fig. 4.8, in the case of an interface parallel to the free surface of material (1), (with $\theta = 0°$), the contribution of the reflected CAP to the full TDBS signal is starting/emerging when the CAP reaches the interface [blue envelope in Fig. 4.10]. Then, the contribution of the reflected CAP falls abruptly with increasing inclination angle, *e.g.*, for $\theta = 6°$, the amplitude of the envelope falls to the $1/e^2$ level quasi-instantly (orange line in Fig. 4.10). Thus, it is safe to say that the contribution of the reflected CAP to the TDBS signal is limited to the vicinity of the interface, and is negligible when the interface is inclined, even for small angles. The reason is found in the discussion related to Fig. 4.6: the deviation angle (2θ) of the reflected CAP propagation direction relative to the probe propagation direction [Fig.

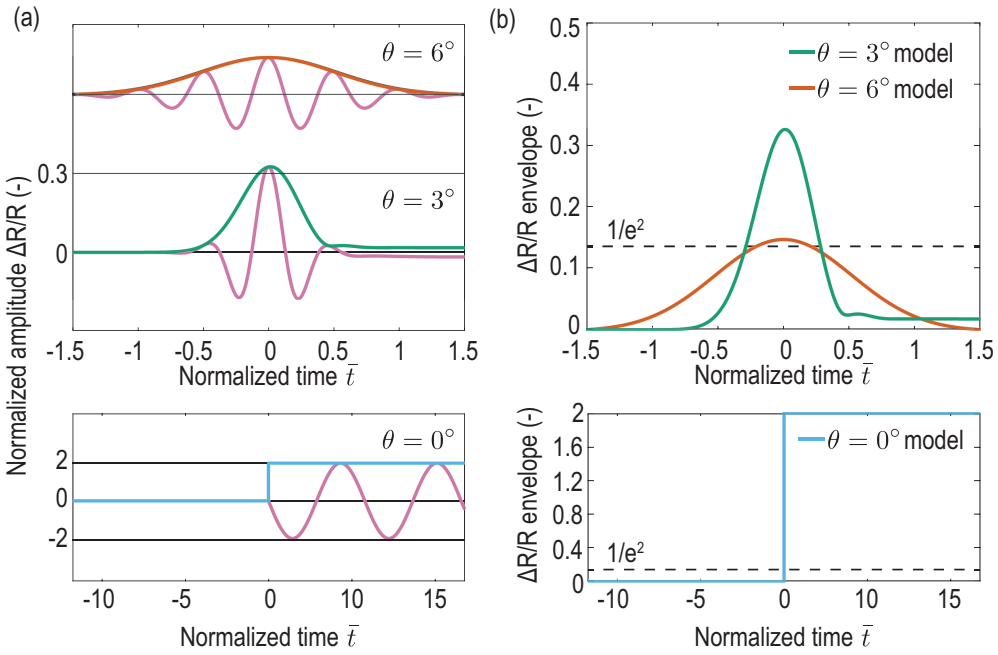

Figure 4.10 – Contribution to the TDBS signal from the reflected CAP [Eq. (4.29) modified according to Eq. (4.33)] as a function of the interface inclination angle θ, using the material properties of ceria as an example. (a) Normalized contribution of the reflected CAP to the TDBS (solid oscillating pink curves) for $\theta = \{0°, 3°, 6°\}$, and associated envelopes (3 colored lines). (b) Normalized contribution of the reflected CAP to the TDBS envelopes (3 colored lines) for $\theta = \{0°, 3°, 6°\}$. The spatial variables in Eq. (4.29) are normalized by the CAP beam radius a_{CAP}, while the carrier (Brillouin) oscillations frequency Ω_B, the CAP velocity v_1 in material (1) and the time t are normalized by the oscillation frequency, the velocity and the period T_{LA}^{min} associated to the slowest LA mode in ceria [Tab. 3.4].

4.9] is such that the number of quasi-collinearly propagating photons and phonons that could satisfy the momentum conservation law in the 180° backward Brillouin scattering is abruptly diminished.

4.3.3 TDBS monitoring of the CAP refraction at an inclined interface: transmitted CAP

Finally, the transmission (refraction) of a CAP across the interface between material (1) and (2) is presented in Fig. 4.11. The assumptions in the following developments are the same as the ones stated in Sec. 4.3.1.

Figure 4.11 (a) schematically present the CAP before and after the transmission of its central part across the interface between the two materials, represented by the cylinders of characteristic radii a_{CAP} and $a_{CAP,t}$, respectively.

Like in Sec. 4.3.1, to evaluate the transient processes, we need to take into account explicitly that the acoustic field of the CAP is distributed in its complete Gaussian beam and is thus non-zero outside the cross section of the presented cylinders. For this purpose, the transmission process is sketched with more

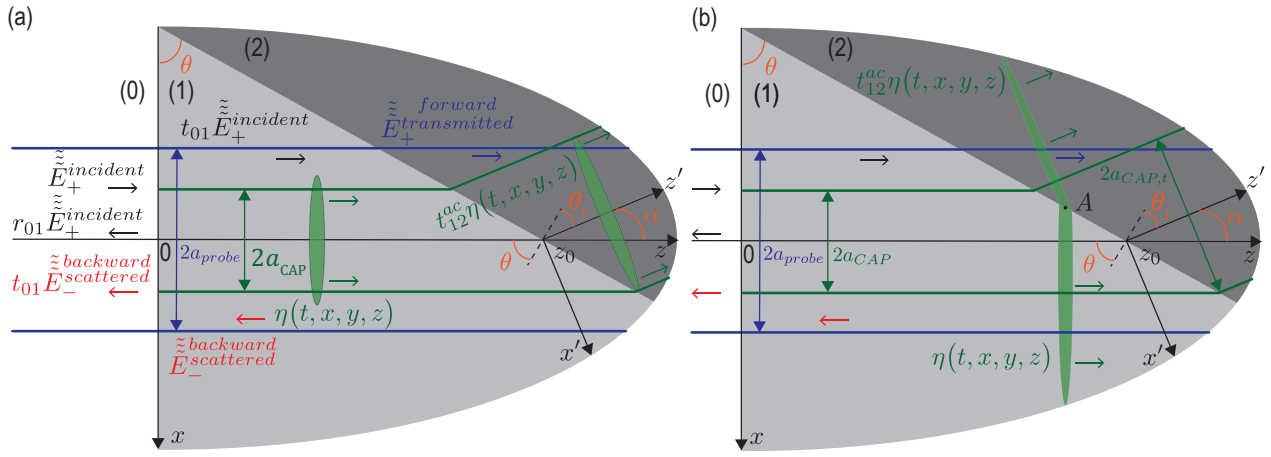

Figure 4.11 – (a) Simplified and (b) detailed sketches of TDBS monitoring of the CAP transmission (refraction) at the interface between two materials inclined at an angle $\pi/4 \leq \theta < \pi/2$ relatively to the free surface ($z = 0$) of material (1) ($z > 0$), in the case $v_1 > v_2$. The probe light beam is not refracted nor reflected by the material interface since both materials have the same optical properties. Continuous green and blue lines present, inside their Rayleigh ranges, the CAP and laser beams respectively. The CAPs are additionally presented by (green) ellipses to illustrate their strong localization along the propagation direction caused by their ultrashort duration. In (b), the simplified CAP beam representation of finite $2a_{cap}$ lateral distribution shown in (a) is made more accurate to account for the infinite lateral dimension of the Gaussian CAP beam.

details in Fig. 4.11 (b). The transmitted acoustic pulse is thus described by:

$$\begin{aligned}\eta_{transmitted}(t,x',y',z') &= t_{12}^{ac}(v_1,v_2,\theta)\eta_0\left(2l_{CAP,t}\right)e^{-2\frac{x'^2}{a_{CAP,t}^2}}e^{-2\frac{y'^2}{a_{CAP}^2}}\delta\left(z'-v_1t\right)\\ &= t_{12}^{ac}(v_1,v_2,\theta)\eta_0\left(2l_{CAP,t}\right)e^{-2\frac{[x\cos\alpha+(z-z_0)\sin\alpha]^2}{a_{CAP,t}^2}}e^{-2\frac{y^2}{a_{CAP}^2}}\delta\left[(z-z_0)\cos\alpha-x\sin\alpha-v_2t\right],\end{aligned} \tag{4.34}$$

with v_2 the acoustic velocity and $2l_{CAP,t} = 2l_{CAP}(v_2/v_1)$ stands for the characteristic length of the CAP in material (2), $t_{12}^{ac}(v_1,v_2,\theta)$ compactly denotes the acoustic transmission coefficient at the interface between the two materials (1) and (2), while the zero instant of time is associated with the arrival of the delta-CAP central ray at the distance $z = z_0$ from the surface $z = 0$.

The angle between the incident and transmitted CAPs propagation directions in Fig. 4.11 is $\alpha = \theta - \theta_t$, where θ and θ_t are commonly defined as the angles of CAP incidence and CAP transmission/refraction, respectively. It is worth mentioning that Eq. (4.34) takes into account the modification in the projection of the transmitted CAP cross section on the x-axis: $a_{CAP,t} = a_{CAP}(\cos\theta_t/\cos\theta)$.

Figure 4.11 was drawn under the particular condition $(v_2/v_1) < 1$. In Fig. 4.11 (b), it is shown that under this particular condition, the transmitted CAP is located in the spatial region $-\infty \leq x \leq x_A(t,v_1,\theta)$, where the integration in Eq. (4.4) should be done for the evaluation of the transmitted pulse contribution

to the TDBS signal. Finally, the contribution to the TDBS signal from the transmitted CAP reads:

$$\left(\frac{\Delta R}{R}\right)_{transmitted} = t_{12}^{ac} P \left[\frac{\eta_0 a_{CAP,t} l_{CAP,t}}{\sqrt{a_{probe}^2 + a_{CAP,t}^2 \cos^2\alpha}}\right] e^{-\frac{k_1^2}{2}\frac{\left(a_{probe}^2 a_{CAP,t}^2 \sin^2\alpha\right)}{\left(a_{probe}^2 + a_{CAP,t}^2\cos^2\alpha\right)}} e^{-2\frac{\sin^2\alpha}{\left(a_{probe}^2 + a_{CAP,t}^2\cos^2\alpha\right)}(v_2 t)^2}$$
$$\times \Im\left\{ e^{i\omega_{B,t}\left[\frac{\left(a_{probe}^2 + a_{CAP,t}^2\right)\cos\alpha}{\left(a_{probe}^2 + a_{CAP,t}^2\cos^2\alpha\right)} t + \frac{z_0}{v_2}\right]} \left[1 + \mathrm{erf}\left(\sqrt{2}\frac{x_A(t)}{a_{overlap,t,\alpha}} + \sqrt{2}\frac{v_2 t \sin\alpha}{a_{CAP,t}^2\cos^2\alpha} a_{overlap,t,\alpha} - i\sqrt{\frac{k_1^2}{2}\frac{\left(a_{probe}^2 a_{CAP,t}^2\sin^2\alpha\right)}{\left(a_{probe}^2 + a_{CAP,t}^2\cos^2\alpha\right)}}\right)\right]\right\}. \tag{4.35}$$

The structure of the transmitted CAP contribution to the TDBS signal, in the case where $(v_2/v_1) < 1$ [Eq. (4.35)], is the same as in the reflected situation where $0 < \theta \leq \pi/4$ [Eqs. (4.29) and (4.33)]. The involved quantities are just scaled from those in material (1) to those in material (2) because of the transmission of the CAP: $v_1 \to v_2$, $l_{CAP} \to l_{CAP,t}$, $r_{12}^{ac} \to t_{12}^{ac}$, $\omega_B \to \omega_{B,t} = (v_2/v_1)\omega_B$, $a_{CAP} \to a_{CAP,t}$ and correspondingly $a_{overlap,\alpha} \to a_{overlap,t,\alpha}$. The dependences of the angle α on the inclination angle of the interface θ in the solutions of Eqs. (4.29) and (4.35) are different: $\alpha = \pi - 2\theta \to \alpha = \theta - \theta_t$. Thus, the physical sense of all the characteristic times influencing the dynamics of the transmitted CAP contribution to the TDBS signal can be revealed from the analysis accomplished in Secs. 4.3.1 and 4.3.2. To finally illustrate the discussion, Fig. 4.12 provides the contribution of the transmitted CAP to the TDBS signal (solid oscillating pink curves) along with their amplitude envelopes, as a function of the inclination θ of the interface, normalized with the parameters associated to ceria. In Fig. 4.12 (b), the envelopes of the contribution to the TDBS signal from the transmitted CAP are presented separately for better appreciation. Three specific envelopes are highlighted with colors, instead of using black lines in Fig. 4.12, corresponding to the cases $\theta = 0°$ (blue), $\theta = 20°$ (green) and $\theta = 40°$ (orange). The situation computed correspond to $(v_2/v_1 = 0.9219 < 1)$ and the normalized time interval is 2.5 times longer than the results of Secs. 4.3.1 and 4.3.2 (incident and reflected CAP contributions) in order to better appreciate the gradual amplitude decrease of the contribution to the TDBS signal associated to the transmitted CAP. In accord with the results of Secs. 4.3.1 and 4.3.2 for the incident and reflected contributions, in the case of an interface parallel to the free surface of material (1), $\theta = 0°$, the contribution of the transmitted CAP to the full TDBS signal is starting/emerging when the CAP reaches the interface [blue envelope in Fig. 4.12]. However, this contribution does not disappear with increasing θ as abruptly as the contribution from the reflected CAP [Fig. 4.10]. Contrarily, the envelope amplitude is decreasing on a larger time scale, *e.g.*, falling to the $1/e^2$ level in more than 30 period T_{LA}^{min} of the slowest LA mode in ceria $(\bar{t}(1/e^2) > 30)$ for $\theta = 20\,°$ [green line in Fig. 4.12 (b)], way after the reflected (less than 1 period) and incident (less than 5 periods) contributions. It also means that the transmitted CAP contribution to the TDBS signal is the strongest contribution to the full TDBS signal after few periods of oscillations T_{LA}^{min}.

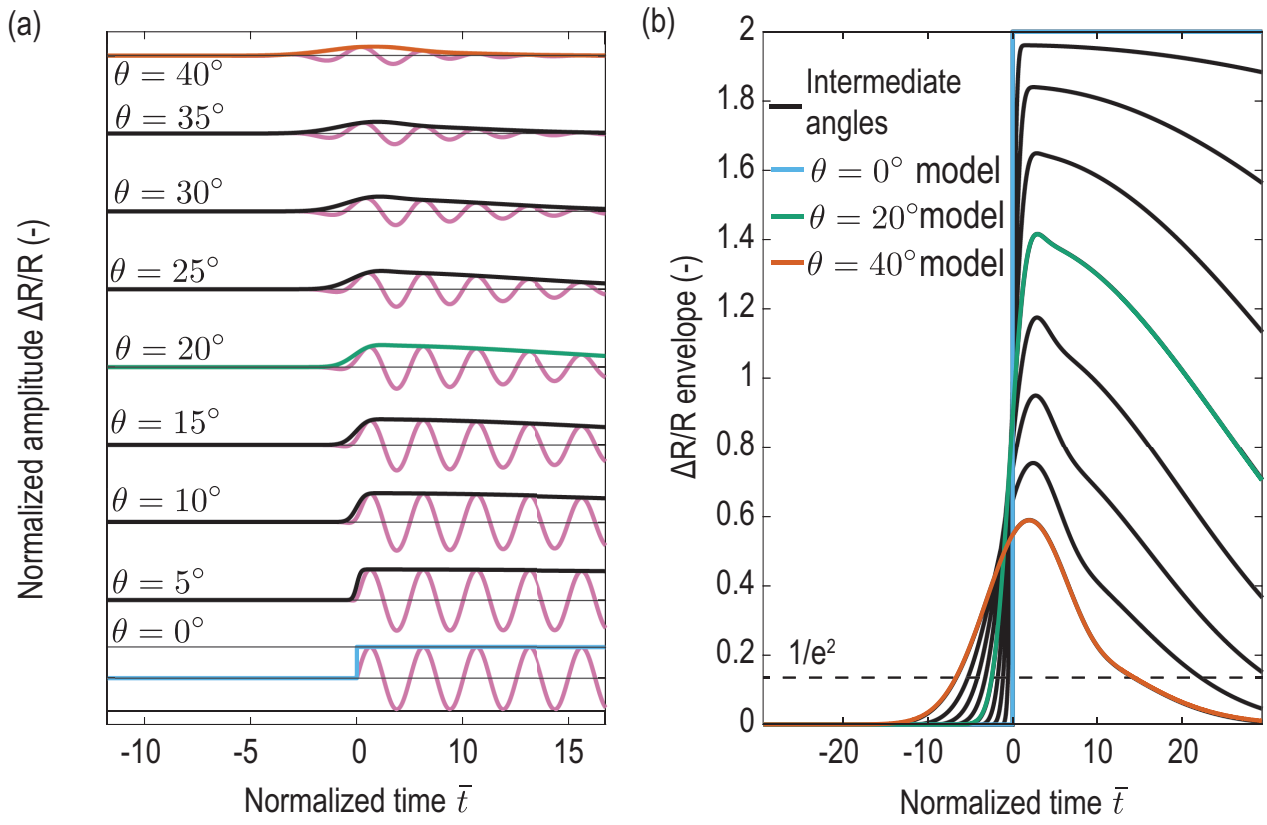

Figure 4.12 – Contribution to the TDBS signal from the transmitted CAP [Eq. (4.35)] as a function of the interface inclination angle θ, using the material properties of ceria as an example. (a) Normalized contribution of the transmitted CAP to the TDBS (solid oscillating pink curves) for $\theta \in [0°, 40°]$, with 5° steps, and associated envelopes (in solid black lines + 3 colored lines). The contributions are upshifted for better visualization. (b) Normalized contribution of the transmitted CAP to the TDBS envelopes (in solid black lines + 3 colored lines) for $\theta \in [0°, 40°]$, with 5° steps. The spatial variables in Eq. (4.29) are normalized by the CAP beam radius a_{CAP}, while the carrier (Brillouin) oscillations frequencies Ω_B and $\Omega_{B,t}$, the CAP velocities v_1 and v_2 in material (1) and (2) and the time t are normalized by the oscillation frequency, the velocity and the period T_{LA}^{min} associated to the slowest LA mode in ceria [Tab. 3.4].

This "disappearance" time scale can again be related to the evolution of the overlap volume of the CAP and probe light beams. Since the deviation angle θ_t between the transmitted CAP and the probe light propagation directions is smaller compared to the deviation angle 2θ between the reflected CAP and the probe light propagation directions, then the overlap volume is decreasing slower in the case of the transmitted CAP than in the case of the reflected CAP.

The complementary case of CAP transmission when $1 < (v_2/v_1) < 1/\sin\theta$ and for $0 \leq \theta < \pi/4$ is illustrated in Fig. 4.13 (note that, for $(v_2/v_1) > 1/\sin\theta$, the CAP incident on the interface exhibits internal reflection). The position of the transmitted CAP front in this case is in the same spatial region as in the previous configuration depicted in Fig. 4.11, which leads to the same integration in Eq. (4.4). Hence, the solution in Eq (4.35) is valid for all possible transformations of the CAP in propagating (non-evanescent) transmitted CAP beam. The modified transient factor of the transmitted CAP contribution

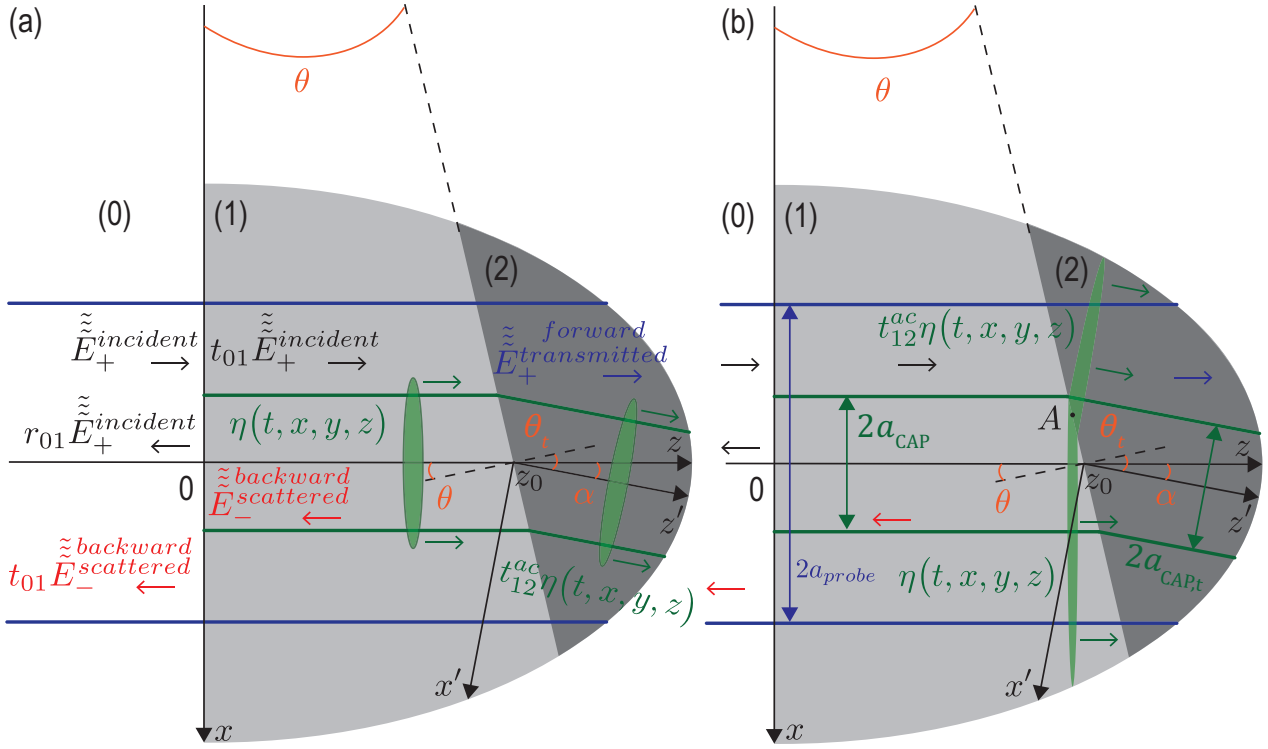

Figure 4.13 – (a) Simplified and (b) detailed sketches of TDBS monitoring of the CAP transmission (refraction) at the interface between two materials inclined at an angle $0 \leq \theta < \pi/4$ relatively to the free surface ($z = 0$) of material (1) ($z > 0$), in the case $1 < v_2/v_1 < 1/\sin\theta$. The probe light beam is not refracted nor reflected by the material interface since both materials have the same optical properties. Continuous green and blue lines present, inside their Rayleigh ranges, the CAP and laser beams respectively. The CAPs are additionally presented by (green) ellipses to illustrate their strong localization along the propagation direction caused by their ultrashort duration. In (b), the simplified CAP beam representation of finite $2a_{cap}$ lateral distribution shown in (a) is made more accurate to account for the infinite lateral dimension of the Gaussian CAP beam.

to the TDBS signal is:

$$G_t\left(\frac{v_2}{v_1} < \frac{1}{\sin\theta}\right) \equiv \left[1 + \mathrm{erf}\left(\sqrt{2}\frac{x_A(t)}{a_{overlap,t,\alpha}} - \sqrt{2}\frac{v_2 t \sin\alpha}{a_{CAP,t}^2\cos^2\alpha}a_{overlap,t,\alpha} + i\sqrt{\frac{k_1^2}{2}\frac{\left(a_{probe}^2 a_{CAP,t}^2\sin^2\alpha\right)}{\left(a_{probe}^2 + a_{CAP,t}^2\cos^2\alpha\right)}}\right)\right]. \tag{4.36}$$

Obviously, the dynamics of the factor G_t can be revealed by scaling the dynamics of $G_r\left(0 < \theta < \frac{\pi}{4}\right)$ [Eq. (4.33)]. The only difference in the mathematical solutions for the transmission dynamics presented in Fig. 4.11 and Fig. 4.13 is that, in the latter case, the following change in the definition of α is required

in Eqs. (4.35) and (4.36), depending on the order relation between v_1 and v_2:

$$\begin{cases} \alpha\left(\dfrac{v_2}{v_1} < 1\right) = \theta - \theta_t, \\ \alpha\left(1 < \dfrac{v_2}{v_1} < \dfrac{1}{\sin\theta}\right) = \theta_t - \theta. \end{cases} \tag{4.37}$$

The theoretical results obtained in the previous three sections, on the contribution to the TDBS signal coming from the incident, reflected and refracted (transmitted) CAPs that are obtained at a material interface, inclined relative to the collinear probe light and incident CAP beams, have been illustrated in a general manner. In the frame of concluding these sections, a final section presents a preliminary attempt of using the developped theory to extract the inclination angle of a material interface observed in the ceria scan [Sec. 3.4.2] from the TDBS signals.

4.3.4 Experimental TDBS measurements with inclined material interfaces: preliminary attempts

In Sec. 3.4.2, the inclination angle of the interface between two differently oriented grains of ceria has been evidenced and estimated via the extraction of the depth at which the frequency of the LA mode was shifted, as well as the depth of the amplitude drop to the noise level of the TA mode. More precisely, the mean inclination of an area of $\sim 3{\times}3$ µm^2, about 3 µm below the OAT / ceria ($z = 0$ µm) interface, was obtained from the two depth-surfaces, and compared to the alphashape results, leading to an agreeing inclination angle of $23.5 \pm 0.5°$. The aim of this final section is to test the developed theory for the TDBS in the vicinity of such inclined interface and, ultimately, estimate the interaction angle of the interface from a single measurement, *i.e.*, on a smaller scale than what was obtained in Sec. 3.4.2, and maybe account for the possible "roughness" (rugosity) character of the interface.

Before starting, the reader should be aware that these results represent ongoing work and that conclusions are yet to be drawn. The discussed results can thus be interpreted as short time-scale "perspectives" of this work.

In Sec. 3.4.2, a second buried interface has been identified even though not discussed in details. Visible in the imaging results of the ceria scan [Fig. 3.23 (e)], this interface is only identified by the frequency shifting of the LA mode, from the upper grain (1) $\sim$ 62 GHz (purple grain) to the lower grain (2) $\sim$ 66 GHz (orange grain), around the area: $x = [10, 20]$ µm and $y = [20, 25]$ µm, at $\sim$ 6 µm from the OAT / ceria ($z = 0$ µm) interface.

One TDBS signal of this area is selected [Fig. 4.14 (a)] to apply the developed theory discussed in the current Chapter. The reason for choosing this interface instead of the one characterized in the imaging results [Sec. 3.4.2] is that, in the situation proposed by this second interface, the LA mode contribution is free from the influence of both TA modes, since the interface is too far ($\sim$ 6 µm) from the OAT / ceria ($z = 0$ µm) interface compared to the estimated maximum depth of TA mode detection ($\sim$ 4 µm, *i.e.* half the LA mode one) [Sec. 3.4.2]. The frequency shifting due to the velocity change in the LA mode

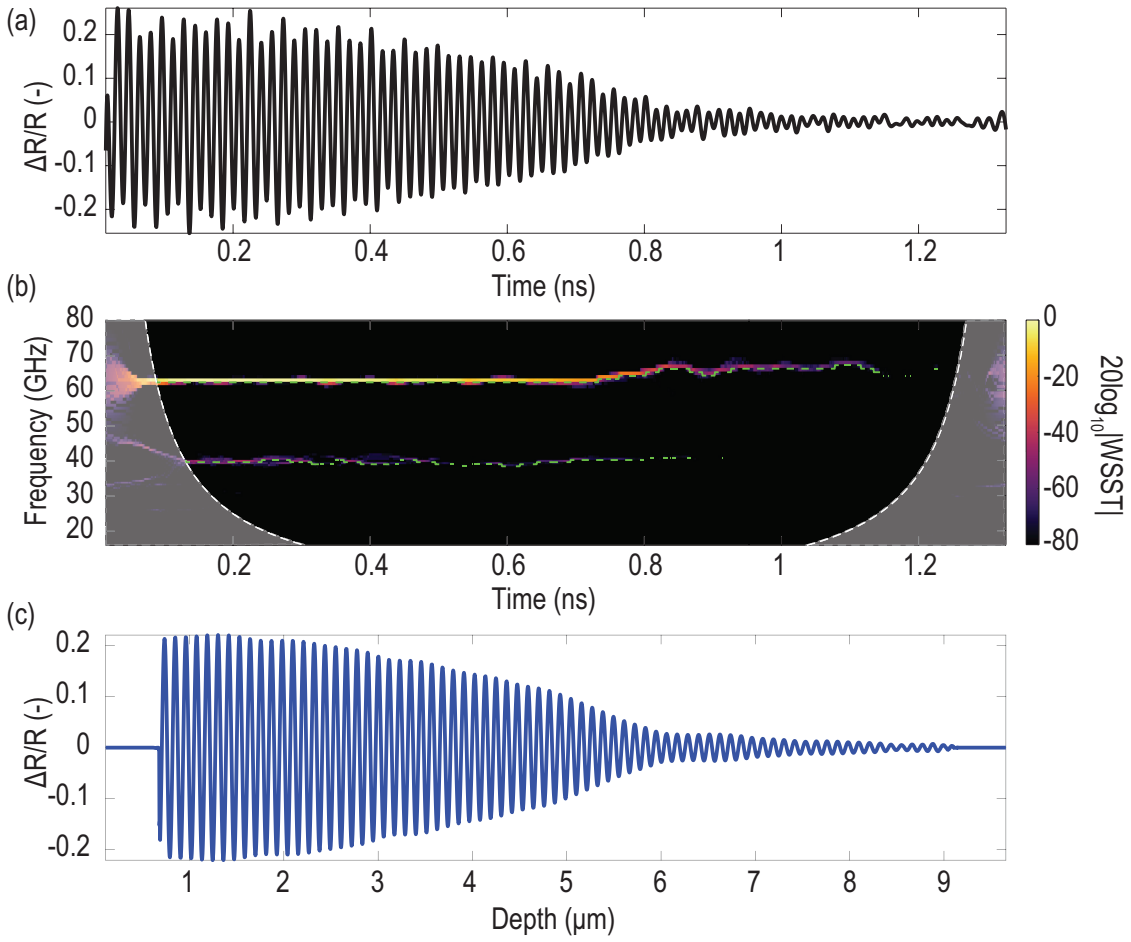

Figure 4.14 – WSST-based study of the signal located at $x = 10.79$ µm and $y = 26.26$ µm of the ceria scan. (a) Acoustic signal (filtered raw TDBS signal) located at coordinates $x = 10.79$ µm and $y = 26.26$ µm of the ceria scan. (b) WSST-based spectrogram of the acoustic signal (a), with associated ridges extracted (dashed green lines). The cone of influence of the CWT is given by the white dashed curves and associated shadowed area from the edges of the signal. (c) Reconstructed mode from the extracted ridge associated to the LA mode contribution [highest frequency ridge in (b)] using the IWSST.

propagation induced when the CAP crosses the interface is clearly resolved in Fig. 4.14 (b) with the ridge associated, extracted from the WSST-based processing of the chosen acoustic signal [Fig. 4.14 (a)] to the propagation of the LA mode (from $\sim$ 62 GHz to $\sim$ 66 GHz). This upshifting observed at $\sim$ 0.8 ns (hence $\sim$ 5.6 µm) corresponds to an acceleration of the LA mode from $\sim$ 6 998 $\mathrm{m\,s^{-1}}$ to $\sim$ 7 450 $\mathrm{m\,s^{-1}}$. The contribution of one TA mode is also observed around $\sim$ 40 GHz but is not discussed since the developed theory is only taking into account the LA mode. The contribution from the LA mode to the TDBS signal is reconstructed by applying the IWSST to the associated ridge, and give access to the targeted signal to be obtained from the theory [Fig. 4.14 (c)]. This signal is mentioned as the LA signal in the following. First, the LA signal is compared with the Gaussian model [Eq. (3.14)] used in Sec. 3.4.2 to assess the limit of depth imaging [Fig. 4.15 (a)]. The Gaussian model uses the parameters linked to

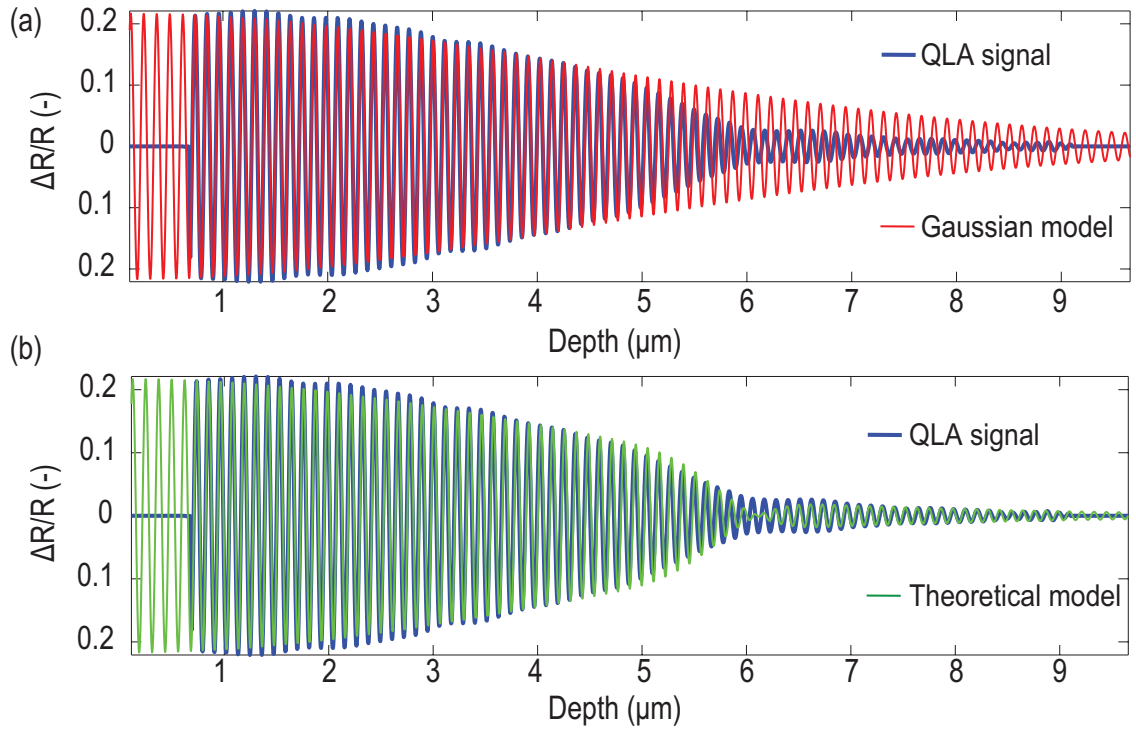

Figure 4.15 – Comparison of the Gaussian model [Eq. (3.14)] and the developed theoretical model to the reconstructed LA signal. (a) LA mode signal and Gaussian model comparison. (b) LA mode signal and theoretical model obtained with Eqs. (4.27) (for the incident part), (4.29) and (4.33) (for the reflected part) and (4.35) (4.36) (for the transmitted part).

the propagation of the CAP before reaching the interface (Brillouin frequency) and the coherence time estimated in Sec. 3.4.2 when estimating the imaging depth limitation. The purpose is to highlight the frequency shifting and the amplitude drop, when compared to the TDBS signal that should have been obtained if the CAP was propagating in an homogeneous grain with the same properties as grain (1), *i.e.*, the upper grain of the interface.

Then, the expected contributions of the incident [Eq. (4.27)], the reflected [Eqs. (4.29) with (4.33)] and the transmitted [Eqs. (4.35) with (4.36)] CAPs are computed for an estimated angle of 30°, the estimated value being obtained with the same technique as in Sec. 3.4.2 with the surface of depth of frequency shifting, and the sum of these three contributions is compared to the LA signal [Fig. 4.15 (b)].

The amplitude tendency between the LA signal and the model are in better agreement than with the Gaussian model [Fig. 4.15 (a)], but are still far from being perfect. What is observed is that the contribution from both the incident and transmitted CAPs are resolved with the good oscillation frequency, but the transition part is still to be better estimated (in both amplitude and phase). To do so, the same fitting techniques as in Secs. 3.3.1 and 3.4.2 were tried but without success so far. The reason might comes from the fact that nonlinear least mean square algorithms might not be suited to such fittings, with particularly complicated models with many parameters.

To conclude, the theory is leading to encouraging results but better fitting / minimisation procedure needs to be used to be capable of optimizing such models as complicated as the one developed with the theory so far. The model could also be simplified by not taking into account the reflected contribution since for these inclination angles, it has been shown that its contribution should be negligible compared to the two others.

4.4 Conclusion

In conclusion, the TDBS theory has been extended to the situation where the CAP is reflected and refracted by a material interface during its propagation, leading to the non-collinear propagation direction between the probe light beam and the CAP beam, under the assumption of Gaussian beams. A first section is dedicated to the study of the expected TDBS signal to be recorded with a photodetector in the case where a CAP, regardless of its generation origin, is interacting at a relative angle with the classical probe light beam with a propagation direction oriented along the normal to the OAT surface. This interaction in "free-space" in a homogeneous and isotropic material predicts a wave packet form for the TDBS signal, which amplitude and carrier frequency are precisely studied.

Interestingly, the carrier frequency of the wave packet is depending on the angle between the probe light and CAP beams propagation directions (as expected), but also on their radius and the CAP length along its propagation direction. It is thus showed that two regimes exist, a classical one where the carrier frequency is only decreasing, and a second one where the frequency first increases up to a maximum before decreasing when the angle is increasing.

The variations of the amplitude of the wave packet is studied as a function of the angle. The TDBS detection appears strongly directive especially for the TDBS imaging configuration where both probe and CAP beams radii are of the same order. An expected strong amplitude drop is evidenced when the interaction angle is increased and explained by the fact that an increase of the inclination angle between the probe light and CAP beams is accompanied by a decrease in the number of photons and phonons propagating collinearly (or quasi-collinearly), hence decreasing the amount of scattered light to be detected via heterodyning.

A second section aims to describe theoretically the situation encountered in ceria imaging where, initially, the probe light and the CAP beams are propagating collinearly, before reaching an inclined material interface where the CAP beam is reflected and refracted, but not the probe light beam. Hence, the expected contributions to the TDBS signal arising from the incident, reflected and refracted CAPs are derived. The variations of these contributions with increasing inclination angle are given and it is possible to conclude that: (i) even for small inclination angles, the contribution from the reflected CAP is negligible when compared to the two others, and (ii) the contribution from the refracted (transmitted) CAP are resolved after crossing the interface for several Brillouin oscillation periods even for important inclination angle, confirming the potential of imaging with TDBS such interfaces. Finally, a first attempt of using the developed theory to estimate, from reasonable larger-scale values obtained with another method, the inclination angle from a material interface in ceria is presented even if conclusions are not drawn upon the results. Dedicated fitting methods for such a complicated model needs to be developed/tested to extract with confidence the parameters, such as the OAT / material interface distance and the inclination angle of the interface.

Perspectives of this work are discussed in the general conclusions of this manuscript.

GENERAL CONCLUSION

Conclusion

This thesis reports on the development of an opto-acousto-optical method to image the 3-D nanometric structure of transparent materials by monitoring with time-domain Brillouin scattering (TDBS) the propagation of laser-generated acoustic pulses.
In a first Chapter, the state of the art, the TDBS method is positioned in relation to a variety of nanoscale imaging techniques relying on different physical mechanisms to probe the sample structure.
A second Chapter introduces the theoretical background of the opto-acousto-optical method used. The thermoelastic generation of acoustic pulses in metallic films is presented in the 1-D case, and the detection of these acoustic pulses in transparent materials via TDBS is detailed. The Chapter concludes with the theoretical and experimental study of the possibility to generate and detect transversal acoustic waves in transparent crystals using the same technique.
In the third Chapter, from the experimental acquisition of transient reflectivity scans, with an ultrasfast setup, a dedicated step-by-step signal processing procedure is developed to reconstruct the structure of the samples studied. The procedure is divided in three steps, a first one to extract the acoustic content from the reflectivity signals, a second step to compute the time-frequency analysis of the acoustic content and finally, a third step, to shape the structure of the scanned samples from the results of the second step.
The processing method is applied to the study of two transparent polycrystalline materials: a high pressure water ice and a cerium dioxyde (ceria) polycrystals. In the first case, a water ice sample is obtained at ambient temperature by the compression of a water droplet up to GPa pressure in a diamond anvil cell. The sample is composed of two ice phases (phase VI and VII) with different crystalline structures. The obtained $100\times100\times10$ µm^3 3-D image of the sample highlights the coexistence of grains of both phases. The imaging results obtained with the longitudinal acoustic mode allow to study the evolution of these grains with depth. In the second sample, ceria, it is by a high-temperature curing of the sample that multiple grains (crystallites) are formed, creating a perfect playground for testing the imaging method. A $30\times30\times8$ µm^3 volume of the sample is analyzed and the 3-D structure of multiple grains is reconstructed with the use of longitudinal acoustic waves and the crucial one of transversal acoustic waves. Indeed, large grains that appeared as homogeneous under the processing of the longitudinal acoustic modes, revealed to be in fact composed of smaller grains thanks to the detection of transversal acoustic modes, as confirmed by an electron backscattering diffraction pattern (EBSD). The surface image of the sample obtained with both acoustic modes matched the EBSD results thanks to higher

sensitivity to anisotropy of the transversal acoustic modes, confirming their necessity for complete 3-D imaging of samples with TDBS. The evolution of the grain boundaries with depth revealed interesting inclined interfaces between differently oriented grains, evidenced by the changes in the phase (amplitude) of the part of the TDBS signal associated to the longitudinal (transversal) mode.
The fourth and final Chapter of this thesis extends the TDBS theory introduced in Chap. 2 for the situation where the probe light beam and the acoustic pulse are propagating in different directions, instead of being collinear. This extension of the theory arises in the frame of studying the reflection and refraction of the acoustic pulse when it reaches a buried inclined interface, like the ones observed in the ceria scan. Study of the interaction of the light and acoustic pulse in free space showed how strongly directive the TDBS detection is, an abrupt amplitude drop in the detected signal being expected when the interaction angle between the propagation directions of light and sound is increased. Changes in the Brillouin frequency showed the expected decreasing behavior on the one hand, as well as an unexpected increase on the other hand, depending on the radius of both light and sound Gaussian beams, and on the acoustic pulse length. Development of the theory to the buried inclined interface situation allowed to anticipate the expected TDBS signals to be detected from the incident, reflected and refracted (transmitted) part of the acoustic pulse. A rather good agreement is found in a first attempt to compare the theory with experimental signals from the ceria scan, but complementary work needs to be done to draw conclusions.

Perspectives

The general perspectives of this work is the progressive enhancement of each step of the imaging, from the experimental TDBS scans to the extension of the actual TDBS theory for non-collinear beams to include more physical phenomena and more complex anisotropic materials.
From the experimental point of view, among the possible imaging-enhancing features, at first, different pump and especially probe wavelengths could be used to scan the sample and maybe enhance the generation and/or detection of transversal acoustic modes, that showed to be required for complete 3-D imaging. Smaller optical wavelength, and tighter focusing would lead to better spatial resolutions with sample that would not suffer damaging. Also, in the ceria scan, some of the "imaged" grains were located by the absence of transversal acoustic mode detection. The use of different probe light wavelength and/or polarizations, or the deviation from the normally-inclined probe could require important technical modifications but would pave the way to complete 3-D imaging of all the grains, for the sample that permits it (for example inclined probe for the compressed ice sample would require more technical modifications to be tried due to the geometry of the diamond anvil cell and the large refractive index of diamond).
The improvement of the TDBS scans will consequently increase the data volume, requiring more work on the signal processing procedure to handle such increased volume, as well as on the improvement of the final image quality and resolution. The limitations of the powerful wavelet synchrosqueezed transform are found in the situation where mode contributions with close frequencies need to be extracted. The

increase of the number of voices per octave when computing the continuous wavelet transform could enhance the resolution (until reaching a point where artefacts would appear during the synchrosqueezing) with the drawback of taking more time for the computation. The main perspective from the code point of view would be its optimization in terms of calculation and time costs, where scans with huge amount of data would face time issues. One possibility could be the use of neural networks in steps 2 and/or 3 of the processing, for the segmentation of data and the "constitution" of the different grains. Deep learning algorithm would ultimately be a good way to process such huge amount of data, like for example in Ref. [87] where they used neural network to retrieve the grain surface orientations from TDBS measurements. Additionally, in relation to this last step, the unfinished transition from coding with MATLAB to coding with PYTHON is necessary.

Finally, obtaining better images of the sample from enhanced scans will require a focus on the developed models, especially in the configuration of non-collinear probe and CAP beams propagation directions, to convincingly explain the observed signals. However, first, the application of the developed theory to retrieve the inclination angle in purposely-designed samples with known inclinations would confirm the starting point of the theory, opening the way to more complexity in the models. Ultimately, the inverse problem could be then applied to estimate the inclination angle of an unknown buried interface of ceria, from a single point measurement. Extension of the theory to more complicated situations could be considered, like taking into account the acoustic mode conversion at the material interface that could justify different frequency components observed in the TDBS signals. To conclude with the acoustic part of the model, the extension of the theory to transversal acoustic mode would permit to use more information from the scan to fit the models (thanks to the mode separation provided by the wavelet synchrosqueezed transform). From the optical point of view, arbitrary polarized probe light, that would require more than a single photoelastic constant for the description of its interaction with phonons, could be considered. The extension to optical anisotropy, would ultimately lead to more complex models, which include different optical modes, but would encompass even more materials candidates. In the situation where all three acoustic modes are included, the reflection and transmission coefficients of the probe light, reflected by the sample and scattered by the acoustic pulse, would need to be considered for each of the optical modes. Adding complexity to the model will increase the number of parameters to be retrieved when solving the (ill-posed) inverse problem, a task for which the signal processing procedure will need to be definitely improved and where the use of neural-network-based approach could be of interest, especially using physics-informed neural networks embedding physical insight in the cost functions.

Appendix A

Table regrouping Au, W and Ti material characteristics for Sec. 2.2 computations

Material parameters (from [163])	Notation	Au	W	Ti
Optical (effective) refractive index at λ_{pump}	n	0.5	3.45	1.81
Extinction coefficient at λ_{pump}	κ	1.86	2.72	2.47
Density ($\mathrm{g\,cm^{-3}}$)	ρ	19.3	19.3	8.96
Specific heat ($\mathrm{J\,kg^{-1}\,K^{-1}}$)	C	129	132	524
Electric resistivity (10^{-8} hom m)	ρ_{elec}	2.255	5.39	39
Deduced material parameters				
Reflection coefficient (optical intensity) with air	$R = \frac{(1-n)^2+k^2}{(1+n)^2+k^2}$	0.65	0.49	0.48
Heat capacity per unit volume (10^6 $\mathrm{J\,m^{-3}\,K^{-1}}$)	C_v	2.49	2.55	2.36
Electric conductivity (10^6 $\mathrm{S\,m^{-1}}$)	σ_{elec}	44.3	18.55	2.56
Light penetration depth at λ_{pump} [Eq. 2.1] (nm)	ζ	5	8.2	10.75
Experimental parameters				
Pump laser wavelength $\lambda_{pump} = 515$ nm				
Pump energy per pulse $Q = 0.3$ nJ				
Pump beam waist radius $a_{pump} = 1.5$ µm				

Table A.1 – Materials parameters used to compute the temperature gradient in Fig. 1.1 (b). The values are taken in Ref. [163] at the following pages: Au: p.12-129 / 12-216, W: p.12.147 / 12.217 and Ti: p.12-146 / 12.217.

BIBLIOGRAPHY

[1]A. G. Bell, "The Photophone", Science **1**, https://www.jstor.org/stable/2900889, 130–134 (1880).

[2]T. H. Maiman, "Stimulated Optical Radiation in Ruby", Nature **187**, 493–494 (1960).

[3]R. M. White, "Generation of Elastic Waves by Transient Surface Heating", Journal of Applied Physics **34**, 3559–3567 (1963).

[4]L. Brillouin, "Diffusion de la lumière et des rayons X par un corps transparent homogène - Influence de l'agitation thermique", Annales de Physique **9**, 88–122 (1922).

[5]L. Mandelstam, "Light scattering by inhomogeneous media", **58**, 146 (1926).

[6]C. Thomsen, J. Strait, Z. Vardeny, H. J. Maris, J. Tauc, and J. J. Hauser, "Coherent Phonon Generation and Detection by Picosecond Light Pulses", Physical Review Letters **53**, 989–992 (1984).

[7]S. Sandeep, T. Thréard, E. De Lima Savi, N. Chigarev, A. Bulou, V. Tournat, A. Zerr, V. E. Gusev, and S. Raetz, "3D characterization of individual grains of coexisting high-pressure H2O ice phases by time-domain Brillouin scattering", Journal of Applied Physics **130**, 053104 (2021).

[8]T. Thréard, E. de Lima Savi, S. Avanesyan, N. Chigarev, Z. Hua, V. Tournat, V. E. Gusev, D. H. Hurley, and S. Raetz, "Photoacoustic 3-D imaging of polycrystalline microstructure improved with transverse acoustic waves", Photoacoustics, 100286 (2021).

[9]V. E. Gusev, T. Thréard, D. H. Hurley, and S. Raetz, "Theory of time-domain Brillouin scattering for probe light and acoustic beams propagating at an arbitrary relative angle: application to acousto-optic interaction near material interfaces", arXiv:2107.05294 [cond-mat, physics:physics] (2021).

[10]E. Abbe, "Beiträge zur Theorie des Mikroskops und der mikroskopischen Wahrnehmung", Archiv für Mikroskopische Anatomie **9**, 413–468 (1873).

[11]T. J. Jones and R. D. Gehrz, "Infrared Imaging Polarimetry of Comet C/1995 01 (Hale–Bopp)", Icarus **143**, 338–346 (2000).

[12]N. Nyayapathi and J. Xia, "Photoacoustic imaging of breast cancer: a mini review of system design and image features", Journal of Biomedical Optics **24**, 121911 (2019).

[13]D. Stucht, K. A. Danishad, P. Schulze, F. Godenschweger, M. Zaitsev, and O. Speck, "Highest Resolution In Vivo Human Brain MRI Using Prospective Motion Correction", PLoS ONE **10**, e0133921 (2015).

[14]S. J. Matzat, J. van Tiel, G. E. Gold, and E. H. G. Oei, "Quantitative MRI techniques of cartilage composition", Quantitative Imaging in Medicine and Surgery **3**, 162–174 (2013).

[15]J. Blitz and G. Simpson, *Ultrasonic Methods of Non-destructive Testing*, Non-Destructive Evaluation Series (Springer Netherlands, 1995).

[16]E. Ruska, "The development of the electron microscope and of electron microscopy", Bioscience Reports **7**, 607–629 (1987).

[17]J. I. Goldstein, D. E. Newbury, J. R. Michael, N. W. Ritchie, J. H. J. Scott, and D. C. Joy, *Scanning Electron Microscopy and X-Ray Microanalysis* (Springer New York, New York, NY, 2018).

[18]A. J. Schwartz, M. Kumar, B. L. Adams, and D. P. Field, eds., *Electron Backscatter Diffraction in Materials Science* (Springer US, Boston, MA, 2009).

[19]G. Binnig, H. Rohrer, C. Gerber, and E. Weibel, "Surface Studies by Scanning Tunneling Microscopy", Physical Review Letters **49**, 57–61 (1982).

[20]K. Bian, C. Gerber, A. J. Heinrich, D. J. Müller, S. Scheuring, and Y. Jiang, "Scanning probe microscopy", Nature Reviews Methods Primers **1**, 36 (2021).

[21]G. Binnig, C. F. Quate, and C. Gerber, "Atomic Force Microscope", Physical Review Letters **56**, 930–933 (1986).

[22]C. Moreno, O. Stetsovych, T. K. Shimizu, and O. Custance, "Imaging Three-Dimensional Surface Objects with Submolecular Resolution by Atomic Force Microscopy", Nano Letters **15**, 2257–2262 (2015).

[23]M. Knoll and E. Ruska, "Das Elektronenmikroskop", Zeitschrift für Physik **78**, 318–339 (1932).

[24]L. E. Franken, K. Grünewald, E. J. Boekema, and M. C. A. Stuart, "A Technical Introduction to Transmission Electron Microscopy for Soft-Matter: imaging, Possibilities, Choices, and Technical Developments", Small **16**, 1906198 (2020).

[25]M. A. O'Keefe, P. R. Buseck, and S. Iijima, "Computed crystal structure images for high resolution electron microscopy", Nature **274**, 322–324 (1978).

[26]R. Ramachandra and N. de Jonge, "Optimized Deconvolution for Maximum Axial Resolution in Three-Dimensional Aberration-Corrected Scanning Transmission Electron Microscopy", Microscopy and Microanalysis **18**, 218–228 (2012).

[27]M. Holt, R. Harder, R. Winarski, and V. Rose, "Nanoscale Hard X-Ray Microscopy Methods for Materials Studies", Annual Review of Materials Research **43**, 183–211 (2013).

[28]P. J. Withers, C. Bouman, S. Carmignato, V. Cnudde, D. Grimaldi, C. K. Hagen, E. Maire, M. Manley, A. Du Plessis, and S. R. Stock, "X-ray computed tomography", Nature Reviews Methods Primers **1**, 1–21 (2021).

[29]J. Daillant and A. Gibaud, eds., *X-ray and Neutron Reflectivity: principles and Applications*, Lecture Notes in Physics (Springer-Verlag, Berlin Heidelberg, 2009).

[30]M. Dierolf, A. Menzel, P. Thibault, P. Schneider, C. M. Kewish, R. Wepf, O. Bunk, and F. Pfeiffer, "Ptychographic X-ray computed tomography at the nanoscale", Nature **467**, 436–439 (2010).

[31]R. S. C. Cobbold, *Foundations of Biomedical Ultrasound* (Oxford University Press, Oxford, New York, Sept. 2006).

[32]M. Maldovan, "Sound and heat revolutions in phononics", Nature **503**, 209–217 (2013).

[33]C. V. Raman, "A new radiation [Reproduced from Indian J. Phys., 1928, 2, 387–398]", Current Science **74**, 382–386 (1998).

[34]T. P. Gill, *The Doppler effect; an introduction to the theory of the effect* (Logos Press, London, 1965).

[35]K. J. Koski and J. L. Yarger, "Brillouin imaging", Applied Physics Letters **87**, 061903 (2005).

[36]G. Scarcelli, W. J. Polacheck, H. T. Nia, K. Patel, A. J. Grodzinsky, R. D. Kamm, and S. H. Yun, "Noncontact three-dimensional mapping of intracellular hydromechanical properties by Brillouin microscopy", Nature Methods **12**, 1132–1134 (2015).

[37]V. Babacic, D. Saleta Reig, S. Varghese, T. Vasileiadis, E. Coy, K.-J. Tielrooij, and B. Graczykowski, "Thickness-Dependent Elastic Softening of Few-Layer Free-Standing MoSe2", Advanced Materials **33**, 2008614 (2021).

[38]T. Vasileiadis, H. Zhang, H. Wang, M. Bonn, G. Fytas, and B. Graczykowski, "Frequency-domain study of nonthermal gigahertz phonons reveals Fano coupling to charge carriers", Science Advances **6**, 10.1126/sciadv.abd4540 (2020).

[39]N. W. Ashcroft, A. W, and N. D. Mermin, *Solid State Physics* (Holt, Rinehart and Winston, 1976).

[40]V. Ė. Gusev and A. A. Karabutov, *Laser optoacoustics*, Translation of: Lazernaia optoakustika (New York : American Institute of Physics, 1993).

[41]P. Ruello and V. E. Gusev, "Physical mechanisms of coherent acoustic phonons generation by ultrafast laser action", Ultrasonics **56**, 21–35 (2015).

[42]C. B. Scruby and L. E. Drain, *Laser Ultrasonics Techniques and Applications* (CRC Press, Jan. 1990).

[43]F. A. McDonald, "Photoacoustic, photothermal, and related techniques: a review", Canadian Journal of Physics, 10.1139/p86-174 (2011).

[44]F. Lepoutre, "Coupled equations of modulated photothermal effects, hypotheses and solutions", Le Journal de Physique Colloques **44**, C6-3-C6–8 (1983).

[45]D. Fournier, B. C. Forget, C. Boué, and J. P. Roger, "Micron scale photothermal imaging. Based on a paper presented as a plenary talk at Eurotherm Seminar No. 57 "Microscale Heat Transfer", Poitiers, France, July 8–10, 1998", International Journal of Thermal Sciences **39**, 514–518 (2000).

[46]J. M. Atkin, S. Berweger, A. C. Jones, and M. B. Raschke, "Nano-optical imaging and spectroscopy of order, phases, and domains in complex solids", Advances in Physics **61**, 745–842 (2012).

[47]S. Manohar, R. G. H. Willemink, F. van der Heijden, C. H. Slump, and T. G. van Leeuwen, "Concomitant speed-of-sound tomography in photoacoustic imaging", Applied Physics Letters **91**, 131911 (2007).

[48]G. Rousseau, A. Blouin, and J.-P. Monchalin, "Non-contact photoacoustic tomography and ultrasonography for tissue imaging", Biomedical Optics Express **3**, 16–25 (2012).

[49]T. F. Fehm, X. L. Deán-Ben, and D. Razansky, "Four dimensional hybrid ultrasound and optoacoustic imaging via passive element optical excitation in a hand-held probe", Applied Physics Letters **105**, 173505 (2014).

[50]G. Wurzinger, R. Nuster, and G. Paltauf, "Combined photoacoustic, pulse-echo laser ultrasound, and speed-of-sound imaging using integrating optical detection", Journal of Biomedical Optics **21**, 086010 (2016).

[51]A. Bychkov, V. Simonova, V. Zarubin, E. Cherepetskaya, and A. Karabutov, "The Progress in Photoacoustic and Laser Ultrasonic Tomographic Imaging for Biomedicine and Industry: a Review", Applied Sciences **8**, 1931 (2018).

[52]H. T. Grahn, H. J. Maris, and J. Tauc, "Picosecond ultrasonics", IEEE Journal of Quantum Electronics **25**, 2562–2569 (1989).

[53]O. Matsuda, M. C. Larciprete, R. Li Voti, and O. B. Wright, "Fundamentals of picosecond laser ultrasonics", Ultrasonics **56**, 3–20 (2015).

[54]E. B. Cherepetskaya, A. A. Karabutov, E. A. Mironova, N. B. Podymova, and A. N. Zharinov, "Contact Laser-Ultrasonic Evaluation of Residual Stress", Applied Mechanics and Materials **843**, 118–124 (2016).

[55]A. A. Karabutov, N. B. Podymova, and E. B. Cherepetskaya, "Determination of uniaxial stresses in steel structures by the laser-ultrasonic method", Journal of Applied Mechanics and Technical Physics **58**, 503–510 (2017).

[56]V. Zarubin, A. Bychkov, A. Karabutov, V. Simonova, and E. Cherepetskaya, "Laser-induced ultrasonic imaging for measurements of solid surfaces in optically opaque liquids [Invited]", Applied Optics **57**, C70–C76 (2018).

[57]V. Zarubin, A. Bychkov, V. Simonova, V. Zhigarkov, A. Karabutov, and E. Cherepetskaya, "A refraction-corrected tomographic algorithm for immersion laser-ultrasonic imaging of solids with piecewise linear surface profile", Applied Physics Letters **112**, 214102 (2018).

[58]H. Maris, "Picosecond Ultrasonics", Scientific American **278**, 86–89 (1998).

[59]*MetaPULSE G System - Onto Innovation*, https://ontoinnovation.com/products/metapulse-g.

[60]E. F. Carome, N. A. Clark, and C. E. Moeller, "Generation of acoustic signals in liquids by ruby laser-induced thermal stress transients", Applied Physics Letters **4**, 95–97 (1964).

[61]F. W. Cross, R. K. Al-Dhahir, P. E. Dyer, and A. J. MacRobert, "Time-resolved photoacoustic studies of vascular tissue ablation at three laser wavelengths", Applied Physics Letters **50**, 1019–1021 (1987).

[62]A. A. Oraevsky, R. O. Esenaliev, S. L. Jacques, and F. K. Tittel, "Laser optic-acoustic tomography for medical diagnostics: principles", in Biomedical Sensing, Imaging, and Tracking Technologies I, Vol. 2676 (Apr. 1996), pp. 22–31.

[63]A. Karabutov, N. B. Podymova, and V. S. Letokhov, "Time-resolved laser optoacoustic tomography of inhomogeneous media", Applied Physics B **63**, 545–563 (1996).

[64]A. A. Oraevsky, V. A. Andreev, A. A. Karabutov, and R. O. Esenaliev, "Two-dimensional optoacoustic tomography: transducer array and image reconstruction algorithm", in Laser-Tissue Interaction X: photochemical, Photothermal, and Photomechanical, Vol. 3601 (June 1999), pp. 256–267.

[65]V. Ntziachristos, J. Ripoll, L. V. Wang, and R. Weissleder, "Looking and listening to light: the evolution of whole-body photonic imaging", Nature Biotechnology **23**, 313–320 (2005).

[66]P. Beard, "Biomedical photoacoustic imaging", Interface Focus **1**, 602–631 (2011).

[67]C. Lutzweiler and D. Razansky, "Optoacoustic imaging and tomography: reconstruction approaches and outstanding challenges in image performance and quantification", Sensors (Basel, Switzerland) **13**, 7345–7384 (2013).

[68]L. V. Wang and L. Gao, "Photoacoustic Microscopy and Computed Tomography: from Bench to Bedside", Annual Review of Biomedical Engineering **16**, 155–185 (2014).

[69]A. Taruttis and V. Ntziachristos, "Advances in real-time multispectral optoacoustic imaging and its applications", Nature Photonics **9**, 219–227 (2015).

[70]L. V. Wang and J. Yao, "A practical guide to photoacoustic tomography in the life sciences", Nature Methods **13**, 627–638 (2016).

[71]G. Wissmeyer, M. A. Pleitez, A. Rosenthal, and V. Ntziachristos, "Looking at sound: optoacoustics with all-optical ultrasound detection", Light: Science & Applications **7**, 53 (2018).

[72]I. Steinberg, D. M. Huland, O. Vermesh, H. E. Frostig, W. S. Tummers, and S. S. Gambhir, "Photoacoustic clinical imaging", Photoacoustics **14**, 77–98 (2019).

[73]A. Danielli, K. Maslov, A. Garcia-Uribe, A. M. Winkler, C. Li, L. Wang, Y. Chen, G. W. Dorn, and L. V. Wang, "Label-free photoacoustic nanoscopy", Journal of Biomedical Optics **19**, 086006 (2014).

[74]S. Park, C. Lee, J. Kim, and C. Kim, "Acoustic resolution photoacoustic microscopy", Biomedical Engineering Letters **4**, 213–222 (2014).

[75]L. V. Wang and S. Hu, "Photoacoustic Tomography: in Vivo Imaging from Organelles to Organs", Science **335**, 1458–1462 (2012).

[76]G. Ku and L. V. Wang, "Deeply penetrating photoacoustic tomography in biological tissues enhanced with an optical contrast agent", Optics Letters **30**, 507–509 (2005).

[77]C. Thomsen, H. Grahn, H. Maris, and J. Tauc, "Picosecond interferometric technique for study of phonons in the brillouin frequency range", Optics Communications **60**, 55–58 (1986).

[78]H. .-N. Lin, R. J. Stoner, H. J. Maris, and J. Tauc, "Phonon attenuation and velocity measurements in transparent materials by picosecond acoustic interferometry", Journal of Applied Physics **69**, 3816–3822 (1991).

[79]V. Gusev and P. Ruello, "Advances in applications of time-domain Brillouin scattering for nanoscale imaging", Applied Physics Reviews **5**, 031101 (2018).

[80]C. Rossignol, J. M. Rampnoux, M. Perton, B. Audoin, and S. Dilhaire, "Generation and Detection of Shear Acoustic Waves in Metal Submicrometric Films with Ultrashort Laser Pulses", Physical Review Letters **94**, 166106 (2005).

[81]T. Dehoux, K. Ishikawa, P. H. Otsuka, M. Tomoda, O. Matsuda, M. Fujiwara, S. Takeuchi, I. A. Veres, V. E. Gusev, and O. B. Wright, "Optical tracking of picosecond coherent phonon pulse focusing inside a sub-micron object", Light: Science & Applications **5**, e16082–e16082 (2016).

[82]S. M. Nikitin, N. Chigarev, V. Tournat, A. Bulou, D. Gasteau, B. Castagnede, A. Zerr, and V. E. Gusev, "Revealing sub-Mm and Mm-scale textures in H 2 O ice at megabar pressures by time-domain Brillouin scattering", Scientific Reports **5**, 1–11 (2015).

[83]J. G. Dil, "Brillouin scattering in condensed matter", Reports on Progress in Physics **45**, 285–334 (1982).

[84]S. M. Nikitin, V. Tournat, N. Chigarev, A. Bulou, B. Castagnede, A. Zerr, and V. Gusev, "Directivity patterns and pulse profiles of ultrasound emitted by laser action on interface between transparent and opaque solids: analytical theory", Journal of Applied Physics **115**, 044902 (2014).

[85]A. M. Lomonosov, A. Ayouch, P. Ruello, G. Vaudel, M. R. Baklanov, P. Verdonck, L. Zhao, and V. E. Gusev, "Nanoscale Noncontact Subsurface Investigations of Mechanical and Optical Properties of Nanoporous Low- k Material Thin Film", ACS Nano **6**, 1410–1415 (2012).

[86]M. Khafizov, J. Pakarinen, L. He, H. Henderson, M. Manuel, A. Nelson, B. Jaques, D. Butt, and D. Hurley, "Subsurface imaging of grain microstructure using picosecond ultrasonics", Acta Materialia **112**, 209–215 (2016).

[87]Y. Wang, D. H. Hurley, Z. Hua, G. Sha, S. Raetz, V. E. Gusev, and M. Khafizov, "Nondestructive characterization of polycrystalline 3D microstructure with time-domain Brillouin scattering", Scripta Materialia **166**, 34–38 (2019).

[88]O. B. Wright, "Thickness and sound velocity measurement in thin transparent films with laser picosecond acoustics", Journal of Applied Physics **71**, 1617–1629 (1992).

[89]K. E. O'Hara, X. Hu, and D. G. Cahill, "Characterization of nanostructured metal films by picosecond acoustics and interferometry", Journal of Applied Physics **90**, 4852–4858 (2001).

[90]A. Devos and R. Côte, "Strong oscillations detected by picosecond ultrasonics in silicon: evidence for an electronic-structure effect", Physical Review B **70**, 125208 (2004).

[91]A. Devos, R. Côte, G. Caruyer, and A. Lefèvre, "A different way of performing picosecond ultrasonic measurements in thin transparent films based on laser-wavelength effects", Applied Physics Letters **86**, 211903 (2005).

[92]F. Hudert, A. Bartels, T. Dekorsy, and K. Köhler, "Influence of doping profiles on coherent acoustic phonon detection and generation in semiconductors", Journal of Applied Physics **104**, 123509 (2008).

[93]C. Mechri, P. Ruello, J. M. Breteau, M. R. Baklanov, P. Verdonck, and V. Gusev, "Depth-profiling of elastic inhomogeneities in transparent nanoporous low-k materials by picosecond ultrasonic interferometry", Applied Physics Letters **95**, 091907 (2009).

[94]A. Steigerwald, Y. Xu, J. Qi, J. Gregory, X. Liu, J. K. Furdyna, K. Varga, A. B. Hmelo, G. Lüpke, L. C. Feldman, and N. Tolk, "Semiconductor point defect concentration profiles measured using coherent acoustic phonon waves", Applied Physics Letters **94**, 111910 (2009).

[95]D. Yarotski, E. Fu, L. Yan, Q. Jia, Y. Wang, A. J. Taylor, and B. P. Uberuaga, "Characterization of irradiation damage distribution near TiO2/SrTiO3 interfaces using coherent acoustic phonon interferometry", Applied Physics Letters **100**, 251603 (2012).

[96]J. Gregory, A. Steigerwald, H. Takahashi, A. Hmelo, and N. Tolk, "Erratum: "Ion implantation induced modification of optical properties in single-crystal diamond studied by coherent acoustic phonon spectroscopy"", Applied Physics Letters **103**, 049904 (2013).

[97]M. Kuriakose, S. Raetz, N. Chigarev, S. M. Nikitin, A. Bulou, D. Gasteau, V. Tournat, B. Castagnede, A. Zerr, and V. E. Gusev, "Picosecond laser ultrasonics for imaging of transparent polycrystalline materials compressed to megabar pressures", Ultrasonics **69**, 259–267 (2016).

[98]C. Rossignol, N. Chigarev, M. Ducousso, B. Audoin, G. Forget, F. Guillemot, and M. C. Durrieu, "In Vitro picosecond ultrasonics in a single cell", Applied Physics Letters **93**, 123901 (2008).

[99]S. Danworaphong, M. Tomoda, Y. Matsumoto, O. Matsuda, T. Ohashi, H. Watanabe, M. Nagayama, K. Gohara, P. H. Otsuka, and O. B. Wright, "Three-dimensional imaging of biological cells with picosecond ultrasonics", Applied Physics Letters **106**, 163701 (2015).

[100]F. Pérez-Cota, R. J. Smith, E. Moradi, L. Marques, K. F. Webb, and M. Clark, "High resolution 3D imaging of living cells with sub-optical wavelength phonons", Scientific Reports **6**, 39326 (2016).

[101]I. Chaban, H. D. Shin, C. Klieber, R. Busselez, V. E. Gusev, K. A. Nelson, and T. Pezeril, "Time-domain Brillouin scattering for the determination of laser-induced temperature gradients in liquids", Review of Scientific Instruments **88**, 074904 (2017).

[102]Y. Wang, D. H. Hurley, Z. Hua, T. Pezeril, S. Raetz, V. E. Gusev, V. Tournat, and M. Khafizov, "Imaging grain microstructure in a model ceramic energy material with optically generated coherent acoustic phonons", Nature Communications **11**, 1597 (2020).

[103]D. H. Hurley, O. B. Wright, O. Matsuda, T. Suzuki, S. Tamura, and Y. Sugawara, "Time-resolved surface acoustic wave propagation across a single grain boundary", Physical Review B **73**, 125403 (2006).

[104] *The Nobel Prize in Physics 1986*, https://www.nobelprize.org/prizes/physics/1986/summary/.

[105]C. Thomsen, H. T. Grahn, H. J. Maris, and J. Tauc, "Surface generation and detection of phonons by picosecond light pulses", Physical Review B **34**, 4129–4138 (1986).

[106]D. Royer and E. Dieulesaint, *Elastic Waves in Solids II: generation, Acousto-optic Interaction, Applications*, Chapter 8.3, pp. 195 - 203. (Springer Science & Business Media, Nov. 1999).

[107]O. Wright and V. Gusev, "Ultrafast generation of acoustic waves in copper", IEEE Transactions on Ultrasonics, Ferroelectrics, and Frequency Control **42**, 331–338 (1995).

[108]T. Pezeril, N. Chigarev, P. Ruello, S. Gougeon, D. Mounier, J.-M. Breteau, P. Picart, and V. Gusev, "Laser acoustics with picosecond collimated shear strain beams in single crystals and polycrystalline materials", Physical Review B **73**, 132301 (2006).

[109]O. B. Wright, "Ultrafast nonequilibrium stress generation in gold and silver", Physical Review B **49**, 9985–9988 (1994).

[110]S. A. Akhmanov and V. É. Gusev, "Laser excitation of ultrashort acoustic pulses: new possibilities in solid-state spectroscopy, diagnostics of fast processes, and nonlinear acoustics", Soviet Physics Uspekhi **35**, 153–191 (1992).

[111]I. L. Fabelinskii, *Molecular Scattering of Light* (Springer US, 1968).

[112]J. Xu and R. Stroud, *Acousto-optic devices: principles, design, and applications*, Wiley Series in Pure and Applied Optics (Wiley, New York, 1992).

[113]A. Ishimaru, "Wave propagation and scattering in random media. Volume 1 - Single scattering and transport theory", Wave propagation and scattering in random media. Vol. 1, by Ishimaru, A.. New York (NY, USA): Academic Press, 267 pp. Research supported by the U.S. Air Force, NSF, and NIH, 1978, `10.1016/B978-0-12-374701-3.X5001-7` (1978).

[114]V. E. Gusev, "Contra-intuitive features of time-domain Brillouin scattering in collinear paraxial sound and light beams", Photoacoustics **20**, 100205 (2020).

[115]S. A. Akhmanov and S. Y. Nikitin, *Physical Optics*, Chapter 14 (Oxford University Press, Oxford, New York, Apr. 1997).

[116]D. H. Hurley, O. B. Wright, O. Matsuda, V. E. Gusev, and O. V. Kolosov, "Laser picosecond acoustics in isotropic and anisotropic materials", Ultrasonics **38**, 470–474 (2000).

[117]T. Pezeril, P. Ruello, S. Gougeon, N. Chigarev, D. Mounier, J.-M. Breteau, P. Picart, and V. Gusev, "Generation and detection of plane coherent shear picosecond acoustic pulses by lasers: experiment and theory", Physical Review B **75**, 174307 (2007).

[118]M. Lejman, G. Vaudel, I. C. Infante, P. Gemeiner, V. E. Gusev, B. Dkhil, and P. Ruello, "Giant ultrafast photo-induced shear strain in ferroelectric BiFeO 3", Nature Communications **5**, 4301 (2014).

[119]T. Pezeril, "Generation and detection of picosecond shear acoustic waves: theory and experiments", Theses (Université du Maine, Nov. 2005).

[120]D. Royer and E. Dieulesaint, *Elastic Waves in Solids I: free and Guided Propagation*, Chapter 4. (Springer Science & Business Media, Nov. 1999).

[121]A. A. Karabutov, M. P. Matrosov, and N. B. Podymova, "Thermooptical generator of wideband shear-wave pulses", Acoustical Physics **39**, 196–197 (1993).

[122]T. Bienville and B. Perrin, "Generation and detection of quasi transverse waves in an anisotropic crystal by picosecond ultrasonics", 4 (2003).

[123]T. Pezeril, C. Klieber, S. Andrieu, and K. A. Nelson, "Optical Generation of Gigahertz-Frequency Shear Acoustic Waves in Liquid Glycerol", Physical Review Letters **102**, 107402 (2009).

[124]O. Matsuda and O. B. Wright, "Theory of Detection of Shear Strain Pulses with Laser Picosecond Acoustics", Analytical Sciences/Supplements **17icpp**, s216–s218 (2002).

[125]O. Matsuda, O. B. Wright, D. H. Hurley, V. E. Gusev, and K. Shimizu, "Coherent Shear Phonon Generation and Detection with Ultrashort Optical Pulses", Physical Review Letters **93**, 095501 (2004).

[126]Y. Wang and M. Khafizov, "Shear waves generation by mode conversion in picosecond ultrasonics: impact of grain orientation and material properties", Journal of the American Ceramic Society, jace.17654 (2020).

[127]V. Gusev, P. Picart, D. Mounier, and J.-M. Breteau, "On the possibility of ultrashort shear acoustic pulse excitation due to the laser-induced electrostrictive effect", Optics Communications **204**, 229–236 (2002).

[128]W. E. Bron, M. Rossinelli, Y. H. Bai, and F. Keilmann, "Surface requirements for piezoelectric generation of high-frequency phonons", Physical Review B **27**, 1370–1375 (1983).

[129]C. Rossignol, B. Perrin, S. Laborde, L. Vandenbulcke, M. I. De Barros, and P. Djemia, "Nondestructive evaluation of micrometric diamond films with an interferometric picosecond ultrasonics technique", Journal of Applied Physics **95**, 4157–4162 (2004).

[130]H. J. McSkimin and P. Andreatch, "Elastic Moduli of Diamond as a Function of Pressure and Temperature", Journal of Applied Physics **43**, 2944–2948 (1972).

[131]*Diamond Anvil Cells and High Pressure Cell Manufacturers - Almax easyLab*, https://www.almax-easylab.com/index.aspx.

[132]R. H. Telling, C. J. Pickard, M. C. Payne, and J. E. Field, "Theoretical Strength and Cleavage of Diamond", Physical Review Letters **84**, 5160–5163 (2000).

[133]M. Kuriakose, S. Raetz, Q. M. Hu, S. M. Nikitin, N. Chigarev, V. Tournat, A. Bulou, A. Lomonosov, P. Djemia, V. E. Gusev, and A. Zerr, "Longitudinal sound velocities, elastic anisotropy, and phase transition of high-pressure cubic H 2 O ice to 82 GPa", Physical Review B **96**, 134122 (2017).

[134]*Neta, homepage, 2016*, https://www.neta-tech.com/fr/, (accessed 01-09-2021).

[135]A. Bartels, F. Hudert, C. Janke, T. Dekorsy, and K. Köhler, "Femtosecond time-resolved optical pump-probe spectroscopy at kilohertz-scan-rates over nanosecond-time-delays without mechanical delay line", Applied Physics Letters **88**, 041117 (2006).

[136]A. Abbas, Y. Guillet, J.-M. Rampnoux, P. Rigail, E. Mottay, B. Audoin, and S. Dilhaire, "Picosecond time resolved opto-acoustic imaging with 48 MHz frequency resolution", Optics Express **22**, 7831 (2014).

[137]D. B. Holland, "Design, Construction, and Applications of a High-Resolution Terahertz Time-Domain Spectrometer", PhD thesis (California Institute of Technology, 2014).

[138]N. Otsu, "A Threshold Selection Method from Gray-Level Histograms", IEEE Transactions on Systems, Man, and Cybernetics **9**, 62–66 (1979).

[139]P. Flandrin, *Time-Frequency/Time-Scale Analysis*, Chapter 2 (Academic Press Inc, San Diego, Sept. 1998).

[140]M. Llobera, "Building Past Landscape Perception With GIS: understanding Topographic Prominence", Journal of Archaeological Science **28**, 1005–1014 (2001).

[141]F. Auger, P. Flandrin, Y.-T. Lin, S. McLaughlin, S. Meignen, T. Oberlin, and H.-T. Wu, "Time-Frequency Reassignment and Synchrosqueezing: an Overview", IEEE Signal Processing Magazine **30**, 32–41 (2013).

[142]S. Meignen, D.-H. Pham, and S. Mclaughlin, "On Demodulation, Ridge Detection and Synchrosqueezing for Multicomponent Signals", IEEE Transactions on Signal Processing **65**, 2093–2103 (2017).

[143]S. Meignen, T. Oberlin, and D.-H. Pham, "Synchrosqueezing transforms: from low- to high-frequency modulations and perspectives", Comptes Rendus Physique **20**, 449–460 (2019).

[144]I. Daubechies and S. Maes, "A Nonlinear Squeezing of the Continuous Wavelet Transform Based on Auditory Nerve Models", in *WAVELETS in Medicine and Biology* (Routledge, 1996).

[145]I. Daubechies, J. Lu, and H.-T. Wu, "Synchrosqueezed wavelet transforms: an empirical mode decomposition like tool", Applied and Computational Harmonic Analysis **30**, 243–261 (2011).

[146]P.-S. Liao, T.-S. Chen, and P. Chung, "A Fast Algorithm for Multilevel Thresholding", J. Inf. Sci. Eng., `10.6688/JISE.2001.17.5.1` (2001).

[147]H. Edelsbrunner, D. Kirkpatrick, and R. Seidel, "On the shape of a set of points in the plane", IEEE Transactions on Information Theory **29**, 551–559 (1983).

[148]H. Edelsbrunner and E. P. Mücke, "Three-dimensional alpha shapes", ACM Transactions on Graphics **13**, 43–72 (1994).

[149]L. Merrill and W. A. Bassett, "Miniature diamond anvil pressure cell for single crystal x-ray diffraction studies", Review of Scientific Instruments **45**, 290–294 (1974).

[150]M. Kuriakose, N. Chigarev, S. Raetz, A. Bulou, V. Tournat, A. Zerr, and V. E. Gusev, "*In situ* imaging of the dynamics of photo-induced structural phase transition at high pressures by picosecond acoustic interferometry", New Journal of Physics **19**, 053026 (2017).

[151]A. Polian and M. Grimsditch, "Brillouin scattering from H 2 O: liquid, ice VI, and ice VII", Physical Review B **27**, 6409–6412 (1983).

[152]H. Shimizu, T. Nabetani, T. Nishiba, and S. Sasaki, "High-pressure elastic properties of the VI and VII phase of ice in dense H 2 O and D 2 O", Physical Review B **53**, 6107–6110 (1996).

[153]M. Lejman, G. Vaudel, I. C. Infante, I. Chaban, T. Pezeril, M. Edely, G. F. Nataf, M. Guennou, J. Kreisel, V. E. Gusev, B. Dkhil, and P. Ruello, "Ultrafast acousto-optic mode conversion in optically birefringent ferroelectrics", Nature Communications **7**, 12345 (2016).

[154]H. Simons, A. King, W. Ludwig, C. Detlefs, W. Pantleon, S. Schmidt, F. Stöhr, I. Snigireva, A. Snigirev, and H. F. Poulsen, "Dark-field X-ray microscopy for multiscale structural characterization", Nature Communications **6**, 6098 (2015).

[155]E. H. R. Tsai, J. Billaud, D. F. Sanchez, J. Ihli, M. Odstrčil, M. Holler, D. Grolimund, C. Villevieille, and M. Guizar-Sicairos, "Correlated X-Ray 3D Ptychography and Diffraction Microscopy Visualize Links between Morphology and Crystal Structure of Lithium-Rich Cathode Materials", iScience **11**, 356–365 (2019).

[156]F.-C. Chiu and C.-M. Lai, "Optical and electrical characterizations of cerium oxide thin films", Journal of Physics D: Applied Physics **43**, 075104 (2010).

[157]C. F. Macrae, I. Sovago, S. J. Cottrell, P. T. A. Galek, P. McCabe, E. Pidcock, M. Platings, G. P. Shields, J. S. Stevens, M. Towler, and P. A. Wood, "Mercury 4.0: from visualization to analysis, design and prediction", Journal of Applied Crystallography **53**, 226–235 (2020).

[158]D. Y. Chung and V. Konecny, "The determination of the orientation of cubic crystals from measured sound velocities", physica status solidi (a) **52**, 29–33 (1979).

[159]A. Duda and T. Paszkiewicz, "Application of ultrasonic measurements to determine the orientation of crystalline samples", Physica B: Condensed Matter **316–317**, 118–121 (2002).

[160]S. A. Self, "Focusing of spherical Gaussian beams", Applied Optics **22**, 658 (1983).

[161]A. P. Prudnikov, Y. A. Brychkov, and O. I. Marichev, *Integrals and series, vol. I: elementary functions* (Gordon and Breach Science Publishers, London, 1998).

[162]R. Côte and A. Devos, "Refractive index, sound velocity and thickness of thin transparent films from multiple angles picosecond ultrasonics", Review of Scientific Instruments **76**, 053906 (2005).

[163]W. M. Haynes, "CRC Handbook of Chemistry and Physics", 2643.

DOCTORAT BRETAGNE SCIENCES LOIRE POUR L'INGENIEUR

Le Mans Université

Titre : Développement de méthodes opto-acousto-optiques pour l'imagerie tridimensionnelle de matériaux par ondes nanoacoustiques de compression et cisaillement.

Mot clés : Diffusion Brillouin résolue en temps (TDBS), Ultrasons lasers, Imagerie 3-D nanométrique, Ondes transversales, Matériaux polycristallins, Interfaces inclinées

Résumé : Des techniques d'imagerie permettant de sonder les propriétés des matériaux à l'échelle nanométrique ont été développées depuis de nombreuses années dans le but de fournir des outils de diagnostic dans les domaines de la science des matériaux et de la médecine. Ces études à l'échelle nanométrique sont importantes, car elles permettent de comprendre les propriétés macroscopiques des matériaux à partir de leur structure nanométrique. L'utilisation de lasers ultrarapides pour générer des impulsions acoustiques nanométrique est couplée à la technique de détection de la diffusion Brillouin résolue en temps (TDBS) pour mesurer la propagation de ces impulsions dans des matériaux transparents. Cette thèse de doctorat s'est concentrée sur le développement d'une procédure de traitement du signal étape par étape dans le but de reconstruire la structure des échantillons en 3-D à partir des scans TDBS. La procédure est divisée en trois étapes : la première permet d'extraire le contenu acoustique des signaux, la seconde donne accès aux évolutions temps-fréquence du contenu acoustique et enfin la troisième forme la structure des échantillons scannés à partir des résultats de la deuxième étape. La méthode de traitement mise au point a été utilisée pour étudier la structure tridimensionnelle de deux matériaux polycristallins transparents : une glace d'eau (H_2O) à haute pression et un polycristal de dioxyde de cérium, ou céria (CeO_2). L'image 3-D de ceria met en évidence une frontière inclinée entre deux grains, justifiant l'extension de la théorie TDBS pour le cas de la réfraction des impulsions acoustiques, où les directions de propagation du laser sonde et des impulsions acoustiques ne sont plus colinéaires.

Title: Development of opto-acousto-optical methods for three dimensional material imaging with nano-acoustic longitudinal and transversal waves.

Keywords: Time-domain Brillouin scattering (TDBS), Laser ultrasonics, Nanoscale 3-D imaging, Transversal waves, Polycrystalline materials, Inclined interfaces

Abstract: Imaging techniques, used to probe material properties at the nanometric scale, have been developed for many years in the aim of providing tools for the diagnostics in the material and medical science fields. Such nanoscale studies are important for the comprehension of macro-scale properties from the nanoscale structure of materials. The use of ultrafast lasers to generate nanoscale acoustic pulses is coupled to the time-domain Brillouin scattering (TDBS) detection technique to monitor the propagation of acoustic pulses in transparent samples. This PhD thesis focused on the development of a step-by-step signal processing procedure for revealing the 3-D reconstruction of the samples from TDBS scans. The procedure is divided in three steps: a first one to extract the acoustic content from reflectivity signals, a second step to compute the time-frequency evolutions of the acoustic content and finally a third step to shape the structure of the scanned samples from the results of the second step. The developed processing method has been employed to investigate the 3-D structure of two transparent polycrystalline materials: a high-pressure water (H_2O) ice and a cerium dioxide, or ceria (CeO_2), samples. The 3-D imaging of a buried inclined boundary between two grains in the ceria scan justified the extension of the TDBS theory to the case of acoustic pulse refraction with non-collinear probe light and acoustic pulse propagation directions.